

ABSTRACT

Title of Document: THE ROLE OF DENSITY GRADIENT IN
LIQUID ROCKET ENGINE COMBUSTION
INSTABILITY

Amardip Ghosh, PhD, 2008

Directed By: Professor Kenneth H. Yu, Department of
Aerospace Engineering

Experimental and analytical studies were conducted to investigate key physical mechanisms responsible for flame-acoustic coupling during the onset of acoustically driven combustion instabilities in liquid rocket engines (LREs). Controlled experiments were conducted in which a turbulent Hydrogen-Oxygen ($\text{GH}_2\text{-GO}_2$) diffusion flame, established downstream of a two-dimensional model shear coaxial injector was acoustically forced by a compression driver unit mounted in a transverse direction and excited through a broad range of frequencies (200Hz-2000Hz) and amplitudes. Characteristic interactions between flame and acoustics visualized through OH^* and CH^* chemiluminescence imaging and dynamic pressure measurements obtained using high frequency dynamic pressure transducers indicated that small acoustic disturbances could be amplified by flame-acoustic coupling under certain conditions leading to substantial modulation in spatial heat release fluctuations. Density gradient between fuel and oxidizer was found to significantly

affect the way acoustic waves interacted with density stratified flame fronts. The particular case of an asymmetric flame front oscillation under transverse acoustic forcing indicated that baroclinic vorticity, generated by the interactions between misaligned pressure gradient (across the acoustic wave) and density gradient (across the fuel oxidizer interface) could further amplify flame front distortions. Asymmetric interaction between flame and acoustics is shown to occur preferentially on flame fronts where controlled waves from the compression driver travel from lighter fluid to denser fluid and the amount of interaction between flame and acoustics is shown to depend strongly on the density ratio between the fluids on either sides of the flame front. This observation is in agreement with the baroclinic vorticity mechanism and a variant of the classical Rayleigh-Taylor instability mechanism. The results provide the first known experimental evidence that baroclinic vorticity could play a role in triggering flame-acoustic interactions associated with LRE shear coaxial injectors. Parametric studies investigating the sensitivity of flame-acoustic interaction on key physical parameters that govern shear coaxial injector operations (including density ratio, velocity ratio, momentum ratio and chemical composition of the fuel) were conducted by varying the parameter of interest independently while holding the other parameters relatively constant. Density ratios ranging from 1 to 16, velocity ratios ranging from 3.02 to 5.27, momentum ratios ranging from 0.67 to 2.12 and fuel mixtures ranging from pure Hydrogen to 10%-90% GH₂-GCH₄ combination were tested. It is shown that in the ranges considered, flame-acoustic interaction is most sensitively affected by density ratio changes. Spectral measurements of flame front oscillations using local chemiluminescence measurements further revealed the non-

linear nature of the interaction process : a flame system forced at 1150 Hz gave rise not only to 1150 Hz oscillations but also triggered flame oscillations occurring at substantially lower frequencies. Analytical models were developed to interpret and predict acoustic modes of a combustion chamber containing a density stratified flowfield subjected to transverse acoustic disturbances. Incorporating both the known phenomenon of jet mixing length and the new experimental result of preferential excitation, the models allow different resonant behaviors to occur for separate regions of the combustor bounded by sudden changes in density. For isothermal experiments where the flow temperatures were known, calculated Eigen frequencies were in good agreement with measured frequencies. Overall, the identification of fuel-oxidizer density ratio as a critical parameter in flame acoustic coupling and the identification of baroclinic vorticity as a potential mechanism in flame acoustic coupling are significant because a reduction in the density gradient between fuel and oxidizer could be used as a control mechanism to improve flame stability in liquid rocket engines.

THE ROLE OF DENSITY GRADIENT IN LIQUID ROCKET ENGINE
COMBUSTION INSTABILITY

By

Amardip Ghosh

Dissertation submitted to the Faculty of the Graduate School of the
University of Maryland, College Park, in partial fulfillment
of the requirements for the degree of
Doctor of Philosophy
2008

Advisory Committee:

Associate Professor Kenneth H. Yu, Chair

Professor Ashwani K. Gupta

Associate Professor David Akin

Associate Professor Christopher Cadou

Associate Professor Arnaud Trouvé

© Copyright by
Amardip Ghosh
2008

Dedication

To my parents for their continuing support and blessings and great faith in all my efforts and endeavors.

Acknowledgements

I am grateful to Dr. Kenneth Yu, my faculty advisor and the director of the space vehicle research institute for his many valuable suggestions and constructive criticisms, both in the course of the research and in the writing of this dissertation. His simple yet keen insight into the nature of various fluid mechanical processes has significantly changed my way of looking at experimental data. Between the times when I started off with this project and now when I am about to finish I feel that this has made me a substantial change in my ability as a researcher. I am grateful to Dr. Arnaud Trouvé and Dr. Tingguang Ma of the Fire Protection Engineering department who worked closely in developing numerical simulations corresponding to some of my experiments. I am grateful to my family here in Timonium and all my friends here at College Park who made life in the lab and on campus enjoyable. Thanks are due to Ipshita Chakraborty, Mike Krasel and Colin VanDercreek for proofreading my thesis, Rebanta Chakraborty for always being curious about my research in particular and my life in general, Qina Diao for helping me in conducting many of the experiments reported in this work, Vivek Gautam for reminding me in the early days of my research that my work was good but not enough, Abhishek, Anand, Siddharth and Sachin for making life at 7422 W Park more like that of a family, Anna Obizhaeva for offering her help in improving the quality of my slides for presentation and Ranjeeta Pal for being an affectionate sister and checking on me every now and then. I am grateful to my committee members for their time and critical evaluation. This research was supported by NASA SVTI with Claudia Meyer as program manager.

The support is gratefully acknowledged. I am grateful to my parents, whose supportive role in my education and upbringing is beyond words. Finally, I am grateful to the humble towns of Hyattsville and College Park, for giving me the chance to live learn and grow.

Table of Contents

Dedication	ii
Acknowledgements	iii
Table of Contents	v
List of Tables	viii
List of Figures	x
Nomenclature	xxi
Chapter 1: Introduction	1
1.1 Background and Motivation	1
1.2 Key Physical Mechanisms	6
1.2.1 Baroclinic Vorticity Driven Instability	6
1.2.2 Rayleigh-Taylor Instability	7
1.2.3 Richtmyer-Meshkov Instability	7
1.3 Technical Objectives	8
1.4 Scope of the Present Work	9
Chapter 2: Literature Review	13
2.1 Thermoacoustic Instabilities in Combustion Systems	13
2.1.1 Introduction	13
2.1.2 Historical Developments	15
2.1.3 Rayleigh's Criterion	17
2.1.4 Representative Work in the Area	20
2.2 Combustion Instability in Liquid Rocket Engines	24
2.2.1 Introduction	24
2.2.2 Representative Work in the Area	26
2.2.3 Prior Research involving Shear-Coax Injector Element	33
2.3 Acoustically Driven Instabilities	35
2.3.1 Introduction	35
2.3.2 Unsteady Atomization under Acoustic Oscillations	35
2.3.3 Unsteady Vaporization under Acoustic Oscillations	38
2.3.4 Flame Response under Acoustic Oscillations	39
Chapter 3: Review of Key Physical Mechanisms	43
3.1 Baroclinic Vorticity Driven Instabilities	43
3.2 RM and RT instability of acoustically accelerated interfaces	46
3.3 Jet Preferred Mode and Wake Mode Instabilities	50
Chapter 4: Experimental Apparatus and Techniques	53
4.1 Introduction	53
4.2 Description of Apparatus	54
4.2.1 Combustor Geometry	54
4.2.2 Inlet Section	55
4.2.3 Supply System for Fuel and Oxidizer	56
4.2.4 Acoustic Driver	56
4.3 Instrumentation and Diagnostics	56
4.3.1 Schlieren Imaging	56

4.3.2 Phase Sensitive OH*/CH* Chemiluminescence Visualizations	57
4.3.3 Dynamic Pressure Measurements	58
4.3.4 High Speed Cinematographic Imaging	59
4.3.5 Hotwire Measurements	59
4.3.6 OH* / CH* Chemiluminescence Oscillation Measurements	59
4.3.7 Other Lab Equipments	60
4.4 Flow Rate Calculations	61
4.5 Injection Arrangement.....	62
4.6 Firing sequence for reacting flow experiments	63
4.6.1 Ignition	63
4.6.2 Extinction	64
Chapter 5 : Experimental and Analytical Characterization of Chamber Acoustics using Broad-Band Forcing	66
5.1 Preliminary Experiments.....	67
5.2 Model Development.....	68
5.2.1 Full Mixing Model / Well Stirred Reactor Model.....	71
5.2.2 Jet Mixing Length Model.....	72
5.2.3 Acoustically Driven Entrainment Model	73
5.3 Comparison of Isothermal Case Data with Model.....	75
5.4 Extension to Density Stratified Reacting Flows	76
Chapter 6: Acoustic Excitation of Density Stratified Non-Reacting Flow Fields	77
6.1 Acoustic Modes.....	78
6.1.1 Characteristic Acoustic Frequencies	78
6.1.2 Acoustic Excitation at Characteristic Frequencies.....	78
6.2 Hydrodynamic Modes.....	82
6.2.1 Characteristic Hydrodynamic Frequencies	83
6.2.2 Acoustic Excitation at Characteristic Hydrodynamic Frequencies.....	85
Chapter 7: Acoustic Excitation of Chemically Reacting Flow Fields	87
7.1 Characteristic Flame Acoustic Interactions.....	87
7.2 Baroclinic Vorticity as a Potential Mechanism.....	89
7.2.1 Pressure Amplitude Change Experiment	92
7.2.2 Density Ratio Change Experiment.....	93
7.2.3 Density Gradient Reversal Experiment.....	95
7.2.4 Further Considerations for the Density Ratio Variation Tests.....	98
7.3 Estimation of Growth Rates for the Flame Perturbations	104
7.4 Parametric Studies.....	105
7.4.1 Dimensional Analysis	105
7.4.2 Effect of Density Ratio.....	108
7.4.3 Effect of Velocity Ratio.	109
7.4.4 Effect of Momentum Ratio	110
7.4.5 Effect of Chemical Composition of Fuel.	112
7.5 Spectral Measurements and High Speed Imaging.....	114
7.5.1 High Speed Imaging Results.....	114
7.5.2 PMT tube OH* Chemiluminescence oscillation results	115
Chapter 8: Summary and Conclusions	119
8.1 Summary of key tasks	119

8.2 Summary of important findings	121
8.2.1 Qualitative characterization of flame-acoustic interactions	121
8.2.2 Identification of new physical mechanism.....	123
8.2.3 Sensitivity analysis and measurements	125
8.2.4 Non-linear response in flame-acoustic interaction.....	129
8.2.5 Model development.....	129
8.3 Concluding remark.....	132
Appendices	133
Appendix A: Images.....	133
Appendix B: Tables.....	221
Appendix C: Gas Properties.....	230
Bibliography.....	231

List of Tables

- Table 3.1. Location of pressure taps. y-axis is streamwise, x-axis is transverse.
- Table 5.1. Comparison of measured spectral peak frequencies and calculated resonance frequencies for no-flow with quiescent air.
- Table 5.2. Flow conditions for the different test runs for model development.
- Table 5.3. Comparison of measured spectral peak frequencies and calculated resonance frequencies for isothermal flow conditions.
- Table 5.4. Comparison of measured spectral peak frequencies under reacting flow conditions.
- Table 7.1. Test conditions for flame response to acoustic forcing at characteristic frequencies.
- Table 7.2. Test conditions for the density ratio variation experiments.
- Table 7.3. Test conditions for the reversal of density gradient experiments.
- Table 7.4. Test conditions for change in flame heat release experiments.
- Table 7.5. Test conditions for variation in jet momentum experiments.
- Table 7.6. Flow conditions for the simultaneous measurement of pressure and chemiluminescence oscillations.
- Table 7.7. Test conditions for velocity ratio experiments.
- Table 7.8. Test conditions for variation in jet momentum through variation in jet densities.
- Table 7.9. Test conditions for variation in jet momentum through variation in jet velocities.

Table 7.10. Test conditions for flame-acoustic experiments using GH2-GCH4 blended fuel and Oxygen.

List of Figures

Figure 1.1. Schematic showing typical flow field in the neighborhood of a LOX- GH2 shear coaxial injector.

Figure 3.1. Baroclinic interactions between pressure gradient and density gradient at a density stratified interface. (a) Destabilizing interaction. (b) Stabilizing interaction.

Figure 3.2. RT unstable configurations. (a) Single-mode case. (b) Multi-mode case (After Kumar, 2003).

Figure 3.3. RT instability, single wavelength initial perturbation (After Youngs 1984).

Figure 3.4. Richtmyer-Meshkov instability (After Sunhara *et al.*,1996).

Figure 3.5. Jet preferred mode instability.

Figure 3.6. Wake mode instability.

Figure 4.1. (a) Physical model. (b) Schematic of the shear-coax injector rig. All dimensions are in inches.

Figure 4.2. Schematic view of shear coax combustor. (a) Overall setup (b) Near injector region showing pressure tap locations. All dimensions are in inches.

Figure 4.3. Physical setup.

Figure 4.4. Physical model of inlet to combustor.

Figure 4.5. Schematic showing dimensions for inlet to combustor. All dimensions are in inches.

Figure 4.6. Schematic showing position and size of through holes for bolts for fixing the side plates between which the center piece is sandwiched. All dimensions are in inches.

Figure 4.7. Schematic showing side plate with injection location for gases. All dimensions are in inches.

Figure 4.8. Schlieren setup. (a) Laboratory arrangement. (b) Schematic.

Figure 4.9. Kistler dynamic pressure sensor locations. cf. Table 3.1. for location of pressure taps. All dimensions are in inches.

Figure 4.10. Injection arrangement for reversal of density gradient test. (a) Normal configuration. (b) Reversed configuration.

Figure 4.11. Injection arrangement for the different tests. (a) Effect of density ratio. (b) Effect of velocity ratio. (c) Effect of chemical composition of fuel.

Figure 5.1. Pressure spectrum at (a) Tap #1, (b) Tap #2, (c) Tap #3, (d) Tap#4 . No-flow conditions. Chamber is excited with band limited white noise forcing.

Figure 5.2. Pressure spectrum of no flow quiescent air excited with white noise redrawn from previous figure. Tap #4.

Figure 5.3. Pressure spectrum of isothermal case excited with white noise. Density ratio = 14.5. (a) Tap #1, (b) Tap #2, (c) Tap #3, (d) Tap #4.

Figure 5.4. Pressure spectrum of isothermal case excited with white noise. Density ratio = 11. (a) Tap #1, (b) Tap #2, (c) Tap #3, (d) Tap #4.

Figure 5.5. Pressure spectrum of isothermal case excited with white noise. Density ratio = 7. (a) Tap #1, (b) Tap #2, (c) Tap #3, (d) Tap #4.

Figure 5.6. Schematic showing distribution of acoustic media in a combustor.

Figure 5.7. Schlieren visualization showing three different acoustic regions of the combustor. Regions 1 and 3 are product dominated and can have different resonant

behaviors in the longitudinal direction because they are bounded from each other by interfaces with sudden density changes.

Figure 5.8. Comparison of experimental and predicted values of resonant frequencies for isothermal case.

Figure 5.9. Pressure spectrum of reacting flow case excited with white noise. Density ratio = 14.5. (a) Tap #1, (b) Tap #2, (c) Tap #3, (d) Tap #4.

Figure 5.10. Pressure spectrum of reacting flow case excited with white noise. Density ratio = 11. (a) Tap #1, (b) Tap #2, (c) Tap #3, (d) Tap #4.

Figure 5.11. Pressure spectrum of reacting flow case excited with white noise. Density ratio = 7. (a) Tap #1, (b) Tap #2, (c) Tap #3, (d) Tap #4.

Figure 6.1. Flow arrangement. Band limited (100Hz – 10KHz) white noise forcing is applied from the left. Center jet of air is at 6m/s and co-flowing Helium jets are at 18m/s.

Figure 6.2. Pressure spectrum of isothermal case excited with white noise. He-18m/s-Air-6m/s-He-18m/s. (a) Tap #1, (b) Tap #2, (c) Tap #3, (d) Tap#4.

Figure 6.3. Pressure spectrum of isothermal case excited with white noise redrawn from previous figure (Tap #4). He-18m/s-Air-6m/s-He-18m/s.

Figure 6.4(a). Baseline case, no forcing, exposure – 30 μ s, He-18m/s-Air-6m/s-He-18m/s.

Figure 6.4(b). Flow response to forcing from left at 200 Hz, 40vpp, exposure – 30 μ s, He-18m/s-Air-6m/s-He-18m/s.

Figure 6.4(c). Flow response to forcing from left at 234.4 Hz, 40vpp, exposure – 30 μ s, He-18m/s-Air-6m/s-He-18m/s.

Figure 6.4(d). Flow response to forcing from left at 400.4 Hz, 40vpp, exposure – 30 μ s, He-18m/s-Air-6m/s-He-18m/s.

Figure 6.4(e). Flow response to forcing from left at 500 Hz, 40vpp, exposure – 30 μ s, He-18m/s-Air-6m/s-He-18m/s.

Figure 6.4(f). Flow response to forcing from left at 625 Hz, 40vpp, exposure – 30 μ s, He-18m/s-Air-6m/s-He-18m/s.

Figure 6.4(g). Flow response to forcing from left at 771.5 Hz, 40vpp, exposure – 30 μ s, He-18m/s-Air-6m/s-He-18m/s.

Figure 6.4(h). Flow response to forcing from left at 820.3 Hz, 40vpp, exposure – 30 μ s, He-18m/s-Air-6m/s-He-18m/s.

Figure 6.4(i). Flow response to forcing from left at 947.3 Hz, 40vpp, exposure – 30 μ s, He-18m/s-Air-6m/s-He-18m/s.

Figure 6.4(j). Flow response to forcing from left at 1016 Hz, 40vpp, exposure – 30 μ s, He-18m/s-Air-6m/s-He-18m/s.

Figure 6.4(k). Flow response to forcing from left at 1094 Hz, 40vpp, exposure – 30 μ s, He-18m/s-Air-6m/s-He-18m/s.

Figure 6.4(l). Flow response to forcing from left at 1094 Hz, 50vpp, exposure – 30 μ s, He-18m/s-Air-6m/s-He-18m/s.

Figure 6.4(m). Flow response to forcing from left at 1250 Hz, 50vpp, exposure – 10 μ s, He-18m/s-Air-6m/s-He-18m/s.

Figure 6.4 (n). Flow response to forcing from left at 1850 Hz, 50vpp, exposure – 10 μ s, He-18m/s-Air-6m/s-He-18m/s.

Figure 6.4 (o). Flow response to forcing from left at 2676 Hz, 50vpp, exposure – 10 μ s, He-18m/s-Air-6m/s-He-18m/s.

Figure 6.5. Acoustic regions of the combustor. Tap #1 measures acoustic signature in Region 1 while Tap #4 measures acoustic signature in Region 3.

Figure 6.6. Comparison of pressure spectrum between Tap #1 and Tap #4 of isothermal case excited with white noise. He-18m/s-Air-6m/s-He-18m/s.

Figure 6.7. Schematic for wake mode instability calculation.

Figure 6.8. (a) Injection arrangement (b) Hotwire probe location.

Figure 6.9. Frequency response of velocity in unforced and forced cases (monotone excitation).

Figure 6.10. Frequency response of velocity in unforced and forced cases (broadband excitation).

Figure 6.11(a). Baseline, no forcing, exposure – 30 μ s, He-18m/s-Air-6m/s-He-18m/s.

Figure 6.11(b). Flow response to forcing from left at 429.7 Hz, 4 Vpp. Exposure – 30 μ s, He-18m/s-Air-6m/s-He-18m/s.

Figure 6.11(c). Flow response to forcing from left at 429.7 Hz, 12 Vpp. Exposure – 30 μ s, He-18m/s-Air-6m/s-He-18m/s.

Figure 6.11(d). Flow response to forcing from left at 429.7 Hz, 16 Vpp. Exposure – 30 μ s, He-18m/s-Air-6m/s-He-18m/s.

Figure 6.11(e). Flow response to forcing from left at 429.7 Hz, 20 Vpp. Exposure – 30 μ s, He-18m/s-Air-6m/s-He-18m/s.

Figure 6.11(f). Flow response to forcing from left at 429.7 Hz, 30 Vpp. Exposure – 30 μ s, He-18m/s-Air-6m/s-He-18m/s.

Figure 6.11(g). Flow response to forcing from left at 429.7 Hz, 40 Vpp. Exposure – 30 μ s, He-18m/s-Air-6m/s-He-18m/s.

Figure 6.11(h). Flow response to forcing from left at 429.7 Hz, 50 Vpp. Exposure – 30 μ s, He-18m/s-Air-6m/s-He-18m/s.

Figure 7.1. Flow arrangement for the GH2 / GO2 / GH2 turbulent diffusion flame system. $V_{O_2} = 6$ m/s, $V_{H_2} = 18$ m/s, $Re_{O_2} = 4900$. Acoustic forcing is from the left.

Figure 7.2. OH* chemiluminescence showing natural instabilities in an unforced GH2 / GO2 / GH2 turbulent flame. $V_{O_2} = 6$ m/s, $V_{H_2} = 18$ m/s, $Re_{O_2} = 4900$.

Figure 7.3. Pressure spectrum from Tap #4 under band limited (100Hz-10kHz) white noise excitation (9 watts).

Figure 7.4. OH* chemiluminescence at various phases of oscillation (0^0 , 90^0 , 180^0 and 270^0) of a GH2 / GO2 / GH2 turbulent flame forced at 300 Hz from the left. $V_{O_2} = 6$ m/s, $V_{H_2} = 18$ m/s, $Re_{O_2} = 4900$. D is the width of the center jet = 0.75 inch.

Figure 7.5. OH* chemiluminescence at various phases of oscillation (0^0 , 90^0 , 180^0 and 270^0) of a GH2 / GO2 / GH2 turbulent flame forced at 1150 Hz from the left. $V_{O_2} = 6$ m/s, $V_{H_2} = 18$ m/s, $Re_{O_2} = 4900$. D is the width of the center jet = 0.75 inch.

Figure 7.6. Contour plots showing flame response to an increasing set of acoustic forcing amplitude. $V_{O_2} = 4.5$ m/s, $V_{H_2} = 13.5$ m/s, $Re_{O_2} = 3700$. Forcing is increasing from left to right and top to bottom, 0 watts, 4.5 watts, 5.3 watts, 7 watts, 9.6 watts and 12.5 watts.

Figure 7.7(a). Instantaneous OH* chemiluminescence images showing a monotonic decay of oscillations as density ratio between fuel and oxidizer is decreased from 15.9 to 5. $V_{O_2} = 4.5$ m/s, $V_{H_2} = 13.5$ m/s, $Re_{O_2} = 3700$.

Figure 7.7(b). Contour plots of ensemble averaged OH* chemiluminescence images showing a monotonic decay of oscillations as density ratio between fuel and oxidizer is decreased from 15.9 to 5. $V_{O_2} = 4.5$ m/s, $V_{H_2} = 13.5$ m/s, $Re_{O_2} = 3700$.

Figure 7.8. Normalized intensity for flame across the width of the combustion chamber for different oxidizer-fuel density ratios at an axial location $y/D=4.7$. At a given axial location, width of flame, $\delta(y) = |r_o - r_i|$, where the horizontal line corresponds to an intensity of 10% of the maximum.

Figure 7.9. Measured flame brush thickness at various density ratios and axial locations.

Figure 7.10. Flame brush thickness as a function of density ratio and acoustic forcing amplitude.

Figure 7.11. UV filtered flame image showing natural instabilities in an unforced Hydrogen-in-the-center turbulent diffusion flame. $V_{O_2/N_2} = 17.8$ m/s, $V_{H_2} = 5$ m/s, $Re_{H_2} \sim 600$, $Re_{O_2/N_2} \sim 8800$.

Figure 7.12(a). UV filtered images at various phases of oscillation (0° , 90° , 180° and 270°) of a Hydrogen-in-the-center turbulent diffusion flame forced at 300 Hz (at 30 Vpp) from the left. $V_{O_2/N_2} = 17.8$ m/s, $V_{H_2} = 5$ m/s, $Re_{H_2} \sim 600$, $Re_{O_2/N_2} \sim 8800$.

Figure 7.12(b). UV filtered images at various phases of oscillation (0° , 90° , 180° and 270°) of a Hydrogen-in-the-center turbulent diffusion flame forced at 580 Hz (55Vpp) from the left. $V_{O_2/N_2} = 17.8$ m/s, $V_{H_2} = 5$ m/s, $Re_{H_2} \sim 600$, $Re_{O_2/N_2} \sim 8800$.

Figure 7.13. Dynamic pressure distribution across the flames. Pressure Tap #1 is closest to the speaker.

Figure 7.14. Variation of density ratio and heat release rate with molar dilution.

Figure 7.15. Comparison of flame-acoustic interaction under similar forcing and heat release, conditions (15 kW) but different density ratios. OH* chemiluminescence images. Density ratios from left to right are as 7.0 or 15.2, 7.0 and 15.2 respectively.

Figure 7.16. Growth rate of flame perturbation thickness as a function of streamwise location

Figure 7.17. Variation of density ratio and jet momentums with molar dilution. Momentum Total = Momentum, center Jet + 2x Momentum, Co-Flow Jet.

Figure 7.18. Outer jet momentum = 0.0055 kg.m/s^2 , center jet momentum = 0.0047 kg.m/s^2 . Density ratio between oxidizer and fuel is ~ 8 . Acoustic forcing is from the left and is held fixed at 15.8 Watts.

Figure 7.19. Outer jet momentum = 0.0055 kg.m/s^2 , center jet momentum = 0.0036 kg.m/s^2 . Density ratio between oxidizer and fuel is ~ 2 . Acoustic forcing is from the left and is held fixed at 15.8 Watts.

Figure 7.20. Pressure spectrum at Tap #1 (a) and at Tap #4 (b) for reacting flow-fields under white noise excitation for density ratios 16, 10 and 6.

Figure 7.21. Location of pressure measurement and OH* chemiluminescence oscillation measurement ports.

Figure 7.22. Comparison of local OH* chemiluminescence fluctuations responding to pressure oscillation at density ratio=14.5. The sensors are located horizontally at $x=-0.67d$ (left column) and $x=0.67d$ (right column), and vertically at (a) $y=5d$, (b) $y=3d$, (c) $y=1d$.

Figure 7.23. Comparison of local OH* chemiluminescence fluctuations responding to pressure oscillation at density ratio=3. The sensors are located horizontally at $x=-$

0.67d (left column) and $x=0.67d$ (right column), and vertically at (a) $y=5d$, (b) $y=3d$, (c) $y=1d$.

Figure 7.24. Classical RT mode instability analysis yields wavelength-dependent growth rate.

Figure 7.25. Amplification in growth rates as function of acoustic cycle.

Figure 7.26. Measured flame brush thickness at various density ratios and streamwise locations.

Figure 7.27. Instantaneous OH^* chemiluminescence images showing flame perturbations affected by fuel-oxidizer velocity ratio. Fuel oxidizer velocity ratios are in increasing order from left to right and from top to bottom. Velocity Ratios are as $u_f / u_o=3.02$, $u_f / u_o=3.36$, $u_f / u_o=3.64$, $u_f / u_o=4.01$, $u_f / u_o=4.51$, $u_f / u_o=5.03$ and $u_f / u_o=5.27$.

Figure 7.28. Time averaged OH^* chemiluminescence images showing flame perturbations affected by fuel-oxidizer velocity ratio. Fuel oxidizer velocity ratios are in increasing order from left to right and from top to bottom. Velocity ratios are as $u_f / u_o=3.02$, $u_f / u_o=3.36$, $u_f / u_o=3.64$, $u_f / u_o=4.01$, $u_f / u_o=4.51$, $u_f / u_o=5.03$ and $u_f / u_o=5.27$.

Figure 7.29. Measured flame brush thickness at various velocity ratios and streamwise locations.

Figure 7.30. Flame perturbations affected by fuel-oxidizer momentum ratio involving no change in velocity ratio. $u_f / u_o = 3$, $\rho_o / \rho_f = 6$, $\rho_o / \rho_f = 5$, $\rho_o / \rho_f = 4$, $\rho_o / \rho_f = 3$, $\rho_o / \rho_f = 2$, $J_o / J_f = 1.99$, $J_o / J_f = 1.67$, $J_o / J_f = 1.33$, $J_o / J_f = 1.00$, $J_o / J_f = 0.67$.

Figure 7.31. Flame perturbations affected by fuel-oxidizer momentum ratio involving no change in density ratio. $\rho_o / \rho_f = 7.99$, $u_f / u_o = 3.36$, $u_f / u_o = 3.64$, $u_f / u_o = 4.01$, $u_f / u_o = 4.51$, $u_f / u_o = 5.27$; $J_o/J_f = 2.12$, $J_o/J_f = 1.80$, $J_o/J_f = 1.49$, $J_o/J_f = 1.18$, $J_o/J_f = 0.86$.

Figure 7.32. Flame perturbations affected by non-dimensionalized fuel-oxidizer momentum difference. (a) Momentum change through velocity change. (b) Momentum change through density change.

Figure 7.33. Lifted flame using 100% CH₄. No acoustic excitation. (a) Instantaneous CH* chemiluminescence image (b) Instantaneous OH* chemiluminescence image (c) Average CH* chemiluminescence image (d) Average OH* chemiluminescence image.

Figure 7.34. 50% CH₄, 50% H₂ fueled flame acoustically excited from left at 1150 Hz (a) Instantaneous CH* chemiluminescence image (b) Instantaneous OH* chemiluminescence image (c) Average CH* chemiluminescence image (d) Average OH* chemiluminescence image.

Figure 7.35. Measured flame brush thickness at various fuel compositions and axial locations.

Figure 7.36. High-speed imaging showing a typical vortex pairing event when the GO₂ / GH₂ turbulent flame is forced at 1150 Hz. $V_{O_2} = 4.5$ m/s, $V_{H_2} = 13.5$ m/s., Center jet width, $D = 0.75$ inch.

Figure 7.37. Time domain and frequency domain measurement of OH* chemiluminescence oscillations using PMT. Probe location $(x, y) = (-0.375", 0.375")$ is shown by the circle on the flame image. $V_{O_2} = 4.5$ m/s, $V_{H_2} = 13.5$ m/s., Center jet width, $D = 0.75$ inch. Forcing is from left at 1150 Hz.

Figure 7.38. Time domain and frequency domain measurement of OH* chemiluminescence oscillations using PMT. Probe location $(x, y) = (-0.375'', 2.25'')$ is shown by the circle on the flame image. $V_{O_2} = 4.5$ m/s, $V_{H_2} = 13.5$ m/s., Center jet width, $D = 0.75$ inch. Forcing is from left at 1150 Hz.

Figure 7.39. Time domain and frequency domain measurement of OH* chemiluminescence oscillations using PMT. Probe location $(x, y) = (-0.375'', 3.75'')$ is shown by the circle on the flame image. $V_{O_2} = 4.5$ m/s, $V_{H_2} = 13.5$ m/s., Center jet width, $D = 0.75$ inch. Forcing is from left at 1150 Hz.

Figure 7.40. Time domain and frequency domain measurement of OH* chemiluminescence oscillations using PMT. Probe location $(x, y) = (-1.375'', 3.75'')$ is shown by the circle on the flame image. $V_{O_2} = 4.5$ m/s, $V_{H_2} = 13.5$ m/s., Center jet width, $D = 0.75$ inch. Forcing is from left at 1150 Hz.

Figure 7.41. Instantaneous OH* chemiluminescence image for a GH₂/GO₂/GH₂ flame forced at 1150 Hz from left (a) and OH* oscillation as picked up by PMT sensor at location marked 'A' (b) and 'B' (c). OH* oscillations are large when acoustic waves from driver are passing from lighter H₂ to denser O₂.

Nomenclature

\dot{m}	=	Mass flow rate
a	=	Speed of sound
ω	=	Vorticity
ρ	=	Density
u	=	Velocity
J	=	Momentum
Y	=	Mole fraction
n	=	Number of moles
δ	=	Excited flame brush thickness
D	=	Width of center jet
x	=	Distance in transverse direction
y	=	Distance in streamwise direction
ρ	=	Density
p	=	Pressure
T	=	Temperature
Re	=	Reynolds number
St	=	Strouhal number
f	=	Frequency
L	=	Length of Combustor
MW	=	Molecular weight

τ_{chem}	= Characteristic chemistry time scale
Q	= Heating rate (Joules/Mole)
μ	= Dynamic viscosity
ν	= Kinematic viscosity
γ	= Ratio of specific heats
A^*	= Choked orifice area
R	= Gas specific gas constant
p_o	= Stagnation pressure
T_o	= Stagnation temperature
I	= Intensity

Subscripts:

o	= Oxidizer
f	= Fuel
a	= Ambient
u	= Universal
p	= Products
max	= Maximum

Abbreviations

LRE	= Liquid Rocket Engine
LOX	= Liquid Oxygen

GO2 = Gaseous Oxygen
GH2 = Gaseous Hydrogen
GCH4 = Gaseous Methane
PMT = Photo-Multiplier-Tube
RT = Rayleigh-Taylor (Instability)
RM = Richtmyer-Meshkov (Instability)
KH = Kelvin-Helmholtz (Instability)
VK = Von Karman
FFT = Fast Fourier Transform
FPS = Frames Per Second
V_{pp} = Volts Peak-to-Peak (Acoustic Forcing Amplitude)
UV = Ultra Violet
RMS = Root Mean Square

Chapter 1: Introduction

1.1 Background and Motivation

Combustion instabilities remain among the most challenging problems encountered in power and propulsion systems in which, large amplitude pressure oscillations, driven by in phase heat release (Rayleigh 1945; Chu 1956; Putnam and Dennis 1954; Culick 1987) adversely affect the stability and survival of the flame, produce intense vibrations, enhance heat transfer rates (Rupe and Jaivin, 1964) and in certain extreme cases lead to catastrophic failures (Williams 1984; Putnam 1971; Candel 1992; Clayton and Rogero 1965).

In confined geometries where combustion occurs inside a combustion chamber, interactions leading to such instabilities take place as a result of acoustic, vortical, and/or entropy coupling (Lieuwen 2003). Acoustic coupling, in particular, involves the interaction of the flame with standing and/or traveling pressure waves, and has been studied both experimentally (Crump *et al.* 1986; Yu *et al.* 1991; Broda *et al.* 1991, Cohen *et al.* 2003; Lieuwen 2002) and theoretically (Marble and Candel 1978; Flandro *et al.* 2004; Lieuwen 2003; Subbaiah 1983; Lieuwen 2001; Zambon and Chelliah 2006). Under certain circumstances, small amplitude acoustic disturbances can cause large amplitude heat release oscillations. Self-sustaining oscillations can eventually be excited if the phase relation between the modulated burning rate variations and pressure oscillations is favorable, as per the Rayleigh's criteria (Rayleigh, Lord, 1945; Sreenivasan and Raghu 2000).

For liquid rocket engines in particular, transverse modes^ψ of the chamber (tangential and radial modes) are known to interact with combustion heat release resulting in high-frequency high-amplitude pressure oscillations (Culick and Yang 1995; Rubinsky 1995). Combustion instabilities characterized by such pressure oscillations are extremely destructive and the hardest ones to control (Crocco *et al.* 1960; Reardon *et al.* 1964). Male *et al.* (1954), for instance, report severe heat transfer rates, sometimes high enough to lead to destructive burnouts of entire thrust chamber assemblies during such instabilities. Reardon (1961), reports peak-to-peak values as high as 300% (of the steady chamber pressure) in the amplitudes of purely transverse modes. Clayton and Rogero (1965) report high amplitude tangential mode rotating detonation like pressure waves excited during resonant combustion of a 20,000 lbs thrust laboratory liquid rocket engine. Ebrahimi *et al.* (2000) report severe vibrations (greater than 1000g) that can practically impair operability of sensitive guidance instruments.

The interaction between transverse pressure waves and the flow field in the vicinity of the injector is critical to the instability problem. Acoustic fluctuations, for instance, in the neighborhood of the injector affect injection, atomization, vaporization, mixing and subsequent combustion of propellants and thereby influence the combustion characteristics and stability behavior of the entire engine. The role of a superimposed oscillatory field on unsteady atomization has consequently been

^ψ Transverse modes of instability dominate the rocket engine environment for various reasons. Firstly, most of these engines have a low length-to-diameter ratio (Fischbach *et al.* 2007) that allows transverse modes of comparable frequencies to be excited. Secondly, the exhaust nozzle dampens longitudinal modes to a greater extent as compared to the tangential modes (Oefelein and Yang 1993). Thirdly, shock waves perpendicular to the engine axis introduce additional dissipation for the longitudinal waves but not for the transverse ones (Maslen and Moore 1956).

investigated by several researchers in the past (cf. Cold flow experimental studies by Miesse (1955), Reba and Brosilow (1960), Buffum and Williams (1967); reacting flow experiments by Heidmann (1965) and Ingebo (1966), Lecourt and Foucaud (1987); Analytical studies by Clark (1964), Buffum and Williams (1967), Heidmann and Groeneweg (1969)). Unsteady vaporization under the influence of acoustic oscillations has also been studied by various investigators (cf. Wieber and Mickelsen (1960), Heidmann and Wieber (1966), Crocco *et al.* (1967), Abramzon and Sirignano (1988), Chiang, Raju and Sirignano (1989), Anderson and Winter (1992), Fichot, Harstad and Bellan (1993)). Combustion response to acoustic oscillations has been studied extensively and a detailed review is presented in section 2.3.4.. Various fluid mechanical and chemical processes that occur near the injector are more sensitive to velocity fluctuations that are parallel to the injector faceplate than to fluctuations that are normal to it. Also, because of higher densities near the injector faceplate, acoustic pressure amplitudes of purely tangential modes are found to be significantly higher near the injector than near the nozzle (Kim and Williams 1998) which contributes to an increase in the sensitivity of acoustic instabilities to the characteristics of flames near the injector. With the near injector region containing practically most of the mechanisms that lead to instability, (Oefelein and Yang 1993) such sensitivity often closes feedback loops and allows the transverse modes to grow through conditions favorable for positive thermo-acoustic coupling.

Although most injectors would be subjected interactions of this kind, for purposes of this research, the scope was restricted to flame acoustic interactions occurring in the near field of the shear coaxial injector. Such injectors, used for

instance in the Space Shuttle Main Engine (SSME), consist of a center jet of liquid Oxygen (LOX) surrounded by an annular co-flow of high speed gaseous Hydrogen (GH₂) (Fig. 1.1). Once injected into the chamber, the LOX jet is atomized and vaporized, and a diffusion flame is formed between GH₂ on one side and GO₂ on the other. At this initial stage of flame development, any physical mechanism that causes flame-acoustic coupling may cause modulations in spatial heat release fluctuation which in turn could allow pressure oscillations in the chamber to couple with it and drive the combustor unstable. Various fluid mechanical and chemical processes that occur near the shear coaxial injector could promote such instabilities. The shear layer between the fuel and the oxidizer, in the neighborhood of the injector is subjected to wake and jet mode instabilities that could be amplified by certain modes of acoustic oscillations in the chamber. Large difference in velocity between fuel and oxidizer makes the interface susceptible to Kelvin-Helmholtz (KH) instability and variants thereof (Rehab *et al.* 1997). The presence of a reacting interface between fuel and oxidizer which can be driven cellular under certain conditions makes it susceptible to thermo-diffusive instabilities (Matalon 2007, Kim *et al.* 1996). Interactions with finite amplitude steep fronted pressure waves^ψ generated through the excitation of chamber acoustics makes the density stratified interface between fuel and oxidizer susceptible to baroclinic vorticity driven instabilities. A variant of the Richtmyer-Meshkov (RM) instability arising from the passage of finite amplitude steep fronted pressure waves through the density stratified interface and a variant of the classic Rayleigh-Taylor (RT) instability arising from the acoustic acceleration of the density stratified

^ψ The flow of combustion energy to the acoustic waves may supersede the losses leading to the formation of non-linear large amplitude shock type steep fronted waves (Ebrahimi *et al.* 2000).

interface can also be triggered (Taylor 1950; Richtmyer 1960; Meshkov 1969; Markstein and Squire 1955). Direct Numerical Simulation (DNS) of violent folding of flame fronts under flame acoustic interaction driven RT instability has recently been reported (Petchenko *et al.* 2006). Once instability is excited through any of the competing processes, small amplitude acoustic disturbances can cause large amplitude fluid movement leading to significant modifications in flame surface area. This in turn can lead to a modulation of heat release oscillations driven at the acoustic excitation frequencies. Self-sustaining oscillations can eventually be excited if the phase relation between the modulated burning rate variations and pressure oscillations is favorable, as per the Rayleigh's criteria.

Unfortunately, although the shear coaxial injector is widely used in liquid rocket engines to deliver fuel and oxidizer into the combustion chamber (Hulka and Hutt 1995; Vingert *et al.* 1995) there is no definitive knowledge regarding which among several competing processes ultimately cause combustion instability in rocket motors that use them (Glogowski *et al.* 1994). Small changes in injector geometry and associated flow field variables like fuel-oxidizer velocity ratio, momentum ratio, injection temperature and injection pressure drop have been found to have significant effect on the overall stability of the engine (Hulka and Hutt 1995). However, physics-based understanding of such correlations are often not satisfactory. Consequently, passive control strategies involving the use of baffles, resonance rods or some modification of geometry that were introduced since the early days of rocket engine development are still in use (Culick and Yang 1995). The present work is motivated by this apparent shortcoming. As a part of this research, flame acoustic interactions in

the near-field of a shear coaxial injector is studied experimentally with the goal of identifying physical mechanisms that could play key role during the onset of acoustically driven instabilities in liquid rocket engines using such injectors.

1.2 Key Physical Mechanisms

In this study, particular attention is given to interactions between density stratified fuel oxidizer interfaces and pressure waves passing through them. As already noted in section 1.1, such interactions give rise to various fluid mechanical instabilities that need to be critically considered for finding physics based mechanisms relevant to the LRE combustion instability problem. It is interesting to note that although the density stratification of the shear coax flowfield is well recognized and the acoustically charged nature of rocket engine combustor is well understood, a study of the interplay between them has not been critically considered in evaluating instability mechanisms in liquid rocket engines. In this thesis, it is shown that under the acoustic environment of the rocket engine, the density gradient between fuel and oxidizer becomes a critical parameter affecting flame acoustic interaction. The interaction could take place through the excitation of intermittent baroclinic vorticity driven instability, Rayleigh-Taylor instability and in extreme cases through the excitation of the Richtmyer-Meshkov instability.

1.2.1 Baroclinic Vorticity Driven Instability^ψ

Baroclinic vorticity is generated when a pressure wave interacts with a density stratified interface between two fluids in such a way that the pressure gradient

^ψ For a detailed discussion, see section 3.1

associated with the former is misaligned with the density gradient associated with the latter. In the context of the liquid rocket engine, such instability can be generated by the interactions between misaligned pressure gradient (across the acoustic wave) and density gradient (across the fuel oxidizer interface). Due to presence of large density gradients across fuel-oxidizer interfaces and large amplitude pressure waves within the combustion chamber, the strength of such vorticity in the near field of the injector can be significant.

1.2.2 Rayleigh-Taylor Instability⁰

When an interface separating two fluids of different densities is accelerated such that the acceleration is directed from the denser fluid to the lighter fluid, the interface separating the two fluids become unstable with initial perturbations growing exponentially in time. The same configuration with acceleration directed in the opposite direction is stable with interfacial perturbations remaining bounded in time. In the context of the liquid rocket engine, the density stratified fuel-oxidizer interface can be acoustically accelerated giving rise to such instability.

1.2.3 Richtmyer-Meshkov Instability⁰

The Richtmyer-Meshkov instability occurs when a density stratified interface is impulsively accelerated (say by the passage of a shock wave). It differs in two primary ways from the Rayleigh-Taylor instability. Firstly, RM instability does not depend on the direction of the acceleration and secondly, the initial interfacial

⁰ For a detailed discussion, see section 3.2

⁰ For a detailed discussion, see section 3.2

perturbations grow linearly in time. In the context of the liquid rocket engine, acoustic waves can undergo wave amplification and wave steepening resulting in steep fronted shock-like waves that can interact with the density stratified fuel-oxidizer interface giving rise to RM instability^ζ.

1.3 Technical Objectives

The technical objectives of this work are as follows:

1. To study the basic physics of acoustically driven combustion instabilities in liquid rocket engines (LREs) that use shear-coaxial injectors.
2. To characterize flame-acoustic interactions in GH₂-GO₂ diffusion flames during the onset of combustion instability involving a 2D model shear-coaxial injector.
3. To assess the relative importance of hydrodynamic and acoustic modes in affecting instability and to study if a hydrodynamic-acoustic coupling mechanism is operative during the onset of instability.
4. To model the relative importance of relevant flow-field parameters affecting flame acoustic interaction in LREs. Parameter space will be limited to four primary variables : fuel-oxidizer density ratio, fuel-oxidizer velocity ratio, fuel-oxidizer momentum ratio and chemical composition of the fuel.

^ζ In practical configurations, an interaction somewhere midway between the RT and RM instabilities might be expected in the LRE flowfield. It should be noted that for both RT and RM instabilities, the basic mechanism for amplification of initial perturbations is still the baroclinic generation of vorticity.

5. To assess the feasibility of actively controlling combustion instability in LREs by gaining key insight into various processes and parameters relevant to the instability problem.
6. To build a detailed dataset for model validation on flame-acoustic coupling as a function of relevant injection parameters such as fuel-oxidizer density ratio, fuel-oxidizer velocity ratio, fuel-oxidizer momentum ratio and fuel composition.

1.4 Scope of the Present Work

Overall, the set of experiments conducted as a part of this study involved an oversimplification of phenomenon associated with real rocket engines. Firstly, in our experiments gaseous Oxygen was used instead of cryogenic Oxygen. Secondly, chamber pressure was atmospheric, which in the case of engines like that of Ariane 5 (Vulcain) could be anywhere around 100 bar. Thirdly, our study dealt with a single element injector whereas real rocket engines have hundreds of coaxial injectors forming a showerhead covering the motor back plane. Finally, the confinement effect provided by the geometry of the combustor used in this study is different from the confinement experienced in real engines.

However, although the absence of a dominating LOX core prevented the characterization of dynamic response of atomization, vaporization, mixing and combustion of the LOX jet to acoustic perturbations, it provided a convenient way of eliminating instability mechanisms associated with the atomization and the vaporization processes and allowed probing into instability mechanisms associated specifically with the flame acoustic interaction process. It should be observed here,

that even in liquid rocket engines, by the time the flame is formed downstream of the injector, it (the flame) essentially sits between vaporized Oxygen and gaseous Hydrogen. This observation is substantiated by Oefelein and Yang's (1997) observation that in cases involving high heating rates, intermolecular forces are reduced which can favor diffusion dominated processes to occur which causes diffusion of the liquid core into the co-flowing gas even before substantial atomization of the liquid core has occurred. The central jet of liquid Oxygen in such cases vaporizes into a continuous fluid in the presence of extremely large density gradients and a well mixed diffusion flame is formed at the interface of the two fluids. The two-dimensional model was chosen mainly for ease of diagnostics so that processes could be studied in detail and data could be generated for model validations. Since the acoustic output of the driver unit was limited, the model experiments were conducted at scaled-down conditions, ensuring relatively strong level of acoustic excitation compared to the level of natural turbulence fluctuations. Consequently, the design retained some of the dominant aspects of fluid behavior occurring in real engines and the results obtained from this study should facilitate an understanding of the real problem under consideration.

The scope of this study is summarized below :

1. A single element 2D shear-coax injector rig with a transversely mounted acoustic driver unit will be used to simulate flame acoustic interactions that could occur near the injector plate of a typical liquid rocket engine with shear coax injectors. Carefully controlled flame experiments will be conducted on

turbulent Oxygen-Hydrogen diffusion flames ($Re_{O_2}^{\S} \sim 5500 - 7300$) acoustically forced at frequencies ranging from 200Hz to 2000Hz.

2. Experiments will be restricted to the study of flame acoustic interactions involving fuel and oxidizer in their gaseous forms. Gaseous fuel would essentially mean GH₂ (gaseous Hydrogen) sometimes diluted with inert gases like Helium and Argon and non-inert gases like Methane. Gaseous oxidizer would essentially mean GO₂ (gaseous Oxygen) sometimes diluted with inert gases like Helium, Argon or Nitrogen.
3. Periodic vortex structures in the interface between reactants will be visualized using phase locked schlieren technique while the time dependant heat release patterns will be characterized using OH* and CH* chemiluminescence at different phases of the acoustic forcing. Hotwire measurements will be conducted to measure natural frequencies in the shear layer for non-reacting flow conditions. Dynamic pressure sensors will be used to capture pressure oscillations and acoustic modes of the chamber. PMT tube with suitable filters will be used to measure frequency of flame oscillations.
4. Parametric studies will be conducted to see the partial dependency of flame excitability to different flow-field variables under given external perturbations. Effects of changing density ratio, velocity ratio, momentum ratio and chemical composition of the fuel on flame-acoustic interaction will be studied. Density ratios ranging from 1 to 16, velocity ratios ranging from 3.02 to 5.27, momentum ratios ranging from 0.67 to 2.12 and fuel mixtures

[§] Re based on width of center jet (0.75in) and velocity of center jet of Oxygen at 4.5m/s and 6 m/s respectively.

ranging from pure Hydrogen to 10%-90% GH₂-GCH₄ combination will be tested.

Chapter 2: Literature Review

2.1 Thermoacoustic Instabilities in Combustion Systems

The first part of this literature review addresses research performed in the broad area of combustion instability. Although systems, ranging from industrial burners and land based gas turbine engines to aero engines and rockets, are extremely different in their constructional and operational details, the fundamental aspects of the instability problem remain the same. In fact, much of the fundamental understanding gained from the study of combustion instability in other systems has proven valuable to the understanding of combustion instability in liquid rockets (Culick and Yang 1995). An overall review of combustion instability with an historical overview is therefore presented to introduce the reader to combustion instabilities in general. The particular case of instabilities in liquid rocket engines will be covered in a separate section.

2.1.1 Introduction

In the early years of solid rocket motor development, test firings were often accompanied by unexpected changes in the mean pressure levels and large amplitude structural vibrations. The role of acoustic waves inside the combustor as responsible for such erratic behavior was indicated by researchers (e.g., Boys and Schofield 1943; Grad 1949) and later established experimentally (e.g., Swanson 1951; Smith and Sprenger 1953). Large amplitude pressure oscillations with frequencies close to the natural resonant modes of the chamber were observed to be excited in these tests.

In the years that followed, various studies on instabilities in propulsion systems ranging from the liquid and solid rocket engines (e.g., Crocco and Cheng 1956; Price 1959; Tsuji and Takeno 1965; Zinn and Powell 1971) to the jet engine afterburners (Langhorne 1988; Bloxsidge *et al.* 1988) and ramjet engines (Yang and Culick 1986; Schadow and Gutmark 1992; Hedge *et al.* 1987; Yu *et al.* 1987; Yu *et al.* 1991; Schadow *et al.* 1987) revealed that a complex feedback type interaction between heat release oscillations and acoustic disturbances in the combustion chamber essentially led to the excitation of the large amplitude pressure oscillations. These oscillations, when excited in the combustor, were found to affect the stability and survivability of the flame, produce intense structural vibrations and thermal stresses, reduce engine life and in certain extreme cases lead to catastrophic failures[§]. Similar instabilities were also observed in the combustion chambers of industrial burners (Putnam 1971) and gas turbine engines (Kydd 1969; Keller 1995; Lieuwen 1999; Mongia *et al.* 2003).

Although the details of the interaction process between flame and acoustics that led to such instabilities were remarkably complex, the basic phenomenological nature of the interaction process was somewhat intuitive. Unsteady combustion generated sound (Chu 1953; Zinn 1986; Dowling 1992; Candel *et al.* 2004). In cases where combustion took place in a confined region, like a typical combustor, the generated sound reflected from the boundaries of the combustor and interacted with the flame system, thereby modulating the source of which they themselves were a product of. Such interactions, under certain conditions, caused more unsteady heat

[§] In the case of pulse combustors, however, these oscillations are desirable since they lead to enhanced rates of heat transfer and/or evaporation (Margolis 1993) and reduces the emission of pollutants like NO_x, CO and soot (Candel 1992).

release, for example, through changes in fuel-air ratio (Richards and Janus 1998), through hydrodynamic instabilities (Poinsot *et al.* 1987, Renard *et al.* 2000), or through flame area variations. In the nonlinear form, heat release modulations sometimes arose from interactions between shock waves and combustion (Rudinger 1958). When the pressure oscillations and the heat release oscillations were sufficiently in phase with one another, amplification in the amplitude of the pressure waves eventually occurred as per the Rayleigh's criterion leading to combustion instability. A brief description of this criterion is provided in section 2.1.3.

2.1.2 Historical Developments

Although technological interest in combustion instability was spurred by the rocket engine programs of the 1930s, combustion driven acoustic oscillations were observed by Higgins (cf. Tyndall 1867) as early as 1777. In what became famous as the 'singing flame' experiment, Higgins found that a Hydrogen diffusion flame placed inside a closed or an open ended tube could produce sound, given, the fuel supply line and the surrounding tube were of certain specific lengths. Later, LeConte (cf. Tyndall 1867) observed the 'Dancing Flame', where a naked flame was seen to pulse with the audible beats of music. In 1850, German physicist C. Sondhauss (cf. Feldman *et al.* 1966, Raun *et al.* 1993) observed sound produced by heating the glass bulb of a glass tube having an opening at one end and glass bulb at the other. Rijke (1859) discovered that an audible sound was produced when metal gauze placed in the lower half of an open ended vertical tube was heated. He observed that the oscillations were strongest when the gauze was located a quarter of the tube length from the bottom. He also observed that if the metal gauze was placed in the upper

half of the tube and heated, instead of driving acoustic oscillations, a dampening of the oscillations occurred. In a similar apparatus called the Bosscha Tube, (cf. Howe 1998) oscillations were found to be driven when a refrigerated gauze was placed in the upper quarter. Extensive reviews on Rijke oscillations are given by Feldman (1968), Raun *et al.* (1993), and Bisio and Rubatto (1999). Early observations on oscillatory combustion were also made by Mallard and Le Chatelier (cf. Mallard and Le Chatelier 1883).

The discovery of the Rijke tube phenomena was an important milestone in the scientific study of combustion instabilities. Although Rijke's own explanation was not sufficient to explain the interplay between heat and sound as observed in his own experiments, it spurred a significant amount of interest in combustion driven instabilities among the scientific community of his time. Moreover, it provided an easy yet excellent setup for which acoustic oscillations could be modeled analytically and generated experimentally in terms of acoustic modes and sound pressure levels (SPL) (McQuay *et al.* 2000). Possibly the first theoretical investigation of the interaction between pressure waves and combustion was made by Lord Rayleigh around 1878 (cf. Rayleigh 1945) in his explanation of Rijke tones. He proposed that thermoacoustic oscillations are encouraged when heat fluctuates in phase with pressure perturbations. Popularly known as the Rayleigh's criteria, it stated that :

“If heat be periodically communicated to, and abstracted from, a mass of air vibrating in a cylinder bounded by a piston, the effect produced will depend upon the phase of the vibration at which the transfer of heat takes place. If heat be given to the

air at the moment of greatest condensation or to be taken from it at the moment of greatest rarefaction, the vibration is encouraged. On the other hand, if heat be given at the moment of greatest rarefaction, or abstracted at the moment of greatest condensation, the vibration is discouraged”.

2.1.3 Rayleigh’s Criterion

The Rayleigh criterion is commonly described by the following inequality:

$$\int_0^{\tau} \int_0^V p'(x, t)q'(x, t)dvdt > \int_0^{\tau} \int_0^V \Phi(x, t)dvdt$$

p' and q' are unsteady pressure and heat release oscillations, respectively, τ is the period of oscillation, V is the combustor volume (control volume) and Φ is the wave energy dissipation rate. Thermoacoustic instability occurs when the inequality in the above equation is satisfied. The LHS of the inequality describes the total mechanical energy added to the oscillations by the heat addition process per cycle and the RHS describes the total energy dissipated by the oscillation per cycle. Normally, the acoustic dissipation in combustors can be assumed very small ($\Phi \approx 0$) and under this assumption, the above equation further simplifies into the following inequality:

$$\int_0^{\tau} \int_0^V p'(x, t)q'(x, t)dvdt > 0$$

This inequality essentially indicates that when p' and q' are sufficiently in phase with one another, the combustor will be driven unstable whereas when p' and q' are sufficiently out of phase with one another, the effect will be a stabilizing one. It is to be noted that the integrals are also spatial, meaning that both effects, destabilizing and stabilizing, can occur in different locations of the combustor, and at different times, and the stability of the combustor will be decided by the net mechanical energy added to the combustor. Rayleigh himself did not indicate how he arrived at such a generalized statement. Noting this shortcoming, Putnam and Dennis (1953) derived a mathematical proof for the phasing requirement between pressure and heat release oscillations. It was essentially a thermodynamic proof that was accomplished by extending a 'customary derivation' of the wave equation for acoustic motions. Neglecting the damping forces, Putnam and Dennis put Rayleigh's Criteria in a very precise form: that "a component of the rate of heat input must be in phase with the pressure to drive the oscillation". In a paper that appeared a year later (cf. Putnam and Dennis 1954), the now well known expression

$$\int_{cycle} Hp dt > 0 \quad (2.1)$$

appeared wherein combustion driven oscillations were expected to occur if the inequality was satisfied. Here H was the heat release rate and p was the fluctuating component of pressure. In a latter work that appeared in 1971 (cf. Putnam 1971) Putnam presented an extensive account of various ways in which the Rayleigh's criterion could be used to suppress combustion instability in industrial systems.

Noting that Putnam's derivation (Putnam and Dennis 1953) was more mathematical than physical, Chu (1956) derived expression (2.1) for the stability of systems with heat sources based on the conservation equations. He stated that "a dynamical system will start to oscillate with increasing amplitude only if energy is fed into the system in such a way that there is a net increase of the total mechanical energy of the system after each cycle of oscillation. The vibration is finally maintained at a given level when the mechanical energy fed into the system per cycle of oscillation is just equal to the sum of that dissipated by viscosity and that radiated away from the system per cycle of oscillation. "In a latter paper, Chu (cf. Chu 1965) used the concept of 'energy in a small disturbance' to derive a generalized form of the Rayleigh's criterion. He also discussed the effects of body forces, heat and material sources in promoting the instability and pointed out certain limitations of the Rayleigh's criterion for the stability of systems with heat sources.

Culick contributed significantly to the mathematical representation of the Rayleigh's criteria. He (cf. Culick 1976) derived an expression for the energy addition to the acoustic mode by considering conservation equations resulting in the following equality.

$$\Delta E = \frac{\gamma - 1}{p_o \gamma} \int dV \int_t^{t+T} p' \dot{Q}' dt ,$$

where p' is the pressure perturbation; \dot{Q}' is the fluctuation of the heat release rate; γ is the gas constant; p_o is the mean ambient pressure; V is the chamber volume; and T is the cycle period. The above expression is an explicit formulation of the Rayleigh's

criterion indicating that instability is excited when heat release fluctuates with the pressure perturbation. Culick (1987) also performed a detailed analysis of the criterion including linear and non-linear thermoacoustic oscillations and arrived at an “explicit rendition of Rayleigh’s criterion in a more general form than commonly used” given by the following expression for “energy” for the n^{th} mode.

$$\Delta \mathcal{E}_n(t) = (\gamma - 1) \frac{\omega_n^2}{E_n^2} \int dV \int_t^{t+\tau_n} \frac{p_n}{\bar{p}} \frac{Q}{\bar{p}} dt,$$

If the energy ($\Delta \mathcal{E}_n(t)$) for the n^{th} mode is positive, then heat addition tends to drive the n^{th} mode.

2.1.4 Representative Work in the Area

Since the existing literature on combustion instability is enormous and adequate summarization is beyond the scope of this work only a few representative works will be cited so as to give the reader familiarity with the important developments in this area throughout the last several decades.

Gaydon and Wolfhard (1960) provided a brief but interesting review of early literature on unstable flames. Studies on the influence of sound on both diffusion flames and premixed flames due to Rayleigh, Brown, Tollmien, Zickendraht, Dubois, Hahnemann, Ehret, Loshak *et al.* were summarized. Toong *et al.* (1965) studied mechanism responsible for triggering, amplification and suppression of acoustic waves, due to the presence of flames and suggested that the interaction between

acoustic waves and flame oscillations could occur through both linear and non-linear mechanisms. Instability of the traveling Tollmien-Schlichting wave was highlighted as a possible mechanism responsible for the self-sustained oscillations of diffusion flames. Price (1969) reviewed contemporary advances in solid propellant combustion instability in rocket engines. A basic case of instability where the combustor is modeled as a closed right cylinder with combustion occurring at the side walls and gas oscillations taking place in the first axial standing mode was elaborated. The solid burning surface was treated as an acoustically active surface that fed energy into the bulk of gas in the combustor. Effects of mean flow were neglected. Marxman and Wooldridge (1969) looked into the driving mechanism of high amplitude axial mode combustion instability in solid-rocket combustion. The case of a shock wave oscillating along the axis was considered. The effect of burning rate perturbation induced by the pressure pulse accompanying the shock on the shock wave itself was analyzed. Sirignano (1969) treated axial-mode shock-wave oscillations in solid rocket-engines and suggested an analytical way of inferring about the combustion process inside the combustor from experimental observation of non-linear pressure traces during oscillatory operation. Thring (1969) discussed combustion oscillations in industrial combustion chambers and classified them into three broad categories: combustion roar, Helmholtz resonator oscillations and acoustic oscillations. Zinn in his comments to this paper (cf. Thring 1969) observed the similarity of the various types of instabilities mentioned by Thring to those observed in solid and liquid rocket engines and suggested a universal way of classifying combustion instabilities arising in various systems. Barrère and Williams (1969) compared combustion instability

found in various types of combustors and defined three classes of instabilities: chamber instabilities, system instabilities and intrinsic instabilities. Chamber instability was further classified into three categories: acoustic instabilities, shock instabilities and fluid-dynamic instabilities. Kydd (1969) performed analytical and experimental work on combustion instability in gas turbine engines and showed that inlet pressure drop and the phasing between heat release rate and inlet flow velocity, both, could have significant effects on the overall stability of the combustor. Pariel and Martin (1969) studied combustion instability in industrial hearths and used Rayleigh's criteria to show how the location of a velocity antinode (or node) with respect to the flame, could influence combustion instability. A time delay parameter that related the time delay of combustion to the period of oscillation in the combustion was introduced. Deckker and Sampath (1971) studied the role of the Tollmien-Schlichting waves in the vibration of enclosed laminar diffusion flames and indicated that the vibrations were sustained when pressure oscillations and heat release oscillations were appropriately phased as per the Rayleigh's criterion. They demonstrated that wave like structures on the interface between the central and annular jet could be amplified if the velocity shear between the center and the co-flow jets was sufficiently high. Williams (1984) provided a fundamental description of combustion instabilities in solid and liquid rocket engines and discussed elaborately on mechanisms responsible for amplification and damping. Hydrodynamic and diffusive instabilities, non linear effects and oscillatory burning in liquid propellant rocket motors were also discussed. This book (Williams 1984) cited 233 references at the end of the chapter on combustion instability. Each of these references are

authoritative sources on various aspects of the instability problem. Oran and Gardner (1985) studied interactions between acoustics and chemistry in combustion systems. Laverdant *et al.* (1986) investigated the spatial structure of pressure oscillations in a combustion chamber. Starting from the conservation equations for mass, momentum, energy and species, Laverdant *et al.* (1986) obtained an expression for the pressure perturbation in a combustion chamber with two source terms. Candel (1992) gave an elaborate review of various hydrodynamic processes that lead to pressure and heat release oscillations getting sufficiently in phase with each other so as to drive the instabilities. Keller and Barr (1994) studied fluid dynamic stretch as a principle delay mechanism preceding ignition of a well stirred mixture of reactants and hot products. They showed that such a mechanism could explain experimental observations of the peak of energy release proceeding through a minimum during peak of reactant injection. Such a delay could influence the phase relation between energy release and resonant pressure waves and could thereby promote (or prevent) instability as per the Rayleigh's criteria. Herding *et al.* (1996) studied flame stabilization mechanisms in cryogenic propellant combustion. The structure of the flame in the near field of a single element coaxial injector fed with liquid Oxygen (center jet) and gaseous Hydrogen (co-flow) was visualized and it was shown that the flame was initiated in the proximity of the injector exhaust plane. Kendrick *et al.* (1996) used a one dimensional acoustic model to predict resonant acoustic modes and corresponding resonant mode shapes for a laboratory dump combustor. A volumetric mass source introduced at a chosen frequency was used to represent the heat addition process. Pressure and velocity matching conditions in which velocity satisfied

volumetric continuity at each segment boundary and pressure satisfied a continuity condition at the interfaces where one segment was connected to another were used to obtain mode shapes for different operating frequencies. A satisfactory analysis of the shift of resonant modes between cold-flow and reacting flow conditions was presented. Büchner and Leuckel (1996) studied the influence of fuel / air mixture oscillations on combustion instabilities in premixed combustors. Sreenivasan and Raghu (2000), extended Chu's 1965 work by including the effect of species generation on combustion instability. They showed that under the following conditions perturbations inside a combustor are expected to decay in time “(a) a periodic mass addition antiphase with pressure fluctuations; (b) periodic body force antiphase with temperature fluctuations ; (c) periodic heat release rate antiphase with temperature fluctuations; (d) species generation antiphase with the appropriate chemical potential”. Since temperature and pressure fluctuations are in phase for a purely acoustic disturbance, (c) is equivalent to saying that perturbations inside a combustor should decay if heat is added antiphase with pressure fluctuations.

2.2 Combustion Instability in Liquid Rocket Engines

2.2.1 Introduction

Work on liquid rocket engine combustion instabilities began in the early 1940s (Culick and Yang 1995). One of the most critical concepts in liquid rocket combustion instability, that of time lag (as a coordinating factor in influencing organized oscillations in liquid rocket combustion chambers) originated around this time in von Kármán's group at the Jet Propulsion Laboratory around 1941 (cf.

Summerfield 1951) shortly after oscillations were observed in early tests in liquid rocket engines in the United States. The essential idea was that there existed a finite time delay when an element of propellant entered the combustor and when heat was released from it. This delay controlled the phasing between heat release and pressure oscillations thereby making the system stable or unstable as per Rayleigh's criteria. In the years that followed, this model was applied to various studies involving combustion instability in liquid rocket engines. Gunder and Friant (1950), Yachter (1951) and Summerfield (1951) analyzed low frequency chugging instability arising from the interaction between feed system and combustion process using a constant time lag model. Crocco (1951;1952) introduced the time varying combustion time lag and used it to analyze high frequency instability. Total time lag was separated into two parts : a constant (insensitive) time lag and a time varying (sensitive) time lag that responded to fluctuations in the chamber conditions and the idea of the 'interaction index' was introduced. Crocco (1951) first applied the sensitive time lag theory to longitudinal oscillations. In the now well known monograph, Crocco and Cheng (1956) expanded and generalized the theory of longitudinal mode combustion instability. The aspect of linear instability was thoroughly considered but this work was published without any experimental verification. The application of the sensitive time lag theory to transverse mode instabilities was first made by Scala (1957) who showed theoretically the destabilizing effect of increasing the nozzle entrance mach number. No experimental results were however shown. Crocco, Grey and Harrje (1960) through a series of experiments, later, showed the apparent validity of the time lag hypothesis.

2.2.2 Representative Work in the Area

Starting from these early days of research, a good volume of work has been conducted in the area of combustion instability in liquid rocket engines. In one of the early experimental works in the field of LRE combustion instability, Berman and Cheney (1953) used slit window photographic methods to study longitudinal modes of oscillations in rocket motors. They observed the development of small disturbances into high amplitude shock type waves with oscillation frequencies coming close to the acoustic frequencies of the combustor. Ellis *et al.* (1953) correlated pressure fluctuation measurements with the optical methods used by Berman and Cheney (cf. Berman and Cheney 1953). The optical studies were also used by Ellis to study transverse mode instabilities in liquid rockets (cf. Ellis 1960). Very large particle velocities and spiral particle trajectories in planes normal to the chamber axis were observed. Bellman *et al.* (1953) used photographic method to investigate combustion instability in a 2 dimensional transparent rocket engine. Various injectors, parallel jets and impinging jets, were used to study various types of combustion. Male, Kerslake and Tischler (1954) at NASA Lewis Research Center conducted optical studies of screaming combustion in liquid rocket engines. They noted the greatly increased heat transfer rates to the combustion chamber walls that is typically associated with transverse modes of instability in rocket engines. They also noted some interaction effects between longitudinal and transverse modes of oscillations. Male and Kerslake (1954) at NASA Lewis Research Center showed experimentally the effectiveness of longitudinal fins in attenuating transverse mode instabilities in rocket engines. They made the important observation that ‘lateral oscillations appeared first at the injector

end and then spread throughout the chamber'. Maslen and Moore (1956) theoretically studied the effects of viscous damping in a cylindrical combustion chamber without combustion. They showed that large amplitude non-shock type waves could exist in the spinning form of the tangential mode when viscosity was neglected. The standing form of the tangential mode was shown to be subject to damping proportional to the amplitude. The 'possible isentropy' of the strong transverse waves was shown to further imply that if energy could be supplied to these waves by coupling with unsteady combustion, extremely violent waves may be more likely in transverse resonance than in the longitudinal resonance. For low values of the chamber length to diameter ratio, the damping of the fundamental longitudinal mode was also shown to be greater than that of the first tangential mode. The authors showed that to a good degree of approximation, the shape and particularly the frequency of resonant transverse modes of oscillations could be described by linear acoustic theory. Baker and Steffen (1958) used high frequency response, water cooled, strain gauge type pressure transducers to study screaming tendency of the GH₂/LOX propellant combination in a 200 lb thrust liquid rocket engine. Four injector classes, a total of 12 different configurations, were tested with the chamber length varying between 3 to 24 inches. Their results indicated that compared to all-liquid propellants, the gaseous Hydrogen liquid Oxygen propellant combination had considerably lower tendency towards screaming. In this work the effects of Hydrogen injection velocity was studied. Wieber *et al.* (1960) conducted a theoretical study of the effects of standing transverse acoustic oscillations on the vaporization of liquid fuel droplets and showed that in an acoustic field, a drop acquires an oscillating transverse velocity and a

fluctuating rate of vaporization. Osborn and Bonnell (1960 a; 1960 b) used a gas rocket system to assess the effects of chamber geometry, chamber pressure and propellant chemistry on combustion instability. They noted important interaction effects between longitudinal and transverse modes. Working with a constant diameter, variable length motor, they observed (for some propellants) that when the chamber length is increased to the point where longitudinal mode instability is possible, there is a sharp change in the stability behavior for transverse modes. They also noted widened instability region with propellants of higher heat release rates. Pickford *et al.* (1960) attempted to use an available energy concept to come out with a method for *a priori* calculation of stability behavior from the knowledge of the physical and chemical nature of the propellants, the injection process etc. Reardon (1961) incorporated Crocco's sensitive time lag hypothesis in his investigation of transverse mode combustion instability in liquid propellant rocket engines. The transverse modes of high frequency were studied both theoretically and experimentally. Reardon showed that the standing forms of the tangential modes were more stable than the spinning forms. Rupe and Jaivin (1964) made experimental investigations of the effects of resonant combustion and injection mass flux distribution on local heat transfer rates for a 20,000 lb thrust liquid rocket engine. Among various other results, variations in heat transfer due to resonant combustion for a particular chamber location, variations in transient temperature distributions due to resonant combustion and the effect of mixture ratio variation on local temperature were reported. For unstable cases, heat transfer rate to the chamber wall near the injector was reported to be an order of magnitude greater than those observed during

steady combustion. Crocco (1965) reviewed early works on rocket engine combustion instability. Clayton and Rogero (1965) used a 20,000 lbs thrust, heavily instrumented laboratory scale liquid rocket engine to experimentally investigate high amplitude tangential mode rotating detonation like pressure waves excited during resonant combustion of the engine. Wanhainen *et al.* (1966) studied the effects of propellant injection area, propellant injection velocity, oxidant tube exit geometry and the effect of Oxygen tube recess on the overall stability of a 20,000 lbs Hydrogen-Oxygen rocket engine. Appearance of self triggering under Hydrogen injection temperature ramping was used to rate the stability of each of the injector designs. Reardon *et al.* (1967) studied velocity effects in transverse mode combustion instabilities in liquid rocket engines. Assuming fluctuations of the radial and tangential velocity components to influence the combustion process rates in a manner analogous to that proposed previously by Crocco for pressure perturbations, the authors showed that tangential velocity fluctuations could destabilize the spinning tangential modes of oscillations but will have no effect on the standing modes. Fluctuations in the radial velocity component were shown to have smaller yet significant effect. Both theoretical work and experimental verifications were performed. Crocco and Sirignano (1967) showed that axial oscillations in the rocket chamber (in the linear regime) could be damped substantially by increasing the length of the convergent section of the nozzle. For the transverse modes however (in both linear and nonlinear regimes) nozzles were almost ineffective in their ability to damp oscillations (cf. Crocco 1969). Harje *et al.* (1967) showed that the effectiveness of the acoustic cavities increased when the passages connecting the cavity with the chamber occurred

at the pressure antinodes of a given mode. Their effectiveness also increased the closer they were placed to the injector. Wanhainen *et al.* (1967) studied Helmholtz type acoustic damping devices in suppressing high frequency combustion instability in Hydrogen-Oxygen rocket engines. Susceptibility to self triggering under varying Hydrogen injection temperatures was used as the criterion for assessing stability. Liner with lowest self triggering temperature was considered most stable. Interestingly, they showed that acoustic absorbing chamber walls could change stability limits and even frequencies of the instability. Sirignano *et al.* (1967) showed (for the acoustic cavity resonator which is derived from the Helmholtz resonator and is used to dampen oscillations in a combustor) that a jet is formed at the exit of the channel connecting the combustion chamber with the resonant cavity. The eventual dissipation of the kinetic energy of the jet provides a non-linear damping mechanism whose effectiveness improves with the oscillation amplitude. Barsotti *et al.* (1968) studied the full scale LOX/LH₂ M1 engine thrust chamber and showed that its stability depended primarily on fuel oxidizer injection velocity ratio. Using the Hydrogen temperature ramping method they showed that higher velocity ratio and higher Hydrogen injection temperature, both improved engine stability. Crocco (1969) presented a detailed analytical framework for dealing with non-linear triggered instabilities in liquid rocket engines. Methods of solving for spinning waves in an annular chamber, application of the sensitive time lag model (cf. Crocco and Cheng 1956) to non-linear instabilities and the use of a droplet evaporation model to find a solution to the non-linear instability problem were detailed. Crocco also observed that the largest oscillation amplitudes for the transverse modes were generally obtained

close to the injector. P.D.McCormack, in his comments to Crocco's paper on combustion instability, (cf. Crocco 1969) actually suggested that considerable experimental and theoretical work should be performed on processes occurring at the injector. This comment primarily came from McCormack's observation that pressure transients in the injector resulted in "rapidly spinning droplets, with greatly increased evaporation rate and change in trajectory". Such a change could essentially change the nature of the applied perturbation (finite or infinitesimal) and in turn could change the resulting instability from one that could be treated through treatments of linear acoustics to one which would necessitate the use of non-linear theory. Zinn and Savell (1969) studied three dimensional linear combustion instability in liquid rockets. A concentrated combustion model (infinitesimally thin combustion zone adjacent to the injector faceplate) with Crocco's time lag hypothesis was used to frame a boundary value problem in which the concentrated combustion zone boundary condition was satisfied at the injector end and nozzle admittance relation was satisfied at the nozzle entrance end. Effects of mach number of the mean flow, length of the combustion chamber and convergence of the nozzle on the linear stability of chamber modes were analyzed. Priem and Rice (1969) made a theoretical investigation of combustion instability in liquid rocket engines with finite axial gas velocities and assessed the effects of mach number, chamber length to radius ratio, nozzle flow response and acoustic liners on the stability of the chamber modes. An irrotational wave formulation was used in conjunction with specific boundary conditions at the injector wall, nozzle entrance and the acoustic liners. Zinn and Powell (1971) studied non-linear combustion instability in liquid rockets. The authors

predicted the existence of stable and unstable finite-amplitude limit cycles and showed that for moderate amplitudes of oscillations and a low mach number mean flow, combustion oscillations in the combustor could be described by a single non-linear wave equation. A modified version of the classical Galerkin method was used to solve the non-linear wave equation. Harrje and Reardon (1972) compiled a comprehensive report dealing with the most significant developments, both theoretical and experimental, in the area of combustion instabilities in liquid rocket engines. Background information on the phenomena of instability, analytical models for low and high frequency instabilities, experimental aspects of the study of combustion instability and a section on the practical guide to designers focusing on the aspects of excitation and damping have been provided in this review. Culick (1975 a) developed a formal framework for analyzing the non-linear growth and limiting amplitude of acoustic waves in rocket engine combustion chambers. Two small parameters (one representing the mean flow field and the other representing the amplitude of oscillations) were used to expand the conservation equations resulting in a nonlinear inhomogeneous wave equation. The normal modes of the chamber with time varying amplitudes were used to synthesize the unsteady pressure and velocity fields. This study was essentially a development of a previous work (Culick 1971) and the methods used were similar to the ones used by Culick to study linear stability of the normal modes of a combustor (cf. Culick 1973; Culick 1975 b). Jahnke and Culick (1994) applied dynamical systems theory approach to model non-linear combustion instabilities. Mitchell (1994) reviewed progress in analytical modeling since 1970 and discussed contemporary developments in modeling the liquid rocket

engine combustion instability problem. Both linear and non-linear approaches have been described in this work providing a good starting point for researchers trying to understand analytical aspects of the problem. Culick and Yang (1995) reviewed combustion instability in liquid rocket engines. Chronological development in the area was surveyed. Linear and non-linear behavior was described and examples of combustion instability in operational engines were summarized. How elementary processes associated with the injection system and the combustion chamber could act as mechanisms for exciting and sustaining combustion instabilities were discussed. Kim and Williams (1998) used a variational method to theoretically study the effects of non-homogeneities (arising, for instance, from density and sound speed variations) on the Eigenmodes of acoustic pressure oscillations in liquid rocket engine combustion chambers. Fischbach *et al.* (2007) theoretically examined acoustic streaming effects in liquid rocket engines with traveling transverse mode oscillations and showed that streaming could promote the development of large amplitude steepened wave fronts.

2.2.3 Prior Research involving Shear-Coax Injector Element

The present study deals with flame acoustic interactions in the near field of the shear coaxial injector. This injector (also known as the multi tube concentric orifice injector) was developed during the late 1940s in the United States and eventually became the preferred injector for most flight engines. They were operated in the early programs without the indication of any combustion instability, a fact often attributed to high Hydrogen injection temperatures (161K) (Hulka and Hutt 1994).

High frequency acoustic instability eventually showed up in exploratory tests in which Hydrogen injection temperature was maintained lower than what that these injectors were normally designed for.

From the early days of its inclusion, people recognized that the overall stability of the liquid rocket engine was somehow correlated with phenomena going on in the near field of the injector. Consequently, starting from the late 1950s, an extensive experimental work on correlating various parameters to engine stability was undertaken at NASA Lewis Research Center (LeRC) and NASA Marshall Space Flight Center (MSFC). Small changes in injector geometry, inclusion of a small recess, changes in fuel oxidizer injection temperature or velocity, changes in injection pressure drop - were all shown to affect the stability behavior of the engine significantly. Hulka and Hutt (1994) compiled an extensive review of such programs at Aerojet, Pratt and Whitney Aircraft, Rocketdyne, LeRC, MSFC and elsewhere since the 1940s that showed that the shear coaxial injector element indeed played a key role in influencing the overall stability of LOX/Hydrogen rocket engines. Oefelein and Yang (1997) conducted experimental investigations on coaxial jets simulating the injector and emphasized that parametric studies needed to be conducted to quantify the combined influence of key physical quantities like density ratio, velocity ratio and momentum ratio associated with the propellant streams to understand prevalent processes. Richecoeur *et al.* (2006) studied a three-element injector system under transverse-mode acoustic excitation. Experiments showed not only substantial modification in flame spread but also in-phase oscillations of heat release as evidenced by OH* emission at the excitation frequency. Non-reacting

experiments (Chehroudi and Talley, 2002; Davis and Chehroudi, 2007) conducted with simulated propellants at near supercritical conditions showed jet core length fluctuations associated with transverse forcing under certain conditions.

2.3 Acoustically Driven Instabilities

2.3.1 Introduction

Combustion instabilities arise due to complex feedback interactions between pressure and heat release oscillations. Acoustical oscillations in velocity and pressure can significantly influence all the critical processes involved in the operation of a liquid rocket engine ranging from atomization, vaporization, unsteady mixing to combustion and in turn help set up such complex feedback loops between pressure and heat release oscillations. When these oscillations are sufficiently in phase, a growth of the initial disturbance results often leading up to catastrophic proportions. In our studies, fuel and oxidizer are in gaseous phases and the effects of acoustics on combustion instability through its indirect influence on atomization and vaporization are not present. However, in order to give the reader a complete picture of why acoustical interactions are so important in the study of liquid rocket combustion instability, a broader review of relevant research is presented in this section.

2.3.2 Unsteady Atomization under Acoustic Oscillations

2.3.2.1 Cold Flow Experiments.

In order to understand the dynamic nature of coupling between acoustic oscillations and the atomization process, Miesse (1955) conducted cold flow

experimental studies to show that considerable amounts of interactions can occur between low speed jets and large amplitude acoustic fields. Reba and Brosilow (1960) studied the influence of longitudinal acoustic waves (created by a siren) on the behavior of liquid jets. In their cold flow experiments, strong interaction between liquid streams and acoustic fields was shown to occur for high acoustic amplitudes ranging from 5 to 30% of mean chamber pressure. Morrell (1963) and Morrell and Povinelli (1963; 1964), in their cold flow experimental studies used high speed direct and streak photography to estimate the breakup time of liquid jets impacted by shock waves. Buffum and Williams (1967) performed cold flow experimental and theoretical investigations on the interactions between a turbulent liquid jet and a standing planar acoustic wave with velocity vector transverse to the jet axis. By varying various parameters (injector orifice diameter, jet specific gravity, viscosity, injection velocity, sound frequency and amplitude) they showed definite velocity coupling between the jet and the acoustic field at amplitudes above 140 dB. Davis and Chehroudi (2007) recently studied the effects of transverse acoustics on coaxial jets under sub, near and supercritical conditions.

2.3.2.2 Reacting Flow Experiments.

Heidmann (1965) studied acoustic field and jet interactions (LOX-GH₂) in a two dimensional circular combustor operating under stable, chugging and spinning transverse instability regions under reacting conditions. Water cooled piezoelectric transducers were used to detect dynamic pressure conditions near the injectors and high speed photography was used to draw correlations between the acoustic field and

the oscillatory jet breakup behavior. Progressive changes in the wave shape, frequency, and amplitude of the pressure oscillations were observed for both chugging and transverse mode instabilities. Heidmann and Feiler (1967), in a later year, filed a patent describing a dynamic method of controlling spinning or travelling transverse mode instabilities by correcting against oscillations as they started. The correction was achieved by injecting the propellant in a tangential way or by changing the vector direction of propellants. By sensing the direction of the travelling wave and by selectively providing a tangential velocity in the combustion chamber in opposition to the travelling wave an attenuation of the instability was aimed. Ingebo (1966), used a photomicrographic technique to experimentally study the atomization of liquid ethanol sprays under high frequency longitudinal acoustic forcing under reacting conditions. Improved atomization and reduced breakup lengths were observed under the oscillatory combustion environment. Resonant and non-resonant conditions were compared. Lecourt and Foucaud (1987) used the forcing method developed by Ingebo to study the stability behavior of several injectors under acoustic excitation. With injectors radially distributed along the midlength of the combustor, the spray and the combustion zones were submitted to acoustic velocity disturbances (velocity coupling) while with injectors distributed axially, the spray and combustion zones were submitted to acoustic pressure disturbances (pressure coupling). A comparison of the effects of pressure and velocity coupling on combustion instability was made and the influence of factors like injector type, chamber pressure and fuel were studied. By considering pressure and velocity couplings separately, the goal was to find which of the two modes of coupling (pressure or velocity) played a stronger

role during spinning transverse mode instabilities in liquid rocket engines with head-end injectors. Anderson *et al* (1998) studied the effects of transverse acoustics on periodic atomization in liquid-fuelled rockets and its effect on combustion instability.

2.3.3 Unsteady Vaporization under Acoustic Oscillations

Strahle (Harrje and Reardon (1972)) identified five vaporization characteristic times : droplet lifetime, liquid thermal inertia, liquid thermal diffusion time, gas phase diffusion time for a locally stagnant gas field, and forced convection gas phase diffusion time. Pressure and velocity oscillations in the gas phase (acoustic perturbations) could influence the vaporization rate of liquid droplets if the period of oscillation corresponded to one of the above-mentioned vaporization characteristic times. Wieber and Mickelsen (1960) developed a theoretical model for the effect of a standing transverse acoustic field on the vaporization of liquid n-octane droplet. Their analysis indicated that a droplet assumed an oscillating transverse velocity and a fluctuating vaporization rate under the superimposed acoustic field. Heidmann and Wieber (1966) used a transfer function representation of the dynamics of vaporization process and developed a linear dynamic response model of a vaporizing droplet subjected to a travelling transverse acoustic excitation. When this analysis was applied to the vaporization of various fuels and oxidizers, a peak value in the dynamic response of the propellants was observed at a particular frequency. Crocco *et al.* (1967) developed a simplified droplet burning model based on a response function approach similar to that of Heidmann and Wieber and showed that under certain conditions the response function attained a maximum value in a certain frequency range. In their experiments, it was shown that vaporization increased significantly at

locations where velocity or pressure was a maximum. Abramzon and Sirignano (1988) and Chiang, Raju and Sirignano (1989) included variable liquid properties into the classical vaporization model. The roles of convection and internal circulation were also considered in their model.

2.3.4 Flame Response under Acoustic Oscillations

As has been already mentioned, acoustic coupling involves the interaction of the flame with standing and/or traveling pressure waves, and has been studied both experimentally (Crump *et al.* 1986; Yu *et al.* 1991; Broda *et al.* 1991, Cohen *et al.* 2003; Lieuwen 2002) and theoretically (Marble and Candel 1978; Flandro *et al.* 2004; Lieuwen 2003; Subbaiah 1983; Lieuwen 2001; Zambon and Chelliah 2006). Acoustic waves can directly modulate heat release oscillations through its coupling with the flame (pressure coupling and velocity coupling) or can modulate heat release indirectly through an intermediate modulation of hydrodynamic instabilities (Candel, 1992). Under such circumstances, coupling between flame and acoustics can take place due to periodic oscillations of equivalence ratio or mixture fractions (Clavin and Sun, 1991; Buckmaster and Clavin, 1992; Lieuwen *et al.* 1998), oscillations of flame surface area due to convective effects (Poinsot *et al.* 1987; Durox *et al.* 2002), oscillations of flame surface area due to acoustically driven accelerations (Putnam and Williams 1952; Markstein 1970; Searby and Rochwerger 1991; Pelcé and Rochwerger 1992) and also from the direct response of chemical reaction rate to pressure in its vicinity (Clavin *et al.* 1990; Ledder and Kapha 1991; McIntosh 1991; McIntosh 1993; McIntosh 1999, Wangher *et al.* 2008). Under favorable

circumstances, small amplitude acoustic disturbances can cause large amplitude heat release oscillations. Self-sustaining oscillations can eventually be excited if the phase relation between the modulated burning rate variations and pressure oscillations is favorable, as per the Rayleigh's criteria (Rayleigh, Lord, 1945; Sreenivasan and Ragu 2000). When unsteady heat release couples sufficiently in phase with the acoustic oscillations, the corresponding eigen frequencies of the combustor may be excited as per Rayleigh's criteria. If this energy gain exceeds that lost on reflection at the ends of the duct, linear acoustic waves grow in amplitude until limited by nonlinear effects (Dowling, 1997).

To mention some of the representative work in the area of flame acoustic interactions, Strahle (1965, 1967) studied the behavior of laminar jet flames subjected to transverse sound waves. McIntosh (1991) studied pressure disturbances of different length scales interacting with conventional flames. Candel (1992) reviewed combustion instabilities coupled by large scale fluid motions in the presence of pressure waves and discussed how hydrodynamic instabilities, vortex-rollup, vortex interactions, pulsations of flame or reacting jets, periodic extinctions and re-ignitions and flame acceleration could lead to oscillatory heat release. Selerland and Karagozian (1998) showed numerically that the response of gaseous diffusion flames to an oscillating strain rate (at the fuel oxidizer interface) is strongly dependent on the amplitude and frequency of oscillation. Ducruix *et al.* (2003), Schuller *et al.* (2003), Preetham and Lieuwen (2004), Preetham and Lieuwen (2005) studied the interaction between harmonic waves and premixed flames. Richecoeur *et al.* (2006) studied high-frequency transverse acoustic coupling in a multiple-injector cryogenic combustor.

Gutmark *et al.* (1989) used acoustic driver[§] upstream of the burner nozzle to study lean flammability limits of an unconfined premixed jet flame. Lang *et al.* (1987) and Gulati and Mani (1992) used acoustic driver mounted in a transverse direction to demonstrate the use of anti sound in controlling combustion instabilities. McQuay *et al.* (2000) experimentally studied the effect of acoustic fluctuations in a Rijke Tube on a propane (gaseous fuel) diffusion flame using an end mounted acoustic driver. They showed that the flame length decreased in regions with high amplitudes of acoustic velocity fluctuations. Enhanced mixing due to such fluctuations was hypothesized for the observed reduction in flame length. Farhat *et al.* (2005) experimentally studied the characteristics of a jet diffusion flame under loudspeaker induced standing waves. RMS amplitudes of pressure and velocity oscillations (along with static pressure amplitudes) were used to explain different kinds of flame acoustic interactions (blue flame, mushroom flame, stable flame etc). However, no detailed mechanism was elucidated and the pressure and velocity measurements were conducted in corresponding cold flow tests. Also, flame interactions were conducted for longitudinal modes and not for transverse interactions. Dattarajan *et al.* (2006) experimentally studied the combustion characteristics (burning rate) of methanol droplets (liquid fuel) when placed at the pressure node (velocity antinode) and pressure antinode (velocity node) of a cylindrical acoustic chamber excited by an end mounted acoustic driver. Significantly greater levels of interaction were observed in microgravity environments. The authors reported a 80% variation in burning rate when the droplet was placed near a pressure antinode and a 100% variation in burning

[§] Annaswamy *et al.* (2000) have shown that the dynamics of the loudspeaker can be modified depending on the shape and size of the housing used. Helmholtz mode oscillations can arise from the volume enclosed by the loudspeaker housing.

rate when placed at a pressure node. The aspect of an ‘effective acoustic acceleration’ was briefly considered in this work. While velocity straining effect leading to an increase in reactant consumption in the vicinity of the burning droplet (Selerland *et al.* 1998) was considered responsible for the observed increase in burning rates, a mechanism responsible for increased burning rates near a pressure antinode was not elucidated. Suzuki *et al.* (2007) used high speed imaging and shadowgraphy to experimentally study the structure and behavior of a Methane jet inside a diffusion flame under transverse acoustic forcing. They showed that jet meandering behavior was synchronous to the external forcing and the meandering motion sometimes diverged into two branches under the influence of the transverse forcing. Baroclinic effects were not explored. Shanbhogue (2008) experimentally studied the role of acoustic forcing in exciting Kelvin-Helmholtz instability in the shear layer of a bluff body stabilized flame. The resulting periodic wrinkling of the flame sheet was shown to be associated with a consequential heat release oscillation.

Chapter 3: Review of Key Physical Mechanisms

Standing and travelling acoustic waves can modulate heat release oscillations directly, by coupling with the flame system within a combustor, or indirectly, by modulating hydrodynamic instabilities inside the combustor. Such interactions can lead to heat release oscillations arising from periodic oscillations of equivalence ratio or mixture fractions, oscillations of flame surface area due to convective effects and oscillations of flame surface area due to acoustically driven accelerations. When the pressure oscillations are sufficiently in phase with the heat release oscillations, a growth in the pressure oscillations can result as per the Rayleigh's criteria.

Since the combustion chamber of a rocket engine provides an acoustically charged environment to an otherwise density stratified flowfield, baroclinically driven hydrodynamic instabilities could be predominant. In the following sections, some of the hydrodynamic instabilities that could play key role during the onset of acoustically driven instabilities in amplifying small disturbances into large scale fluid motions are discussed.

3.1 Baroclinic Vorticity Driven Instabilities

Baroclinic vorticity is generated when a pressure wave interacts with a flame front in such a way that the pressure gradient associated with the former is misaligned with the density gradient associated with the latter (Fig. 3.1). The strength of the rotational motion is given by the vorticity ω defined as the curl of the velocity field. The evolution of vorticity is given by the vorticity transport equation, Eq. 3.1, which is derived by taking the curl of the Momentum equation. The first term on the right

hand side of Eq. 3.1 is the baroclinic torque term which is produced from the interactions between misaligned density and pressure gradients and can be significant in shear-coaxial injector flowfields due to the presence of large density gradients across fuel-oxidizer interfaces and large amplitude pressure waves within the combustion chamber.

$$\frac{D\bar{\omega}}{Dt} = \frac{\nabla\rho \times \nabla p}{\rho^2} + (\bar{\omega} \bullet \nabla)\bar{u} - \bar{\omega}(\nabla \bullet \bar{u}) + \nu \nabla^2 \bar{\omega} + (\nabla \nu) \times \nabla^2 \bar{u} \quad (3.1)$$

It is clear that this term increases in proportion with (1) the strength of the density gradient, (2) the strength of the pressure gradient, (3) the sine of the angle between pressure and density gradient vectors and (4) the reciprocal of the square of the density (that is the effect is more pronounced at lower densities, usually associated with higher temperatures). The other four terms on the right-hand side of Eq. 3.1 describe, respectively, the rate of change of vorticity ω due to stretching and tilting of the vortex lines, dilatation of the velocity field, viscous diffusion and vorticity production due to viscosity gradients. For the present two dimensional flow, the contribution due to stretching is zero. Expansion of gases due to exothermic reactions cause velocity divergence to be positive and the dilatational term essentially represents an attenuation of any vorticity that may already be present in the reaction zone. The diffusion term causes a spreading of the vorticity in space and a reduction of the local vorticity (Ashurst and McMurtry, 1989). Since vorticity production from a viscosity gradient across a flame is negligible (Sinibaldi *et al.*, 1998), the baroclinic torque term $(\nabla \rho \times \nabla p) / \rho^2$ is the only dominant source of additional vorticity that

could be created at the flame interface. In a combusting environment where the production of vorticity due to baroclinicity arising from misaligned density and pressure gradients is always accompanied by a decay of vortex strength because of gas expansion or dilatation (Sinibaldi *et al.*, 1998), there will be a threshold such that flame perturbations arising from baroclinicity would occur only if vorticity generated through baroclinic interactions is greater than that attenuated due to thermal expansion. As illustrated in Fig. 3.1, the resulting rotational motion arising from baroclinic vorticity can lead to strong roll-up of the flame surface or its stabilization depending on the direction of the vorticity field that is established. For instance, compression waves approaching the GH₂/GO₂ flame front from left could lead to either unstable interaction or stable interaction depending on the direction of the density gradient at the GH₂/GO₂ interface and the direction of the pressure gradient imposed on it. Across the flame, density gradient vector $\nabla \rho$ is normal to the wrinkled flame surface and is directed from Hydrogen to Oxygen while the pressure gradient in the compression wave traveling from left to right is directed from right to left. The new vorticity that is created from this baroclinic effect is essentially a vector cross product between the pressure and density gradients at the interface of the two fluids that generating counter-rotating vortex pairs. If the resulting fluid motions are as shown in Fig. 3.1a, it leads to an amplification of the initial wrinkling of the flame front whereas if the resulting fluid motions are as shown in Fig. 3.1b, it leads to a stabilization of the initial interfacial perturbations. When the pressure and density gradients are properly oriented, baroclinicity can thus amplify low amplitude acoustic fluctuations into large amplitude fluid motions. In a reacting environment, heat

release oscillations can arise out of these large amplitude periodic motions of the fluid and in turn be coupled with pressure oscillations within the chamber. Favorable coupling between pressure oscillations and heat release oscillations can eventually lead to the onset and growth of large amplitude combustion instabilities. Baroclinic interactions occurring in premixed flames arising from pressure gradients acting across the flame surfaces separating dense unburnt reactants from lighter burnt products leading to similar folding events have been detailed in several papers (Sinibaldi *et al.*, 1998; Batley *et al.*, 1994; Batley *et al.*, 1996). An extension of these analyses and results to explain baroclinicity produced across a diffusion flame front, is, to a first approximation, pretty straight forward.

3.2 RM and RT instability of acoustically accelerated interfaces

When an interface separating two fluids of different densities is accelerated such that the acceleration is directed from the denser fluid to the lighter fluid, the interface separating the two fluids become unstable with initial perturbations growing exponentially in time (Fig 3.2 and Fig 3.3). The same configuration with acceleration directed in the opposite direction is stable with interfacial perturbations remaining bounded in time. The Richtmyer-Meshkov instability, on the other hand, occurs when a density stratified interface is impulsively accelerated. Such a situation can occur due to the passage of a shock wave through a density stratified interface. (Fig. 3.4). It differs in two primary ways from the Rayleigh-Taylor instability. Firstly, RM instability does not depend on the direction of the acceleration and secondly, the initial interfacial perturbations grow linearly in time.

For the liquid rocket engine problem, a variant of the Richtmyer-Meshkov (RM) instability arising from the passage of finite amplitude steep fronted pressure waves through the density stratified interface and a variant of the classic RT instability arising from the acoustic acceleration of density stratified interfaces can be triggered (Taylor 1950; Richtmyer 1960; Meshkov 1969; Markstein and Squire 1955). During such interactions, the flame simply acts as a density stratified interface between the fuel and the oxidizer, undergoing acceleration. Consequently the well-known Rayleigh-Taylor instability can be excited, with the acceleration due to gravity in the classical RT equation replaced by that due to a fluctuating pressure gradient arising from acoustic interactions. The baroclinic roll-up of the interface is simply a more accentuated form of the Rayleigh-Taylor instability. Such instabilities in acoustically accelerated flames have been studied by Markstein and Squire (1955) and by Petchenko *et al.* (2006). The acoustic oscillations, in these experiments are seen to produce an effective acceleration field at the flame front leading to a strong Rayleigh-Taylor instability during every second half of the oscillation period. It has been further observed that under such instability, the flame front becomes strongly corrugated with elongated jets of heavy fuel mixture penetrating the burnt gas (Petchenko *et al.* 2006). The differences in density at different lateral locations encountered by the planar pressure wave with pressure gradient directed from the higher density fluid to the lower density fluid leads to differential induced velocities. This then causes a spike to develop such that a “finger” of higher density fluid is pushed into the fluid with lower density. If the pressure gradient is in the other direction then the instability is suppressed (Liu *et al.* 1993; Sharp, 1984).

For the RT instability, the interface amplitude grows as

$$\frac{d^2\eta}{dt^2} - kgA\eta = 0 \quad (3.2)$$

where η is the amplitude of the sinusoidal perturbation of the discontinuous interface between two incompressible fluids under acceleration g , k is the wave number for the perturbation and A is the Atwood number across the interface defined as $(\rho_2 - \rho_1)/(\rho_2 + \rho_1)$. Here g is directed from ρ_2 to ρ_1 . ($\rho_2 > \rho_1$) Eq. 3.2 indicates that η grows exponentially with time if $A > 0$, showing that the interface is unstable, or oscillates if $A < 0$, showing stability. The growth rate for this classical instability, $n_{classical}$ is given as

$$n_{classical} = (gkA)^{1/2} \quad (3.3)$$

Instead of the acceleration field being created due to gravity, in the present problem acceleration is due to passage of acoustic waves through the density stratified fuel-oxidizer interface. If the complex form of the harmonic solution for the acoustic pressure of a plane wave is written as (Kinsler *et al.*, 1982),

$$p = Ae^{j(\omega t - kx)} + Be^{j(\omega t + kx)} \quad (3.4)$$

then the associated particle velocity (u_+ and u_-) and acceleration due to acoustic forcing (a_+ and a_-) is,

$$u_+ = +\left(\frac{p_+}{\rho_o c}\right) \text{ And } u_- = -\left(\frac{p_-}{\rho_o c}\right) \quad (3.5)$$

$$a_+ = +\left(\frac{j\omega p_+}{\rho_o c}\right) \quad a_- = -\left(\frac{j\omega p_-}{\rho_o c}\right) \quad (3.6)$$

c is the speed of sound. Because of the frequency term (ω), acceleration due to acoustics can be significant although the period through which such acceleration would act would decrease as the frequency is increased. Furthermore, viscosity would tend to stabilize the growth rate of the interface such that in real applications, there will be a wave number (k) for which the growth rate (n) will reach a maximum (Chandrasekhar,1961). The growth rate vs. wave number for a given dynamic viscosity for the two fluids can be obtained by letting y vary from 1 to ∞ in Eq. 3.7 from Chandrasekhar (1961) and finding pairs of values for k (wave number) and n (growth rate) for every combination of $Q(y)$ and y . Using a as the speed of sound, and ν as kinematic viscosity, Q in this particular context is defined as

$$Q = \frac{a}{k^3 \nu^2}$$

$$Q(y) := \left[\frac{(y-1)}{(\alpha_2 - \alpha_1)} \right] \cdot \left[y^3 + (1 + 4\alpha_1 \cdot \alpha_2) \cdot y^2 + (3 - 8\alpha_1 \cdot \alpha_2) \cdot y - (1 - 4\alpha_1 \cdot \alpha_2) \right] \quad (3.7)$$

$$k_v(y) := \left(\frac{a}{\nu^2} \right)^{\frac{1}{3}} \cdot \left(\frac{1}{Q(y)^{\frac{1}{3}}} \right)$$

$$n(y) := \left(\frac{a^2}{\nu} \right)^{\frac{1}{3}} \cdot \left[\frac{(y^2 - 1)}{Q(y)^{\frac{2}{3}}} \right]$$

$$\alpha_1 = \frac{\rho_{H2}}{\rho_{H2} + \rho_{O2}} \quad \alpha_2 = \frac{\rho_{O2}}{\rho_{H2} + \rho_{O2}} \quad v = \frac{v_{O2} + v_{H2}}{2}$$

In this work, the possible presence of acoustically driven RT instability is shown experimentally and wave numbers for which high growth rates can be expected are evaluated. Through a linear analysis of the growth of a RT unstable interface and considering the effects of viscosity, it is shown that more than 200% growth in the amplitude of perturbations with the most unstable wavelength can be attained during half a period of the acoustic oscillation at certain frequencies. In reality, the interface between two fluids will have finite initial thickness. Since the baroclinic torque, being proportional to density gradient, is initially responsible for the RT growth, the initial growth of finite thickness interfaces, as in the present case, will be slower than that of discontinuous interfaces for the same density jump because the density gradient is smaller in the former. RT instability of interfaces having initial finite thickness has been studied by Lelevier *et al.* (1955) and Duff *et al.* (1962). Hsieh (1978) has formulated a general problem for interfacial Rayleigh–Taylor instability for fluids flow with heat and mass transfer.

3.3 Jet Preferred Mode and Wake Mode Instabilities

Apart from instabilities arising from the acceleration of density stratified interfaces, the shear coaxial flowfield is also subjected to wake mode and jet preferred mode instabilities.

The jet preferred mode (Fig 3.5) is usually described as the mode with the largest growth rate of the shear layer formed between a jet and the surroundings. Defined in terms of the Strouhal number $St = fD/U$, the most dispersive modes correspond to frequencies which make the Strouhal Number fall somewhere between 0.30 and 0.60. The precise value of the Strouhal number depends on the details of the jet, the injector and other associated parameters.

The wake mode (Fig 3.6) on the other hand is related to vortex shedding behind a bluff body and it generally corresponds to a Strouhal number of 0.20 in the turbulent regime. This mode of instability leads to the shedding of vortices at some preferred frequency which might not correspond to the frequency of the most amplified KH mode. For high Reynolds number flows, a relation from Prasad and Williamson (1997) places the frequencies of the two instabilities as

$$f_{KH} = 0.0235 f_{VK} Re^{0.67}$$

The calculation of the wake mode frequency associated with the shear coaxial flow field relevant to this study needed a few special considerations. Firstly, the above criterion of Strouhal number = 0.21 has been experimentally verified for non reacting turbulent flows with Re in the range $10^2 < Re < 10^7$ whereas the flow of interest is reacting and the shedding frequency could be influenced by buoyancy driven effects due to heat release. Secondly, dilatation due to heat release can lead to the stabilization of the VK mode behind a bluff body as has been suggested by recent numerical simulations due to Erickson *et al.* (2006). Although Erickson's study has

been for a bluff body stabilized premixed flame, a similar reasoning could be applied to diffusion flames established in the wake of a bluff body. Thirdly, the flow around our bluff body (the splitter between fuel and oxidizer jets) has two different fluids (fuel and oxidizer) flowing around it at different velocities as shown in the schematic of Fig. 3.6 which makes the application of the $St = fD/U$, equation with $S = 0.21$ slightly less straightforward.

Such instabilities of the shear layer between the fuel and the oxidizer, in the neighborhood of the injector can be amplified by certain modes of acoustic oscillations within the chamber. Sheridan *et al.* (1992) for instance showed that under the influence of harmonic excitation, the separated shear layer can roll up into vortices with a frequency commensurate with the forcing frequency. In a recent study, Shanbhogue *et al.* (2008) experimentally studied the role of acoustic forcing in exciting Kelvin-Helmholtz instability in the shear layer of a bluff body stabilized flame and showed that the resulting periodic wrinkling of the flame sheet was associated with a consequential heat release oscillation.

Chapter 4: Experimental Apparatus and Techniques

4.1 Introduction

A model shear coaxial injector rig was designed to conduct flame acoustic interaction experiments relevant to the liquid rocket engine instability problem. A transversely mounted acoustic driver was used to simulate acoustic conditions occurring in the neighborhood of such injectors. As the acoustic output of the driver unit was limited, the model experiments were conducted at scaled-down conditions, ensuring relatively strong level of acoustic excitation compared to the level of natural turbulence fluctuation.

Fig. 4.1a shows a schematic of the near injector region for a liquid rocket engine with two shear coaxial injectors, each comprising of a center jet of liquid Oxygen (LOX) surrounded by co-flowing regions of high speed gaseous Hydrogen (GH₂). Once injected into the combustor, the liquid jet of Oxygen is atomized, vaporized and a diffusion flame system is eventually formed between gaseous Hydrogen and vaporized Hydrogen.

The interactions between acoustics and the turbulent multiphase reacting flow field in the vicinity of the injector is very complex and involve processes associated with periodic atomization and vaporization of the liquid core, unsteady mixing between fuel and oxidizer and flame interactions with travelling and standing waves. As the goal of this study was to identify instability mechanisms associated in particular with interactions between flame and acoustics, a simpler physical model that considered the interactions between acoustic waves and GO₂-GH₂ diffusion

flame fronts was accepted as a good starting point for design of apparatus . This model, shown as an inset in Fig. 4.1a, appears physically meaningful because even in real rocket engines using LOX, by the time the flame is produced downstream of the injector, it essentially sits between vaporized Oxygen and gaseous Hydrogen. A schematic of the resulting shear coaxial injector rig, based on this simplified model, is shown in Fig. 4.1b with quartz glass windows, acoustic driver, parker skinner valves for flow control and Setra pressure transducers for static pressure measurements upstream of choked orifices on the gas lines. The schematic in Fig 4.2 shows a more detailed view of the combustor along with the locations for pressure measurement taps. Fig. 4.3 shows a detailed view of the experimental rig setup for schlieren visualization.

4.2 Description of Apparatus

4.2.1 Combustor Geometry

The combustion chamber used in this study was of a rectangular waveguide geometry and had a dimension of 15"x 3.5"x 0.375". As shown in Fig 4.2, it was equipped with a 2D shear coaxial injector element at one end while the other end was open to the atmosphere. The two-dimensional injector had a center jet that was 0.75 inch wide and two co-flow jets each 0.25 inch wide. Lip thickness between center jet and co-flow was 0.125 inch. The injector end of the combustor was also provided with 0.125" slots near the side walls for wall jet injection. Wall jets were only used for igniting the combustor and were turned OFF once the diffusion flame system between the center and the co-flowing jets was established. 1 inch thick quartz glass

windows gave full access to the test section and allowed direct examination of the flame structure, schlieren and shadowgraph imaging and chemiluminescence measurements. For studies involving pressure measurements, one of the quartz glass sidewalls was replaced by a stainless steel sidewall with pressure taps that allowed the flush mounting of water cooled dynamic pressure transducers. Locations of the taps on the steel block corresponded to pressure tap locations shown in Fig 4.2b.

4.2.2 Inlet Section

The inlet section, located upstream of the injector faceplate, connected the combustion chamber with the fuel and oxidizer lines. Inside the fuel and oxidizer lines stainless steel honeycomb sections were used to flatten inlet velocity profile, reduce turbulence level, and provide flashback protection. Fig. 4.4 shows an inside view of the inlet section with one of the side blocks intentionally removed for easy visual access. It shows injection points and flow paths for center, co-flow and wall jets along with flow straighteners for the center and the co-flow jets. In the backdrop, it also shows vibration dampers on the breadboard, one way check valves on the gas lines to prevent back flow of oxidizer or reactant gases and Setra pressure transducers to measure pressure on gas lines upstream of their choked orifices. Fig.4.5 and Fig 4.6 show dimensional details of the injector plate. Fig. 4.7 shows inlet locations for center, co-flow and wall jet gases. Port 1 is injection location for the center jet gas, 2a and 2b for co-flowing gas and 3a and 3b for wall-jets. Open circles indicate the position of through holes used for bolting the side plates with the injector plate. All dimensions are in inches.

4.2.3 Supply System for Fuel and Oxidizer

Pressurized tanks of Hydrogen and Oxygen supplied fuel and oxidizer to the chamber while Argon, Helium and Methane tanks served to dilute individual streams in modifying densities, velocities and chemical compositions of individual jets in specific experiments. Fuel, oxidizer and diluent gas lines were metered by choked orifices. Pressure transducers (Setra model - 206) were used to sense pressure upstream of each orifice and the pressure values were read off directly from Setra Datum 2000 metering units. Electrically operated, normally closed Parker Skinner valves with 0.25" orifices were used for switching purposes on the gas supply lines.

4.2.4 Acoustic Driver

An acoustic driver of nominal impedance 16 ohms and a maximum power rating of 100 watts, mounted in a transverse fashion was used to produce controlled compression waves at various frequencies and amplitudes. A transition block connected the driver unit to the combustor side wall providing a smooth transition from a circular section (driver end of effective diameter of 0.75") to a 1" x 0.125" rectangular slit (combustor end). The acoustic driver had a range of optimal operability between 100Hz to 100,000 Hz.

4.3 Instrumentation and Diagnostics

4.3.1 Schlieren Imaging

The schlieren system (cf. Yang 2001) for the setup featured a typical Z configuration (Fig. 4.8). The light from an arc lamp of 10 W nominal power was

collimated by a 60" focal length, 6" diameter spherical mirror. For extremely short exposure phase locked schlieren imaging, a 12 bit ICCD DiCam Pro camera was used with exposure times that could be controlled to go down to as low as 3ns. In our schlieren experiments, images with exposure times as low as 10 μ s were recorded. For phase locked imaging, synchronized pulses from the same wave generator were fed into an IDT Laser Timing Control board, which in conjunction with ProVision II software running on a Windows machine triggered a DicamPro 12 bit ICCD Camera at different phases of the acoustic forcing.

4.3.2 Phase Sensitive OH*/CH* Chemiluminescence Visualizations

To improve our understanding of the instability driving mechanism it was necessary to collect some information on the heat release process. A simple technique that indicates the rate of combustion involves measuring chemiluminescent radiation from the free OH* radical. This radical appears almost exclusively in the reaction zone and their emitted light intensity can be directly related to the chemical reaction rate or, equivalently to the heat release rate. The relation maybe assumed linear (Poinsot *et al.* 1987; Langhorne 1988). A DiCam Pro ICCD camera with a UV lens and a 308 nm band pass filter was used to pick OH* Chemiluminescence from the oxy-hydrogen flame. For phase locked imaging, synchronized pulses from the same wave generator were fed into an IDT Laser Timing Control board, which in conjunction with a ProVision II software running on a Windows machine triggered a DicamPro 12 bit ICCD Camera at different phases of the acoustic forcing. Images with exposure times as low as 8 μ s were recorded. For instantaneous and ensemble averaged imaging, the light emitted by the diffusion flame system was imaged by an

UV lens with a 308nm bandpass filter onto a S20 Multialkali photocathode for the OH* chemiluminescence. For the ensemble averaged images, the camera exposure was increased to the order of 500ms – 750ms and a neutral density filter was used along with the bandpass filters to control the net amount of light falling on the CCD sensor. For CH* chemiluminescence (in cases where a blended fuel of H₂ and CH₄ was used), a 430 nm band pass filter was used.

4.3.3 Dynamic Pressure Measurements

To investigate the spectral content of pressure oscillations in the chamber, one of the quartz windows was replaced with a stainless steel plate with pressure taps onto which the dynamic pressure transducers along with their water cooled adapters could be flush mounted. The location of the taps are shown in Fig 4.9.

Kistler 211B5 voltage mode high bandwidth dynamic pressure transducers with measuring range of 0 to 250 psi were used for dynamic pressure measurements. Each Piezotron miniature pressure sensor, housed within a Kistler 228P water-cooled adapter was well suited for fast transient measurements under extreme environmental conditions. Sensor output was passed through a Kistler 5134A1 Piezotron coupler and then fed into a National Instruments Digital Acquisition Card which interfaced with a LabVIEW monitoring program. The Piezotron coupler allowed filtering and amplification of signal from the sensors. A filter of 10 kHz and a gain of 100 on the coupler were typically used. Data was sampled at a sampling rate of 20 kHz. The LabVIEW VI not only performed a runtime FFT on the sampled data but also saved the data in data files which were subsequently loaded into and analyzed with FFT codes in MATLAB.

4.3.4 High Speed Cinematographic Imaging

A Photron Fastcam Ultima 1024 high speed camera was used for high speed imaging of flame front oscillations. In particular, it was used to observe the rollup of the diffusion flame front under transverse acoustic forcing and subsequent pairing and merging of vortices. A desktop PC running the Photron Fastcam software was used to capture and record images. The camera had an acquisition rate of 60-16000 frames per second (monochrome) and shutter speeds from 0.016 to 7.8E-6 s. For the requirements of the current investigation, the camera was operated at a framing rate of 1000 fps with an associated exposure of 1ms.

4.3.5 Hotwire Measurements

The frequency of structures in the mixing layer between the center jet and the co-flow jets (for the non-reacting case) was measured using a conventional miniature hotwire probe (film sensor) and a constant temperature anemometer (TSI Model 1750). The 1750 CTA provided trim control (to optimize the frequency response for a given cable length) and gain control that is set at the factory according to the type of sensor used (film or wire). A power source with an output of 25 volts DC was used to power the device.

4.3.6 OH* / CH* Chemiluminescence Oscillation Measurements

A photomultiplier tube (PMT) using a HAMAMATSU R3788 High Sensitivity, Bi-Alkali Photocathode (8mm x 24mm) with good spectral response between 185nm – 750 nm was used to measure frequencies at which flame front oscillated naturally or under the influence of external forcing. The PMT tube itself

had a circular cross section with ID $\sim 0.875''$ and OD $\sim 1.25''$. For measuring the oscillations of the Oxy-Hydrogen diffusion flame, a 308nm circular bandpass filter was mounted inside the PMT tube in front of the photocathode sensor. A TENMA™ Regulated DC Power Supply supplied the required 15 V DC for stable PMT operation while a potentiometer allowed amplification of the voltage signal from the PMT to a level suitable for data acquisition. For high frequency flame oscillations (forced at $\sim 1150\text{Hz}$) LabVIEW based instrumentation acquired data at a sampling rate of 20kHz while a low pass filter filtered out signals above 10kHz. For low frequency flame oscillations (caused by eventual pairing and merging of flame front wrinkles) LabVIEW based instrumentation acquired data at a sampling rate of 3 kHz. The signal from the PMT was passed through a Dual Channel Filter and was band pass filtered between 1 Hz and 1.5 kHz. Since the oscillatory component of flame front oscillations was desired, AC coupling was used on the Dual Channel Filter to remove any DC bias in the signal from the PMT. The PMT was set up on a graduated mounting rail so that precise position of the sensor area with respect to the injector could be recorded.

4.3.7 Other Lab Equipments

4.3.7.1 Signal Generator and Amplifier

To be able to excite the chamber acoustically at various frequencies and amplitudes, a Wavetek 40MHz Universal Waveform generator was used. This signal generator provided various monotone and sweep signals which were amplified through a Bogen C-100 amplifier and fed into the 100 watts 16 ohm compression

driver. For certain experiments where broadband signals and band limited white noise signals were required, LabVIEW based signal generators were also used.

4.3.7.2 Oscilloscope and Filter

A Tektronix TDS 3014 four channel color digital phosphor oscilloscope was used for visualizing signals to and from sensors and actuators whereas a STANFORD RESEARCH SYSTEMS SR650 Dual Channel Filter was used for filtering signal from sensors as and where applicable.

4.3.7.3 LabVIEW Based VIs

For data acquisition, LabVIEW 8 based VIs running on a Pentium 4 Windows based PC was used. A BNC 2120 Data Acquisition Board connected to a PCI -6251 Card was used to read data from sensors into the VIs.

4.4 Flow Rate Calculations

The flow rates for fuel, oxidizer and diluents were established using choked orifices and Setra static pressure transducers mounted upstream of the orifices. Pressure and choked orifice area values were used to calculate mass flow rates by applying the well known equation for mass flow rate through a choked nozzle (orifice)

$$\dot{m} = \left(\frac{p_o A^*}{\sqrt{T_o}} \right) \sqrt{\frac{\gamma}{R} \left(\frac{2}{\gamma + 1} \right)^{(\gamma+1)/(\gamma-1)}}$$

where symbols have their usual meanings. In some particular cases where mass flow requirement of diluent gases was too small, Bernoulli's equation was used to calculate mass flow. While bottled gases from Airgas Inc. were used for fuel oxidizer and diluents, air flow was established from the university's compressed air supply system.

4.5 Injection Arrangement

The oxidizer and the fuel lines were needed to be suitably adapted for performing various experiments reported in this thesis. In the reversal of density gradient experiments for instance, the switching of density gradient was achieved by interchanging the position of the denser oxidizer and the lighter fuel jets. In the configuration shown in Fig. 4.10a, denser gas (Oxygen) and lighter gas (Hydrogen) forms the center-jet and co-flow jets respectively whereas in the configuration shown in Fig. 4.10b, denser gas (Oxygen diluted with nitrogen) and lighter gas (Hydrogen) forms the co flow and center jets respectively. This interchange of position between the denser and the lighter gases while maintaining the same direction of acoustic forcing provided a convenient way of reversing the direction of the density gradient vector at the fuel-oxidizer interface with respect to the acoustic driver. One configuration then served as the baseline for the reversed configuration when the interface was acoustically accelerated from the same side.

For the density ratio tests performed as a part of this work, the center jet of Oxygen was diluted with Helium while the outer jet was diluted with Argon. This allowed changing the density ratio between oxidizer and fuel from 16:1 to 1:1 while keeping jet velocities and heat release relatively constant (Fig. 4.11a).

For the velocity ratio tests, the center jet was pure Oxygen while the outer jet was a mixture of Hydrogen, Argon and Helium. A mixture of 5.235% Argon and 94.765% Hydrogen (by mole fractions) gave a mixture molecular weight of 4.002 g/mole which was same as that of pure Helium. Addition of Helium to such a mixture of Argon and Hydrogen served to change the velocity of the outer jet while keeping its density unchanged (Fig. 4.11b).

For the effect of chemical composition tests, the center jet was a mixture of Oxygen and Argon while the outer jet was a mixture of Hydrogen, Helium and Methane (Fig. 4.11c). For the momentum effect tests, data collected as part of the density effect tests and the velocity effect tests were used.

4.6 Firing sequence for reacting flow experiments

4.6.1 Ignition

Particular attention was given to prevent ignition of a pre-mixed charge of fuel and oxidizer that could form near the injector region of the combustor under certain conditions. This was achieved by first allowing air to flow into the combustion chamber through the wall jets lines of the combustors. Once airflow was established, a butane igniter was lit and placed near the exit of the combustor. Pilot Hydrogen gas was then switched ON and a air-Hydrogen flame was established. The initial flow of air ensured that Hydrogen did not accumulate near the injector before ignition and that the oxidizer was always present in abundance compared to the amount of fuel. Once the initial flame was established, Oxygen was switched ON. At this time air was switched OFF and the flow rate of Hydrogen was increased until H₂ and O₂ were in

stoichiometric or near stoichiometric[‡] proportions. Given the particular type of test, other gases like Argon, Helium and / or Methane were introduced at this stage and the diffusion flame system was acoustically forced at the desired frequency and amplitude and related measurements were made. The steps for igniting the combustor are reiterated for convenience of reading.

1. Air ON
2. Butane Igniter Flame ON.
3. Hydrogen pilot ON.
4. Oxygen ON.
5. Air OFF.
6. Hydrogen mains ON.
8. Inert gases and /or secondary fuels ON. (if applicable)
7. Acoustic excitation ON.

4.6.2 Extinction

The steps for extinguishing the flame in the combustor on the other hand followed the following sequence. Once again, the primary goal was to prevent too much fuel from being surrounded by too little oxidizer.

1. Air ON
2. Hydrogen mains and secondary fuels (If applicable) OFF

[‡] Near stoichiometric for cases where Methane was also used. In such cases, the entire Methane-Hydrogen-Oxygen combination would be stoichiometric once Methane was introduced.

3. Oxygen OFF
4. Inert gases OFF.(If applicable)
5. Air OFF when combustor is sufficiently cooled

Chapter 5 : Experimental and Analytical Characterization of Chamber Acoustics using Broad-Band Forcing

Since interactions between acoustic waves and density stratified reacting and non-reacting flowfields inside a combustion chamber with a given geometry was key to this investigation, it was important to characterize the acoustic modes of the chamber so that interactions at different frequencies and amplitudes could be better interpreted. However, the analytical derivation of modal frequencies for a combustor with a non-homogenous flow field is usually complicated by the presence of non-homogeneity in density and temperature, and hence in the speed of sound. Such heterogeneity affects the eigen frequencies and the eigen modes of the chamber (Kim and Williams 1998) and makes it necessary to use both the geometry of the combustor and the distribution of acoustic media within that geometry to obtain the dominant modes.

A more straightforward approach is to find the dominant frequencies of the combustor experimentally by exciting it acoustically with white noise forcing. Resulting pressure spectra inside the combustor, measured using wall mounted pressure transducers could then be used to understand the resonance behavior of the experimental setup with local maxima and minima in pressure spectral intensity indicative of standing wave behavior due to acoustic resonance.

5.1 Preliminary Experiments

With this consideration in mind, non-reacting flow tests were conducted at four different flow conditions as shown in Table 5.2. Band-limited (< 5000 Hz) white noise forcing (at a speaker power rating of ~ 9 watts) using LabVIEW based instrumentation was used to acoustically excite the chamber. Dynamic pressure response of the combustor to the externally imposed white noise excitation was measured using wall mounted Kistler 211B5 piezoelectric transducers. Tap locations for the measurement ports are shown in Fig.4.9. The time trace of the pressure signal was converted to frequency domain spectra using a standard FFT code written in Matlab. About 400 spectra were averaged to obtain the results, which showed distinct spectral peaks corresponding to various acoustic modes of the chamber. Data acquisition was carried out at a sampling frequency of 20 kHz using a Pentium IV PC equipped with a National Instruments PCI-6251 Multifunction DAQ card.

Fig. 5.1 shows the resulting pressure spectra at Taps #1 through #4 under no-flow conditions (quiescent air). Fig. 5.2 shows pressure spectrum from Tap #4 redrawn from previous figure with some of the characteristic frequencies labeled and tabulated for easy visual reference. Table 5.1 compares some of these experimentally obtained characteristic frequencies with calculated values. Fig. 5.3 through Fig. 5.5 represent pressure spectra corresponding to the first three flow conditions in Table 5.2 without reaction. For these tests, the combustor was excited at a speaker power rating of ~ 9 watts. For each density ratio condition, pressure spectra corresponding to the first four tap locations at $y=0.5$ -in are presented. In general, there were up to three distinctive spectral peaks worth noting that have been denoted as f_1 , f_2 , and f_3 in the

ascending order of frequency in the figures. From a comparison of the peak frequencies between the different taps and the three different flow conditions (cf. Table 5.3) the following observations[§] could be made :

1. The frequency f_1 was relatively unaffected by tap locations and flow conditions. This indicated that it was possibly related to the oxidizer condition which was held constant throughout the various tests.
2. The frequency f_2 changed substantially among different flow conditions but relatively little between the tap locations. This indicated that it was possibly a longitudinal mode of the chamber that was related to the product conditions.
3. The frequency f_3 also changed substantially among different flow conditions but practically remained constant across the tap locations. This indicated that it was possibly a transverse mode of the chamber and related to the product conditions as well.

5.2 Model Development

To be able to interpret and understand modal behavior for both non-reacting and reacting flows, a simple model was developed in which the average speed of sound was used to calculate modal frequencies. Since experimental data relating to species concentration was not available, it was necessary to model the distribution of fuel, oxidizer and fuel-oxidizer mixture in various regions of the combustor in a physically meaningful way such that the average speed of sound could be calculated

[§] The pressure spectra corresponding to the last flow conditions were omitted because they were less interesting. Both the density ratio and velocity ratio were small in this case, and the resulting spectra resembled those of the no-flow condition with numerous spectral peaks.

from its speed in individual media. For example, for the non-reacting flow situation shown in Fig. 5.6, the products could simply be assumed to be a stoichiometric mixture of fuel and oxidizer as dictated by initial flow rates^Ω and the first quarter-wave mode in the transverse direction could be calculated using the simple expression:

$$f_{\lambda/4} = \frac{1}{4 \left[\left(\frac{W_o}{a_o} \right) + 2 \left(\frac{W_f}{a_f} \right) + \left(\frac{W - W_o - 2W_f}{a_p} \right) \right]} \quad (5.1)$$

where a_o , a_f , and a_p denote speed of sound as it travels through oxidizer, fuel and products respectively, while W , W_o and W_f denote chamber width, width of oxidizer jet and width of individual fuel jets respectively.

In Eqn. 5.1, one finds that the frequency of the transverse mode depends on the assumption one uses to arrive at the product composition. Along with using a stoichiometric mixture of fuel and oxidizer as dictated by the initial inflow rates to estimate product composition, two more approaches were considered that incorporated the known phenomenon of jet mixing length and a new experimental result of preferential excitation under transverse acoustic forcing to estimate the product composition. The essential idea was to model the product composition in the product dominated regions (1 and 3 in Fig. 5.7) and to use the corresponding speed of sound in the product a_p in calculating the frequency of transverse modes and

^Ω It will be shown in the model development section that the fully mixed model is based on the assumption of a stoichiometric mixture. Corrections due to mixing length and acoustically driven entrainment are considered in the other two models.

longitudinal modes associated with the product column. For isothermal experiments where flow temperatures were known, calculated Eigen frequencies from these models were in good agreement with measured frequencies. The following section introduces each of these model in some detail. The models essentially differ in the way they control the value of the parameter ψ in the standard equations 5.2 - 5.5 applied to the reaction between a blended fuel of Hydrogen and Methane with Oxygen

(cf. Table 5.2). η_{O_2} , η_{CH_4} , η_{H_2} represent the number of moles involved in a stoichiometric reaction between the gases.

$$MW_{mix}(\psi, \eta_{H_2}, \eta_{O_2}, \eta_{CH_4}) = \left(\frac{\eta_{H_2}}{\eta_{H_2} + \eta_{CH_4} + \psi\eta_{O_2}} \right) MW_{H_2} + \left(\frac{\eta_{CH_4}}{\eta_{H_2} + \eta_{CH_4} + \psi\eta_{O_2}} \right) MW_{CH_4} + \left(\frac{\psi\eta_{O_2}}{\eta_{H_2} + \eta_{CH_4} + \psi\eta_{O_2}} \right) MW_{O_2} \quad (5.2)$$

$$\gamma_{mix}(\psi, \eta_{H_2}, \eta_{O_2}, \eta_{CH_4}) = \left(\frac{\eta_{H_2}}{\eta_{H_2} + \eta_{CH_4} + \psi\eta_{O_2}} \right) \gamma_{H_2} + \left(\frac{\eta_{CH_4}}{\eta_{H_2} + \eta_{CH_4} + \psi\eta_{O_2}} \right) \gamma_{CH_4} + \left(\frac{\psi\eta_{O_2}}{\eta_{H_2} + \eta_{CH_4} + \psi\eta_{O_2}} \right) \gamma_{O_2} \quad (5.3)$$

$$R_{mix}(\psi, \eta_{H_2}, \eta_{O_2}, \eta_{CH_4}) = \frac{R_{univ}}{MW_{mix}(\psi, \eta_{H_2}, \eta_{O_2}, \eta_{CH_4})} \quad (5.4)$$

$$a_{mix}(\psi, \eta_{H_2}, \eta_{O_2}, \eta_{CH_4}) = \sqrt{\gamma_{mix}(\psi, \eta_{H_2}, \eta_{O_2}, \eta_{CH_4}) R_{mix}(\psi, \eta_{H_2}, \eta_{O_2}, \eta_{CH_4}) T} \quad (5.5)$$

5.2.1 Full Mixing Model / Well Stirred Reactor Model

According to this model, average speed of sound is calculated using a fully premixed mixture of fuel and oxidizer in the product regions. Molar concentrations based on volumetric flow rate of fuel and oxidizer jets (isothermal case) are used. In our tests, since the volumetric flow rates were chosen to maintain stoichiometric mixture of fuel and oxidizer, this model essentially gave us a stoichiometric mixture of fuel and oxidizer. In the reacting flow scenario, this model would imply using equilibrium products of reaction to calculate the speed of sound in the product regions.

$$\psi = 1$$

$$a_{ang}(\psi, \eta_{H_2}, \eta_{O_2}, \eta_{CH_4}) = a_{mix}(\psi, \eta_{H_2}, \eta_{O_2}, \eta_{CH_4})$$

The frequency of the three quarter longitudinal mode of the combustor, for example could then be calculated as

$$f(\psi, \eta_{H_2}, \eta_{O_2}, \eta_{CH_4}) = \frac{a_{ang}(\psi, \eta_{H_2}, \eta_{O_2}, \eta_{CH_4})}{(4 \frac{L'}{3})}$$

$$\text{Where, } L' = L + 0.6 \left(\frac{D}{2} \right) \text{ (End correction)}$$

5.2.2 Jet Mixing Length Model

This was a velocity ratio and potential core length based mixing model. It was argued that between the injector face plate and the distance from the injector where the potential core of the center jet ceases to exist, the velocity ratio between center and co-flow jets will bias the mixture towards the slow moving jet in the product region. Because of greater residence time, the slower jet will contribute more to the mixture fraction than if the two jets were at the same velocity. A correction factor was used to account for this increase in molar concentration of the slower jet using the velocity ratio of the two jets. This correction was applied only in a small region near the injector $0 < y < 6D$. Beyond $y > 6D$, a full mixing model was assumed. According to this model, for an isothermal stoichiometric flow of GH_2 and GCH_4 as fuel and GO_2 as oxidizer, with velocity ratio $\psi = (V_{\text{H}_2 / \text{CH}_4} / V_{\text{O}_2})$ the frequency of the three quarter mode in the longitudinal direction associated with the product column would be calculated as below :

$$\psi = \frac{V_{\text{H}_2 / \text{CH}_4}}{V_{\text{O}_2}}$$

$$a_{\text{ang}}(\psi, \eta_{\text{H}_2}, \eta_{\text{O}_2}, \eta_{\text{CH}_4}) = \frac{L'}{\left[6 \frac{D}{a_{\text{mix}}(\psi, \eta_{\text{H}_2}, \eta_{\text{O}_2}, \eta_{\text{CH}_4})} \right] + \left[\frac{L' - 6D}{a_{\text{mix}}(1, \eta_{\text{H}_2}, \eta_{\text{O}_2}, \eta_{\text{CH}_4})} \right]}$$

$$f(\psi, \eta_{\text{H}_2}, \eta_{\text{O}_2}, \eta_{\text{CH}_4}) = \frac{a_{\text{ang}}(\psi, \eta_{\text{H}_2}, \eta_{\text{O}_2}, \eta_{\text{CH}_4})}{\left(4 \frac{L'}{3}\right)}$$

5.2.3 Acoustically Driven Entrainment Model

Entrainment (ζ), of the center jet fluid into the co-flow, is affected by the ratio between transverse jet momentum (due to the acoustic driver) and momentum of main flow. If the acoustic amplitude is kept fixed (which in turn implies that the transverse jet momentum is kept fixed), the entrainment of the center jet fluid into the co-flow would be dependant on the momentum of the main flow. According to this model, fuel oxidizer mole fractions in the mixture is corrected using entrainment of Oxygen (or the center jet fluid) into the co-flow regions and this correction is applied along the entire length of the combustor $0 < y < L$. It should be noted that while more of the center jet is entrained into the driver side co-flow (Region 1 in Fig. 5.7), there is a decrease in the amount of the center jet fluid available to be entrained into the wall-side co-flow (Region 3 in Fig. 5.7). This difference in the composition of the two co-flows arising from this discrepancy in entrainment of center jet fluid into the driver side co-flow and wall side co-flow possibly accounts for the difference in frequency of the three quarter mode (longitudinal) of the chamber as observed in the experimentally obtained pressure spectra.

For an isothermal stoichiometric flow of a GH_2/GCH_4 fuel (co-flow with a flow momentum given by $J_{\text{H}_2/\text{CH}_4}$) and GO_2 oxidizer (center jet with a flow momentum given by J_{O_2}), the frequency of the three quarter mode in the longitudinal direction can be calculated using Eq. 5.2 - 5.5, in which, ψ , under the assumptions of this model, would represent a measure of the entrainment of the center jet Oxygen into the co-flow regions. This factor will depend on the ratio between the acoustically

driven transverse jet momentum (J_A) and the total momentum of the main flow ($J_{total}=J_{O_2}+2J_{H_2/CH_4}$).

On the driver side, entrainment of center jet fluid will increase when total jet momentum is decreased (while the transverse jet momentum is kept fixed). As fluid from the center jet is entrained into the co-flow on the driver side, a decrease in the amount of center jet fluid available to be entrained into the co-flow region away from the driver side would result. The value of the control parameter ψ could then be expressed as

$$\psi = 1 + \sigma_1 \left(\frac{J_{reference}}{J_{total}} \right) \quad \text{Driver side}$$

$$\psi = 1 - \sigma_2 \left(\frac{J_{reference}}{J_{total}} \right) \quad \text{Wall side}$$

Constants $J_{reference}$, σ_1 and σ_2 are obtained from experimental results.

$$a_{ang}(\psi, \eta_{H_2}, \eta_{O_2}, \eta_{CH_4}) = a_{mix}(\psi, \eta_{H_2}, \eta_{O_2}, \eta_{CH_4})$$

$$f(\psi, \eta_{H_2}, \eta_{O_2}, \eta_{CH_4}) = \frac{a_{ang}(\psi, \eta_{H_2}, \eta_{O_2}, \eta_{CH_4})}{\left(4 \frac{L'}{3}\right)}$$

It can be seen that as the total jet momentum (J_{total}) becomes arbitrarily large, correction due to entrainment factor approaches 1 on both wall side and driver side. This would then lead to the frequency of the three quarter longitudinal mode of the

chamber measured in the product column to be less dissimilar in value between the driver side and the wall side. Including the effects of entrainment on both driver side and wall side frequencies, the predicted frequencies of the three quarter mode improve significantly as is shown in the next section.

5.3 Comparison of Isothermal Case Data with Model

Fig. 5.8 compares values obtained from experiments and from the various models for the isothermal flow conditions. Comparing experimental data from isothermal case with values predicted by the model, the following general observations could be made.

1. Resonance at the lowest frequency (f_1), shown to be the one quarter longitudinal mode of the oxidizer post was well predicted.
2. Resonance at the second lowest frequency (f_2), shown to be the three quarter longitudinal mode of the chamber, was adequately predicted by various models. The jet mixing length model biased the result towards the lower frequencies; full mixing model biased it towards the higher frequencies while the acoustically driven entrainment showed good agreement with modal frequencies on both driver side and wall side.
3. Resonance at the third lowest frequency (f_3), shown to be the first quarter transverse mode of the chamber was under-predicted by complete reaction model. This implied that the fuel content was actually higher than the equilibrium approximation used to calculate the frequency.

5.4 Extension to Density Stratified Reacting Flows

In a similar manner as in the previous section, reacting flow experiments were conducted with band-limited white noise excitation. Test conditions were similar to the non-reacting flow conditions as detailed in Table 5.2, only this time the fuel-oxidizer system was ignited. Again, the first three flow conditions resulted in well-defined spectral peaks as shown in Fig. 5.9 through Fig.5.11. In these experiments, only two spectral peaks were worth noting, marked as f_1 and f_2 . Values for frequencies f_1 and f_2 from the reacting flow tests are summarized in Table 5.4. Although the actual frequencies were different from those in the isothermal experiments, the nature of the two dominant modes appeared to be similar to the f_1 and f_2 mode for their non-reacting counterparts. More precisely, the frequency f_1 appeared to be related to the quarter-wave mode of the Oxygen post and the frequency f_2 appeared to be the three-quarter-wave mode of the combustion chamber. Since temperature measurements were not available at the time these tests were performed, the validity of the model for the reacting flow conditions could not be tested. However, a reverse approach in which the models were used to back calculate temperature of products given the experimentally obtained value for frequency gave product temperatures within reasonable ranges. Further experiments involving the measurement of product temperature are needed for accurate assessment.

Chapter 6: Acoustic Excitation of Density Stratified Non-Reacting Flow Fields

Since reacting flow tests do not offer the convenience of extensive exploratory investigations, simultaneous studies were conducted involving the acoustic excitation of a density stratified He / Air flow configuration. Phase locked Schlieren and Shadowgraphic imaging techniques were used to visualize flow structures under acoustic excitation; Dynamic pressure sensors were used to measure resonant characteristics under white noise excitation. Hotwire probes, placed in the shear layer between the center jet and the co-flowing jet were used to measure dominant frequencies that could be associated with wake mode and jet mode instabilities.

It is natural to expect that acoustic forcing at frequencies close to the acoustic modes of the chamber (for a given flow-field configuration) would undergo resonant amplification and cause greater flow field activity with the flow responding to the standing waves set up in the chamber. Forcing at frequencies that are removed from the resonant modes of the chamber would on the other hand lead to flow field interacting with travelling waves. Acoustic forcing at frequencies close to the hydrodynamic modes would cause greater flow field activity leading to organized large scale motions of the fluid system. It is the purpose of this chapter to investigate such phenomena in greater detail so as to form a ‘feel’ for the way acoustic waves might be expected to interact with flame system in the reacting flow cases. It should however be noted that the absence of heat release in the cold flow studies prevents any chance of amplification of pressure oscillations through favorable coupling with heat release oscillations (Thermoacoustic Coupling). Consequently, interactions in the

reacting flow studies can be expected to be significantly different from their cold flow counterparts when such amplifications become operative.

6.1 Acoustic Modes

6.1.1 Characteristic Acoustic Frequencies

Fig 6.1 shows the flow arrangement for the cold flow tests with a center jet of air at 6m/s and co-flow jets of Helium at 18 m/s. Velocity ratio between the fuel-oxidizer simulants was maintained at 3 because this was the default velocity ratio between fuel and oxidizer in the reacting flow tests. Fig. 6.2 shows acoustic spectra for the chamber (with the given flow field) acoustically excited by a band limited (100Hz – 10KHz) white noise excitation at a speaker power rating of ~ 10 W (RMS) from the left. About 400 spectra were averaged to obtain these results, which show distinctive spectral peaks corresponding to various acoustic resonance modes.

6.1.2 Acoustic Excitation at Characteristic Frequencies

The pressure spectrum from Tap #4 is redrawn in Fig. 6.3 showing spectrum in the frequency range of interest. Using the pressure trace from Tap # 4 as representative of the chamber modes for the combustor, the flow configuration shown in Fig. 6.1 was excited at some of the characteristic frequencies from left and the nature of the interaction between flow and acoustics was investigated using phase locked schlieren imaging at 90° phase intervals. Fig. 6.4 shows a series of such images of flow field excited acoustically from the left. Since the exposure times in the images is very short (10μs - 30μs) turbulent structures can be seen along with the

dominant fluid modes. While forcing at frequencies close to f_1 , f_2 and f_4 (cf. Fig. 6.3) showed flow interactions with longitudinal waves close to resonance, forcing at frequencies close to f_3 showed flow interactions with non-resonant travelling waves from the acoustic driver. The frequencies f_1 , f_2 , f_4 and f_6 could, to a good level of confidence, be recognized as the first quarter mode (longitudinal) of the chamber, first quarter mode (longitudinal) associated with the oxidizer post, three quarter mode (longitudinal) of the chamber and first quarter mode (transverse) of the chamber, respectively.

A few observations can be made from the visualizations shown in Fig 6.4. Compared to the unexcited baseline case (Fig.6.4a) it can be seen that near the longitudinal resonant frequencies f_1 and f_2 (cf. Fig 6.4b, 6.4c, and 6.4d) flow responds strongly to the external forcing and exhibits well defined phase-locked varicose mode oscillations. It is apparent from the rather symmetric nature of the disturbance that the flow lacks immediate knowledge of the exact location of the source of disturbance (i.e. the location of the acoustic driver) and responds, rather, to the resonant oscillations setup in the chamber under the agency of such external forcing.

Forcing at frequencies between f_2 and f_4 (cf. Fig.6.4e, 6.4f, 6.4g, 6.4h) causes the main flow to curve away from the driver, an interaction that indicates that acoustic waves originating from the driver (at off-resonant frequencies) are compression strong and rarefaction weak, such that, on the average, the main flow is subjected to a cross flow originating from the acoustic driver. Compared to flow response under longitudinal response where seemingly the flow has no apparent

knowledge of the exact location of the source of disturbance, flow here knows where the source of disturbance is and in some sense curves away from it under acoustic excitation. The interaction can be looked upon as a main flow interacting with a transversely oriented synthetic jet. The compression pulses of the transversely oriented synthetic jet originating from the driver mounted on the left penetrate deep into the flow field and interact with the main flow causing a strong push effect. The rarefaction pulses, on the other hand, do not penetrate deep into the flowfield to cause any significant pull effect. In fact, during the rarefaction cycle of the driver, fluid is drawn in from the immediate neighborhood of the driver exit and the rarefaction pulses are neutralized in the vicinity of the driver mount itself. The synthetic jet behavior of acoustic waves generated by the driver in the non-resonant band of frequencies is important to understand because it forms the basis of the baroclinic vorticity generation argument that will be presented in the reacting flow experiments. Because of this behavior, acoustic waves from the driver (in this frequency band) have a preferred direction for the pressure gradient vector they carry along. It will be shown in the reacting flow experiments that when this pressure gradient is allowed to interact with the density gradient (across the density stratified fuel-oxidizer interface), a plausible baroclinic interaction is generated causing significant flame-acoustic interactions leading to violent flame front oscillations.

It is to be noted that because of a center jet of air flowing between co-flowing jets of Helium, acoustic boundaries created by air-Helium interfaces essentially divide the 3.5" span of the combustor into 3 acoustic regions (columns) as shown in Fig.6.5. Tap #1 and Tap #4 then measure acoustic signatures in the driver side

column and wall side column respectively. It is interesting to note that when the pressure spectrum from Tap #1 and Tap #4 are considered together, there is an observable difference in the frequency of the three quarter mode of the chamber (longitudinal) measured on either sides of the center jet (Fig. 6.6). This difference in frequency between the driver side and wall side product columns could arise due to source effects (the acoustic driver being near Tap #1) or due to differential entrainment of the center jet fluid into the co-flow as already discussed in section 5.2.3^ψ. Forcing at frequencies close to f_4 (cf. Fig. 6.3), where such asymmetry in longitudinal resonance occurs between driver side and wall side product columns results in partly asymmetric interaction (Fig. 6.4i, 6.4j, 6.4k, 6.4l) with the driver side interface showing more interfacial activity than the wall side interface. In fact, it becomes a matter of apparent conjecture as to if the difference in resonance frequency between the driver side and wall side product columns is a cause for this asymmetric interaction or is a product thereof.

Forcing at frequencies beyond f_4 (cf. Fig. 6.3), leads to the flow ‘straightening up’ (Fig. 6.4m, 6.4n, 6.4o) with no significant interactions in this range of frequencies for the range of forcing amplitudes that were tested.

In summary, a frequency of interest (denoted by f_3 in Fig. 6.3) was found that could be used to generate a transversely directed travelling acoustic wave with the characteristics of a synthetic jet. It corresponded to the frequency associated with the trough between the first quarter mode of the oxidizer post and three quarter mode of the product column in the acoustic spectrum at Tap #4 (wall side). Although the

^ψ cf. Acoustically driven Entrainment Model, section 5.2.3

precise value of this frequency would depend on the particular fuel oxidizer combination used and would differ between reacting and non-reacting flows, it would still be possible to locate it from its position in the pressure spectrum calculated using pressure data from the wall side sensor. For the reacting flow case using GO₂ and GH₂, such a mode was obtained at 1150 Hz. Interactions between travelling acoustic waves and density stratified GO₂-GH₂ flame fronts revealed interesting insight into mechanisms of flame acoustic coupling. Details of such interactions are discussed in Chapter 7.

6.2 Hydrodynamic Modes

To study any potential amplification of fluid motions due to acoustic coupling with hydrodynamic modes, the wake mode and the jet preferred mode frequencies associated with the flow field were calculated and shear layer response to acoustic excitation at those hydrodynamic mode frequencies experimentally tested through hotwire anemometry. Since the splitter plate between fuel and oxidizer had two different fluids flowing on either sides of it, a slightly modified approach was taken to calculate the wake mode frequency. The thickness of the splitter plate was divided into two parts x and y (Fig. 6.7) such that frequencies of shedding on either side of the splitter matched each other and the following conditions were satisfied.

$$x + y = T_{wake}$$

$$S_t = 0.21$$

$$f = \left(\frac{S_t U_o}{2x} \right) = \left(\frac{S_t U_H}{2y} \right)$$

$$\left(\frac{x}{y}\right) = \left(\frac{U_o}{U_H}\right)$$

The calculated value of the wake mode frequency f for this case was 794 Hz. Based on a flow speed of 6m/s (speed of center jet of air) across a bluff body of width T_{wake} this frequency would be 397 Hz while based on a flow speed of 18m/s (speed of co-flowing Helium) across a bluff body of the same width, the wake mode frequency would be 1191 Hz. The jet preferred mode frequency[§], based on the velocity of the center jet ($V_{O_2} \sim 6\text{m/s}$) ranged from $\sim 80 \text{ Hz} - 200 \text{ Hz}$ (based on width of the center jet) and $\sim 118 \text{ Hz} - 283 \text{ Hz}$ (based on hydraulic diameter of center jet).

6.2.1 Characteristic Hydrodynamic Frequencies

Fig. 6.8a shows a schematic of the flow arrangement with a center jet of air at 6m/s and co-flowing jets of gaseous Helium flowing at 18 m/s used for the hot wire tests. Fig. 6.8b shows location of the hot wire probe with respect to the shear layer between center and co-flow jets. The exact location of the probe was 1.375 inches away from the driver side wall and 0.819 inches away from the injector plate. Signal from the probe was filtered using a low pass filter (5 KHz cut-off) with an input gain of 10dB and the input was AC coupled. Sampling was done at 20,000 samples per second and 32 seconds of data was collected and processed. Forcing was from left, the side closer to the sensor.

Fig. 6.9 shows preliminary frequency response characteristics of velocity fluctuations in the shear layer between the center and the co-flowing jets. For baseline

[§] Calculated based on $St \sim 0.25 - 0.60$.

case, the frequency domain representation of the signal from the hotwire showed a series of low quality peaks in the spectrum with peaks centered at 429.7 Hz and two of its higher harmonics. It should be noted that the second harmonic at ~ 860 Hz falls close to the calculated value of 794 Hz of the wake mode. Although one of the acoustic modes from the density stratified cold flow case (the one associated with the quarter mode of the oxidizer post) also came close to this frequency, the broad band nature of this particular signal was indicative of its hydrodynamic origin.

It seems probable that for the given combustor geometry and the operating conditions under which data was collected, both the quarter mode frequency of the oxidizer post and the wake mode frequency (for the given velocities and splitter plate thickness) occurred in close proximity. It might be noted here that unlike hydrodynamic modes, acoustic modes of chambers are typically have higher qualities. Interestingly, it was observed that when the Helium-Air flow field was excited at frequencies of 351.6 Hz, 429.7 Hz, 500 Hz and 600 Hz respectively (with the forcing amplitudes kept constant at 2 Vpp) the amount of amplification of each of these modes closely followed the amplitude of the un-forced jet frequency response (Fig. 6.9). The plot shown in Fig. 6.9 is a good example demonstrating that acoustic forcing at preferred modes (either acoustic or hydrodynamic) would cause greater flow field activity compared to excitation at non-preferred modes. Since various competing mechanisms would be operative in the flame acoustic interaction process, the identification of various frequencies at which such amplified interactions occur are important to the investigation because it provides a systematic way of including or

eliminating physical mechanisms that could be operative in the flame acoustic interaction process.

When the flow field was excited with a broadband source of sound (100Hz to 1500Hz with frequency spacing of 2Hz) a response curve as shown in Fig. 6.10 was obtained. Broadband forcing at low amplitudes showed a trend similar to the unforced response but with an increase in the amplitude of forcing, a shift of the response curves to lower frequencies was observed. For large amplitude broadband excitation, significant departure of the response curve from the unforced response was observed. This change could possibly be attributed to either a decrease in velocity in the neighborhood of the wire due to an increase in local pressure, a decrease in velocity due to an increase in cross-flow or due to the shear layer now starting to move away from the jurisdiction of the sensor filament.

6.2.2 Acoustic Excitation at Characteristic Hydrodynamic Frequencies

Fig. 6.11 shows a series of phase locked schlieren images (imaged at 90° phase intervals) of the flow arrangement shown in Fig. 6.8a interacting with acoustic waves at the experimentally determined predominant roll-up frequency of 429.7 Hz. Interaction for a range of forcing amplitudes is shown. Large, persistent, two-dimensional rollers are observed as the shear layer is excited at the natural rollup frequency at increasing levels of acoustic forcing amplitudes.

In summary, this chapter detailed experimental studies on cold flows excited acoustically at preferred mode frequencies. The preferred modes included both acoustic and hydrodynamic modes. While forcing at characteristic frequencies that corresponded to the acoustic modes of the chamber showed flow interactions with

standing and travelling waves, forcing at near the hydrodynamic mode frequency showed the excitation of wake mode instability. Since the frequency of the preferred hydrodynamic mode, 429.7 Hz corresponded close to an acoustic mode of the chamber a possible hydrodynamic-acoustic coupled interaction was noted in Fig. 6.11. Such interactions (where the external forcing couples simultaneously with both acoustic and hydrodynamic modes) could be stronger than when the external forcing just couples exclusively with either acoustic mode or some preferred hydrodynamic mode of the combustor.

Chapter 7: Acoustic Excitation of Chemically Reacting Flow Fields

The present chapter details results from the acoustic excitation of chemically reacting flow fields and constitutes the most important chapter of this thesis. While the previous chapters mostly serve the purpose of ‘preparation’, it is this chapter that systematically examines the acoustic excitation of model shear-coaxial diffusion flames formed between gaseous Hydrogen (GH_2) and gaseous Oxygen (GO_2)^z to characterize flame-acoustic interactions that could typically occur in liquid rocket engines during the onset of combustion instability. In this chapter, characteristic interactions between flame and acoustics at various frequencies are presented, important parameters in flame acoustic coupling are identified and the first known experimental evidence that suggests baroclinic vorticity as a potential mechanism in triggering flame-acoustic interactions associated with LRE shear coaxial injectors is reported.

7.1 Characteristic Flame Acoustic Interactions

Preliminary reacting flow tests involved transverse acoustic excitation of a diffusion flame system formed between a center jet of gaseous Oxygen and co-flowing jets of gaseous Hydrogen through a broad range of frequencies (200 Hz-2000 Hz) and amplitudes. Fig. 7.1 shows the flow field arrangement and the location of the compression driver with respect to the flowfield. Velocity of the center jet of Oxygen

^z Depending on the goal of particular tests, individual jets of fuel and oxidizer were mixed with other gases like Helium, Argon and Methane.

(V_{O_2}) was 6m/s while that of co-flowing Hydrogen (V_{H_2}) was 18 m/s. The velocity ratio of 3 used in the current experiment is well within the range of velocity ratios studied by others (cf. Foust *et al.* 1996, Tucker *et al.* 1997) ¹. Reynolds number of the center jet based on hydraulic diameter was ~ 4900 while that based on the width of the center jet was ~ 7300 . In the range of Reynolds numbers considered, the flowfield could be regarded as sufficiently turbulent.

Since acoustic excitations at various frequencies could be further amplified or suppressed by the resonant characteristics of the system, the amplitudes at which acoustic waves interacted with the flame fronts would not only be functions of forcing frequencies and input voltages but would also be functions of the system geometry. Fig. 7.3 shows spectral content in pressure response from Tap #4 obtained using band-limited (100Hz-10kHz) white noise excitation of the combustor with the turbulent reacting flowfield inside at a speaker power rating of ~ 9 watts. Resonant modes were observed around $f_1 \sim 300\text{Hz}$, $f_2 \sim 500\text{ Hz}$ and $f_4 \sim 1500\text{ Hz}$ while a suppressed mode was observed around $f_3 \sim 1150\text{ Hz}$.

Table 7.1 lists flow parameters and forcing conditions for the baseline case and two other cases where characteristic flame acoustic interactions were observed. Fig. 7.2 shows an instantaneous OH* chemiluminescence image of the unforced GH2 / GO2 / GH2 flame exhibiting small amplitude spontaneous oscillations and provides a baseline case to compare flame response to externally imposed acoustic excitations. Fig. 7.4 shows phase locked instantaneous OH* chemiluminescence images (imaged at 90° phase intervals) of the reacting flow field forced at 300Hz

¹ For a detailed list of injector parameters used in more realistic rocket engine cf. Santoro (1997) and Conley (2007).

from the transverse direction. An almost symmetric varicose mode oscillation of the flame fronts is observed that indicates possible coupling of acoustic waves at this frequency with a longitudinal mode of the chamber. It is apparent from the rather symmetric nature of the disturbance that the flow lacks knowledge of the exact location of the source of disturbance (i.e. the location of the acoustic driver) and responds, rather, to the resonant oscillations setup in the chamber under the agency of the external forcing. Figure 7.5 shows phase locked instantaneous OH* chemiluminescence images (imaged at 90° phase intervals) of the flame system forced at $f_3 \sim 1150$ Hz. This frequency corresponds to a suppressed mode between the two resonant modes f_2 and f_4 in the pressure spectrum obtained from Tap #4 (cf. Fig. 7.3). Under this condition of forcing, the flame front located closer to the acoustic driver interacted strongly with the acoustic waves resulting in violent flame front oscillations. Flame front located away from the driver showed almost no interaction in the neighborhood of the injector. The stable side was eventually affected when the forcing amplitude was increased substantially over the threshold at which the interactions on the driver side showed up. Significant feedback from the flames to the acoustic driver was also noted under this condition when the amplitude of forcing was arbitrarily increased.

7.2 Baroclinic Vorticity as a Potential Mechanism

Among various mechanisms that could explain the asymmetric wrinkling of flame fronts observed at around the 1150 Hz forcing[¶], one that seemed physically

[¶] This frequency was much lower than the first transverse cut-off frequency of the chamber thereby indicating that the observed interaction was not due to a standing wave in the transverse direction.

plausible was that due to baroclinicity. It was hypothesized that favorable baroclinic torque generated at the flame front located closer to the acoustic driver caused by misalignment of density gradient at the fuel-oxidizer interface and pressure gradient in acoustic waves generated by the acoustic driver could be responsible for the observed asymmetric interactions. The mechanism for baroclinicity has already been introduced in a general sense in section 3.1. To argue that this mechanism plays key role in the particular case of the asymmetric interaction observed at 1150 Hz, a few preliminary considerations are needed. It should be noted from a comparison of the pressure spectrum plots of Fig. 6.3 and Fig. 7.3, that the suppressed mode f_3 for the reacting flow field configuration (cf. Fig. 7.3) corresponds to the suppressed mode f_3 for the non-reacting flow field configuration (cf. Fig. 6.3). Acoustic forcing of the non-reacting density stratified flow field at frequencies close to $f_3 \sim 750$ Hz (cf. Fig. 6.3) resulted in a ‘curving away’ of the main flow from the acoustic driver (cf. Fig. 6.4f, 6.4g, 6.4h). It was argued that this effect was due to the main flow interacting with a transversely directed travelling acoustic wave (cf. Section 6.1.2). The characteristic deflection of the main flow indicated that the incident waves were ‘compression strong’ which created the apparent ‘push effect’ causing the main flow to bend away from the source of the disturbance (compression driver in this case). Although the exact value of the frequency for the f_3 mode for the reacting flow configuration differed from the frequency of the f_3 mode for the non-reacting flow configuration, a qualitative similarity in the nature of acoustic waves generated at these frequencies between reacting and non-reacting flow field configurations could still be expected. Acoustic forcing at 1150 Hz for the chemically reacting flow could

then be considered to generate a transversely directed synthetic jet travelling from left to right away from the acoustic driver. Sufficiently removed from the source of disturbance, such waves could be stronger on the compression pulse but weaker on the rarefaction. This could lead to wave fronts travelling from left to right with pressure gradients that are directed from right to left (cf. Fig. 3.1). Although density gradient is present at both the reacting interfaces separating denser Oxygen from lighter Hydrogen, the particular direction of the pressure gradient in the travelling wave determines on which interface favorable baroclinic torque would be generated. For instance, when the pressure wave passes through the flame front located close to the acoustic driver, it travels from lighter Hydrogen to denser Oxygen. Given the direction of the pressure gradient across the acoustic wave and density gradient across the interface, this leads to an unstable baroclinic interaction leading to the amplification of interfacial perturbations as described in Fig. 3.1a. Violent flame front folding occurs as a result of this interaction. On the other hand, when this pressure wave travels from denser Oxygen to lighter Hydrogen, a stable baroclinic interaction as shown in Fig. 3.1b occurs. This leads to the suppression of any perturbations already present in the flame front located away from acoustic driver leading to its apparent stability.

The remainder of this section discusses, through various validation tests, if baroclinic vorticity could be regarded as a plausible mechanism in the onset of combustion instability in liquid rocket engines. The aspect of baroclinicity becomes intuitive in the rocket engine instability problem when one recognizes that a rocket engine combustor essentially houses a highly density stratified reacting flowfield

inside an acoustically charged environment. Although experimental confirmation of the possible role of baroclinic vorticity in driving such instabilities is presented, more work needs to be done before this theory can be proved or disproved with a sufficient level of confidence.

7.2.1 Pressure Amplitude Change Experiment

Since baroclinic torque is given by the cross product between density gradient and pressure gradient, $(\nabla \rho \times \nabla p) / \rho^2$, a change in the magnitude or the direction of the density gradient vector at the fuel-oxidizer interface would affect the nature and intensity of the interaction for a given pressure gradient passing through the interface. Also for a given density gradient across the fuel oxidizer interface, the intensity of the interaction will depend on the strength of the pressure gradient imposed on the interface.

Fig. 7.6 shows ensemble averaged OH* chemiluminescence images (contour plot) of the oscillating flame (exposure time ~ 750 ms) with the intensity of acoustic forcing increased in steps from 0 to 12.5 watts. For these tests, velocity of center jet Oxygen (V_{O_2}) was 4.5 m/s, velocity of co-flowing Hydrogen jet (V_{H_2}) was 13.5m/s and Reynolds number based on the center jet hydraulic diameter (Re_{O_2}) was 3700. An increase in the acoustic forcing amplitude was seen to cause greater perturbation of the flame front located close to the acoustic driver where the acoustic waves travelled from lighter Hydrogen to denser Oxygen. Flame front away from the driver did not show any appreciable increase in interaction where the waves travelled from denser Oxygen to lighter Hydrogen. Although in keeping with the baroclinic vorticity

mechanism, no strong conclusion in favor of the mechanism could be drawn from this observation because the gradual increase in the level of interactions could be attributed to an increase in the transverse acoustic velocity imposed directly on the flame front located closer to the acoustic driver without any intermediate baroclinicity.

7.2.2 Density Ratio Change Experiment

Following the previous test, the acoustic forcing level was fixed at 12.5 watts (40 Vpp) and the density ratio between fuel and oxidizer was systematically varied by adding small amounts of noble gases (Helium to Oxygen and Argon to Hydrogen), while holding other flow field characteristics relatively constant. For a fixed level of acoustic forcing, it is reasonable to expect, that an increase in the magnitude of density gradient across the fuel-oxidizer interface would lead to increase in the amount of flame acoustic interaction as per the baroclinic vorticity mechanism. Use of noble gases to dilute fuel and oxidizer streams allowed an exponential change in density ratio between fuel and oxidizer while keeping velocities of individual jets to remain unchanged. Although a small change in heat release was introduced across the span of density ratios tested, from practical considerations this approach was ideal for isolating and testing the effect of density on the baroclinic vorticity production term in the vorticity transport equation. Table 7.2 summarizes density ratio (ρ_o/ρ_f), velocity ratio (u_f/u_o), and mole fraction (Y) for the 16 cases considered as a part of the density ratio change experiments. Fuel and oxidizer were introduced in stoichiometric proportions. With equi-molar dilution ranging from 0 to 45% , density ratios from 16:1 to 1:1 between center and co flow jets were systematically created and the

interaction with pressure waves generated by an acoustic driver of nominal impedance 16Ω driven at a fixed frequency of 1150Hz at a forcing amplitude of 12.5 watts from the left was quantified through flame oscillation measurements.

Fig. 7.7a shows instantaneous flame wrinkling images (OH* chemiluminescence) with the density ratio between oxidizer and fuel decreased from 15.9 to 5.0 while Fig. 7.7b shows contour plots corresponding to ensemble averaged OH* chemiluminescence images for the same cases. Acoustic forcing was kept constant in amplitude and was applied from the same location in all the tests. Both the instantaneous and ensemble averaged images showed a monotonic decay of oscillations as density ratio between fuel and oxidizer was decreased from 15.9 to 5. Since the level of acoustic forcing and most other physical parameters were kept unchanged, this test highlighted the importance of the magnitude of density gradient between fuel and oxidizer in controlling the level of interaction between flame and acoustics. The extent of flame-acoustic interaction was quantified by measuring the thickness of perturbed flames from ensemble averaged images. The thickness of the acoustically perturbed flame-front at a given streamwise location (y) was defined as $\delta_{flame}(y) = |r_o - r_i|$, such that the intensity $I(y,x)$ satisfied

$$I_{max}(y) - I(y, x_o) = I_{max}(y) - I(y, x_i) = 0.9 [I_{max}(y) - I_{background}(y)]$$

In other words, flame wrinkling amplitude, δ_{flame} , was defined as the thickness beyond which the flame intensity fell below 10% of its maximum intensity and was measured from the ensemble averaged images through image processing routines

developed in Matlab. Fig. 7.8 shows flame thickness at a non-dimensionalized streamwise location $(y/D) = 4.7$ for several different density ratios. Fig. 7.9 shows flame width vs. density ratio for three different streamwise locations from the injector faceplate. A strong correlation between flame perturbation thickness (δ_{flame}) and fuel-oxidizer density ratio is observed with the level of interaction increasing significantly as density ratio between oxidizer and fuel is increased from 3 to 15.9. Fig. 7.10 shows the effect when the amplitude of excitation and the density ratio between fuel and oxidizer were both varied. Flames with higher fuel oxidizer density ratios, not only responded to acoustic waves at lower amplitudes of forcing but also showed steeper response as the forcing was gradually increased. Consequently, the strong dependence of flame-acoustic interaction on the density ratio between fuel and oxidizer was in agreement with the hypothesis that periodic baroclinic vorticity strengthened by large density gradient in shear-coaxial injector element could be a potential mechanism influencing the degree of interaction between flame and acoustics.

7.2.3 Density Gradient Reversal Experiment

Since baroclinic torque is a cross product between pressure gradient and density gradient, a change in the direction of one of the vectors while keeping the direction of the other unchanged would reverse the direction of the torque produced. To test the effect of changing the direction of the density gradient vector at the fuel oxidizer interface, a nearly opposite injector configuration was considered with central Hydrogen jet and surrounding oxidizer flow. Test conditions are summarized in Table 7.3 and compared with test conditions for Oxygen-in-the-center case.

Although the Hydrogen-in-the-center jet configuration was not a practical one, it provided an opportunity to reverse the direction of the density gradient at the fuel-oxidizer interfaces. Flame front closer to the acoustic driver now had density gradient directed from right to left while flame front away from the acoustic driver had density gradient directed from left to right. Acoustic waves generated by the acoustic driver travelled away from the driver from left to right through the two interfaces with pressure gradients directed from right to left as in all the previous cases. Fig. 7.11 shows an instantaneous UV filtered image of an unforced GO₂-GN₂/GH₂/GO₂-GN₂ turbulent flame exhibiting spontaneous flame front oscillations. Velocity of the central Hydrogen jet (V_{H_2}) was 5 m/s and velocity of the co-flowing jet of air (V_{O_2 / N_2}) was 17.8 m/s. Reynolds number of the center jet based on the hydraulic diameter (Re_{H_2}) was 600 while that based on the co-flowing Oxygen jet based on the hydraulic diameter (Re_{O_2/N_2}) was 8800. The flow arrangement is schematically shown in Fig. 4.10b. When excited acoustically at 300 Hz, the Hydrogen-in-the-center flame responded to the acoustic forcing in a discernable sinuous mode oscillations with both flame fronts participating in the interaction. Fig. 7.12a shows UV filtered phase locked images (imaged at 90° phase intervals) of flame fronts undergoing such interactions. Asymmetric interaction eventually showed up when the flame system was excited acoustically at a frequency of 580 Hz. Fig. 7.12b shows UV filtered phase locked images (imaged at 90° phase intervals) of flame fronts undergoing such interactions. Large amplitude flame front wrinkles were observed on the flame front located away from the acoustic driver while the flame front located closer to the driver showed comparatively little interaction. The elongated spikes of denser

oxidizer pushing into lighter Hydrogen and “tongues” of lighter center jet protruding into the denser co-flow seen in Fig. 7.12b on the flame front located away from the driver resemble structures commonly encountered in the Rayleigh-Taylor (RT) instability in the linear and early non-linear stages.

It is interesting to note that the simple reversal of the density gradient vector at the fuel oxidizer interface changed the flame-front which underwent selective flame-front oscillation under transverse acoustic forcing. For this configuration where the lighter gas formed the center jet, unstable baroclinic interaction as shown in Fig. 3.1a occurred at the flame front located away from the acoustic driver with pressure waves traveling from lighter to denser medium. The interaction of pressure waves with the flame front closer to the acoustic driver on the other hand caused a stabilizing interaction as shown in Fig. 3.1b.

To investigate if the asymmetric oscillations of the flame fronts under transverse forcing could be attributed to differences in dynamic pressure fluctuations near the flames instead of a baroclinic interaction, pressure oscillation amplitudes across the combustor span were measured using wall-mounted pressure transducers. Locations of the transducers are shown in Fig. 4.9 and RMS values of dynamic pressure fluctuations for asymmetric interactions for both the Oxygen-in-the-center case and Hydrogen-in-the-center case are shown in Fig 7.13. Preliminary pressure data indicated that flame oscillations could not be attributed solely to the RMS value of local pressure oscillations. Pressure amplitude at Tap #2 for the Oxygen-in-the-center case showed large increase in dynamic pressure fluctuations that correlated to large flame front oscillation in its neighborhood. However, pressure amplitude at Tap

#2 for the Hydrogen-in-the-center case didn't show any significant difference from that at Tap #3, yet flame front in the neighborhood of Tap #3 showed large amplitude flame front oscillations. This anomaly suggested that the amplitude of local pressure fluctuations was not solely responsible for the asymmetric interactions observed in the experiments and that some other mechanism was operative.

7.2.4 Further Considerations for the Density Ratio Variation Tests

7.2.4.1 Effect of Heat Release Variation

Although equimolar dilution of individual fuel oxidizer jets (cf. Table 7.2) allowed the injection velocities of fuel and oxidizer remain unchanged, there was a gradual decrease in the overall heat release as more and more Argon replaced Hydrogen (cf. Fig. 7.14). To ascertain that the change in the amplitude of flame wrinkling at different molar dilutions of Oxygen and Hydrogen with Helium and Argon respectively as reported in section 7.2.2, was not solely due to heat release changes, an experiment was performed with test conditions given in Table 7.4. From Fig. 7.14, in which two plots for density ratio variation are shown, density change is achieved either by adding Argon to Hydrogen and Helium to Oxygen (the way density of fuel and oxidizer jets were tailored in the density ratio variation experiments) or by adding Argon to Oxygen and Helium to Hydrogen. The latter allows a gradual change in density ratio as compared to the exponential change facilitated by the former. Also, for a given percentage dilution, although the two approaches can produce very different density ratios, both of them will produce the same heat release.

Fig. 7.15a shows OH* chemiluminescence image (contour plot) of the baseline case with 6% molar dilution but no acoustic forcing. In the arrangement shown in Fig. 7.15b, 6% dilution by mole is achieved by adding Argon to Hydrogen and Helium to Oxygen whereas in Fig. 7.15c, 6% dilution by mole is achieved by adding Helium to Hydrogen and Argon to Oxygen. So while the molar dilution and the heat release is maintained same between the cases shown in Fig. 7.15b and Fig. 7.15c, the density ratio between oxidizer and fuel is 7 for the case shown in Fig. 7.15b and 15.2 for the case shown in Fig. 7.15c. It is seen that although associated with the same heat release, the configuration in Fig. 7.15c with higher density ratio between fuel and oxidizer undergoes greater acoustic perturbation when subjected to the same amplitude of forcing as the configuration in Fig. 7.15b. Fig. 7.16 shows the growth rate of flame perturbations as a function of streamwise locations for the different cases mentioned above. From Fig. 7.15 and Fig. 7.16, acoustic forcing is seen to cause greater flame wrinkling for the higher density ratio case although most other factors, including heat release, were maintained same between the configurations.

7.2.4.2 Effect of Total Jet Momentum Variation

Although equimolar dilution of individual jets allowed injection velocities of fuel and oxidizer to be kept unchanged, the addition of Argon to Hydrogen at a given injection velocity increased the outer jet momentum significantly. While the addition of Helium to Oxygen decreased center jet momentum, the total momentum of the jets was progressively increased as more and more Argon replaced Hydrogen (Fig. 7.17). To ascertain that the sharp decrease in the amplitude of flame wrinkling with the

decrease of density ratio between fuel and oxidizer did not arise exclusively from a fixed amount of acoustic forcing (transverse flow) interacting with a main flow with progressively increasing total jet momentums, a simple validation test was performed. Table 7.5 shows test conditions for the two cases. Fig. 7.18a and Fig. 7.18b show instantaneous and time averaged OH* chemiluminescence images of a GH₂+He / GO₂ / GH₂+He diffusion flame with an outer jet momentum of 0.0055 kg.m/s² and an inner jet momentum of 0.0047 kg.m/s² undergoing transverse acoustic excitation at 1150 Hz at a power rating of 15.8 watts. Fig. 7.19a and Fig. 7.19b on the other hand show instantaneous and time averaged OH* chemiluminescence images of a GH₂+Ar / GO₂+He / GH₂+Ar diffusion flame with an outer jet momentum of 0.0055 kg.m/s² and an inner jet momentum of 0.0036 kg.m/s² undergoing transverse acoustic excitation at the same frequency and amplitude. Although the outer jet momentums were same and the center jet momentum for the case shown in Fig. 7.18 was greater than the center jet momentum for the case shown in Fig. 7.19, greater flame acoustic interaction was noted for the flame shown in Fig. 7.18. It might be noted that although the momentums of the individual jets for the arrangement shown in Fig. 7.19 were less than or equal to the momentums of individual jets for the arrangement shown in Fig. 7.18, the density ratio between fuel and oxidizer for the configuration shown in Fig. 7.19 was around 2 while for the other arrangement it was 8. Even with higher momentums of individual jets, the flame with greater fuel to oxidizer density ratio showed greater flame acoustic interaction highlighting the role of density gradient in such interactions.

7.2.4.3 Effect of Change in Acoustic Mode Shape

Although equimolar dilution of individual jets allowed injection velocities of fuel and oxidizer to be kept unchanged, it changed various critical acoustic parameters of the system including densities of individual fuel and oxidizer jets, total heat release, acoustic impedance at the fuel-oxidizer interfaces etc. It was necessary then to check if the pressure spectrum (resonance characteristics) had shifted significantly during the course of the density ratio change experiments resulting from density tailoring using inert gases. Such a change in resonance characteristics could change the amplification of a mode at a given frequency and could cause a change in the level of flame acoustic interaction. Although this would still emphasize the role of fuel and oxidizer densities in affecting flame acoustic interactions, it would decrease confidence in considering baroclinicity as a potential mechanism. A change in flame acoustic interaction could then be attributed to a change in local amplitude of pressure oscillations inside the combustor making it difficult to justify the intermediate mechanism of baroclinicity, even though it might still be operative.

To address this issue, resonance characteristics of the chamber for some of the density ratios tested were considered. Pressure spectrum collected from Tap #1 and Tap #4 for three different density ratios (16, 10 and 6) under reacting flow conditions and subjected to band limited white noise excitation are shown in Fig. 7.20a and 7.20b respectively. Fig. 7.20a, represents modal characteristics on the driver side (Tap #1) and show similar spectral signatures around the forcing frequency of interest (1150 Hz). Since flame oscillations in the neighborhood of Tap #1 have been

compared in the density ratio variation test, it is reasonable to assume that the sharp change in flame acoustic interaction with the change in density ratio between fuel and oxidizer is not totally due to changes in resonance characteristics of the chamber. Care should however be exercised to ascertain how much of the interaction is due to density gradient and how much is due to acoustic amplitude. There could be cases where a higher density ratio flame could undergo lower flame acoustic interaction as compared to a lower density ratio flame if the modal characteristics are such that a resonant peak for the lower density ratio case falls very near the forcing frequency while it is far removed for the higher density ratio flame. Acoustic signature from Tap #4 also showed slight variations in the pressure spectrum with the crest between the first two dominant modes shifting to lower frequencies as density ratio was decreased from 16 to 6. It is not very clear how much such shifts in pressure spectrum around Tap #4 would actually influence the flame acoustic interaction process near Tap #2. The fact that local amplitudes of pressure fluctuations do not entirely correlate with the amount of flame acoustic interaction in its neighborhood has already been shown (cf. Section 7.2.3) and will be considered again in Section 7.2.5. Furthermore, it should also be appreciated that acoustic forcing of the flowfield can in itself affect the f_4 mode of the chamber (cf. Fig 7.20) through redistribution of acoustic media in the volume of interest by causing perturbation and folding of interfaces and through acoustically driven entrainments (cf. Section 5.2.3). Unlike pressure spectra obtained from volumes with a fixed distribution of acoustic media using white noise excitation, in this particular configuration, the imposed forcing in itself changes the distribution of acoustic media and in effect changes the spectral characteristics of the chamber

depending on factors like amplitude of forcing, density ratio between fuel and oxidizer etc. Consequently, near the forcing frequency of 1150 Hz where such effects can be present, care should be exercised in using the spectral characteristics as indicative of wave amplification due to chamber resonance.

7.2.5 Simultaneous Measurement of Pressure and Heat Release Oscillations

Simultaneous measurement of pressure and heat release oscillations were conducted to be able to show that for the same level of pressure perturbations imposed on an interface, a larger density ratio interface would typically lead to greater flame acoustic interactions. For this, a Photomultiplier Tube with a 308nm band pass filter was used for the OH* chemiluminescence oscillation measurements while a Kistler Dynamic Pressure sensor was used for local pressure oscillation measurements. Two cases (as shown in Table 7.6) of density ratios 14.5 and 3.0 (using a blended GH₂/GCH₄ fuel mixture) were acoustically excited at a forcing frequency of 1150 Hz (40 Vpp) and simultaneous measurement of pressure and OH* chemiluminescence oscillations (plausibly representative of heat release oscillations) were conducted at 6 different locations as shown in Fig. 7.21. In Fig. 7.21, an ensemble averaged OH* chemiluminescence image (contour plot) for DR 14.5 case under acoustic excitation at 1150 Hz, ~ 40 Vpp is used as backdrop to show sensor location with respect to the excited flames.

When the DR 14.5 case was forced at 1150 Hz, which corresponded to a suppressed mode in the pressure spectrum at Tap#4 (cf. Fig. 5.9) it was seen that although the amplitude of pressure oscillations were similar at both the flame fronts,

flame front closer to the acoustic driver where acoustic waves travelled from lighter to denser fluid showed greater heat release oscillations (Fig. 7.22). While the same trend was observed for the lower density ratio case, the amount of heat release oscillation for the same amount of pressure perturbation was significantly decreased (Fig. 7.23). This observation was particularly true for measurement locations D1, W1, D2 and W2. This test indicated that both the direction and the magnitude of density gradient at the fuel oxidizer interface are critical in influencing flame interactions under imposed acoustic excitations.

7.3 Estimation of Growth Rates for the Flame Perturbations

As observed by Markstein and Squire (1954) and Petchenko *et al.* (2006), acoustic waves can give rise to acoustic acceleration driven RT instability in flames (cf. Section 3.2). Because of the frequency term, acceleration due to acoustics can be significant at high frequencies although the period through which such acceleration would act would decrease as the frequency is increased. Consequently, one has to check if the instability has sufficient time to develop. For that purpose characteristic growth rate of the RT instability for an acoustically accelerated Hydrogen-Oxygen interface at 580 Hz excitation and peak pressure amplitude of 0.03 psi is evaluated. This frequency and pressure amplitude correspond to the situation near the flame front located away from the acoustic driver (cf. Fig. 7.12b) for the Hydrogen-in-the-center flame under 580 Hz acoustic excitation showing significant flame front oscillations.

A GO₂/GH₂ interface has an Atwood number of 0.88. A 580 Hz acoustic signal with peak pressure of 0.03 psi generates a peak acceleration of 1100 m/s².

Using these values and performing a linear RT stability analysis using a viscous interface, first the most unstable wavelength for the instability was obtained. The rate of growth of this most unstable wavelength was then plotted as a function of the acoustic period within which it could develop. Fig. 7.24 shows growth rates that could be expected under a forcing frequency of 580Hz with different pressure fluctuation amplitudes for the physical case shown in Fig. 7.12b at the flame front located away from the acoustic driver. Since higher frequency and higher pressure means higher acoustic acceleration, the maximum value for the growth rate increases with frequency and pressure fluctuation amplitudes. For a gas-gas interface, viscosity plays a stabilizing role. Hence there is always a critical wave number where maximum growth occurs beyond which the growth rate falls off. In Fig. 7.25, the amplification of the growth rate for the most preferred wavelength corresponding to the 580Hz, 0.03psi RMS case, as a function of the fraction of the acoustic cycle is shown. Even though acceleration is intermittent, it is sufficiently large so to cause significant amplification of perturbations in the time scale over which it acts. Up to 200% amplification for the most preferred wavelengths is observed in less than half a cycle of acoustic forcing.

7.4 Parametric Studies

7.4.1 Dimensional Analysis

Flames interacting with transverse acoustics undergo violent flame front wrinkling that essentially leads to an increase in the excited flame brush thickness. One can thus measure the average flame brush thickness (δ) and use it as a measure

of flame wrinkling or flame-acoustic interaction. It is easy to see that acoustically-excited flame brush thickness will depend on many parameters including fuel and oxidizer properties as well as acoustic amplitude. When the surrounding conditions such as acoustic amplitude and temperatures are held constant, one can express this relationship in the following general form:

$$\delta = f(y, \rho_o, \rho_f, u_o, u_f, Y_1, \dots, Y_n, \dots)$$

The mole fractions Y_1, \dots, Y_n can be further simplified by introducing a characteristic chemistry time scale τ_{chem} to denote the propensity of the fuel-oxidizer combination for rapid reaction. The above equation can then be simplified as

$$\delta = f(y, \rho_o, \rho_f, u_o, u_f, \tau_{chem})$$

There are 7 dimensional variables in this equation while the number of primary dimensions is only 3, namely dimensions for mass, length, and time. Thus, according to the Buckingham Pi theorem, there will be 4 dimensionless variables. Using such a dimensional analysis, one can reduce this problem into:

$$\frac{\delta}{y} = f\left(\frac{\rho_o}{\rho_f}, \frac{u_f}{u_o}, \frac{\tau_{chem}}{y/u_o}\right)$$

Since the distance y is continually varying, it may be easier to take into the consideration a scaling aspect by using the center post diameter D . Then, one can measure δ/D at a fixed y . Also, instead of using the Damkohler number for chemistry time scale, it may be possible to use the fuel mole fraction if more than one fuel is used. So, the problem is slightly modified to investigate (δ/D) at fixed y , fixed temperature conditions, and fixed forcing conditions. Thus,

$$\frac{\delta}{D} = f\left(\frac{\rho_o}{\rho_f}, \frac{u_f}{u_o}, \frac{Y_{CH_4}}{Y_{CH_4} + Y_{H_2}}\right)$$

By quantitatively obtaining partial derivative functions, one can assess how sensitively flame-acoustic interaction will be affected by each of these non-dimensional variables. In other words, the propensity of shear-coaxial injector flames to couple with acoustic forcing can be obtained as partial sensitivity of acoustically-excited flame brush thickness to each of these variables. The following will be measured in the experiments while holding all other conditions as constant as possible:

$$\frac{\partial(\delta/D)}{\partial(\rho_o/\rho_f)}, \frac{\partial(\delta/D)}{\partial(u_f/u_o)}, \frac{\partial(\delta/D)}{\partial(Y_{CH_4}/(Y_{CH_4} + Y_{H_2}))}$$

Also, by normalizing the variables, they can be written in the following equivalent forms:

$$\frac{\delta}{D} = f\left(\frac{\rho_o - \rho_f}{\rho_o + \rho_f}, \frac{u_f - u_o}{u_f + u_o}, \frac{Y_{CH_4}}{Y_{CH_4} + Y_{H_2}}\right)$$

$$\frac{\partial(\delta/D)}{\partial((\rho_o - \rho_f)/(\rho_o + \rho_f))}, \frac{\partial(\delta/D)}{\partial((u_f - u_o)/(u_f + u_o))}, \frac{\partial(\delta/D)}{\partial(Y_{CH_4}/(Y_{CH_4} + Y_{H_2}))}$$

Apart from density ratio, velocity ratio and fuel mixture fraction, the effect of momentum ratio will also be tested. Since momentum of the jets could be changed by changing either jet velocity or jet density, two different measures of partial sensitivity will be obtained for the effect of momentum ratio of the jets. In one case, the momentum of the outer jet will be varied by varying the velocity of the outer jet while keeping its density constant while for the other case, momentum of the outer jet will be varied by varying the density of the outer jet while keeping its velocity constant.

7.4.2 Effect of Density Ratio.

Using flame brush thickness data obtained as a part of the density ratio variation experiments (cf. Section 7.2.2), the following exponential curve fit provided a good correlation between perturbed flame thickness and normalized density difference at given axial locations $4.7 < y/D < 6.1$ as shown in Fig. 7.26:

$$\left(\frac{\delta}{D}\right)_u = C_1 \exp\left(C_2 \cdot \frac{\rho_o - \rho_f}{\rho_o + \rho_f}\right) \quad \text{Where } C_1 \sim 0.02 \text{ and } C_2 \sim 5.1$$

The results can be explained using periodic baroclinic torque generated by misaligned density gradient and pressure gradient. The direction of pressure waves is such that the resulting baroclinic torque amplifies the disturbances on the left side flames while it stabilizes the disturbances on the right side. The strength of baroclinic torque increases with the increase in density across the fuel-oxidizer interface as expected.

7.4.3 Effect of Velocity Ratio.

A series of tests were conducted to study the effect of velocity ratio on flame acoustic coupling. A mixture of 5.235% Argon and 94.765% Hydrogen (by mole fractions) gave a mixture molecular weight of 4.002 g/mole which was same as that of pure Helium. Further addition of Helium to this mixture of Hydrogen and Argon then gave a convenient way of changing (increasing) the velocity of the outer jet while keeping its density unchanged. Hence, while the velocity of the outer jet was increased from 13.5m/s to 23.57m/s by adding different amounts of Helium to the outer jet, its density could be kept constant at 0.163 kg/m³. The center jet was of pure Oxygen flowing at 4.47m/s. The flow rates were adjusted in such a way so that fuel and oxidizer were in stoichiometric proportions. Test conditions are summarized in Table 7.7. Instantaneous and ensemble averaged OH* chemiluminescence images are shown in Fig. 7.27 and Fig 7.28 respectively. For each velocity ratio, instantaneous images were captured with an exposure time of 15 μ s whereas average images were captured with an exposure time of 750 ms. In all the images, shown in Fig. 7.27 and Fig. 7.28, acoustic excitation was applied from the left at a power rating of 15.82 watts (45volt peak to peak at an impedance of 16 ohms). Fig. 7.29 shows average

linear regression fit obtained for the empirical trend in the range of axial locations $4.7 < y/D < 6.1$. The dependence on velocity change could be expressed in linear form as:

$$\left(\frac{\delta}{D}\right)_\rho = C_3 \left(\frac{u_f - u_o}{u_f + u_o}\right) + C_4 \quad \text{where } C_3 \sim -3.5 \text{ and } C_4 \sim 3.6$$

While flame perturbation had an exponential dependence on non-dimensionalized density difference, its dependence on non-dimensionalized velocity difference was linear. A possible cause for this slight reduction in flame-acoustic interaction with increase in outer jet velocity appeared to be the decrease in volumetric heat release because of the addition of an inert gas to the outer jet in successively higher amounts. The increase in the total momentum of the main flow for a fixed acoustically driven cross flow momentum could also be responsible.

7.4.4 Effect of Momentum Ratio

Since momentum of a flow could be changed either by changing velocity or density or both, two sets of flame acoustic interaction tests were conducted. In one, jet momentum was varied by varying velocity while holding density constant while in the other, jet momentum was varied by varying density while holding velocity constant. Table 7.8 shows test conditions for experiments in which jet momentum was varied by varying the density of the jets while their velocities were kept unchanged. Table 7.9 shows test conditions where outer jet momentum was varied by varying the velocity of the outer jet while keeping the densities of the individual jets

as well as the velocity of the center jet constant. It is to be noted that the outer jet momentums in Table 7.8 and Table 7.9 are exactly matched.

When excited acoustically at a power rating of 15.82 watts (45volt peak to peak at an impedance of 16ohms) from the left, flames under conditions shown in Table 7.8 showed steeper flame-acoustic response as compared to cases shown in Table 7.9. Fig. 7.30 shows instantaneous and ensemble averaged OH* chemiluminescence images of flame acoustic interactions for test conditions given in Table 7.8 while Fig. 7.31 shows instantaneous and ensemble averaged OH* chemiluminescence images of flame acoustic interactions for test conditions given in Table 7.9.

As the outer jet momentum was progressively increased, there was a decrease in flame response amplitude. A linear regression fit yielded the following dependence on non-dimensionalized momentum difference when the outer-jet momentum was increased by increasing the outer jet velocity while keeping individual densities of the center and co-flow jets unchanged as shown in Fig. 7.32a. In the range of axial locations $4.7 < y/D < 6.1$

$$\left(\frac{\delta}{D}\right)_\rho = C_7 \left(\frac{J_f - J_o}{J_f + J_o}\right) + C_8 \quad \text{Where } C_7 \sim -1.24 \text{ and } C_8 \sim 1.25$$

The dependence of flame perturbation on non-dimensionalized momentum difference was found to follow an exponential curve when the outer-jet momentum was increased by increasing the outer jet density while keeping individual velocities

of the center and co-flow jets unchanged as shown in Fig. 7.32b. In the range of axial locations $4.7 < y/D < 6.1$

$$\left(\frac{\delta}{D}\right)_u = C_9 \exp\left(C_{10} \cdot \frac{J_f - J_o}{J_f + J_o}\right) \quad \text{Where } C_9 \sim 0.29 \text{ and } C_{10} \sim -2.85$$

This observation reiterated the importance of density ratio in flame acoustic coupling. The decrease in flame brush thickness for an increase in jet momentum could be attributed to a fixed cross flow momentum interacting with an increasing main flow momentum. For the decrease in momentum that was accompanied by a decrease in density ratio between fuel and oxidizer (cf. Table 7.8) additional damping of flame oscillations could have resulted from a decrease in density gradient across the flame front from 6.0 to 2.0.

7.4.5 Effect of Chemical Composition of Fuel.

Effect of fuel composition on flame-acoustic interaction was studied by adding Methane to the Hydrogen fuel line. The configuration is shown in Fig. 4.11c. Methane was included in the study of the effect of chemical composition of fuel for two primary reasons. First, a Methane Hydrogen mixture may be considered for space exploration mission if Methane can be harvested from Mars in the future. Furthermore, because Methane is substantially denser than Hydrogen, it can also be used to control fuel-oxidizer density ratio that sensitively affects the flame-acoustic interaction process. Thus, a blended fuel could be considered for instability control purpose as well. In this experiment, Methane-Hydrogen mixture was used for the fuel

line and the mole fraction was varied by 10% increment. The fuel and oxidizer streams were appropriately diluted with inert gases to maintain the fuel-oxidizer density ratio and velocity ratio constant. The resulting test conditions are shown in Table 7.10. The flames were subjected to a fixed-amplitude acoustic excitation as before, and the resulting flame acoustic interaction was measured using OH* and CH* chemiluminescence measurements.

When only Methane was used, however, it resulted in lifted flame structure quite different from others (cf. Fig. 7.33). In all cases containing 10% or more Hydrogen, the general flame structure was very similar to the Hydrogen only flame case (cf. Fig. 7.34).

Fig. 7.35 shows the processed results obtained when the flame system was excited from the left at a power rating of ~ 19.5W. As the Methane mole fraction was increased, there was a slight decrease in flame response amplitude. A linear regression fit yielded the following dependence on Methane mole fraction when density ratio and velocity ratio were held constant in the range of axial locations $4.1 < y/D < 5.2$:

$$\left(\frac{\delta}{D}\right)_{\rho,u} = C_5 \left(\frac{Y_{CH_4}}{Y_{CH_4} + Y_{H_2}} \right) + C_6 \quad \text{Where } C_5 \sim -0.87 \text{ and } C_6 \sim 2.3$$

Since the density ratio and velocity ratio were held constant, the effect was mainly due to the change in mole fraction. The main cause for this slight reduction in flame-acoustic interaction with Methane mole fraction appeared to be the decrease in thermal output. As more and more Methane replaced Hydrogen when the amount of

Oxygen available was fixed, the total heat release output was reduced as seen in Table 7.10. This meant that the amplification due to heat release was reduced at higher Methane mole fraction. When the fuel was exclusively Methane, the flame was lifted because the ignition time of Methane is longer than that of Hydrogen. Thus for the same fuel and oxidizer velocities, the location of ignition of pure Methane was farther from the injector than Hydrogen. Although a dependency on Methane mole fraction was obtained, it is difficult to say if the correlation is indicative of flame acoustic interaction under varying chemistry time scales. The presence of hydrogen in the mixture (even in small quantities) seems to drive the chemistry time scale of the mixture towards that of Hydrogen and makes an unbiased study of the effect of chemistry time scale on flame acoustic coupling, by varying methane and hydrogen mole fractions, possibly inappropriate.

7.5 Spectral Measurements and High Speed Imaging

7.5.1 High Speed Imaging Results

To gain further insight into physical processes occurring in flame acoustic interactions for the shear co-flow injector, spectral measurements and high speed imaging of flames under transverse excitation were conducted. Tests indicated that downstream of the injector plate, difference in velocities between center jet and the co-flow jets caused stretching and merging of vortex structures initially excited by the baroclinic interactions between flame and acoustics. For all these tests, the Oxygen-in-the-center GO_2/GH_2 diffusion flame was excited by the transversely mounted acoustic driver at a frequency of 1150 Hz and at an amplitude of 40 Vpp from left.

Velocity of center jet Oxygen was 4.5 m/s while velocity of co-flowing Hydrogen was 13.5 m/s.

7.5.1.1 Vortex Pairing and excitation of secondary modes

A series of high-speed images of the flame front oscillations captured at 1000 fps revealed distinct vortex pairing events leading to the apparent decrease in flame front oscillation frequencies. In Fig. 7.36, a clear vortex pairing event is circled in the images taken from $t=0\text{ms}$ to $t=25\text{ms}$.

7.5.2 PMT tube OH* Chemiluminescence oscillation results

A photo multiplier tube with a 308nm filter was used at various streamwise and span wise locations to measure the OH* chemiluminescence oscillations at the flame fronts subjected to acoustic excitation at 1150 Hz. Scoping locations and the corresponding flame front oscillation frequencies are reported in Fig. 7.37, Fig. 7.38, Fig. 7.39 and Fig. 7.40. In all the flame front oscillation measurement experiments using PMT as reported in this section, an Oxygen-in-the-center GO₂/GH₂ diffusion flame was acoustically forced at 1150 Hz at an amplitude of 40 V_{pp} from the left.

7.5.2.1 Near and far field frequencies

Fast Fourier Transform of OH* chemiluminescence oscillations collected from various streamwise locations using a Photo Multiplier Tube with a 308nm band pass filter showed that near the injector plate, the flame oscillated at the frequency at which it was driven. Beyond around $y/D \sim 3.5$, spectral measurements revealed non-linear nature of the interaction process in which that flame system forced at 1150 Hz

gave rise not only to 1150 Hz oscillations but also triggered flame oscillations occurring at substantially lower frequencies. Large amplitude flame front folding events developed in this region that continued downstream. It is important to recognize that such a scenario could allow other modes of the combustor (typically the low frequency bulk modes) to be excited by coupling with heat release fluctuations associated with these low frequency but large amplitude flame front oscillations.

Although structures at the forcing frequency were not apparent on these large scale wrinkles, FFT of PMT signal revealed that the high frequency structures were still present embedded in the low frequency large amplitude convolutions (Fig. 7.41). An apparent preference for the selection of flame sections where these high frequency oscillations selectively appeared was noted. The possibility of a RT driven instability arising from acoustic acceleration of a density stratified interface or a baroclinic interaction between pressure waves from the driver passing through the density stratified interface could be responsible for such an interaction and is considered in the next section.

7.5.2.2 Secondary Evidence of Acoustically Driven RT Instability

Downstream of the injector, the convolutions on the flame front merged and paired (cf. Fig. 7.36) and gave rise to oscillations at considerably lower frequencies than the frequency at which the flame was forced. OH* chemiluminescence oscillation results as showed in Fig. 7.41b and Fig. 7.41c obtained through PMT measurements at locations marked A and B respectively of the oscillating flame front

(cf. Fig. 7.41a), indicated two interesting features. Firstly, although low frequency flame oscillations showed up downstream beyond $y/D \sim 3.5$, the high frequency component was still present embedded within the low frequency large scale wrinkles. Secondly, and more interestingly, the high frequency oscillations had a preference as to which side of the low frequency large amplitude convolution they would typically occur.

As shown in Fig. 7.41a, at a PMT probing location marked A, the passage of a large amplitude low frequency flame structure essentially involves the passage of two flame fronts - one with Hydrogen on the top and Oxygen on the bottom and the other with Oxygen on the top and Hydrogen on the bottom. As the structures convect downstream across the PMT sensor at location A, OH* chemiluminescence oscillations are recorded by the sensor located there. As shown in Fig 7.41b, OH* chemiluminescence oscillation measurements from this sensor at location A show 1150 Hz high frequency oscillations (associated with the forcing frequency) riding on the 'falling' slope of the low frequency OH* chemiluminescence oscillation trace (associated with the low frequency resulting from pairing and merging of vortices).

A closer look at the OH* chemiluminescence oscillation plot (Fig 7.41b) reveals that the flame front where the 1150 Hz oscillations predominantly show up correspond to the interface that separates GH₂ and GO₂ such that as acoustic waves from the driver travel from GH₂ to GO₂ across this it. As per our earlier discussion, this interface is RT unstable (heavier fluid GO₂ on top of lighter fluid GH₂ with respect to the pressure gradient due to acoustic wave) and hence leads to an amplification of structures at the forcing frequency.

Similarly, a closer look at the OH* chemiluminescence oscillation plot (Fig 7.41c) reveals that the flame front where the 1150 Hz oscillations predominantly show up correspond to the interface that separates GH2 and GO2 such that as acoustic waves from the driver travel from GH2 to GO2 across this it. Consequently, 1150 Hz oscillations appear on the ‘rising’ slope of the underlying low frequency OH* chemiluminescence oscillation trace.

Chapter 8: Summary and Conclusions

An experimental investigation was conducted to study physical mechanisms related to the onset of acoustically coupled combustion instabilities that predominate in liquid rocket engines (LREs) particularly in the vicinity of the injector. Flame acoustic interactions of this kind play critical role in many types of combustion instabilities, because they can amplify small amplitude acoustic disturbances during the onset of combustion instability leading to very large amplitude self-sustaining combustion oscillations that are detrimental to the operability and survivability of the engine. The following sections will summarize key tasks and important findings related to this work.

8.1 Summary of key tasks

1. An experimental setup was designed to simulate the near field of a shear-coaxial injector typically used in liquid rocket engines and a transversely mounted acoustic driver was used to simulate acoustic conditions occurring in the neighborhood of such injectors. Since the acoustic output of the driver unit was limited, the model experiments were conducted at scaled-down conditions, ensuring relatively strong level of acoustic excitation compared to the level of natural turbulence fluctuation.

2. Acoustic modes of the chamber under no-flow, isothermal-flow and reacting-flow conditions were experimentally identified and a set of analytical models to interpret acoustic modes of a combustor with a density stratified flow field was developed. For these tests, a mixture of gaseous H₂ and CH₄ was used as fuel and O₂

was used as oxidizer. The combustor was acoustically excited using band limited white noise excitation. A Fast Fourier Transform (FFT) was applied to pressure data collected using wall mounted high bandwidth dynamic pressure transducers to obtain Eigen frequencies of the chamber.

3. Carefully controlled flame experiments were conducted, in which, a turbulent GH₂-GO₂ diffusion flame created between co-flowing jets of Oxygen and Hydrogen and confined between two parallel plates was acoustically forced by the transversely mounted driver unit. Forcing parameters and flow parameters were varied and the interaction between flame and acoustics qualitatively and quantitatively studied.

Forcing parameters that were varied included:

- Frequency of forcing
- Amplitude of forcing

Flow Parameters that were varied included:

- Relative orientation of fuel and oxidizer jets[¶]
- Fuel -oxidizer Density ratio
- Fuel-oxidizer Velocity ratio
- Fuel-oxidizer Momentum ratio
- Chemical composition of fuel (GCH₄-GH₂ blended fuel used)

[¶] Change in the orientation of fuel and oxidizer jets with respect to the acoustic driver was used to change the direction of the density gradient vector at the fuel-oxidizer interface.

4. Resulting flame-acoustic interactions were visualized using phase-locked schlieren, shadowgraphy and OH* / CH* chemiluminescence imaging. Direct flame front visualizations were made using high speed cinematographic imaging. Pressure data from the combustor was captured using high bandwidth dynamic pressure transducers. OH* / CH* oscillations (associated with oscillations of the flame fronts) were captured using Photo-Multiplier-Tube (PMT) measurements. LabVIEW based instrumentation was used to generate and log data while Matlab based routines were used to process collected data.

8.2 Summary of important findings

The specific findings, both experimental and analytical, obtained as a part of this thesis work are summarized in the next few sections.

8.2.1 Qualitative characterization of flame-acoustic interactions

When excited acoustically by the driver unit mounted in a transverse direction, the diffusion flame system showed characteristic flame acoustic interactions. Flame oscillations were affected by excitation frequency, excitation amplitude, and the configuration of the Oxygen-Hydrogen interface.

1. Low-frequency asymmetric forcing that excited longitudinal acoustic modes of the chamber (and oxidizer post) resulted in symmetric flame front oscillations. This happened both for Oxygen-in-the-center and Hydrogen-in-the-center cases. The Oxygen-in-the-center case produced varicose-mode flame front oscillations. The Hydrogen-in-the-center case produced sinuous-mode oscillations. Pressure sensors near the flames recorded almost similar RMS pressure amplitudes

and flame structures showed almost equal amplitudes of oscillations. This indicated that for low frequency forcing, with wave motion dominant in the longitudinal direction, wrinkling on flame fronts was directly correlated to the amplitude of RMS pressure fluctuation near the flame fronts.

2. In the neighborhood of certain frequencies^ψ, asymmetric acoustic forcing of the GO₂-GH₂ flame system resulted in asymmetric flame front oscillations. For the Oxygen-in-the-center case, large asymmetric flame front wrinkles were observed on the flame front that was located close to the acoustic driver while for the Hydrogen-in-the-center case large amplitude asymmetric wrinkles were observed on the flame front that was located away from the acoustic driver. This observation indicated that the direction of the density gradient at the fuel oxidizer interface influenced the way acoustic waves (at certain frequencies) interacted with the fuel-oxidizer interface.

3. For the case resulting in asymmetric flame front oscillations, while there was a slight correlation between flame wrinkling and the RMS amplitude of local pressure fluctuations for Oxygen-in-the-center case, there was no correlation between local RMS amplitude of local pressure fluctuations and flame wrinkling for the Hydrogen-in-the-center case. For this case, the flame front, which was further away from the acoustic driver, wrinkled more severely, even though the RMS pressure amplitudes appeared to be similar near both the flame fronts. This indicated the presence of other physical mechanisms that potentially affected flame front wrinkling as observed in the experiments.

^ψ 1150 Hz for Oxygen-in-the-center case and 580 Hz for Hydrogen-in-the-center case. Combustor dimension was 15”x3.5”x 0.375”

4. For asymmetric flame-acoustic interactions observed in the Oxygen-in-the-center case, evidence of the influence of the direction of density gradient at the fuel-oxidizer interface was also observed downstream of the injector face plate where the initial small amplitude wrinkles (driven at the frequency of the external forcing) paired and merged into flame front oscillations that were significantly larger in size and lower in frequency. A selective manifestation of high frequency wrinkles (driven at the frequency of forcing) was noted on flame fronts allowing the passage of acoustic waves from lighter to denser media while they were absent on flame fronts allowing the passage of acoustic waves from denser to lighter media.

8.2.2 Identification of new physical mechanism

1. A Baroclinic Vorticity based mechanism, in which the pressure gradient in a transversely directed acoustic wave interacted with a misaligned density gradient at the fuel-oxidizer interface generating baroclinicity was proposed for the first time as a driving mechanism for combustion instability in Liquid Rocket Engines. This mechanism was theoretically conjectured, experimentally verified (to a good level of confidence) and successfully adapted to explain the strong asymmetric flame-acoustic interactions observed in our experiments.

Since a baroclinic interaction would depend strongly on the direction and magnitude of the density gradient at the fuel-oxidizer interface, three tests were conducted to verify baroclinicity as a potential instability mechanism in flame acoustic interactions.

- In the first test, the direction of the density gradient at the fuel oxidizer interface was reversed and the resulting flame system was subjected to acoustic excitation from the same direction. Flame front oscillations were observed to occur selectively on the interface where acoustic waves travelled from lighter to denser media. For the Oxygen-in-the-center case, asymmetric interactions were observed on flame front closer to the acoustic driver whereas for Hydrogen-in-the-center case, similar oscillations were noted on flame front located away from the acoustic driver.
- In the second test, the magnitude of the density gradient at the fuel-oxidizer interface was systematically changed by the addition of noble gases and the degree of interaction between flame and acoustics was quantified for a fixed level of acoustic forcing. Forcing at a fixed amplitude from the same direction was noted to cause lesser and lesser flame-acoustic interaction as the magnitude of the density gradient at the fuel-oxidizer interface was gradually decreased. An exponential dependency was noted.
- In the third test, a diffusion flame system using a Hydrogen Methane ($\text{GH}_2 / \text{GCH}_4$) blended fuel mixture was acoustically forced and simultaneous measurements of OH^* Chemiluminescence oscillations and pressure oscillations were made at various locations inside the combustor. For all valid measurement locations, although the amplitude of pressure oscillations were similar, the flame front closer to the acoustic driver where acoustic waves travelled from lighter to denser fluid showed greater heat release oscillations.

Results from all the tests showed that there was a preferred orientation of pressure and density gradients under which flames responded strongly to acoustic forcing, sometimes folding up into violent flame front oscillations. It supported the notion that periodic baroclinic vorticity strengthened by large density gradient in shear-coaxial injector flow-field could be a problem, making the affected configuration susceptible to combustion instability. Such physical mechanism involving intermittent baroclinic torque has never been considered in rocket motor combustion instabilities.

2. The possible role of an acoustically accelerated Rayleigh-Taylor Instability in driving the flame acoustic coupling process was also explored. Quantification of the possible growth rates of the interfacial perturbations using a time dependent acoustically driven acceleration field indicated that more than 200% growth of perturbation amplitudes is possible in less than half a cycle of acoustic forcing at certain frequencies.

8.2.3 Sensitivity analysis and measurements

Sensitivity analysis and measurements of flame-acoustic coupling to other flowfield parameters were conducted.

1. Using dimensional analysis and an intuitive argument to replace Damkohler number with fuel mixture fraction, three non-dimensional groups were identified as important in flame acoustic interaction problems. These included non-dimensionalized density difference, velocity difference and a measure of chemistry. Measure of chemistry was represented by the Methane mole fraction in a Hydrogen - Methane blended fuel.

$$\frac{\delta}{D} = f\left(\frac{\rho_o - \rho_f}{\rho_o + \rho_f}, \frac{u_f - u_o}{u_f + u_o}, \frac{Y_{CH_4}}{Y_{CH_4} + Y_{H_2}}\right)$$

Partial sensitivities of flame acoustic coupling to each of these non-dimensional variables were described in terms of first order partial derivative functions :

$$\frac{\partial(\delta/D)}{\partial((\rho_o - \rho_f)/(\rho_o + \rho_f))}, \frac{\partial(\delta/D)}{\partial((u_f - u_o)/(u_f + u_o))}, \frac{\partial(\delta/D)}{\partial(Y_{CH_4}/(Y_{CH_4} + Y_{H_2}))}$$

2. While the parameter under investigation was gradually varied, other parameters were kept almost unchanged in these tests. The resulting flame system was perturbed by fixed-amplitude acoustic forcing and the extent of flame perturbation was quantified by measuring the flame brush thickness through OH* and CH* chemiluminescence imaging. Throughout these tests, the temperature and the total pressure were held unchanged. In the ranges tested, the amount of flame-acoustic interaction was most sensitive to changes in density ratio. Changes in velocity ratio and fuel mixture ratio produced relatively small effects.

Results from the tests are summarized below:

- In the first parametric test, the density ratio between oxidizer and fuel was varied between 16 and 5, while the velocity ratio and the fuel composition were held constant. Density ratio possibly affected flame-acoustic interaction

by changing the amplitude of periodically applied baroclinic torque on the mixture interface. The observed dependence on density ratio was exponential.

$$\left(\frac{\delta}{D}\right)_u = C_1 \exp\left(C_2 \cdot \frac{\rho_o - \rho_f}{\rho_o + \rho_f}\right) \quad \text{Where } C_1 \sim 0.02 \text{ and } C_2 \sim 5.1$$

- In the second test, the velocity ratio was varied between 3.0 and 5.3, while the density ratio and the fuel composition were held constant. Increasing the outer jet velocity reduced the amount of interaction almost linearly. This effect was attributed to the decrease in acoustic energy per mass flow rate. The observed dependence on non-dimensionalized velocity difference was found to be :

$$\left(\frac{\delta}{D}\right)_\rho = C_3 \left(\frac{u_f - u_o}{u_f + u_o}\right) + C_4 \quad \text{Where } C_3 \sim -3.5 \text{ and } C_4 \sim 3.6$$

- In the third test, a Hydrogen-Methane mixture fuel was tested by varying the mixture fraction while both the density ratio and the velocity ratio were held constant. Increasing the Methane mole fraction also reduced the amount of interaction linearly. This effect was attributed to the reduction in total heat release rate which affected the amplification mechanism. The observed dependence on Methane mole fraction was found to be :

$$\left(\frac{\delta}{D}\right)_{\rho,u} = C_5 \left(\frac{Y_{CH_4}}{Y_{CH_4} + Y_{H_2}} \right) + C_6 \quad \text{Where } C_5 \sim -0.87 \text{ and } C_6 \sim 2.3$$

- Using data collected as part of the velocity ratio test and the density ratio test, the effect of momentum ratio on flame acoustic coupling was also studied. Increase in outer jet momentum for a fixed level of acoustic forcing also caused a reduction in the amount of interaction. For cases where outer jet momentum was increased by increasing outer jet velocity while keeping outer jet density constant (density ratio between outer and inner jet remained constant in the process) flame brush thickness decreased linearly as outer jet momentum was increased. The observed dependence on momentum ratio was found to be :

$$\left(\frac{\delta}{D}\right)_{\rho} = C_7 \left(\frac{J_f - J_o}{J_f + J_o} \right) + C_8 \quad \text{Where } C_7 \sim -1.24 \text{ and } C_8 \sim 1.25$$

- For cases where outer jet momentum was increased by increasing outer jet density while keeping outer jet velocity constant (density ratio between outer and inner jet decreased in the process) the flame brush thickness decreased exponentially as the outer jet momentum was increased indicating the stronger role played by fuel-oxidizer density ratio in controlling flame-acoustic interaction. The observed dependence on momentum ratio was found to be :

$$\left(\frac{\delta}{D}\right)_u = C_9 \exp\left(C_{10} \cdot \frac{J_f - J_o}{J_f + J_o}\right) \quad \text{Where } C_9 \sim 0.29 \text{ and } C_{10} \sim -2.85$$

8.2.4 Non-linear response in flame-acoustic interaction

1. High speed imaging and spectral measurements of the flame system under transverse acoustic forcing showed that downstream of the injector face plate, the initial small amplitude wrinkles (driven at the frequency of the external forcing) paired and merged into flame front oscillations that were significantly larger in amplitude and lower in frequency as compared to the initial interaction zone near the injector face plate. Various time scales showed up in the flame oscillations downstream of the injector with high frequency small amplitude oscillations at the forced frequency riding over large amplitude low frequency ones.

2. This showed that large amplitude heat release oscillations could essentially occur at frequencies that were significantly different from the frequency of forcing. As a result of this, other modes of the combustor whose Eigen frequencies do not correspond to the forcing frequency could also be excited leading to the excitation of lower frequency modes of the combustor.

8.2.5 Model development.

Three different analytical models were developed to interpret and explain experimentally observed acoustic modes of the chamber under density stratified isothermal and reacting flow conditions. The experimental results showed good quantitative agreements with the model computation. Interestingly enough, the

acoustically driven entrainment model was even able to account for the discrepancy of the frequency of the $3\lambda/4$ -mode of the chamber length (closed-open boundaries) measured on either sides of the central flame zone.

The three models were based on (1) well-stirred reactor , (2) jet mixing length, and (3) acoustically driven entrainment models. The models differed in the way the average molecular weight and gamma of the medium inside the combustor was calculated. It essentially involved using a correction factor ψ to correct the average molecular weight and the average ratio of specific heat equations used by each of them.

$$MW_{mix}(\psi, \eta_{H_2}, \eta_{O_2}, \eta_{CH_4}) = \left(\frac{\eta_{H_2}}{\eta_{H_2} + \eta_{CH_4} + \psi\eta_{O_2}} \right) MW_{H_2} + \left(\frac{\eta_{CH_4}}{\eta_{H_2} + \eta_{CH_4} + \psi\eta_{O_2}} \right) MW_{CH_4} + \left(\frac{\psi\eta_{O_2}}{\eta_{H_2} + \eta_{CH_4} + \psi\eta_{O_2}} \right) MW_{O_2}$$

$$\gamma_{mix}(\psi, \eta_{H_2}, \eta_{O_2}, \eta_{CH_4}) = \left(\frac{\eta_{H_2}}{\eta_{H_2} + \eta_{CH_4} + \psi\eta_{O_2}} \right) \gamma_{H_2} + \left(\frac{\eta_{CH_4}}{\eta_{H_2} + \eta_{CH_4} + \psi\eta_{O_2}} \right) \gamma_{CH_4} + \left(\frac{\psi\eta_{O_2}}{\eta_{H_2} + \eta_{CH_4} + \psi\eta_{O_2}} \right) \gamma_{O_2}$$

- In the Well Stirred Reactor based model, the average molecular weight and gamma of the mixture were calculated assuming a fully premixed mixture of fuel and oxidizer, in stoichiometric proportions($\psi = 1$)

- In the Jet Mixing Length based Model, two separate length scales were used. To a distance equivalent to the potential core length of the center jet from the injector faceplate, the average molecular weight and gamma of the mixture was calculated assuming a fully premixed mixture of fuel and oxidizer, mixed in their stoichiometric proportions but corrected using the velocity ratio between fuel and oxidizer. Beyond this region, a fully premixed stoichiometric mixture was used.

$$\psi = \frac{V_{fuel}}{V_{o_2}}, \text{ for } 0 \leq y \leq 6D$$

$$\psi = 1 \text{ for } y \geq 6D.$$

- In the acoustically driven entrainment based model, two separate values of ψ were used near the driver and away from the driver regions because an excess entrainment of the center jet into the co-flow on the driver side would lead to a decrease in the amount of the center jet fluid entrained by co-flow on the far side of the driver. Values for σ_1 and σ_2 were experimentally determined

$$\psi = 1 + \sigma_1 \left(\frac{J_{reference}}{J_{total}} \right) \text{ Driver side}$$

$$\psi = 1 - \sigma_2 \left(\frac{J_{reference}}{J_{total}} \right) \text{ Wall side}$$

8.3 Concluding remark

This work highlighted the role of the density gradient between fuel and oxidizer as a facilitator for initiating combustion instability. Reducing the density gradient between fuel and oxidizer was shown to increase the resistance of flames to acoustic coupling providing a greater margin of stability. In fully unstable combustion inside a rocket thrust chamber, the amplitude of pressure oscillations becomes rather large, making flame-acoustic coupling inevitable. However, during the onset of combustion instability the pressure oscillation amplitude would be small, but could be just large enough to cause further amplification through coupled heat release. The present results show that baroclinic interactions could amplify heat release coupling. Experimental confirmation of the possible role of density gradient in promoting heat release oscillations is presented, but more work needs to be done before this theory can be proved or disproved with a sufficient level of confidence. Nonetheless, this is a useful finding because it suggests reducing the density gradient between fuel and oxidizer as a possible control mechanism. Reducing the density gradient between fuel and oxidizer would lead to greater resistance to flame-acoustic coupling, thus providing a greater margin of stability. Needless to say, such extrapolation of the present results must be taken with caution because a change in chemical kinetics could have even more sensitive effect on flame stability.

Appendices

Appendix A: Images

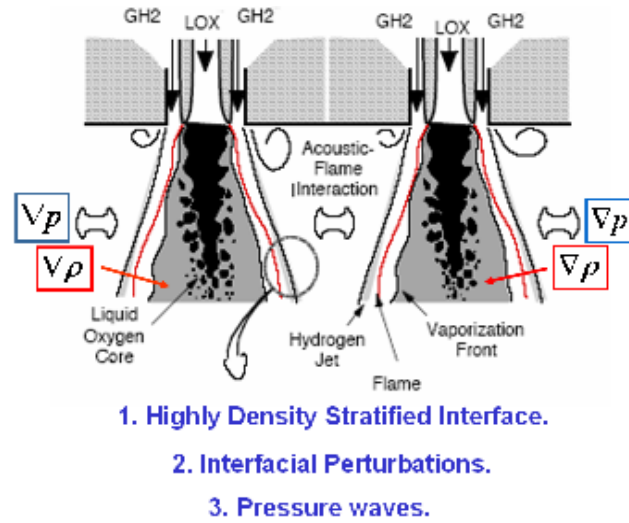


Figure 1.1. Schematic showing typical flow field in the neighborhood of a LOX- GH2 shear coaxial injector.

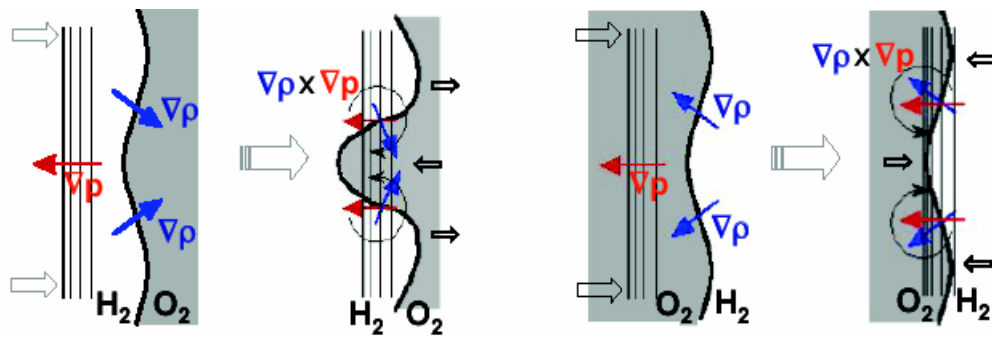


Figure 3.1. Baroclinic interactions between pressure gradient and density gradient at a density stratified interface. (a) Destabilizing interaction. (b) Stabilizing interaction.

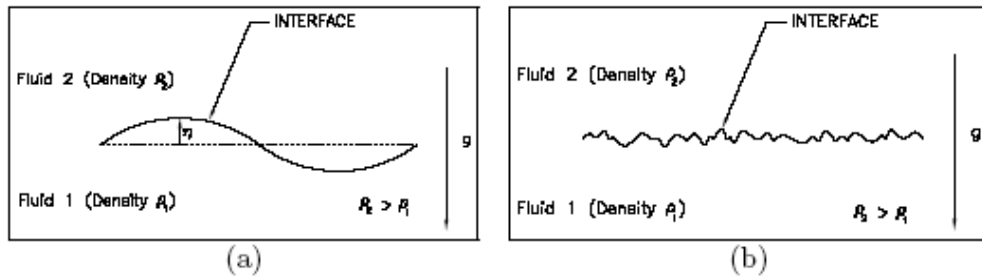


Figure 3.2. RT unstable configurations. (a) Single-mode case. (b) Multi-mode case (After Kumar, 2003).

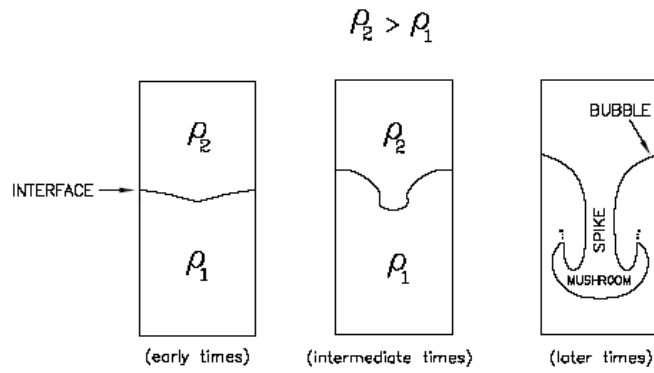


Figure 3.3. RT instability, single wavelength initial perturbation (After Youngs 1984).

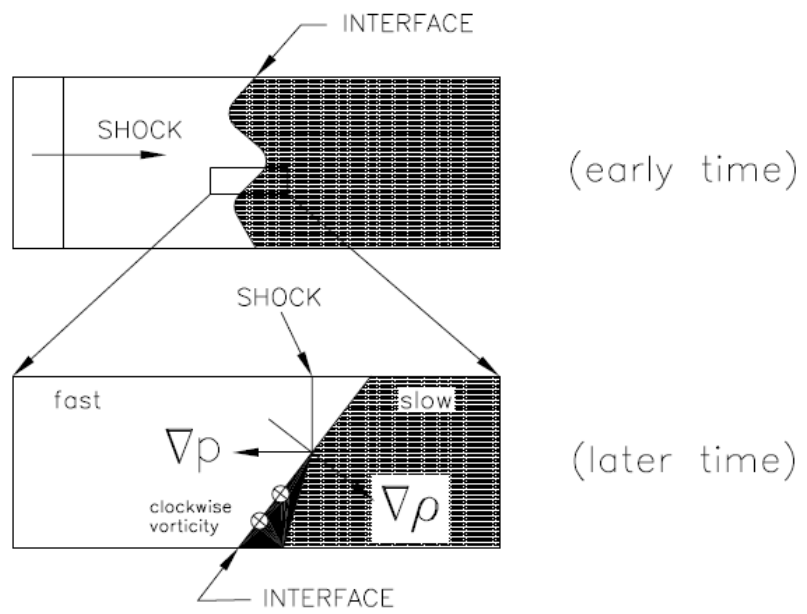


Figure 3.4. Richtmyer-Meshkov instability (After Sunhara *et al.*,1996).

St = 0.25 - 0.60

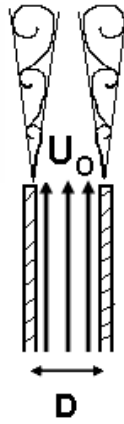


Figure 3.5. Jet preferred mode instability.

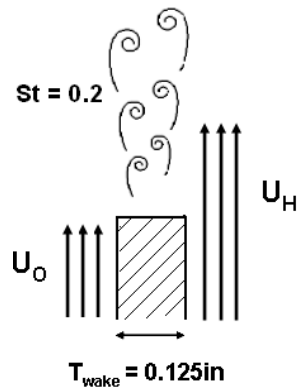


Figure 3.6. Wake mode instability.

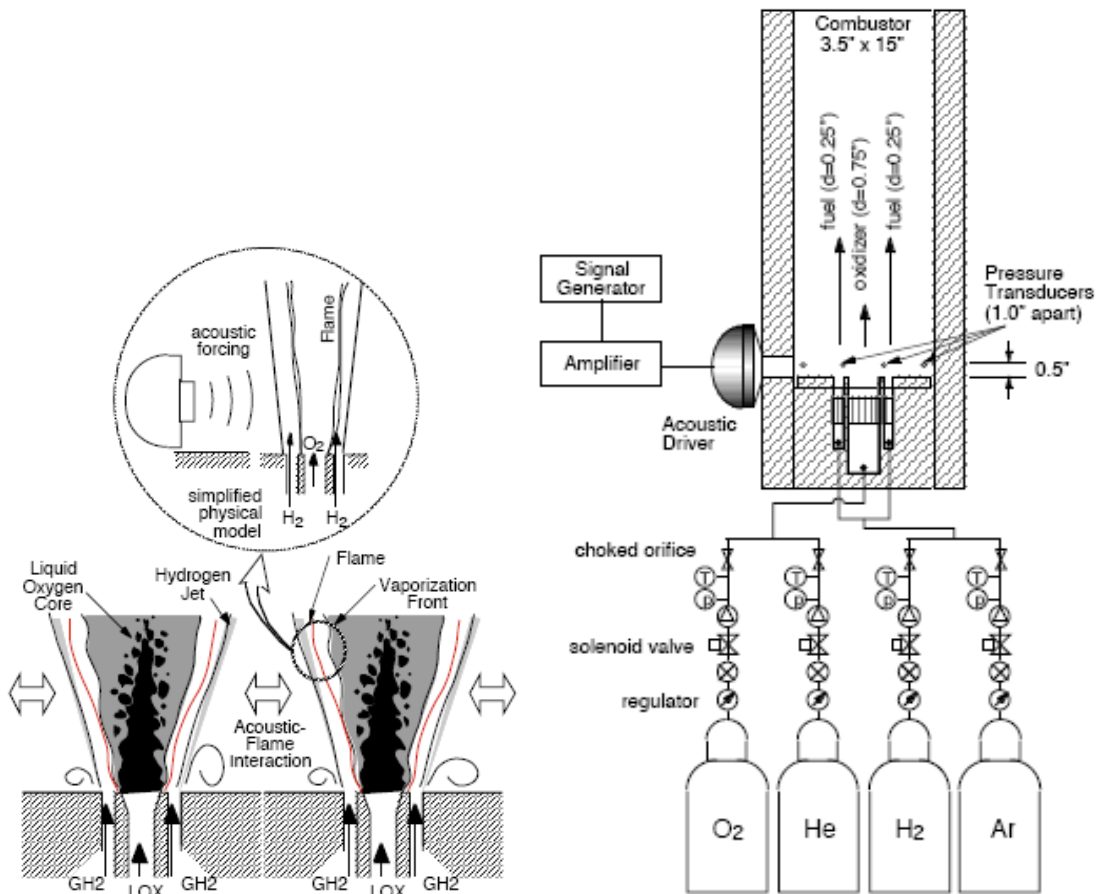


Figure 4.1. (a) Physical model. (b) Schematic of the shear-coax injector rig. All dimensions are in inches.

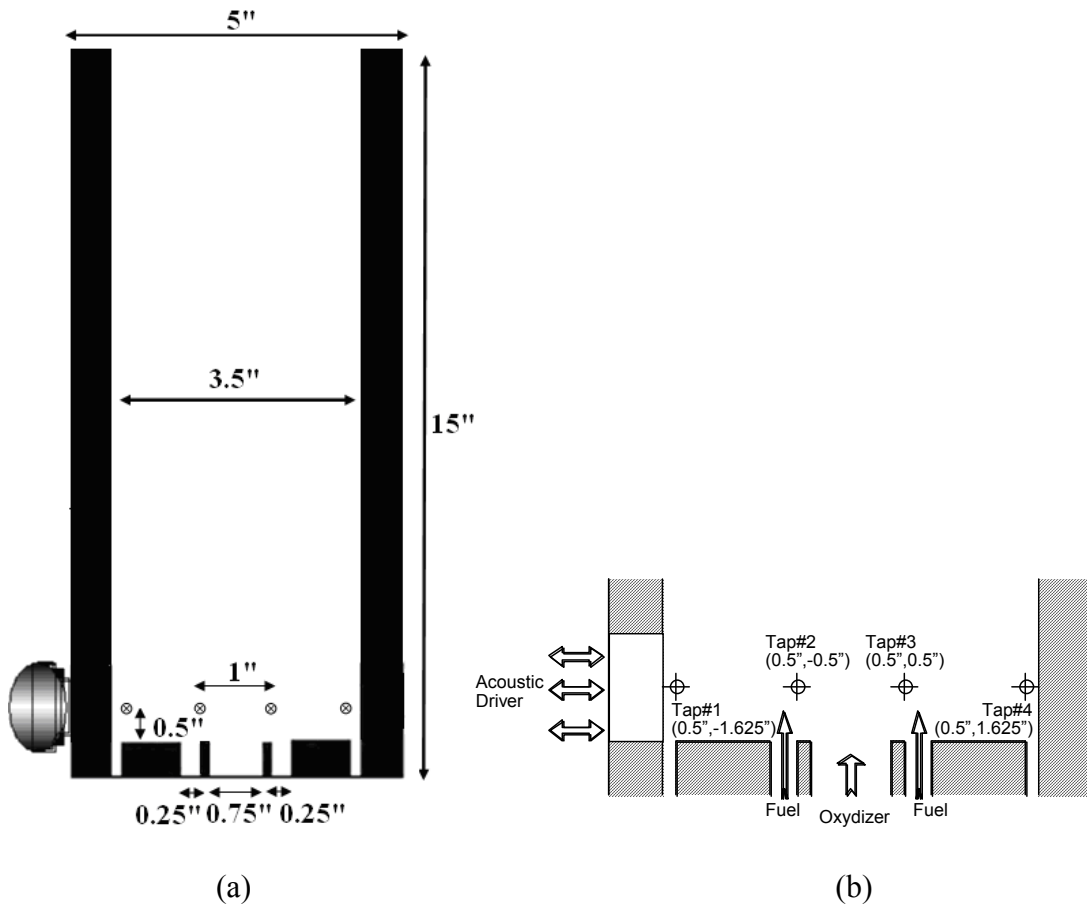


Figure 4.2. Schematic view of shear coax combustor. (a) Overall setup. (b) Near injector region showing pressure tap locations. All dimensions are in inches.

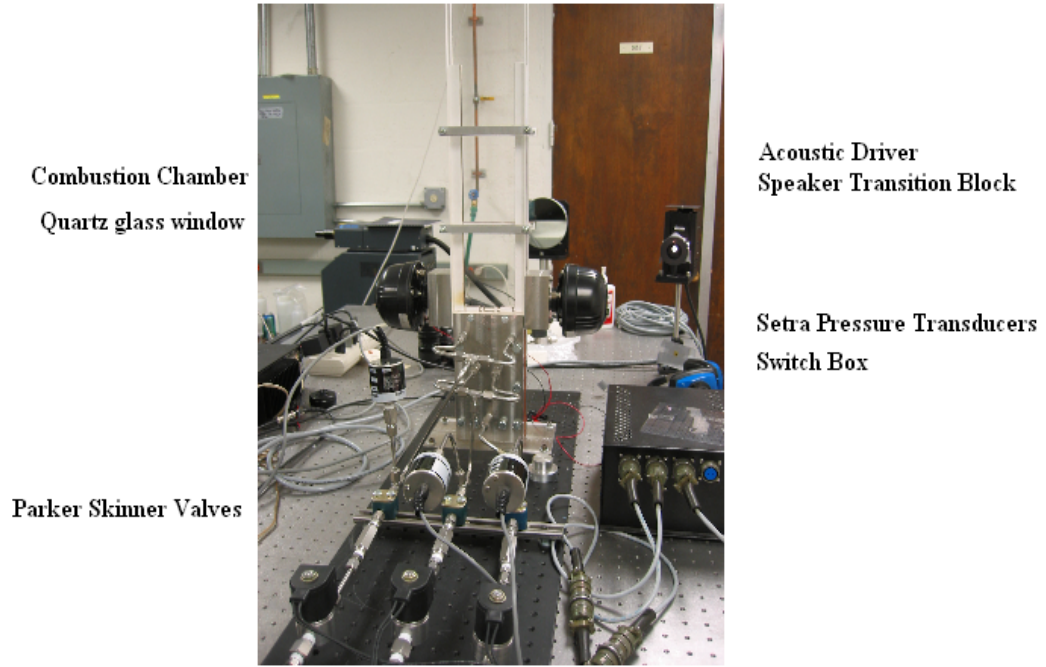


Figure 4.3. Physical setup.

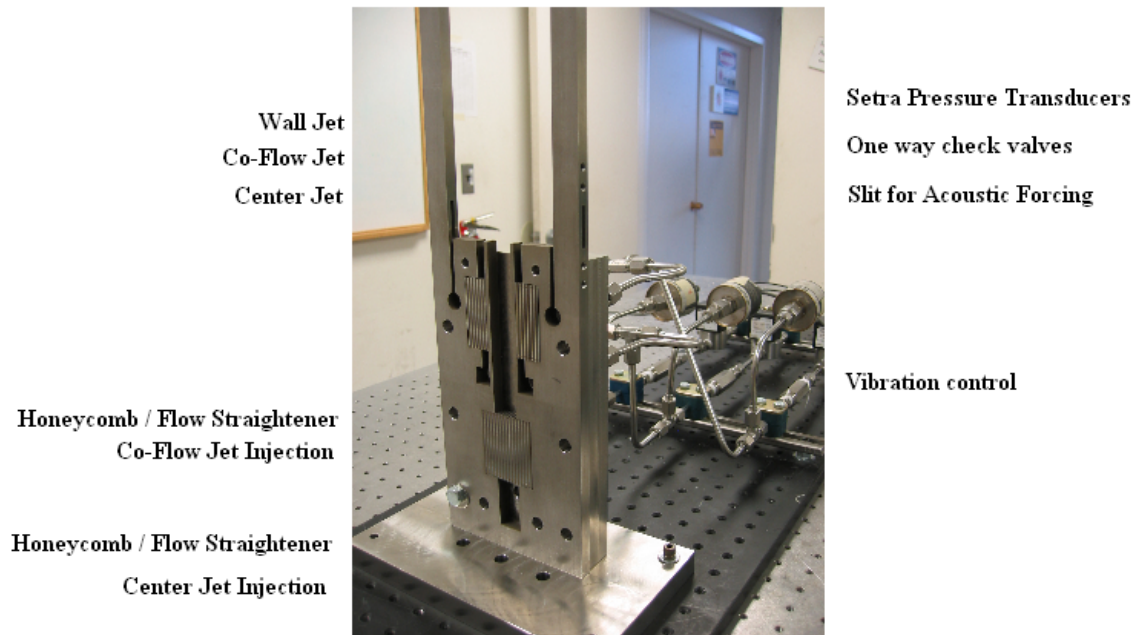


Figure 4.4. Physical model of inlet to combustor.

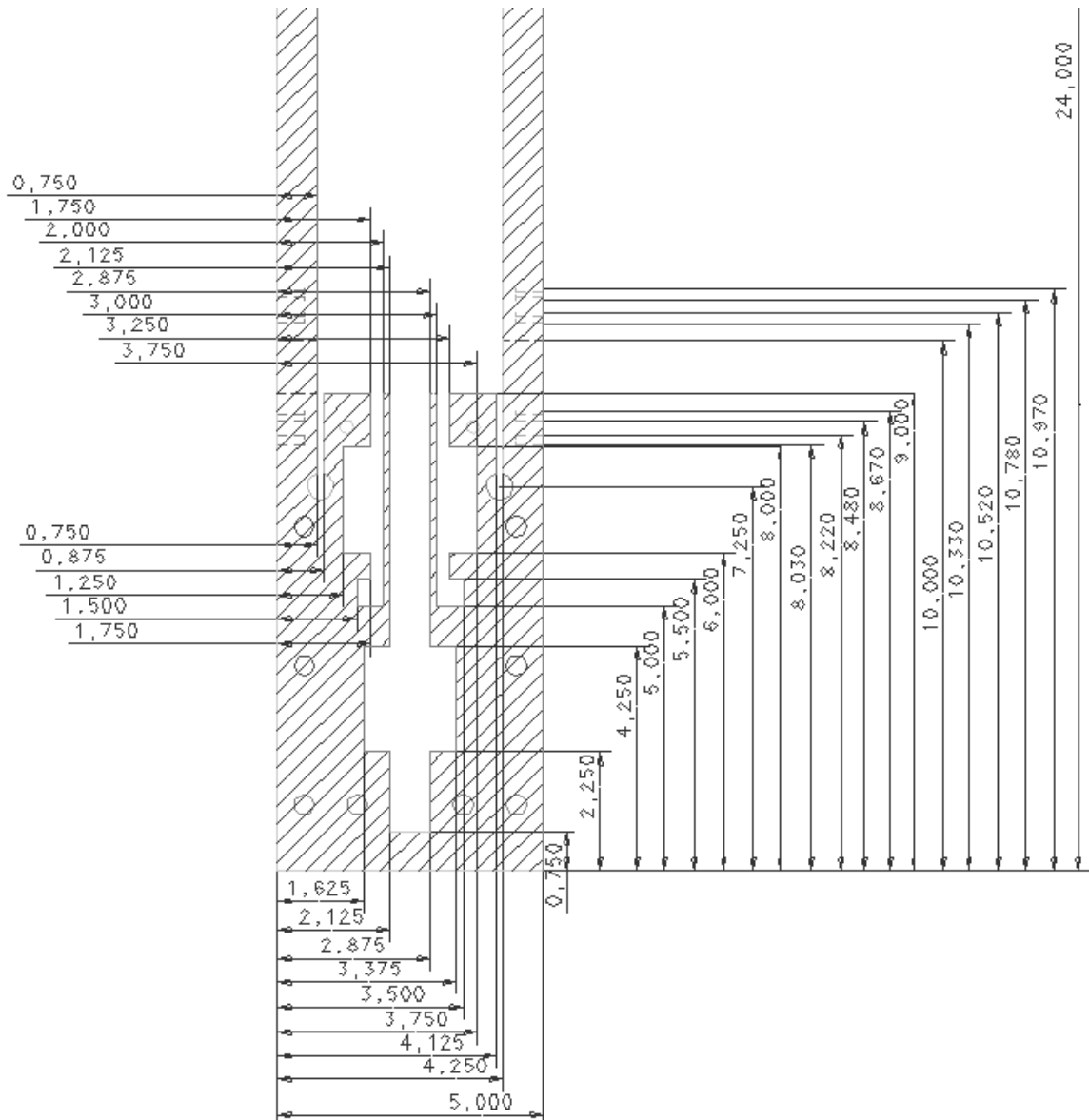


Figure 4.5. Schematic showing dimensions for inlet to combustor. All dimensions are in inches.

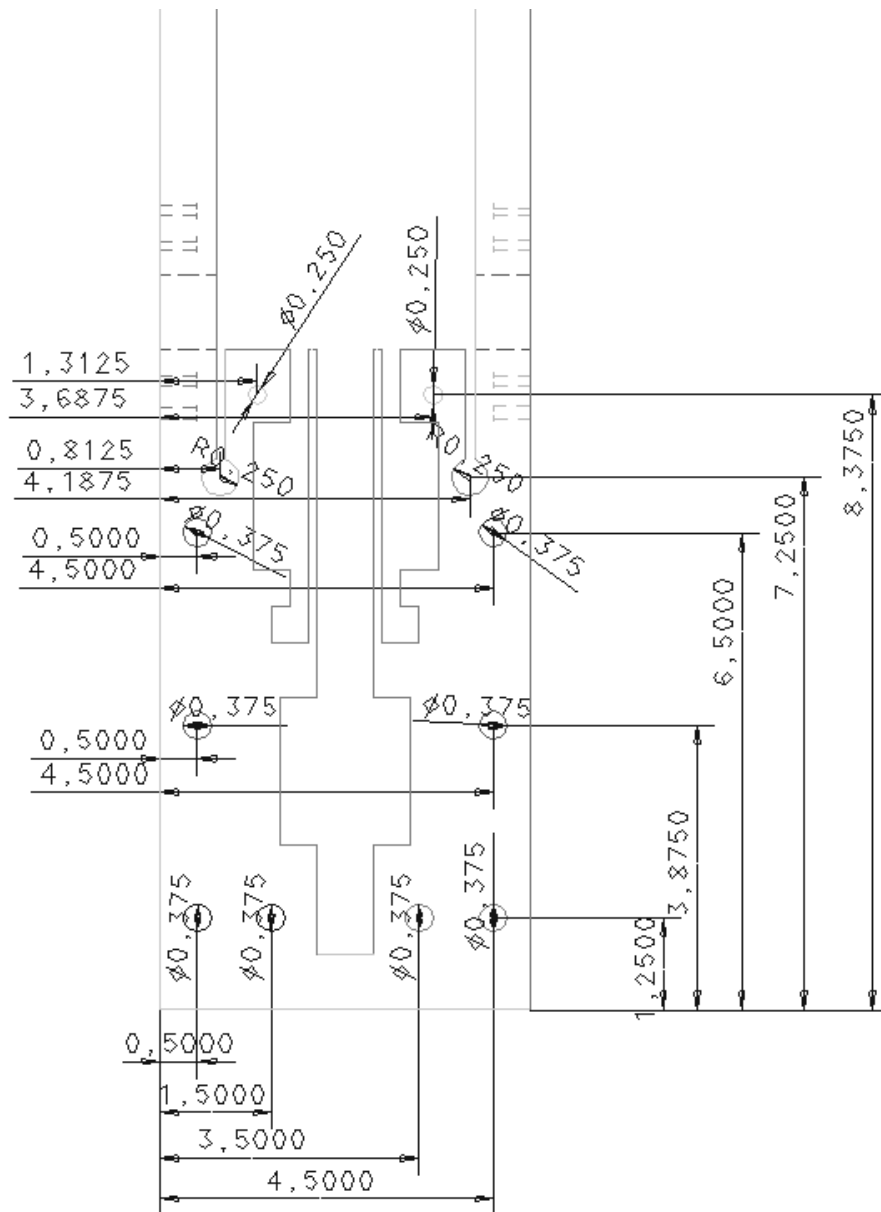


Figure 4.6. Schematic showing position and size of through holes for bolts for fixing the side plates between which the center piece is sandwiched. All dimensions are in inches.

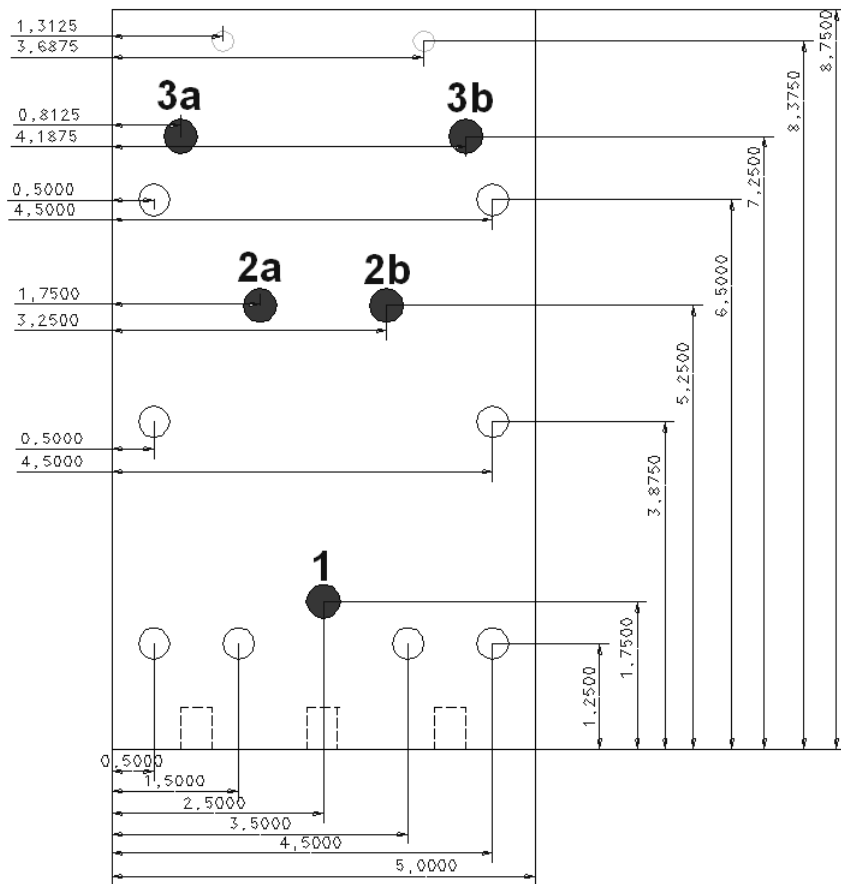
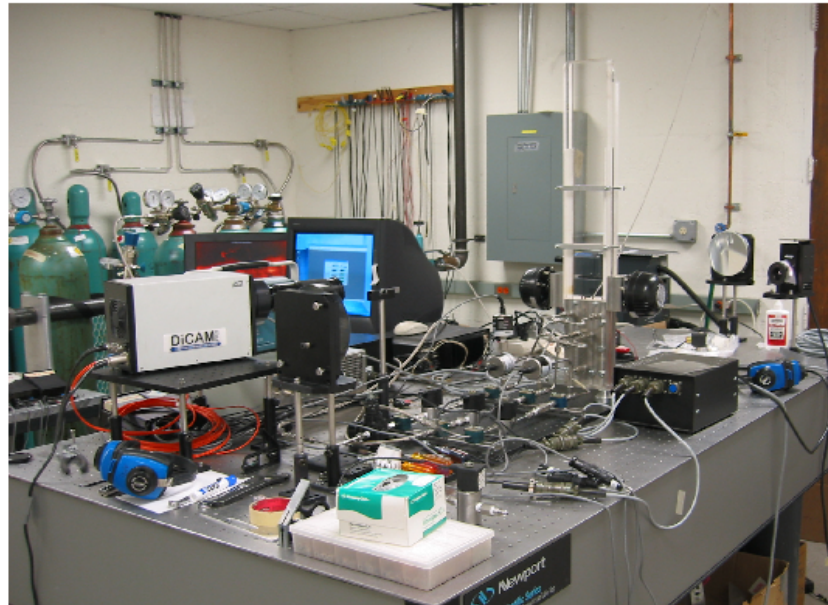


Figure 4.7. Schematic showing side plate with injection location for gases. All dimensions are in inches.

Computer for phase locking

Dicam Pro ICCD Camera
Mirror 2



Test Rig
Light Source
Mirror 1
Acoustic Driver

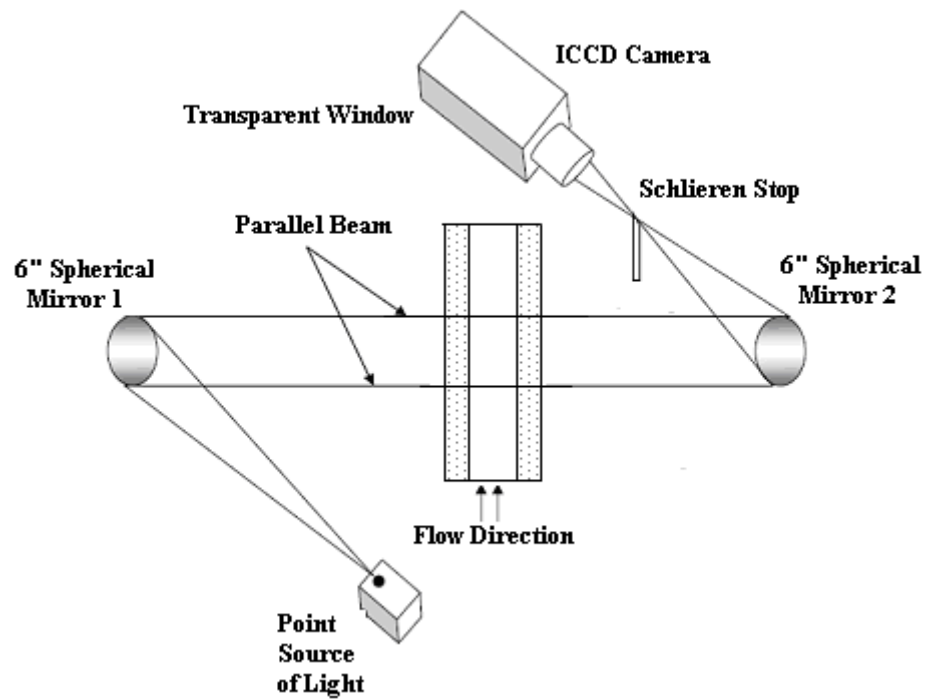


Figure 4.8. Schlieren setup. (a) Laboratory arrangement. (b) Schematic.

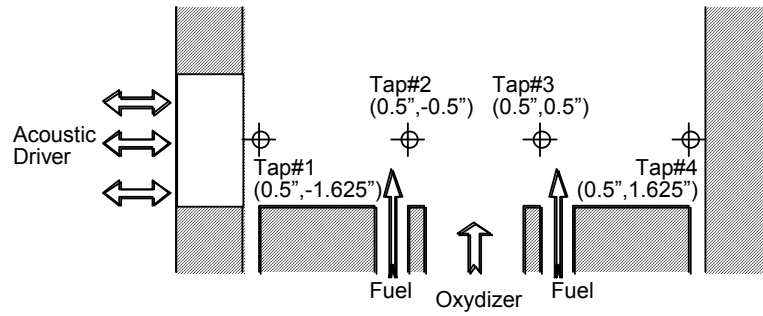


Figure 4.9. Kistler dynamic pressure sensor locations. cf. Table 3.1. for location of pressure taps. All dimensions are in inches.

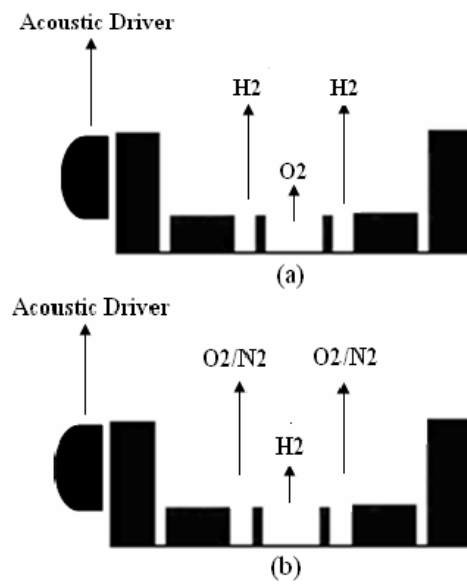
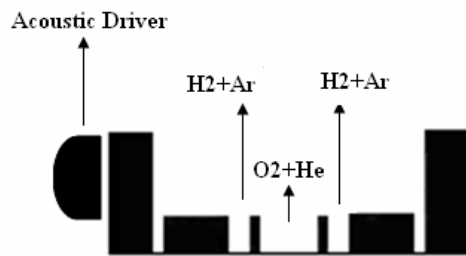
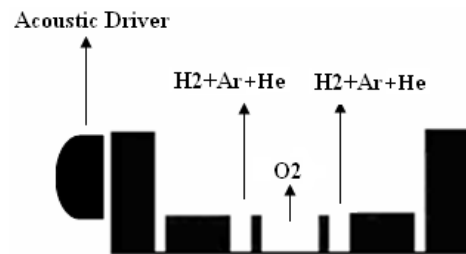


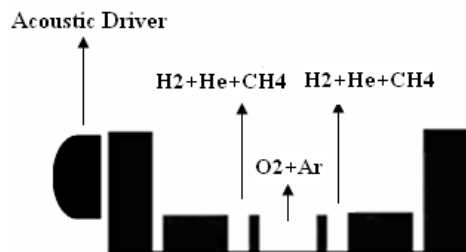
Figure 4.10. Injection arrangement for reversal of density gradient test. (a) Normal configuration. (b) Reversed configuration.



(a)



(b)



(c)

Figure 4.11. Injection arrangement for the different tests. (a) Effect of density ratio. (b) Effect of velocity ratio. (c) Effect of chemical composition of fuel.

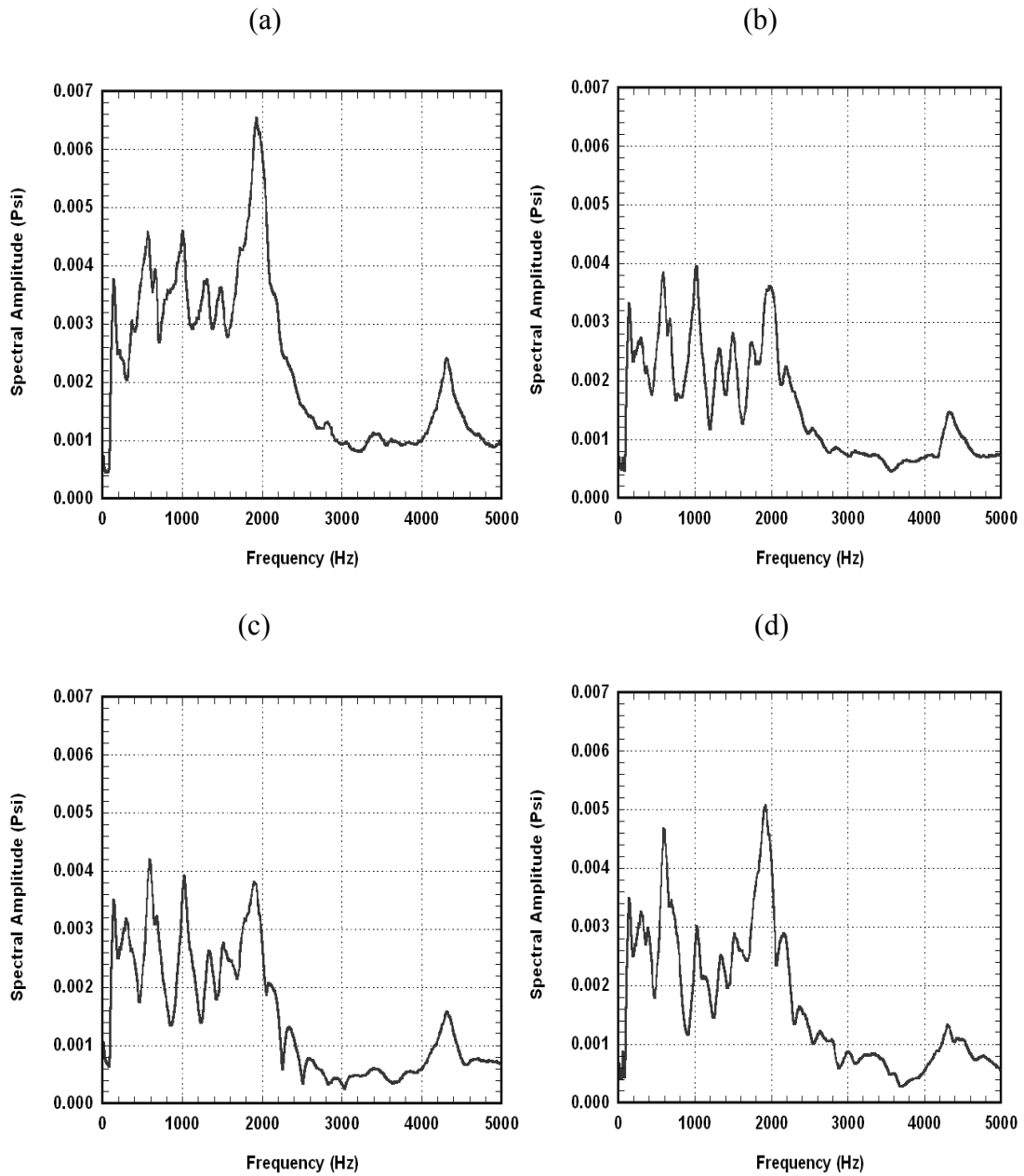
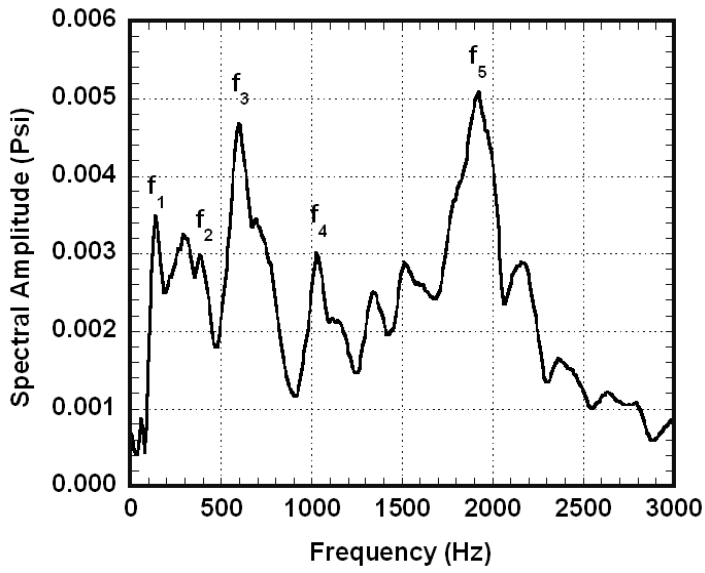


Fig. 5.1. Pressure Spectrum at (a) Tap #1, (b) Tap #2, (c) Tap #3, (d) Tap#4 . No-Flow Conditions. Chamber is excited with band limited white noise forcing.



Symbol	Frequency (Hz)
f_1	136
f_2	392
f_3	600
f_4	1024
f_5	1920

Figure 5.2. Pressure spectrum of no flow quiescent air excited with white noise redrawn from previous figure. Tap #4.

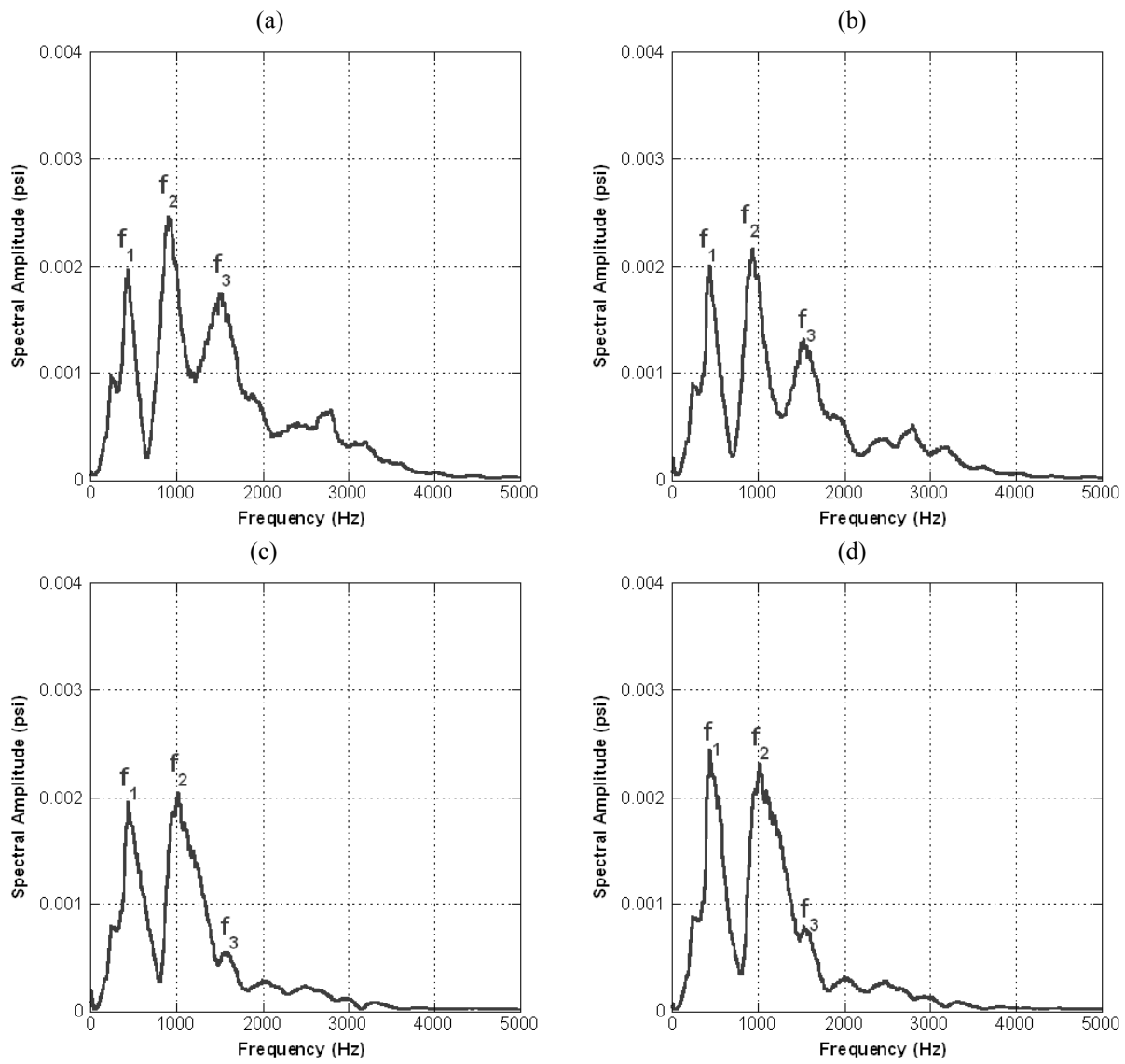


Figure 5.3. Pressure spectrum of isothermal case excited with white noise. Density ratio = 14.5. (a) Tap #1, (b) Tap #2, (c) Tap #3, (d) Tap #4

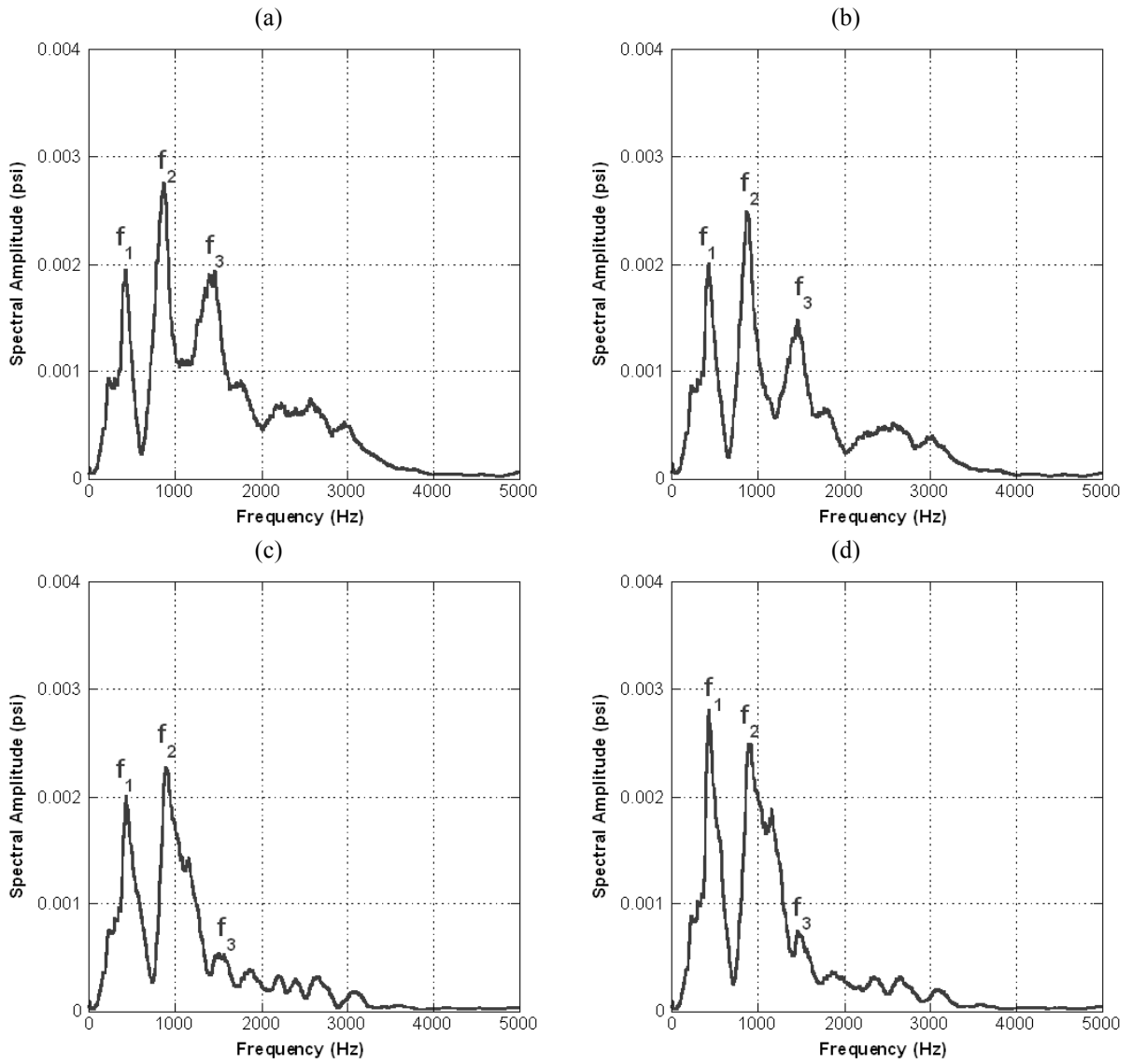


Figure 5.4. Pressure spectrum of isothermal case excited with white noise. Density ratio = 11. (a) Tap #1, (b) Tap #2, (c) Tap #3, (d) Tap #4

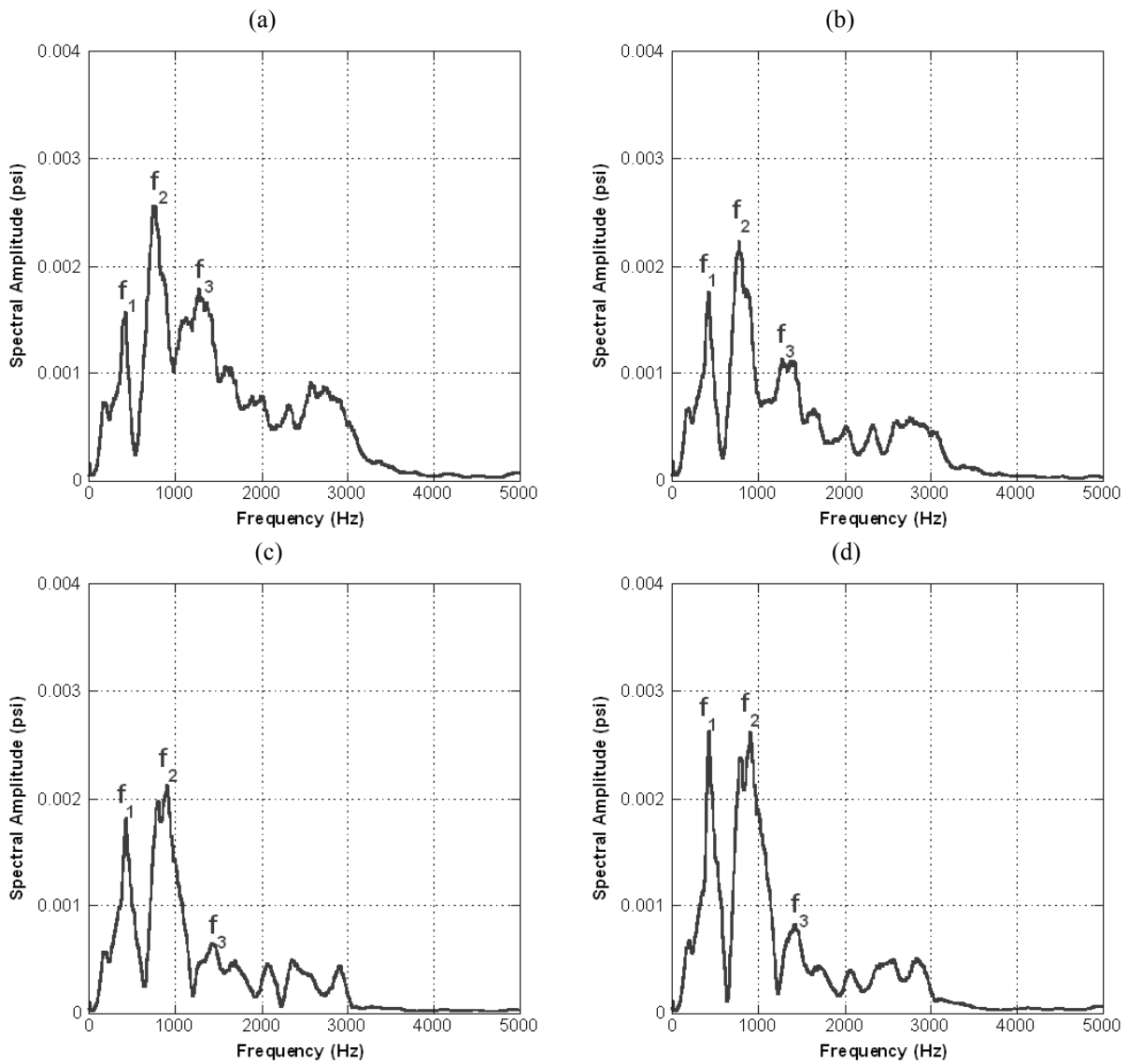


Figure 5.5. Pressure spectrum of isothermal case excited with white noise. Density ratio = 7. (a) Tap #1, (b) Tap #2, (c) Tap #3, (d) Tap #4

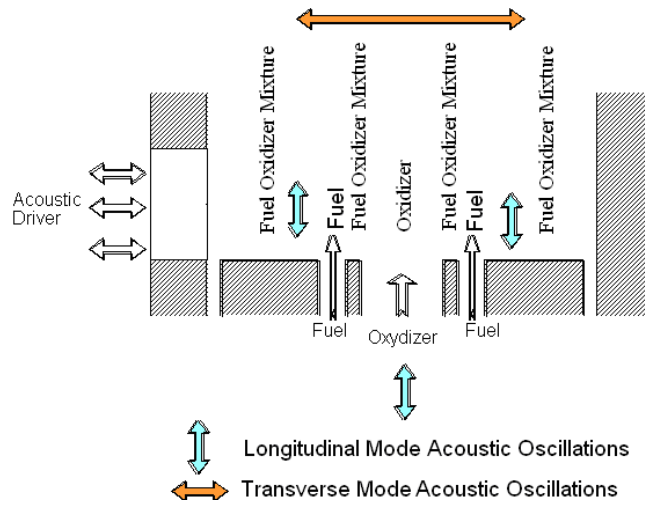


Figure 5.6. Schematic showing distribution of acoustic media in a combustor.

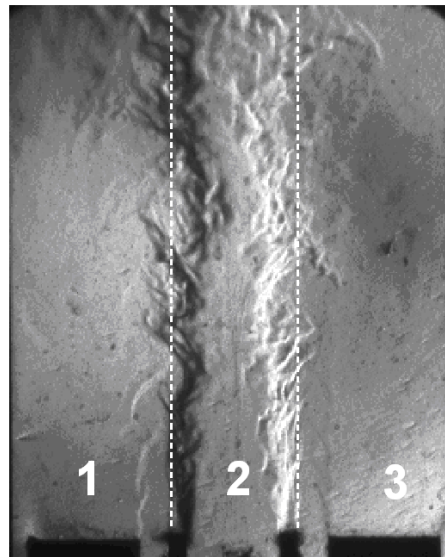


Figure 5.7. Schlieren visualization showing three different acoustic regions of the combustor. Regions 1 and 3 are product dominated and can have different resonant behaviors in the longitudinal direction because they are bounded from each other by interfaces with sudden density changes.

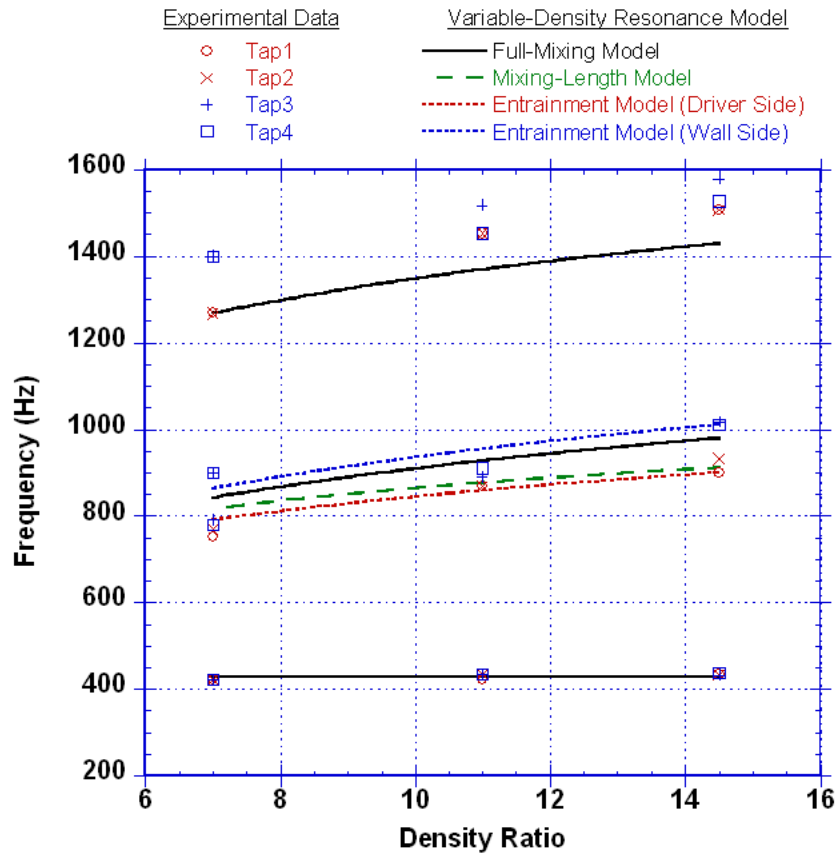


Figure 5.8. Comparison of experimental and predicted values of resonant frequencies for isothermal case.

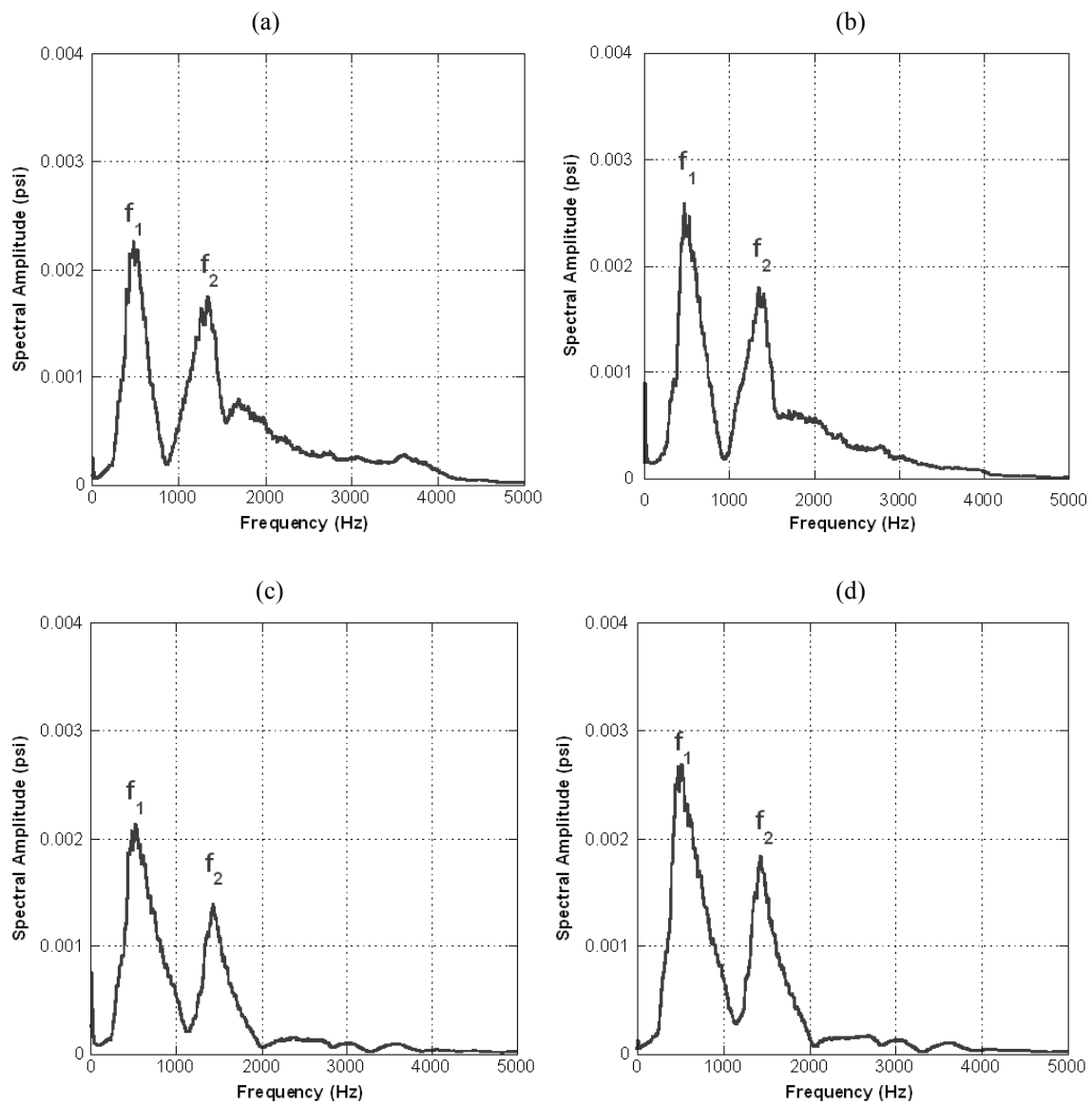


Figure 5.9. Pressure spectrum of reacting flow case excited with white noise. Density ratio = 14.5. (a) Tap #1, (b) Tap #2, (c) Tap #3, (d) Tap #4

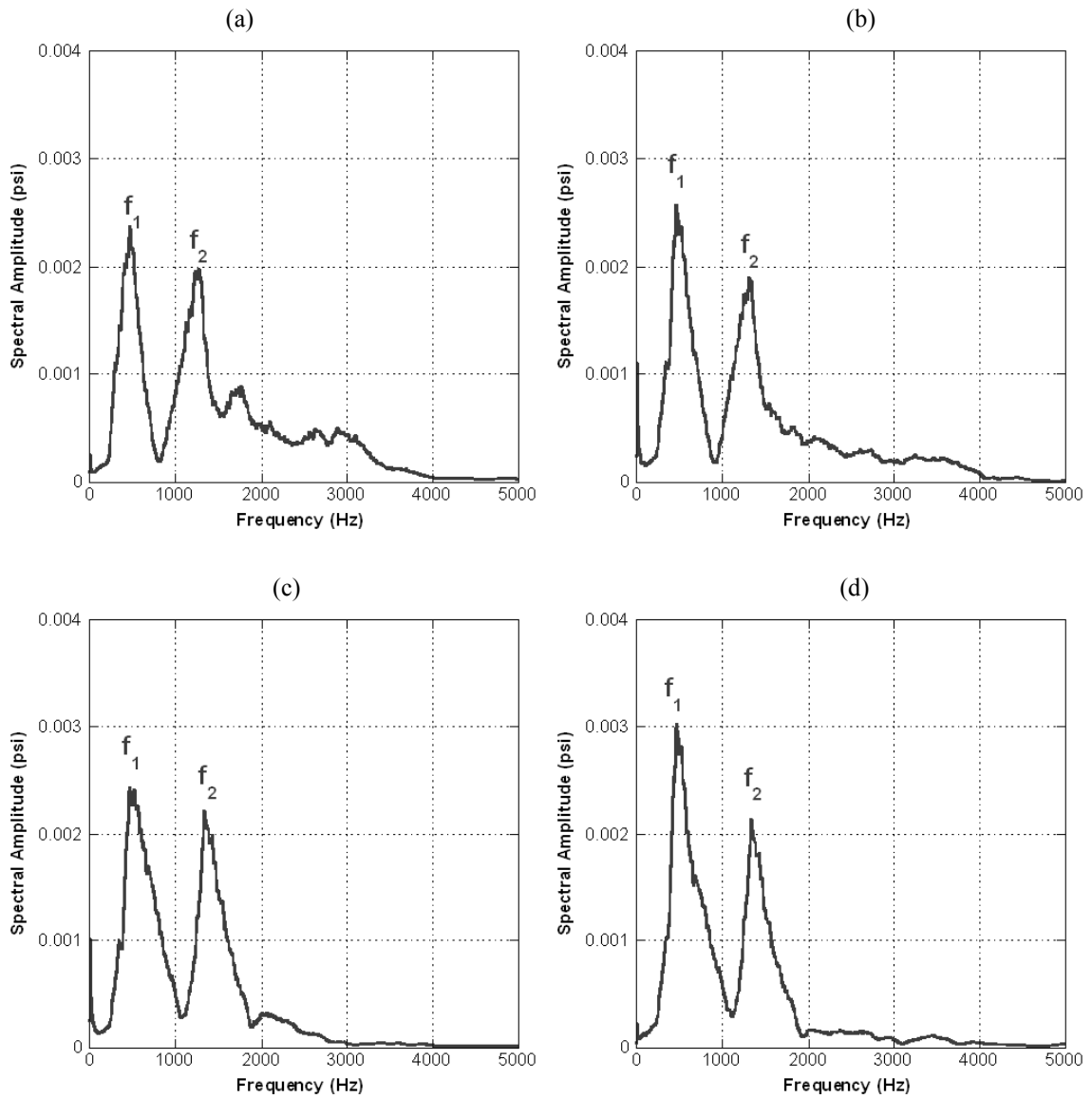


Figure 5.10. Pressure spectrum of reacting flow case excited with white noise. Density ratio = 11. (a) Tap #1, (b) Tap #2, (c) Tap #3, (d) Tap #4.

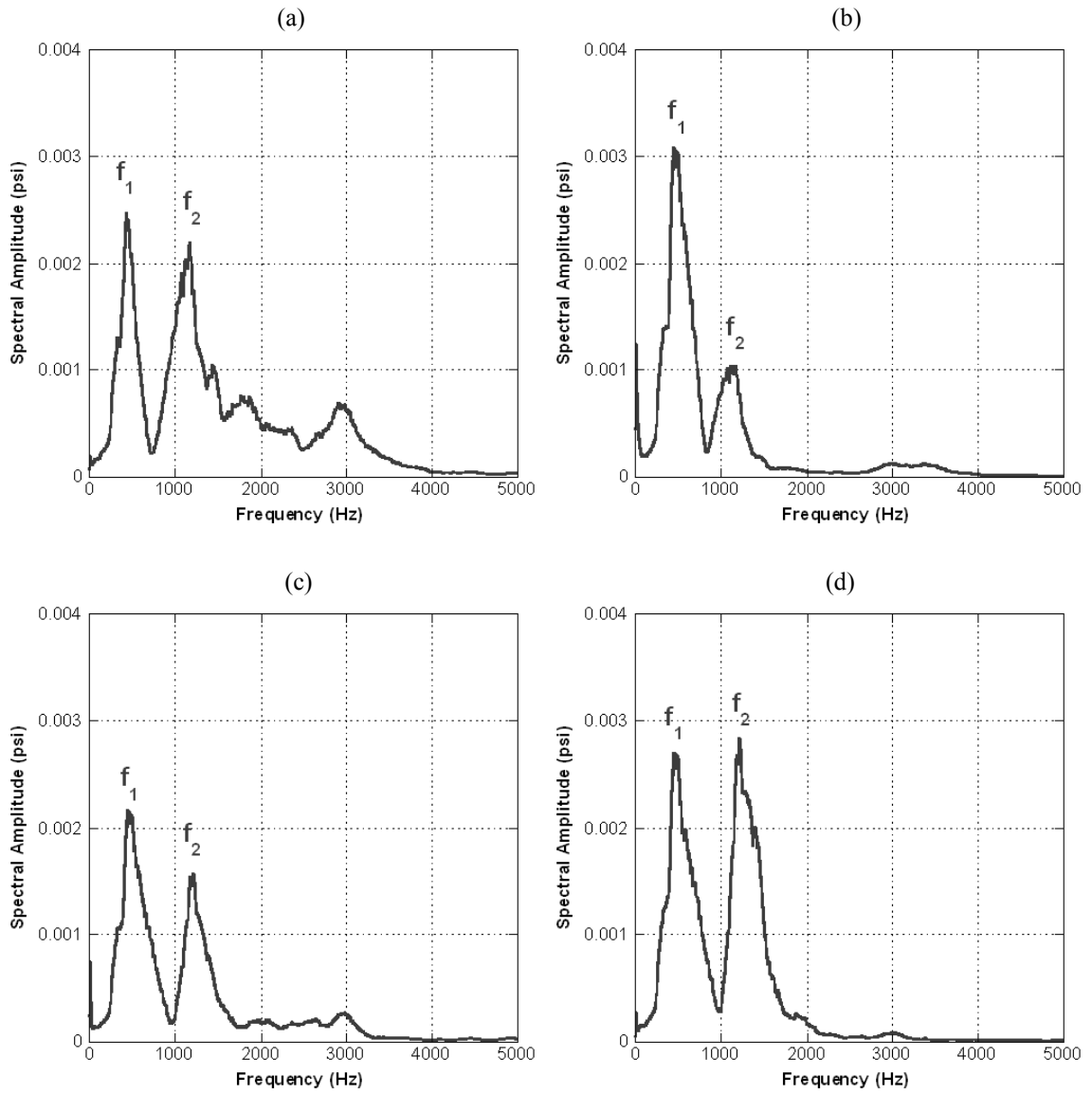


Figure 5.11. Pressure spectrum of reacting flow case excited with white noise. Density ratio = 7. (a) Tap #1, (b) Tap #2, (c) Tap #3, (d) Tap #4.

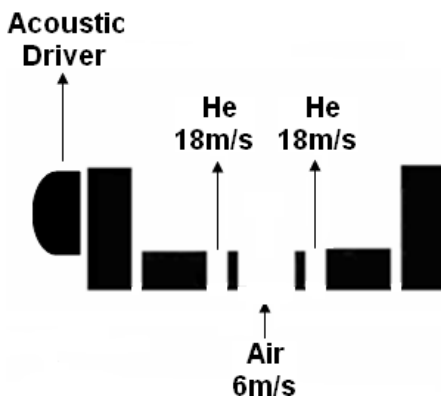


Figure 6.1. Flow arrangement. Band limited (100Hz – 10KHz) white noise forcing is applied from the left. Center jet of air is at 6m/s and co-flowing Helium jets are at 18m/s.

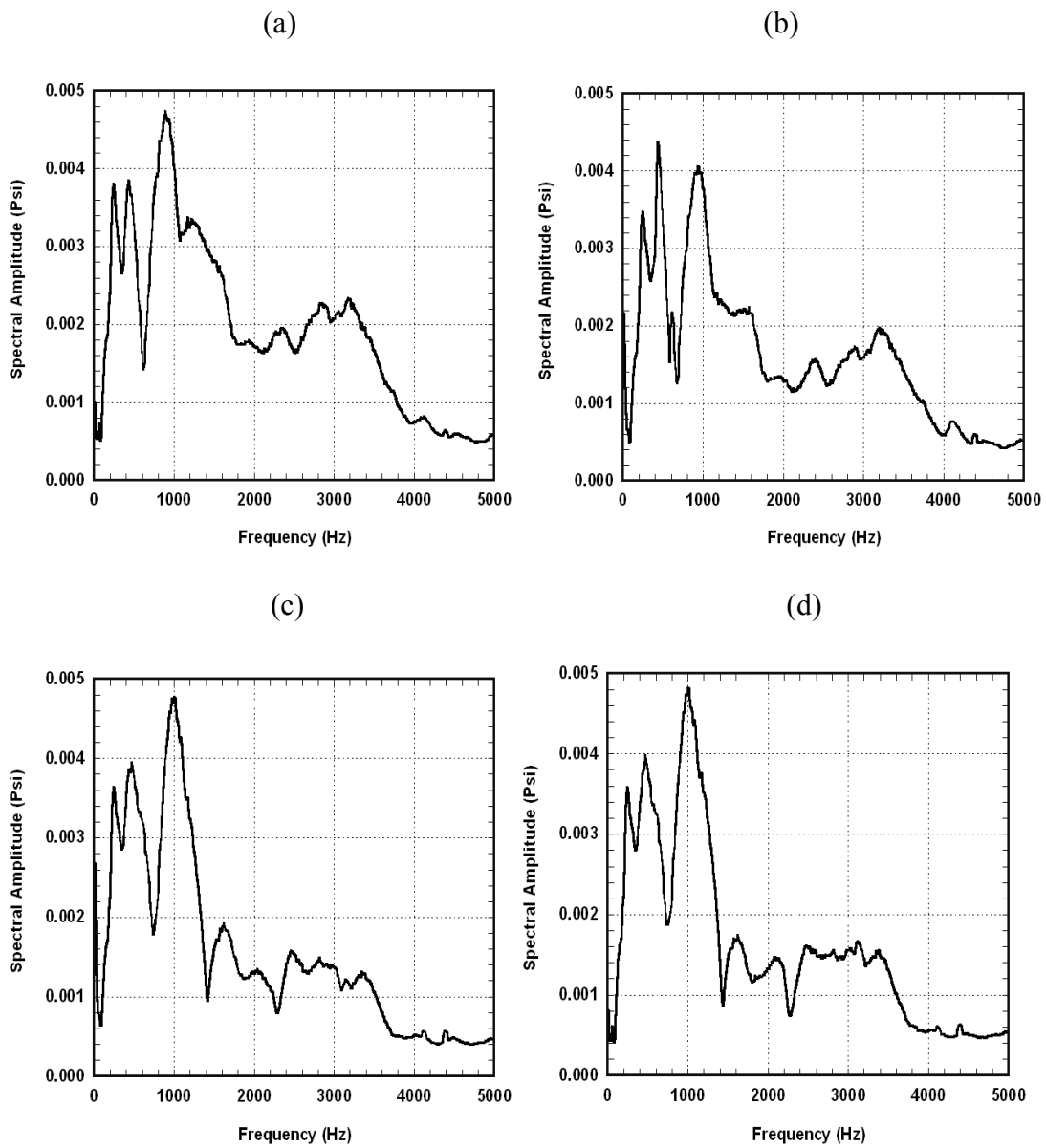
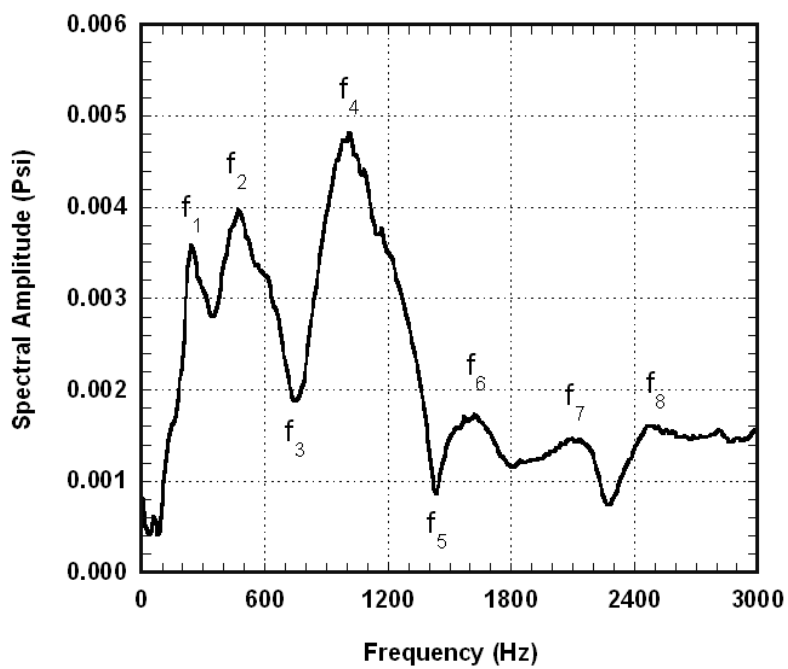


Figure 6.2. Pressure spectrum of isothermal case excited with white noise. He-18m/s-Air-6m/s-He-18m/s. (a) Tap #1 , (b) Tap #2, (c) Tap #3, (d) Tap#4.



Symbol	Frequency (Hz)
f_1	234
f_2	458
f_3	750
f_4	1016
f_5	1433
f_6	1608
f_7	2100
f_8	2466

Figure 6.3. Pressure spectrum of isothermal case excited with white noise redrawn from previous figure (Tap #4). He-18m/s-Air-6m/s-He-18m/s.

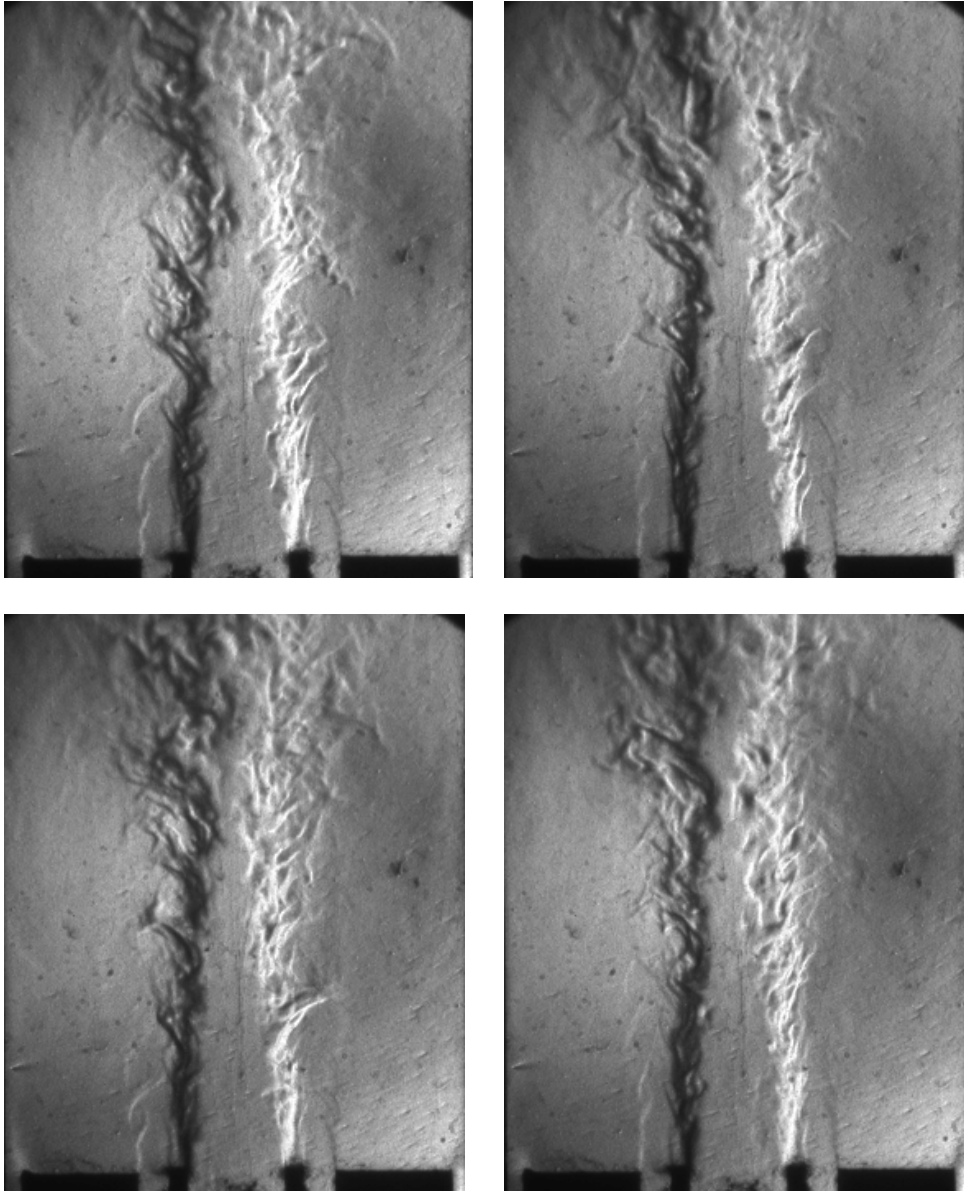


Figure 6.4(a). Baseline case, no forcing, exposure – $30\mu\text{s}$. He-18m/s-Air-6m/s-He-18m/s.

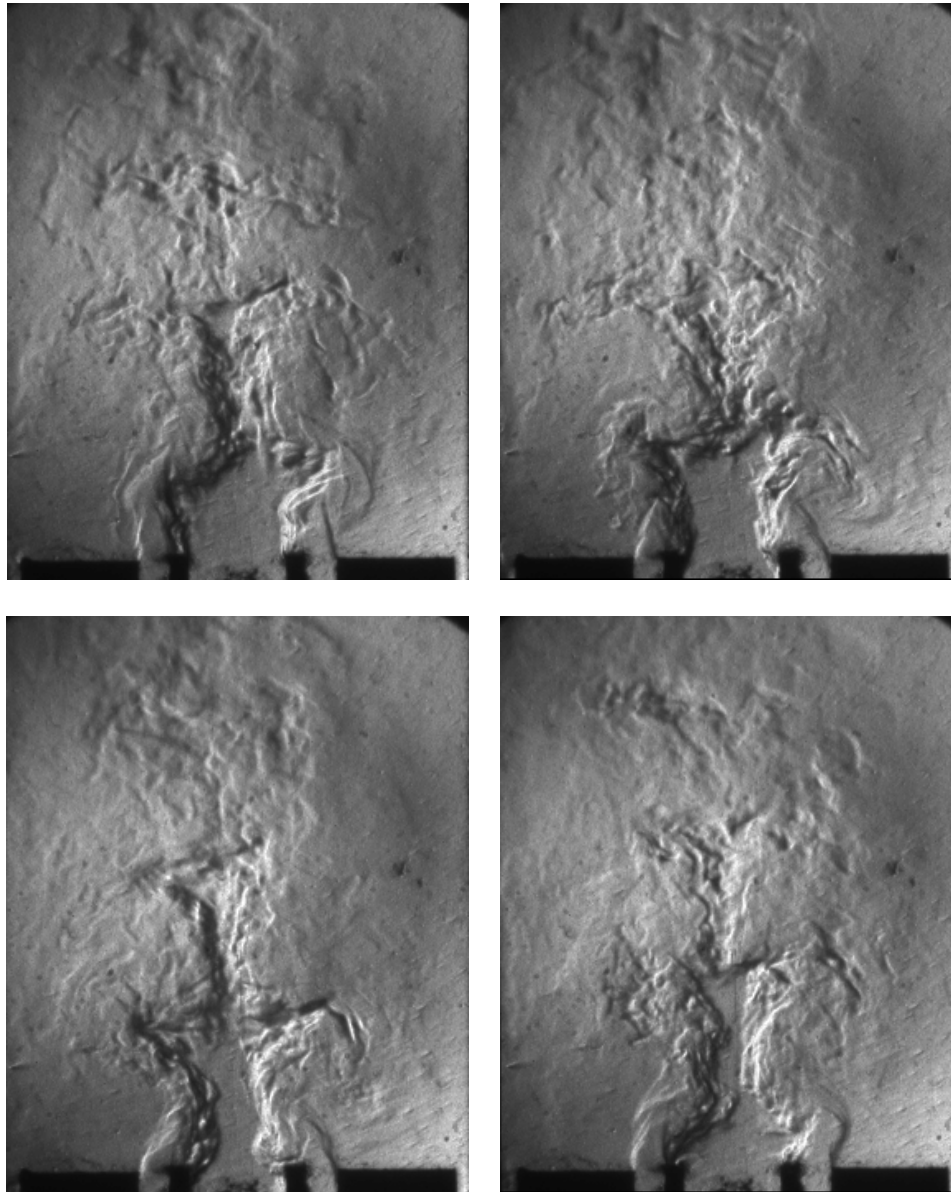


Figure 6.4(b). Flow response to forcing from left at 200 Hz, 40Vpp, exposure – 30 μ s, He-18m/s-Air-6m/s-He-18m/s.

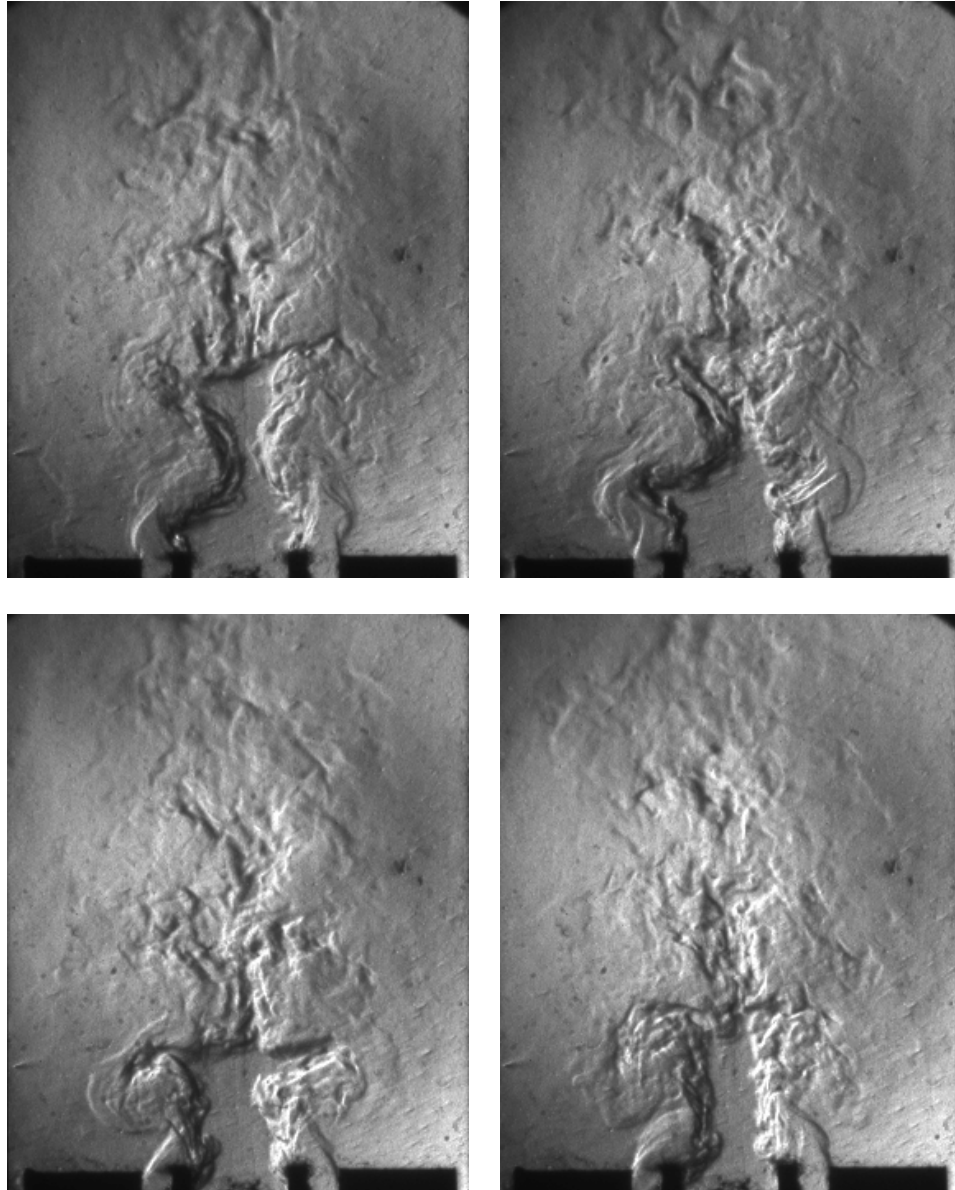


Figure 6.4(c). Flow response to forcing from left at 234.4 Hz, 40Vpp, exposure – 30 μ s, He-18m/s-Air-6m/s-He-18m/s.

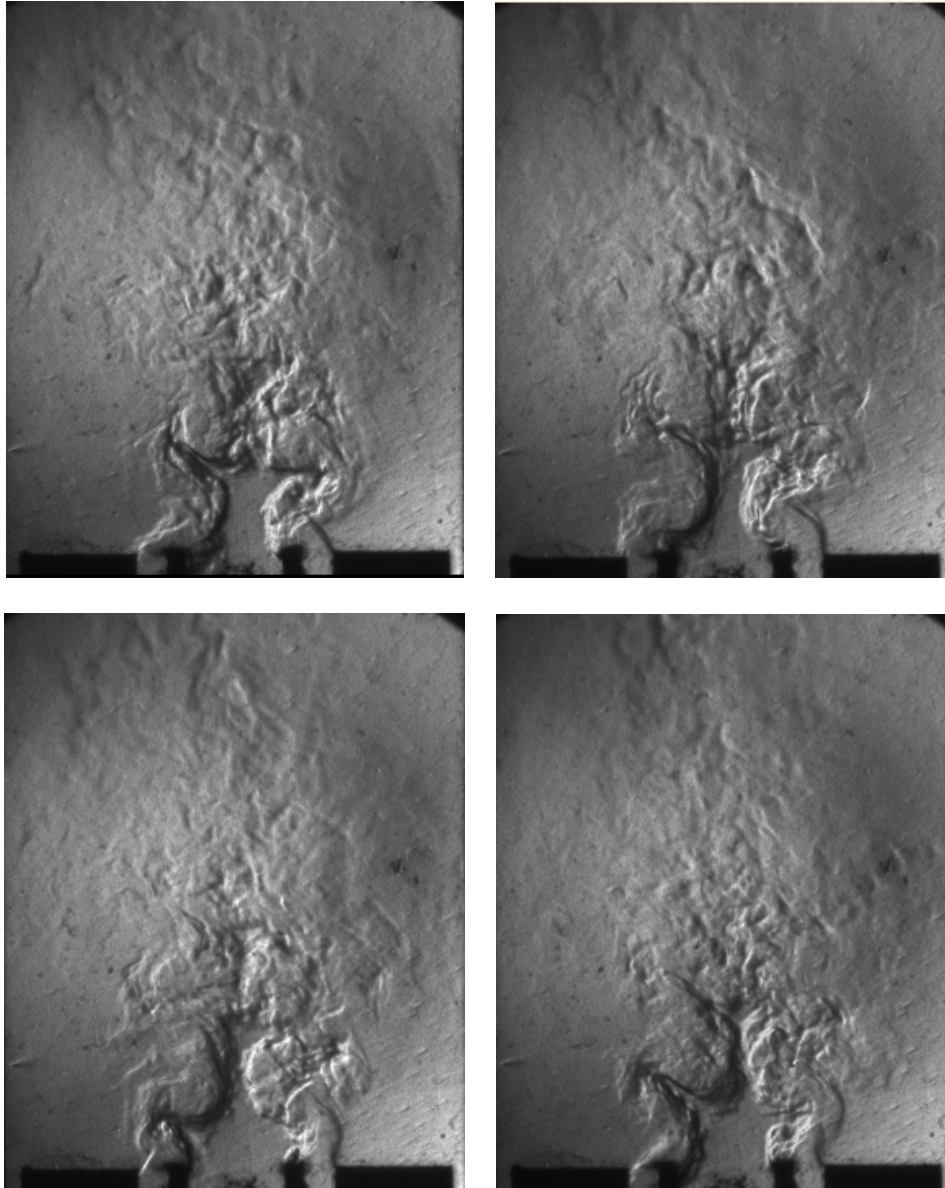


Figure 6.4(d). Flow response to forcing from left at 400.4 Hz, 40Vpp, exposure – 30 μ s, He-18m/s-Air-6m/s-He-18m/s.

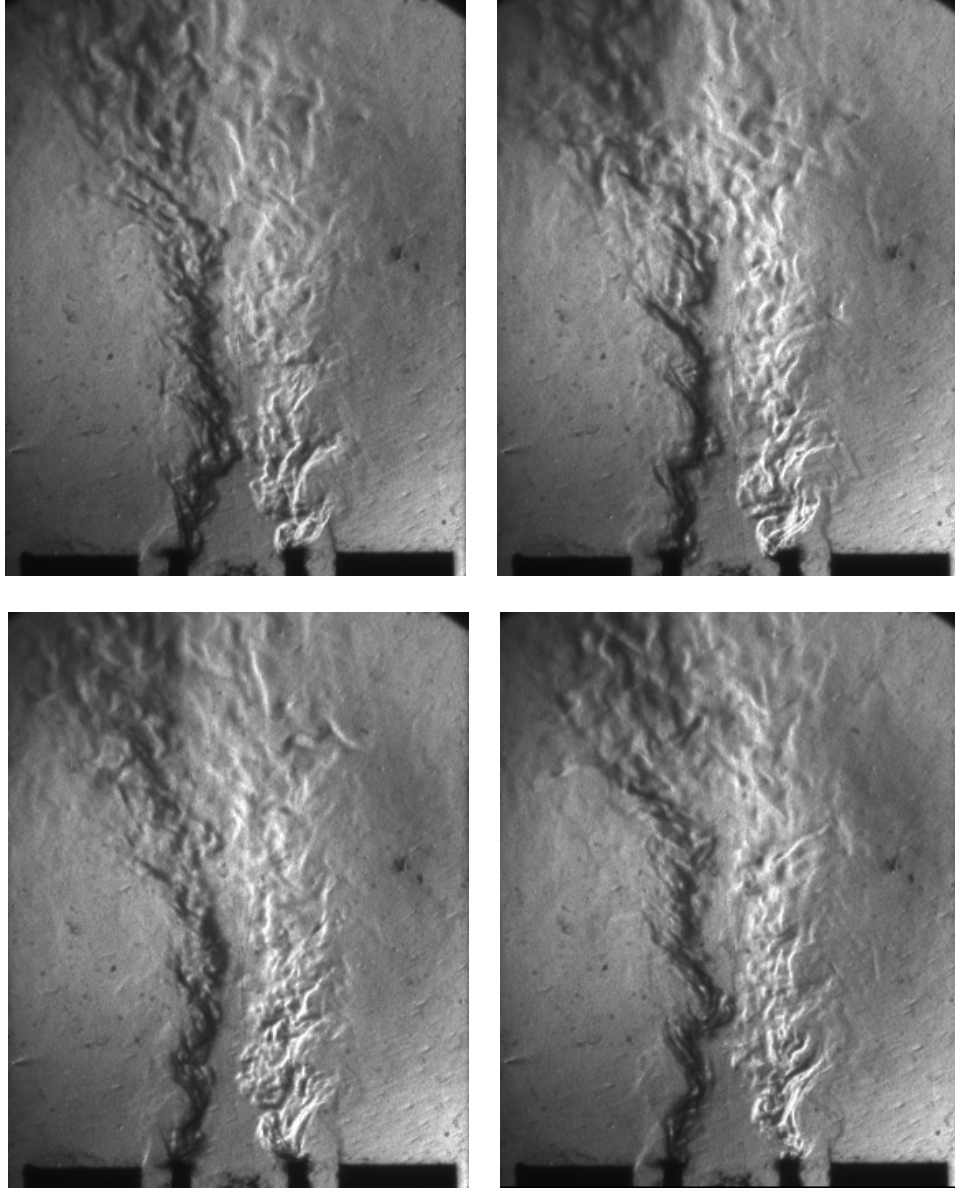


Figure 6.4(e). Flow response to forcing from left at 500 Hz, 40Vpp, exposure – 30 μ s, He-18m/s-Air-6m/s-He-18m/s.

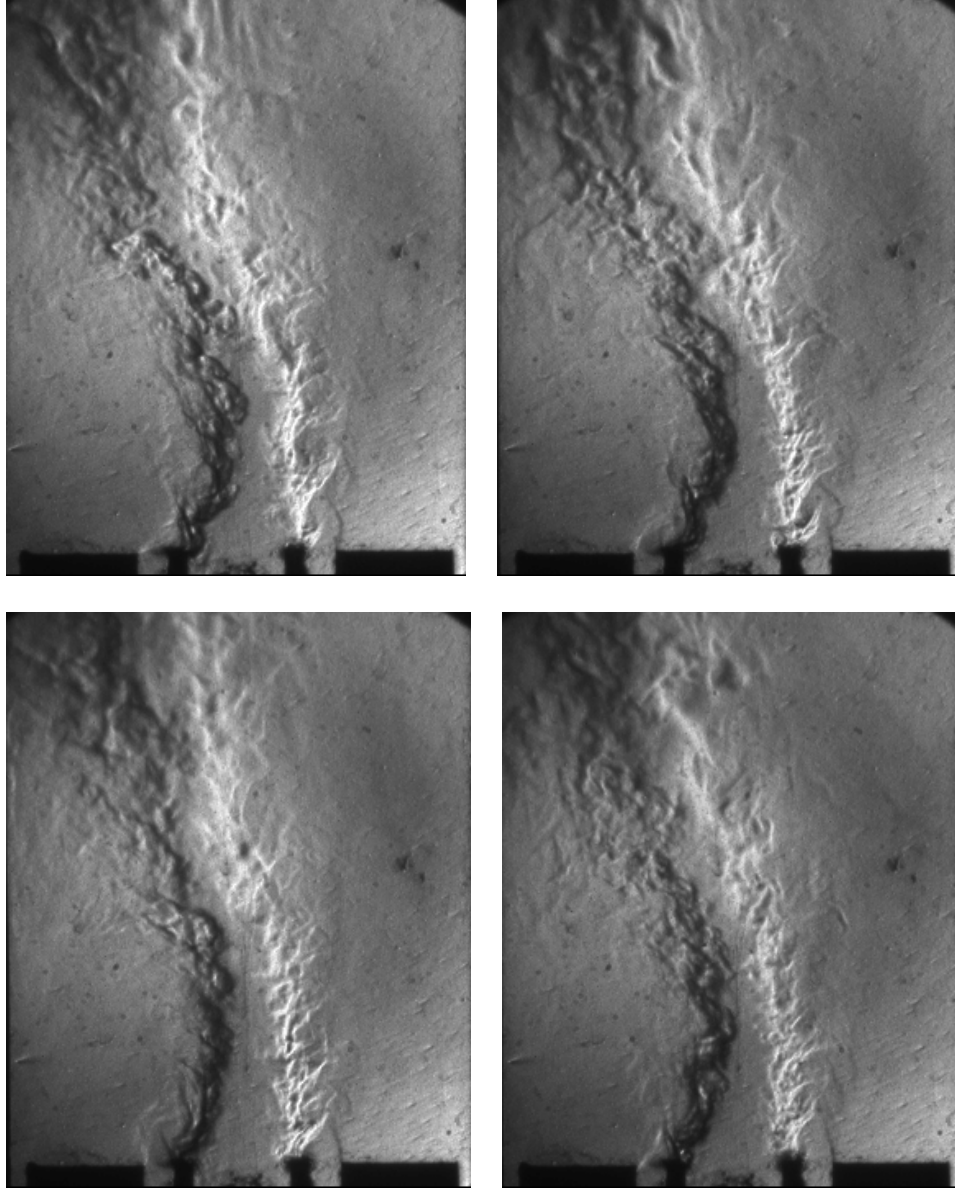


Figure 6.4(f). Flow response to forcing from left at 625 Hz, 40Vpp, exposure – 30 μ s, He-18m/s-Air-6m/s-He-18m/s.

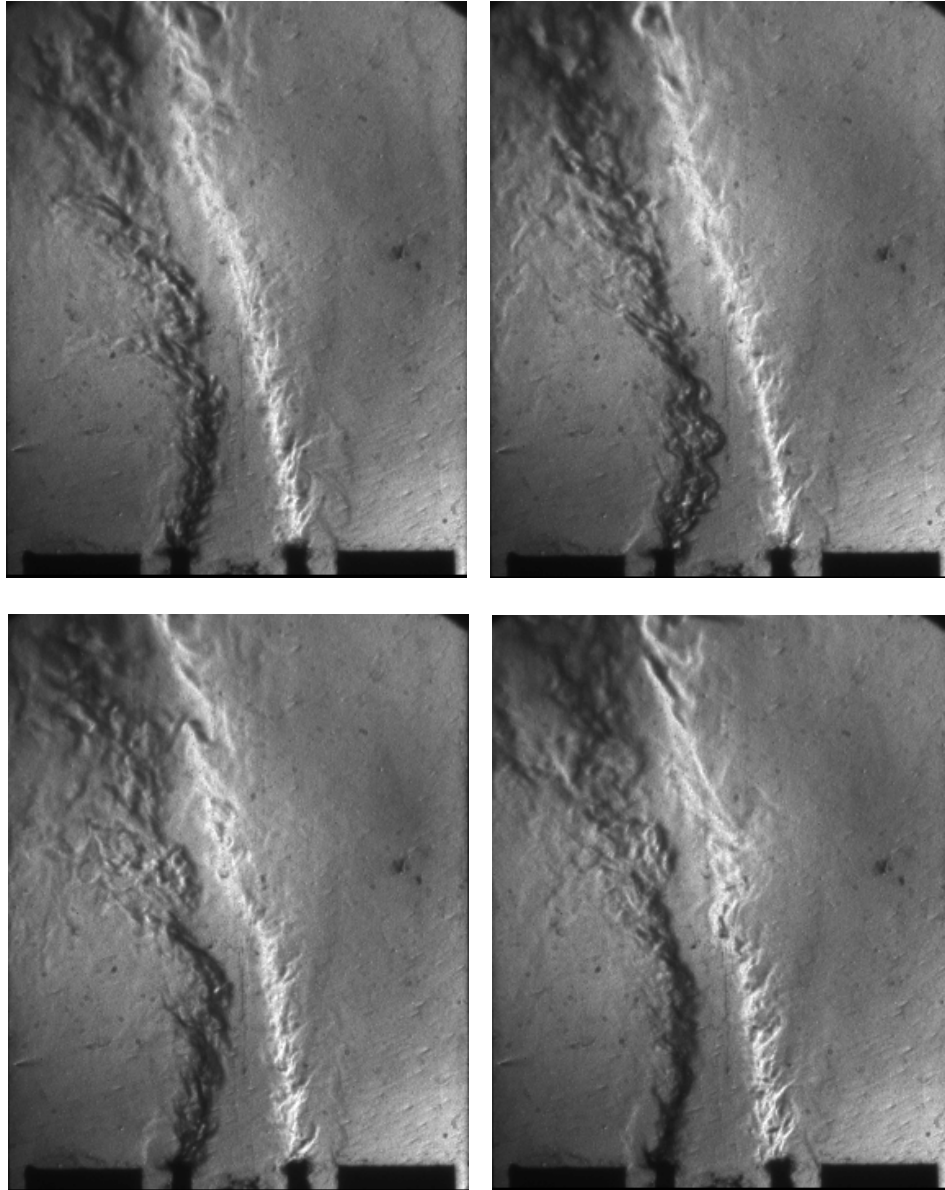


Figure 6.4(g). Flow response to forcing from left at 771.5 Hz, 40Vpp, exposure – 30 μ s, He-18m/s-Air-6m/s-He-18m/s.

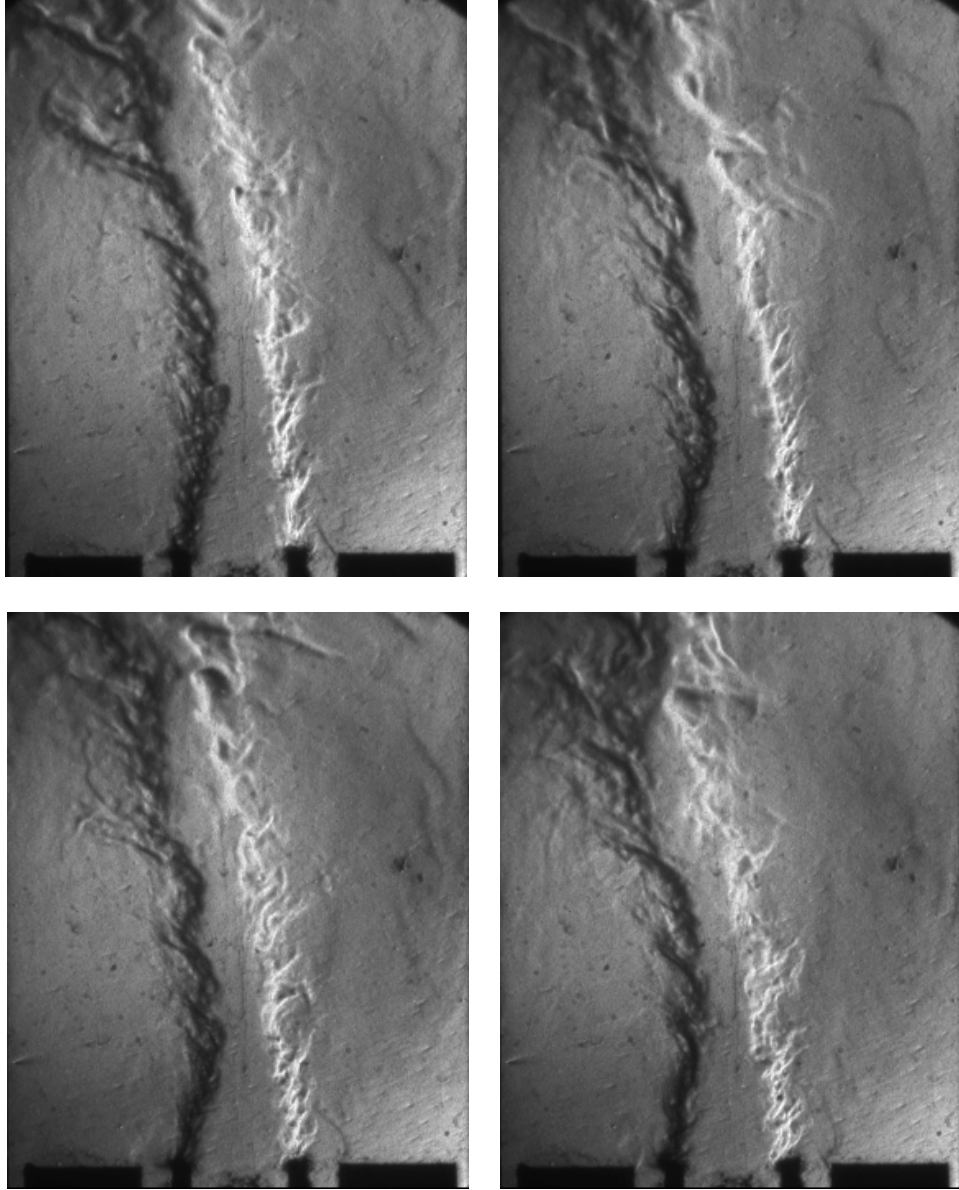


Figure 6.4(h). Flow response to forcing from left at 820.3 Hz, 40Vpp, exposure – 30 μ s, He-18m/s-Air-6m/s-He-18m/s.

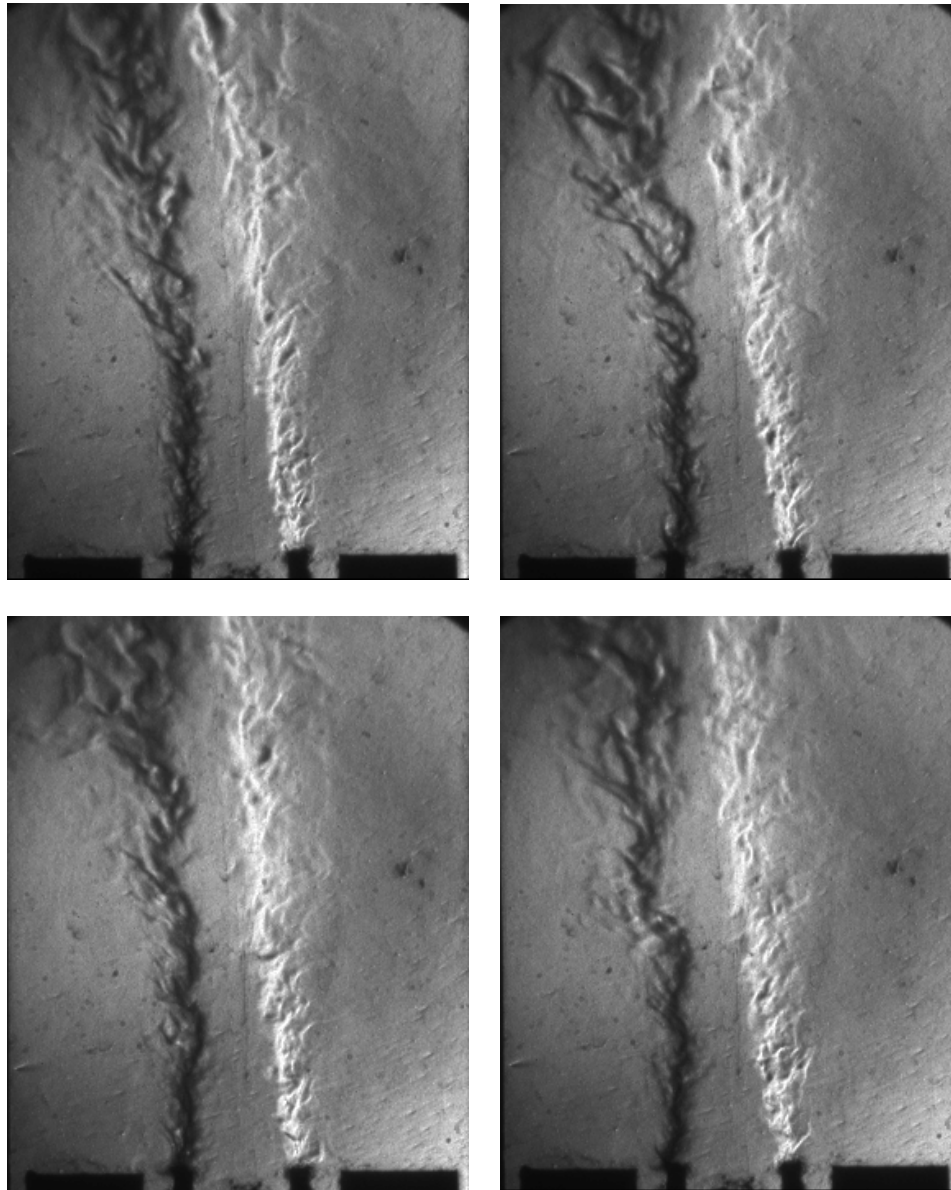


Figure 6.4(i). Flow response to forcing from left at 947.3 Hz, 40Vpp, exposure – 30 μ s, He-18m/s-Air-6m/s-He-18m/s.

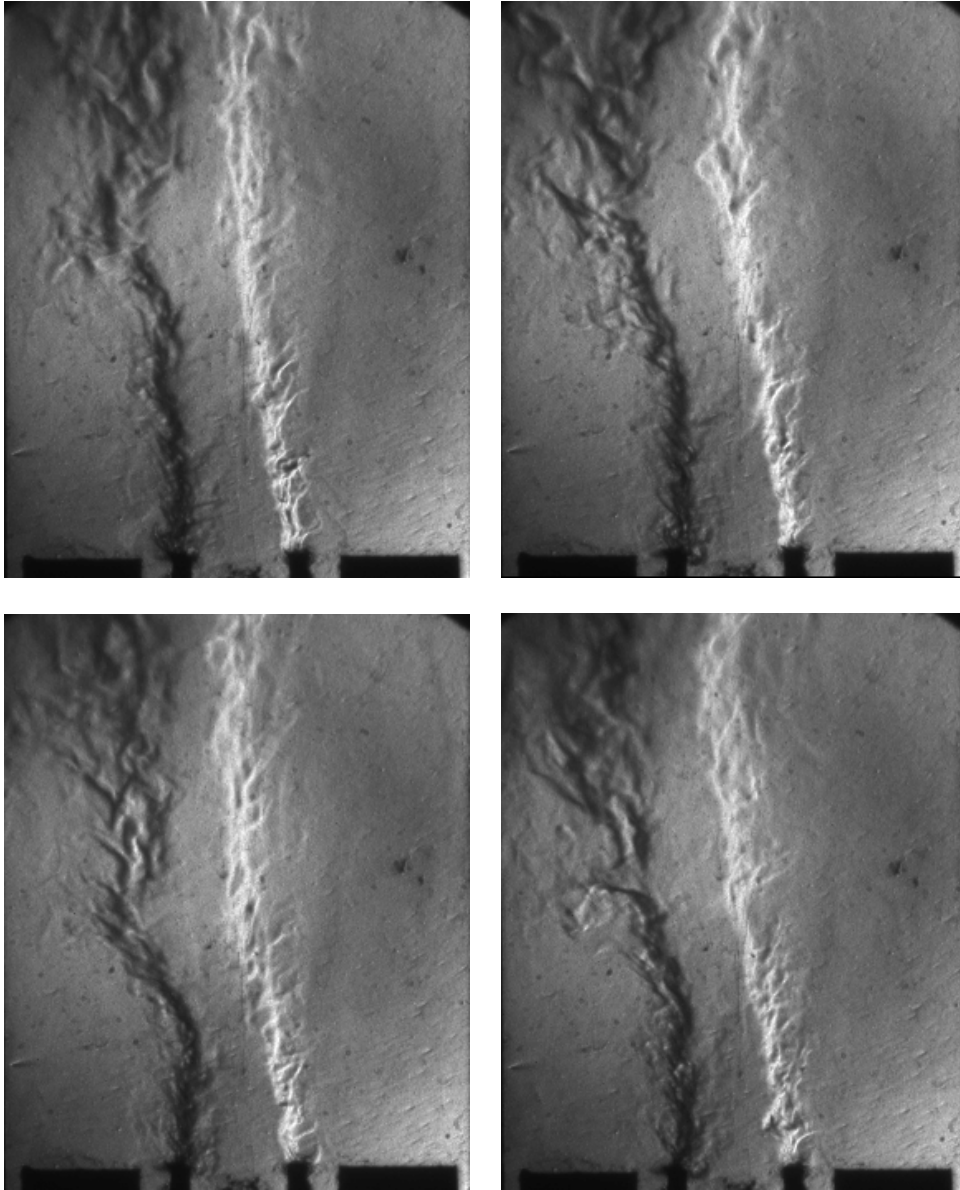


Figure 6.4(j). Flow response to forcing from left at 1016 Hz, 40Vpp, exposure – 30 μ s, He-18m/s-Air-6m/s-He-18m/s.

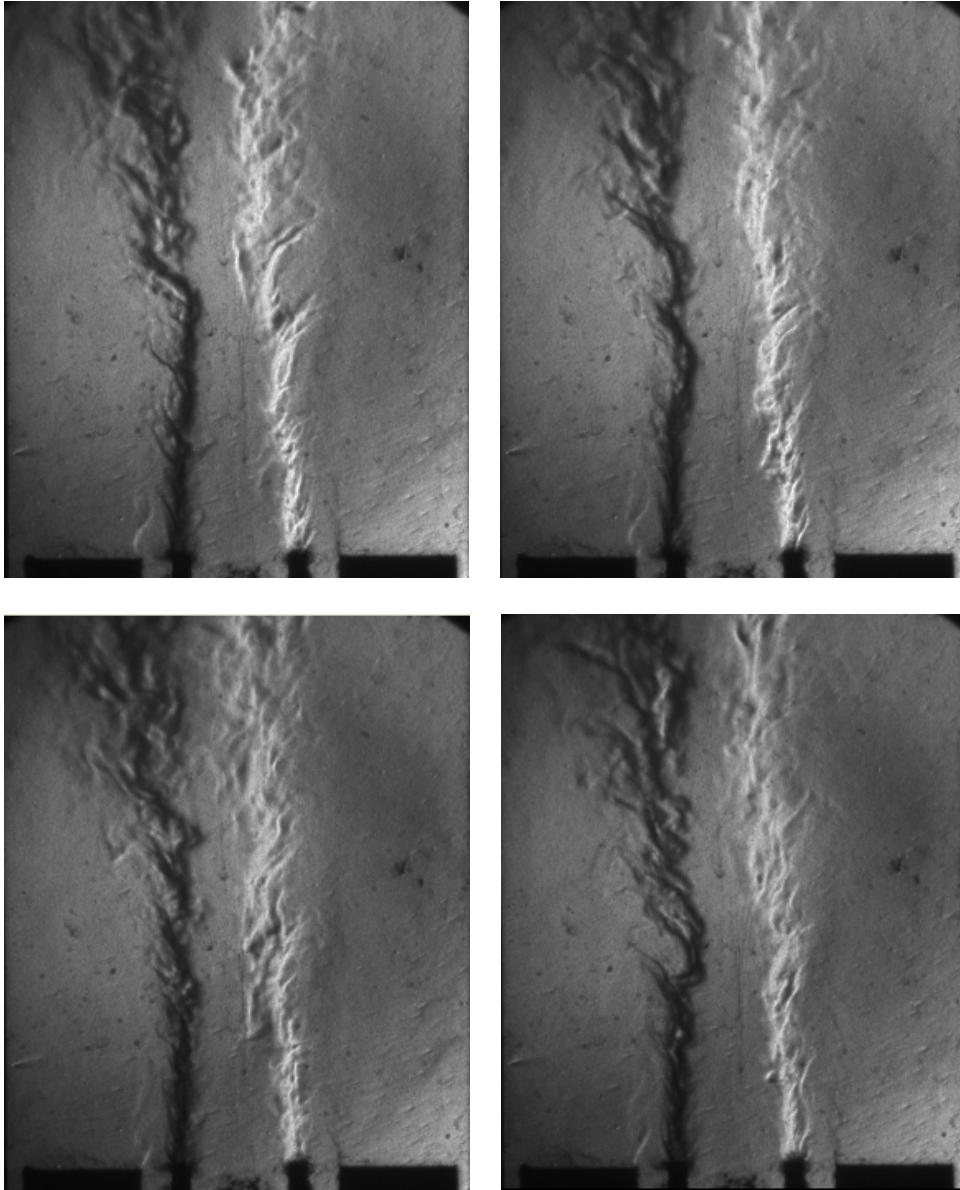


Figure 6.4(k). Flow response to forcing from left at 1094 Hz, 40Vpp, exposure – 30 μ s, He-18m/s-Air-6m/s-He-18m/s.

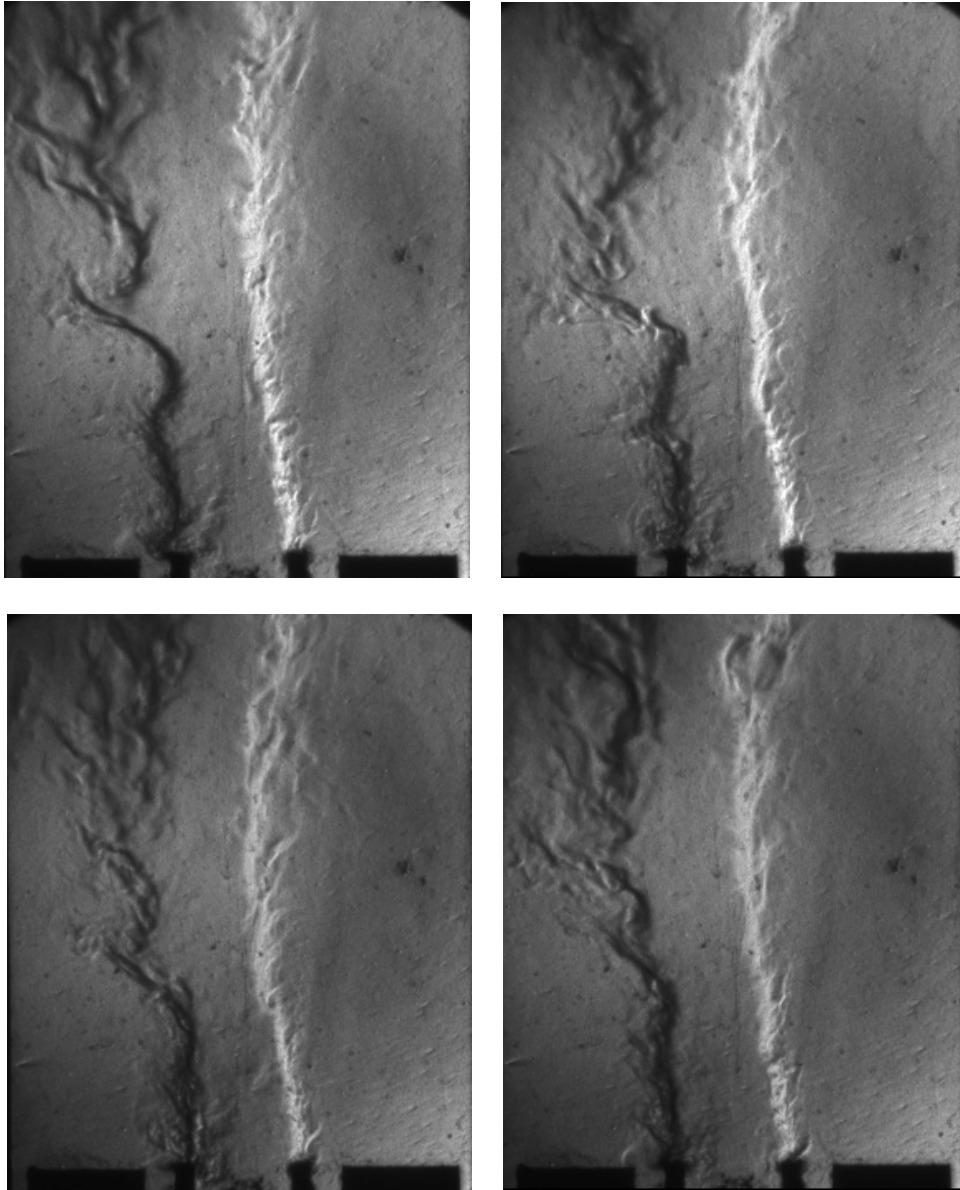


Figure 6.4(1). Flow response to forcing from left at 1094 Hz, 50 Vpp exposure – 30 μ s, He-18m/s-Air-6m/s-He-18m/s.

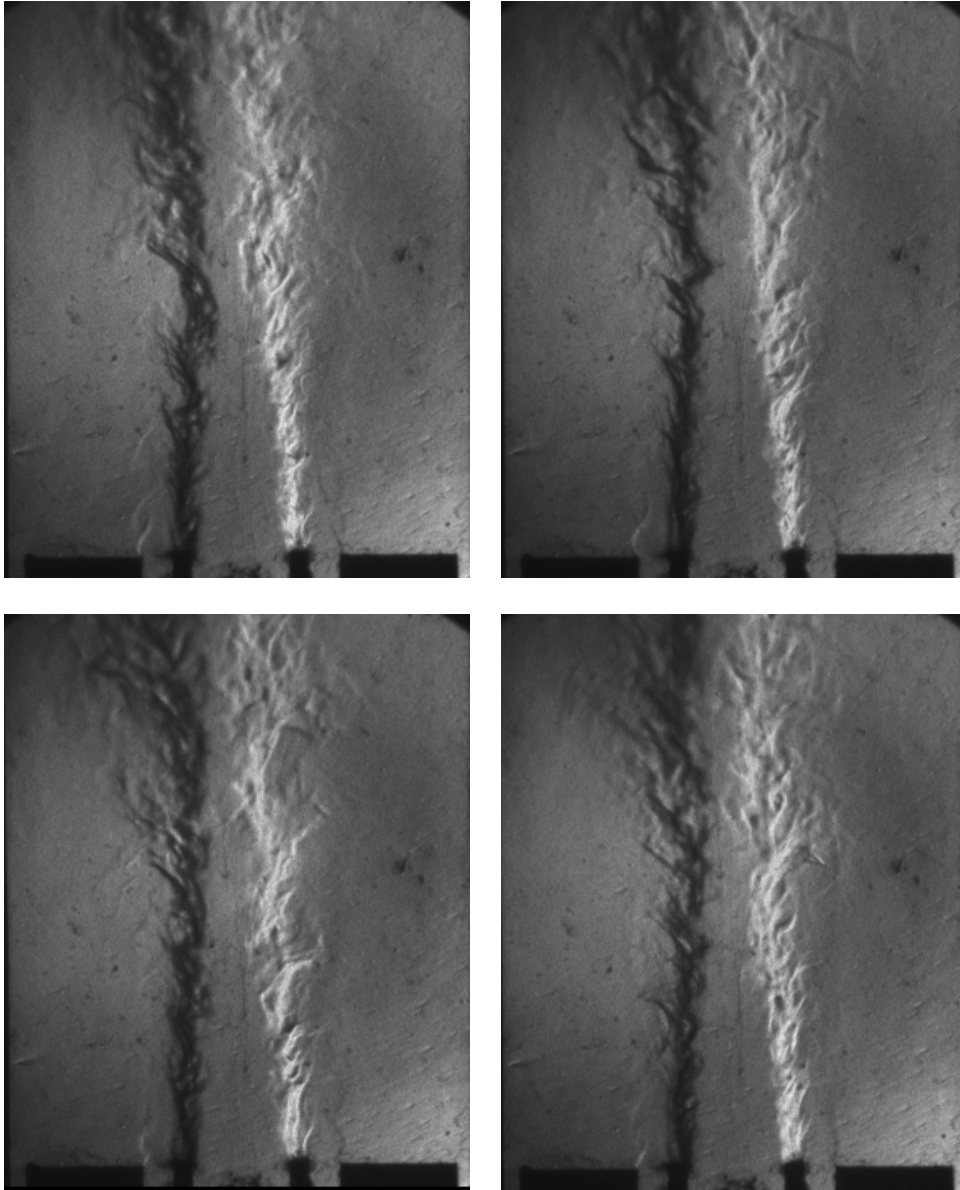


Figure 6.4(m). Flow response to forcing from left at 1250 Hz, 50Vpp, exposure – 10 μ s, He-18m/s-Air-6m/s-He-18m/s.

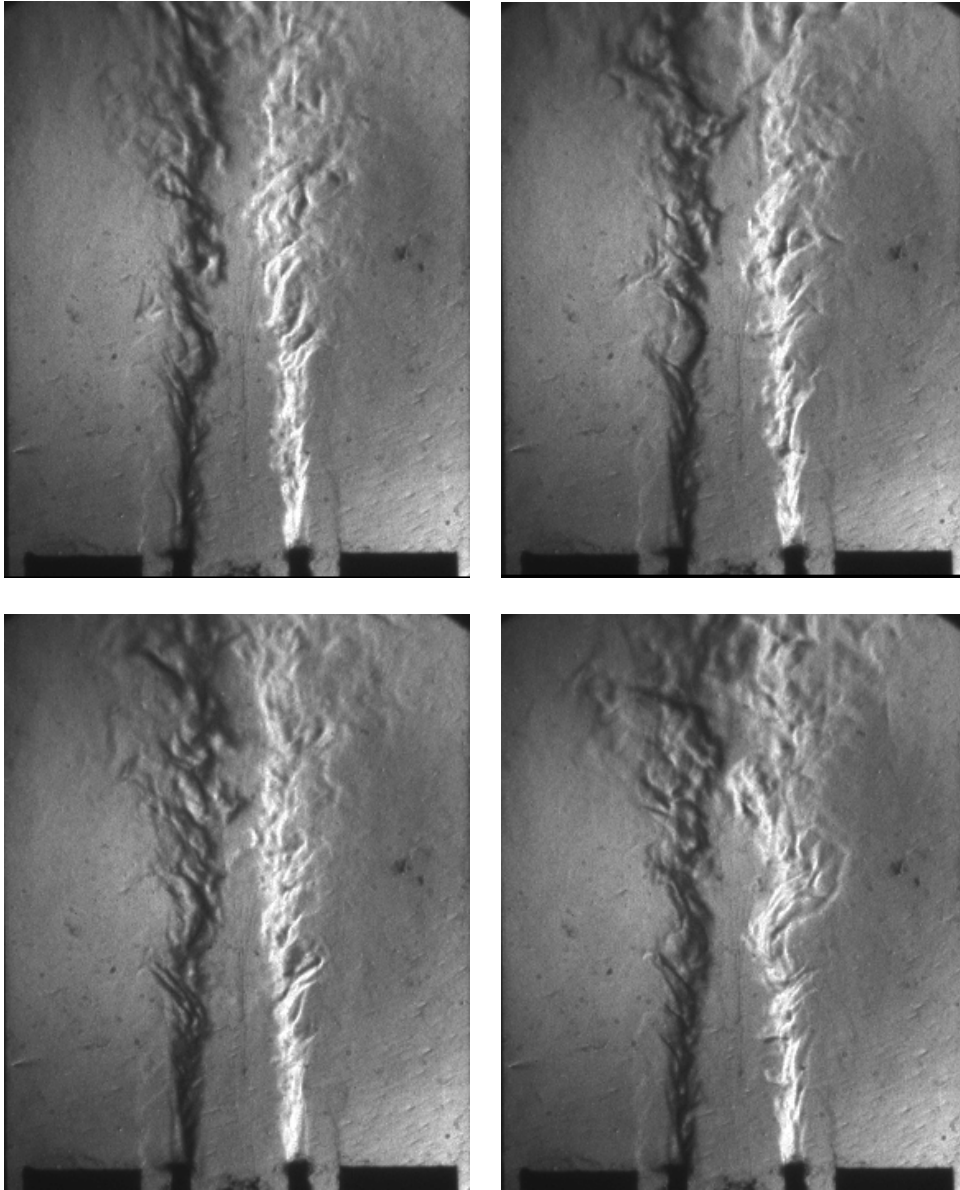


Figure 6.4(n). Flow response to forcing from left at 1850 Hz, 50Vpp, exposure – 10 μ s, He-18m/s-Air-6m/s-He-18m/s.

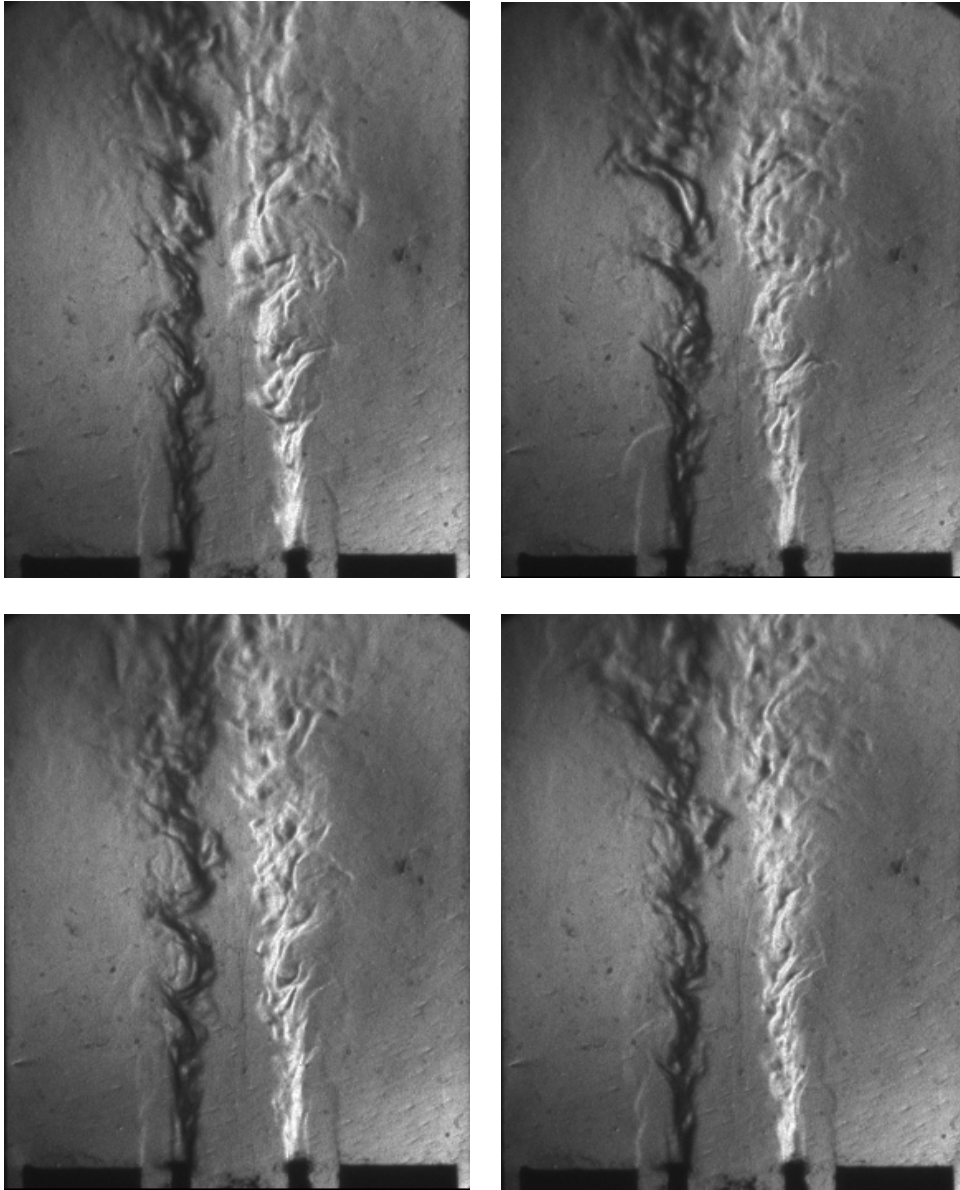


Figure 6.4(o). Flow response to forcing from left at 2676 Hz, 50Vpp, exposure – 10 μ s, He-18m/s-Air-6m/s-He-18m/s.

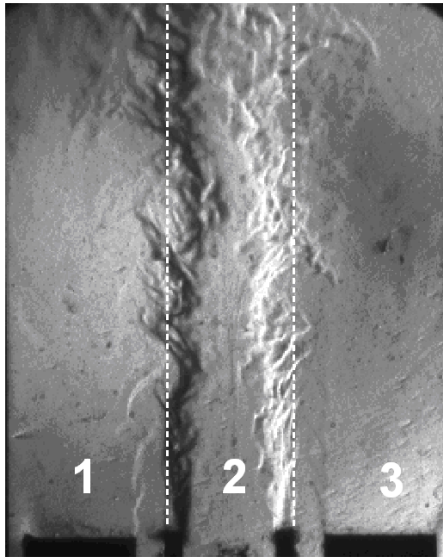
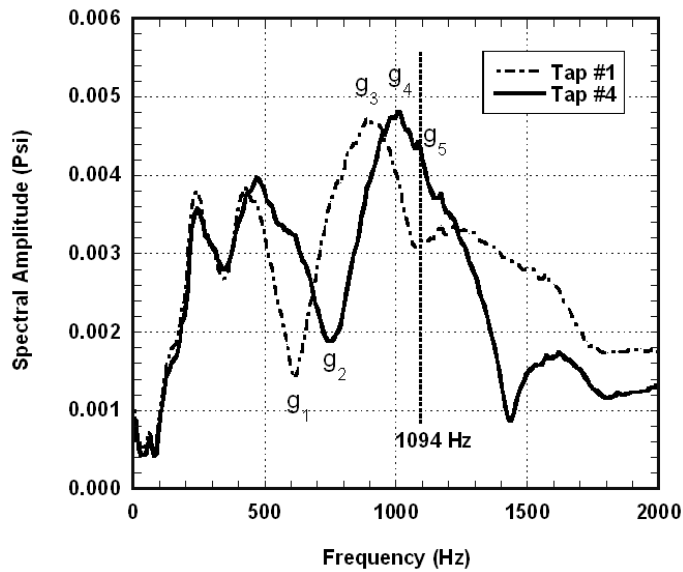


Figure 6.5. Acoustic regions of the combustor. Tap #1 measures acoustic signature in Region 1 while Tap #4 measures acoustic signature in Region 3.



Symbol	Frequency (Hz)
g_1	611
g_2	750
g_3	889
g_4	1016
g_5	1094

Figure 6.6. Comparison of pressure spectrum between Tap #1 and Tap #4 of isothermal case excited with white noise. He-18m/s-Air-6m/s-He-18m/s.

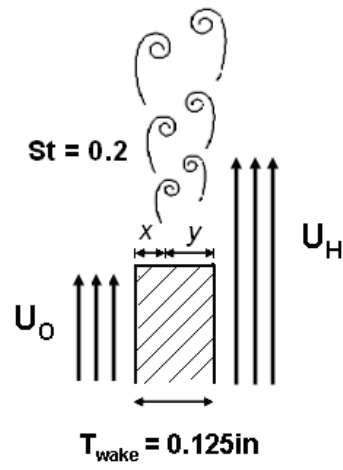


Figure 6.7. Schematic for wake mode instability calculation.

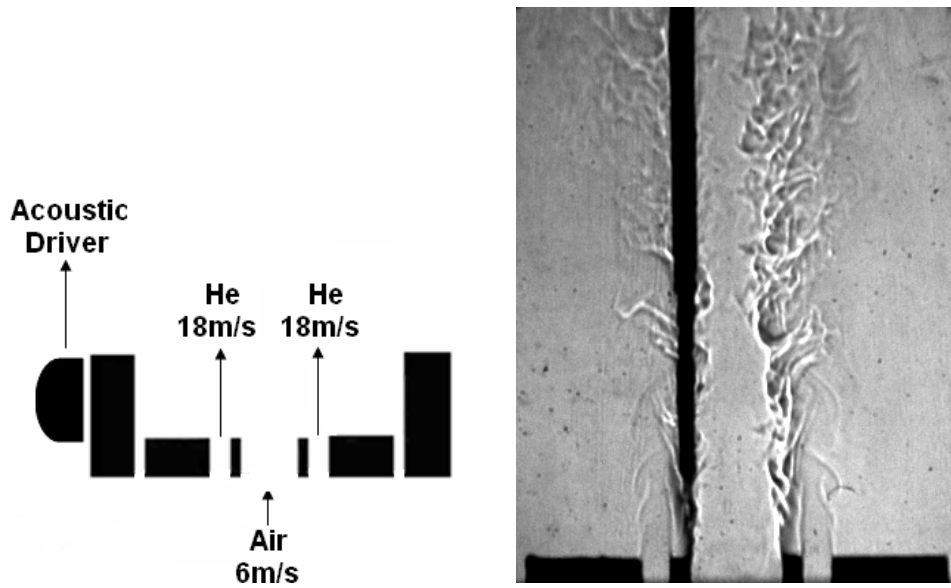


Figure 6.8 (a) Injection arrangement (b) Hotwire probe location

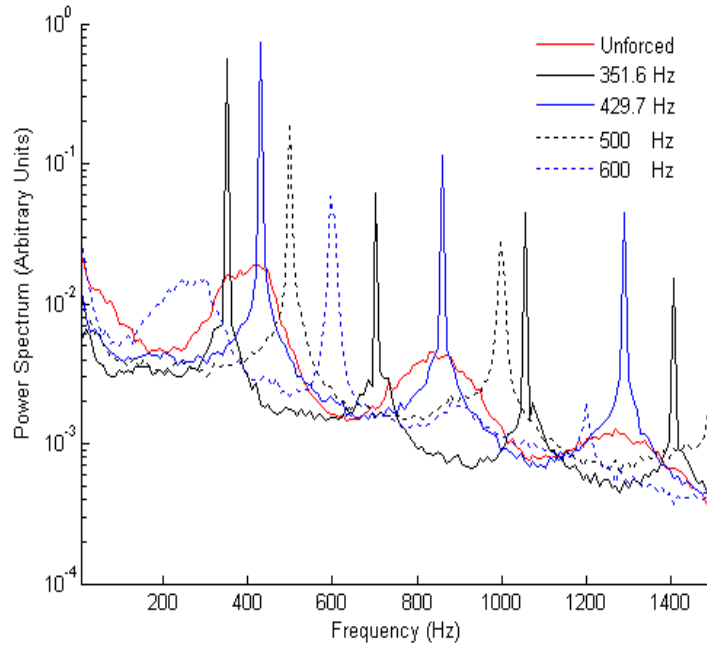


Figure 6.9. Frequency response of velocity in unforced and forced cases (monotone excitation).

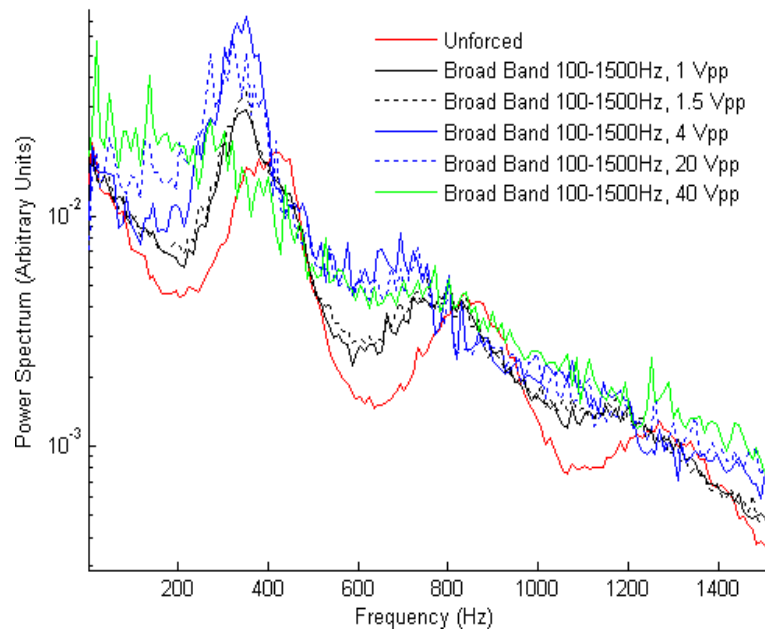


Figure 6.10. Frequency response of velocity in unforced and forced cases (broadband excitation).

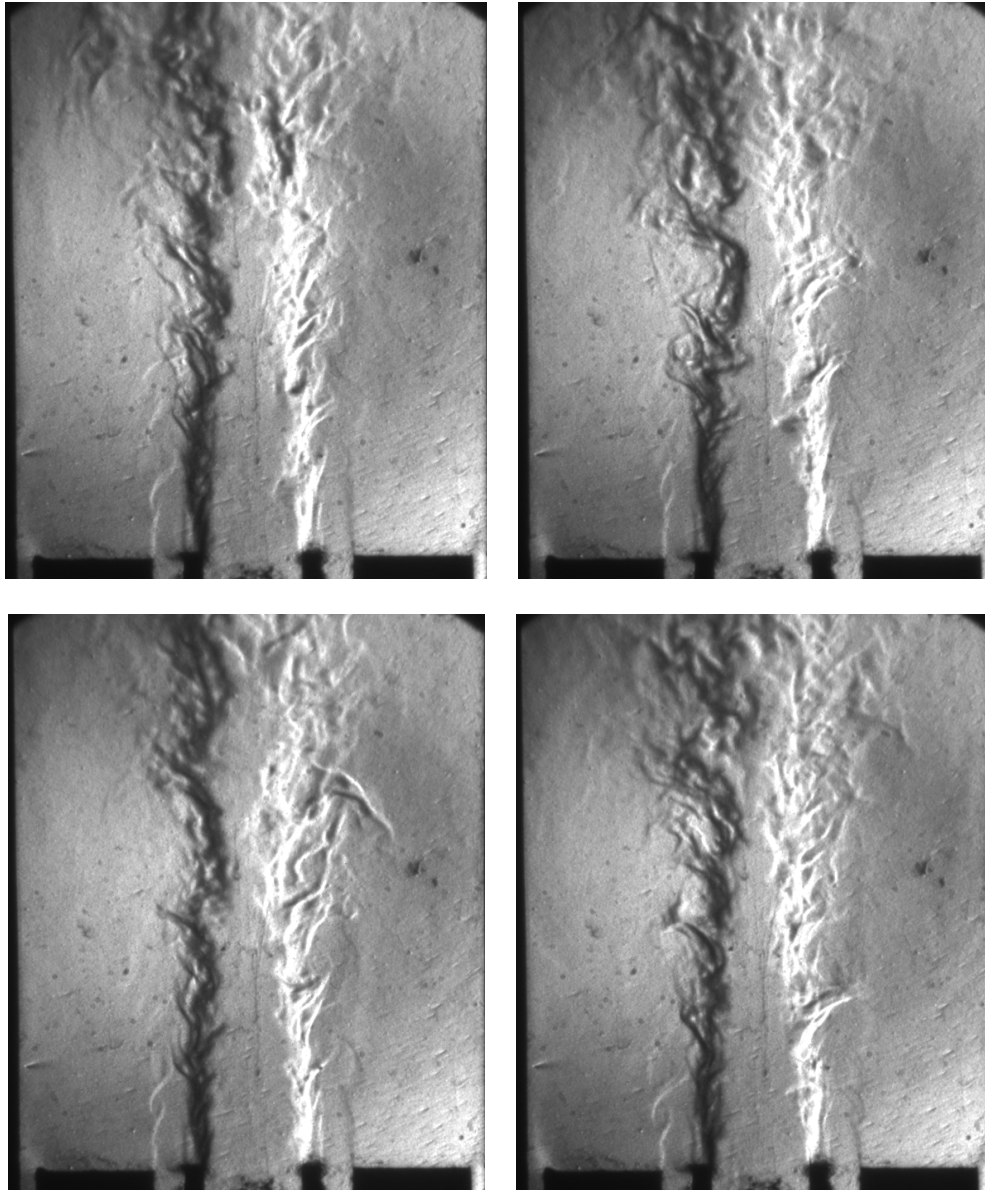


Figure 6.11(a). Baseline, no forcing, exposure – $30\mu\text{s}$, He-18m/s-Air-6m/s-He-18m/s.

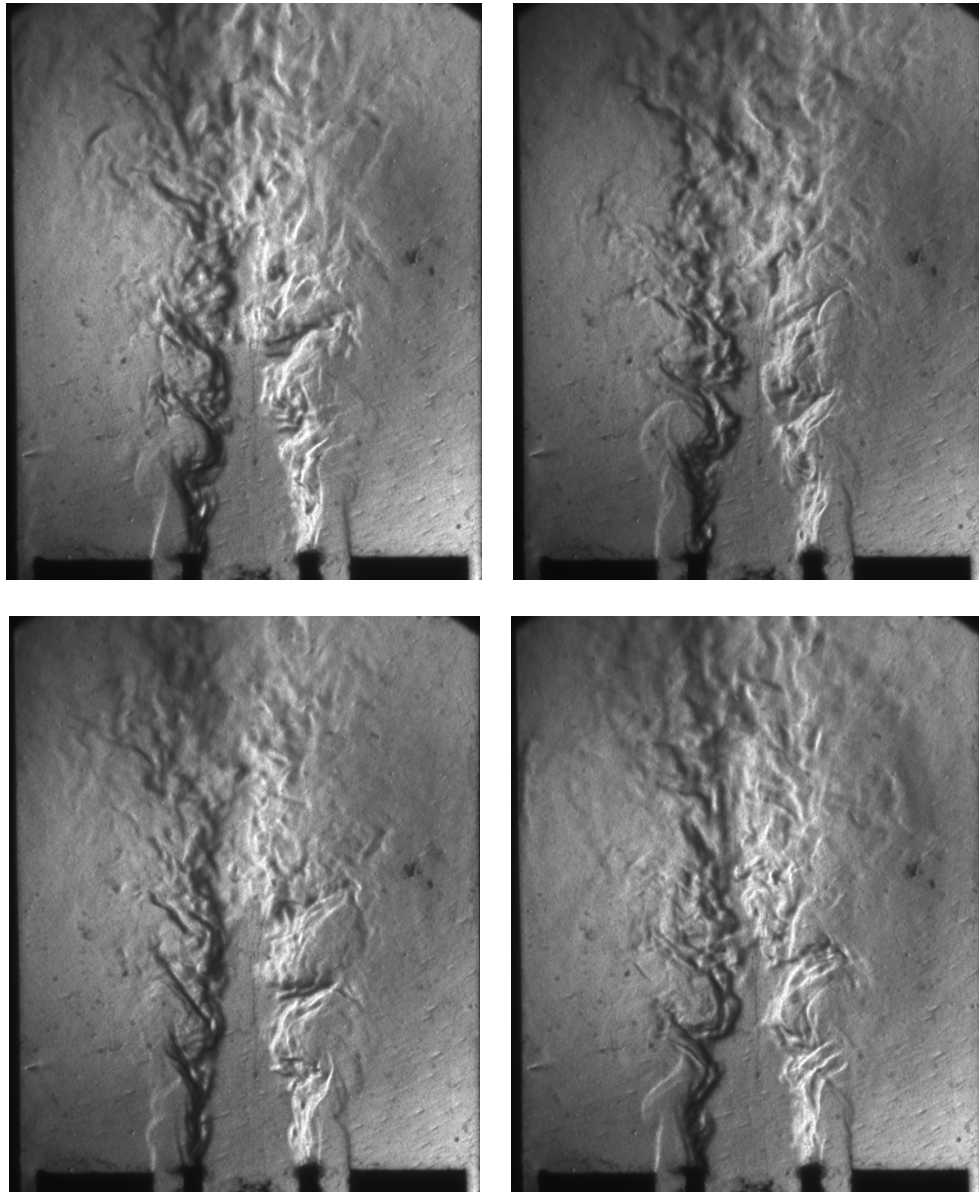


Figure 6.11(b). Flow response to forcing from left at 429.7 Hz, 4 Vpp.
Exposure – 30 μ s, He-18m/s-Air-6m/s-He-18m/s.

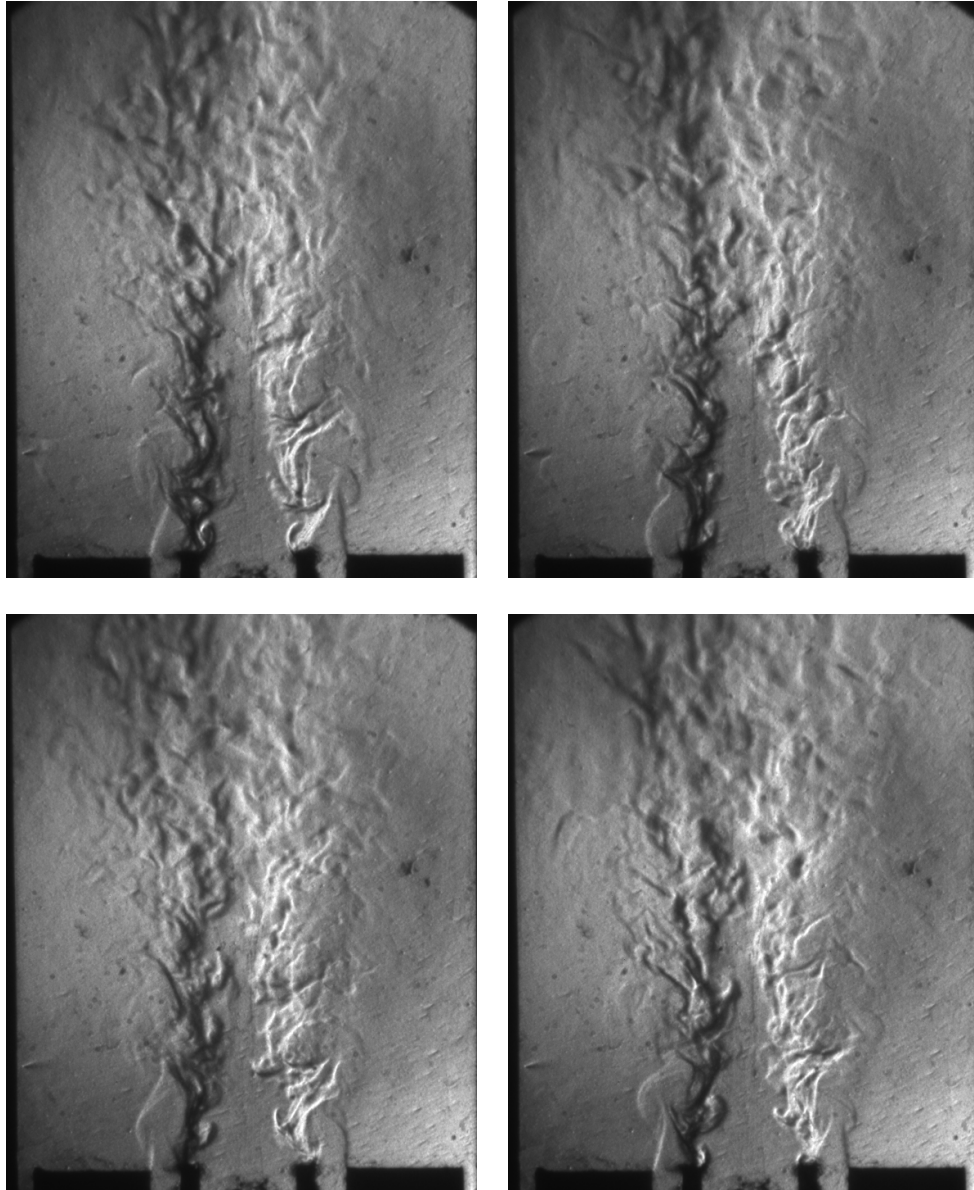


Figure 6.11(c). Flow response to forcing from left at 429.7 Hz, 12 Vpp.
Exposure – 30 μ s, He-18m/s-Air-6m/s-He-18m/s.

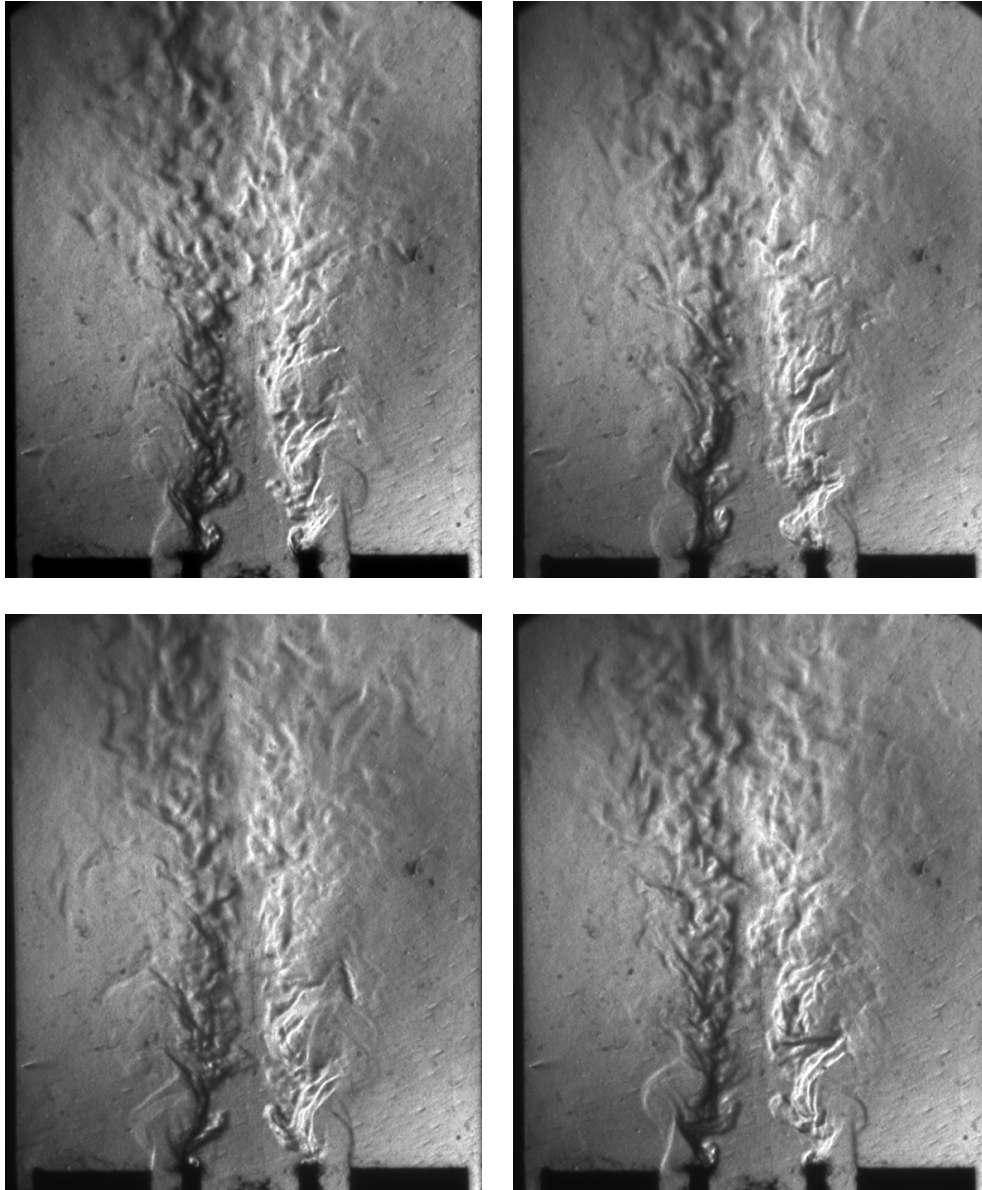


Figure 6.11(d). Flow response to forcing from left at 429.7 Hz, 16 Vpp.
Exposure – 30 μ s, He-18m/s-Air-6m/s-He-18m/s.

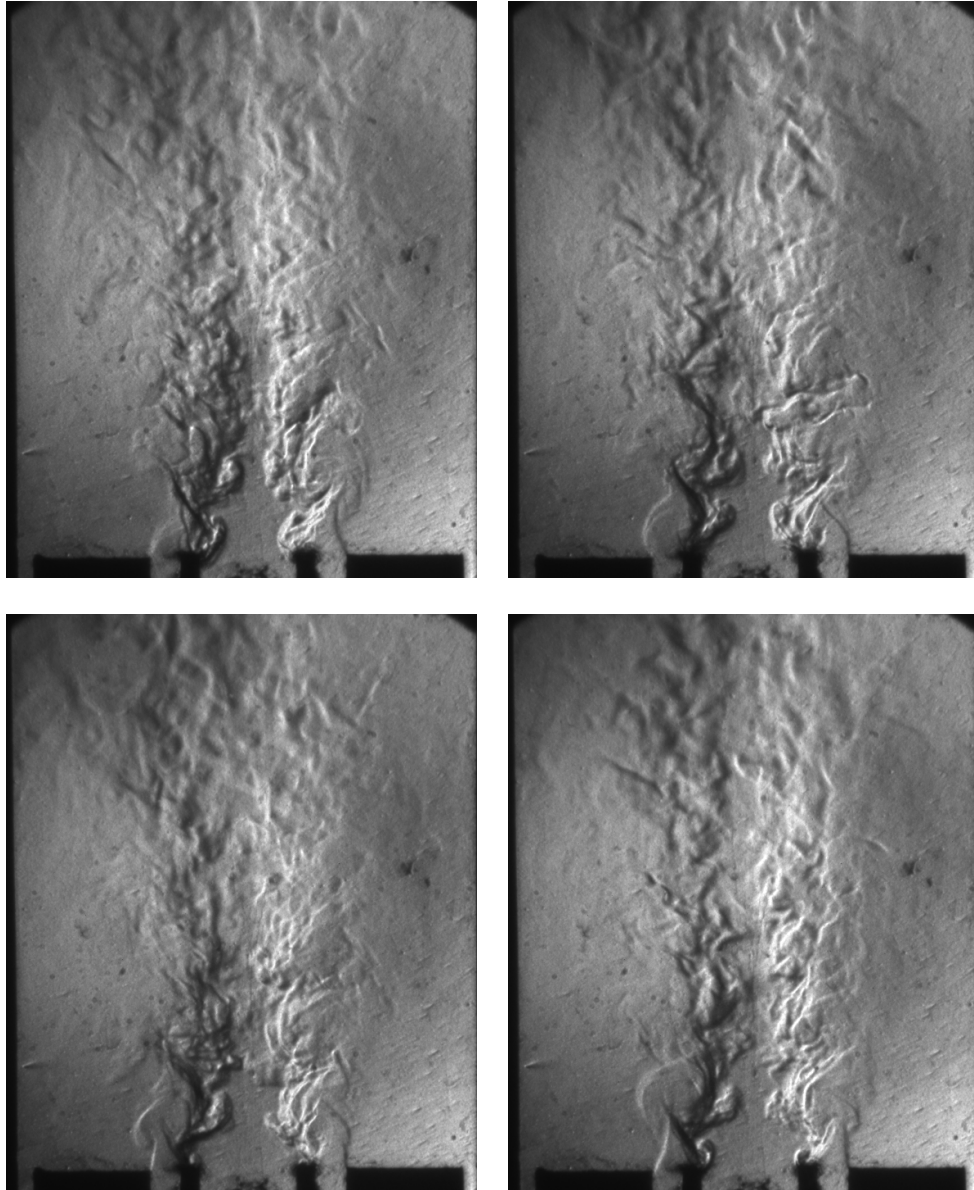


Figure 6.11(e). Flow response to forcing from left at 429.7 Hz, 20 Vpp.
Exposure – 30 μ s, He-18m/s-Air-6m/s-He-18m/s.

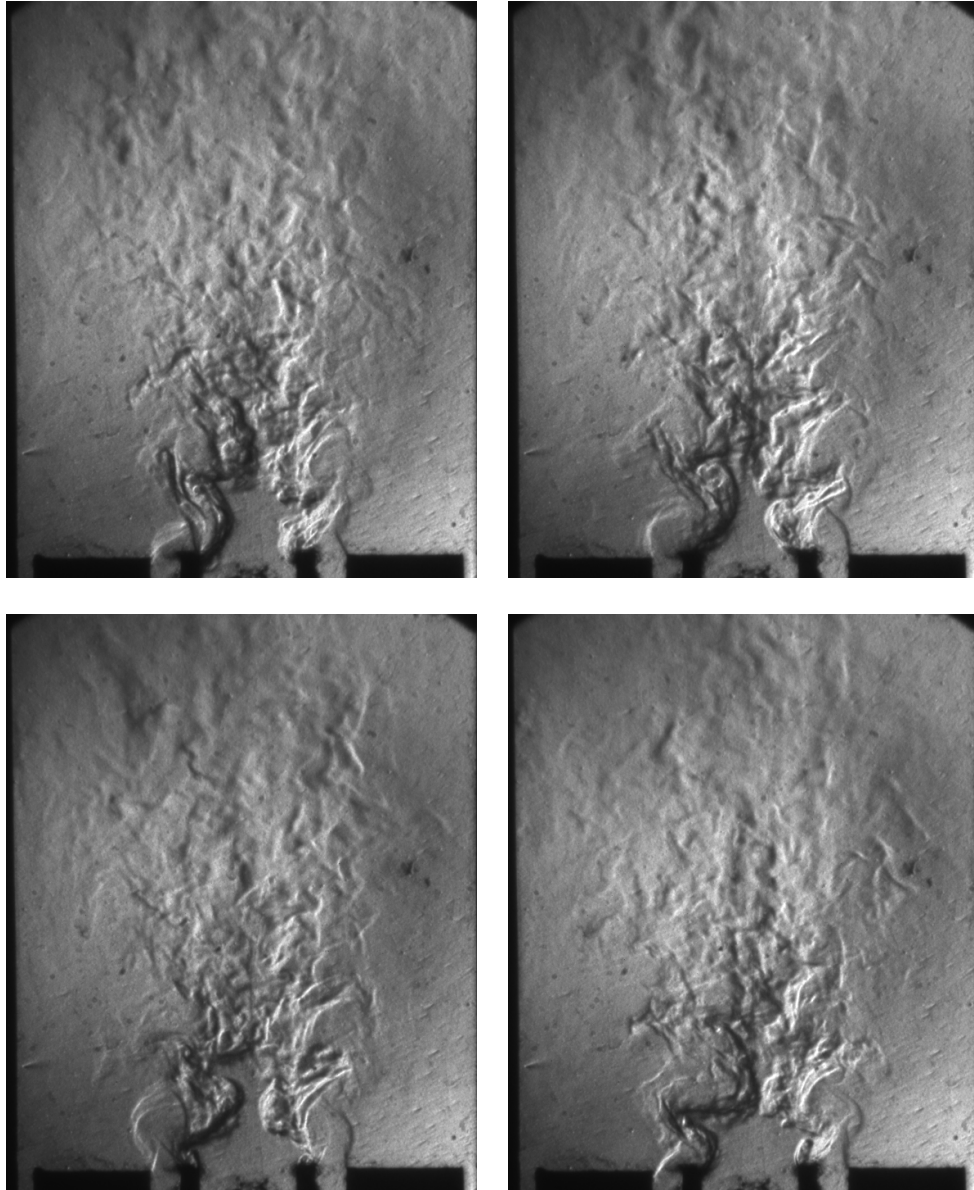


Figure 6.11(f). Flow response to forcing from left at 429.7 Hz, 30 Vpp.
Exposure – 30 μ s, He-18m/s-Air-6m/s-He-18m/s.

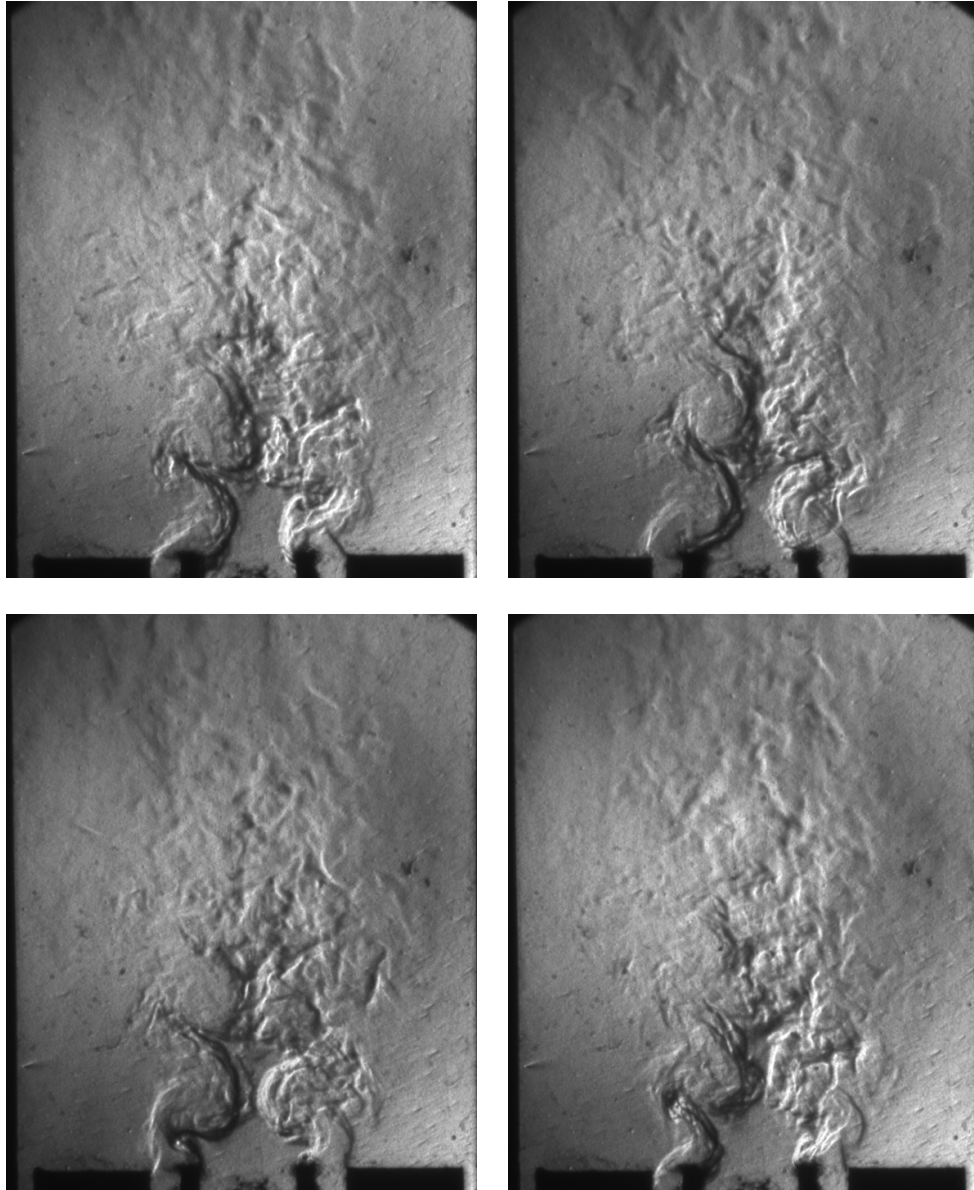


Figure 6.11(g). Flow response to forcing from left at 429.7 Hz, 40 Vpp.
Exposure – 30 μ s, He-18m/s-Air-6m/s-He-18m/s.

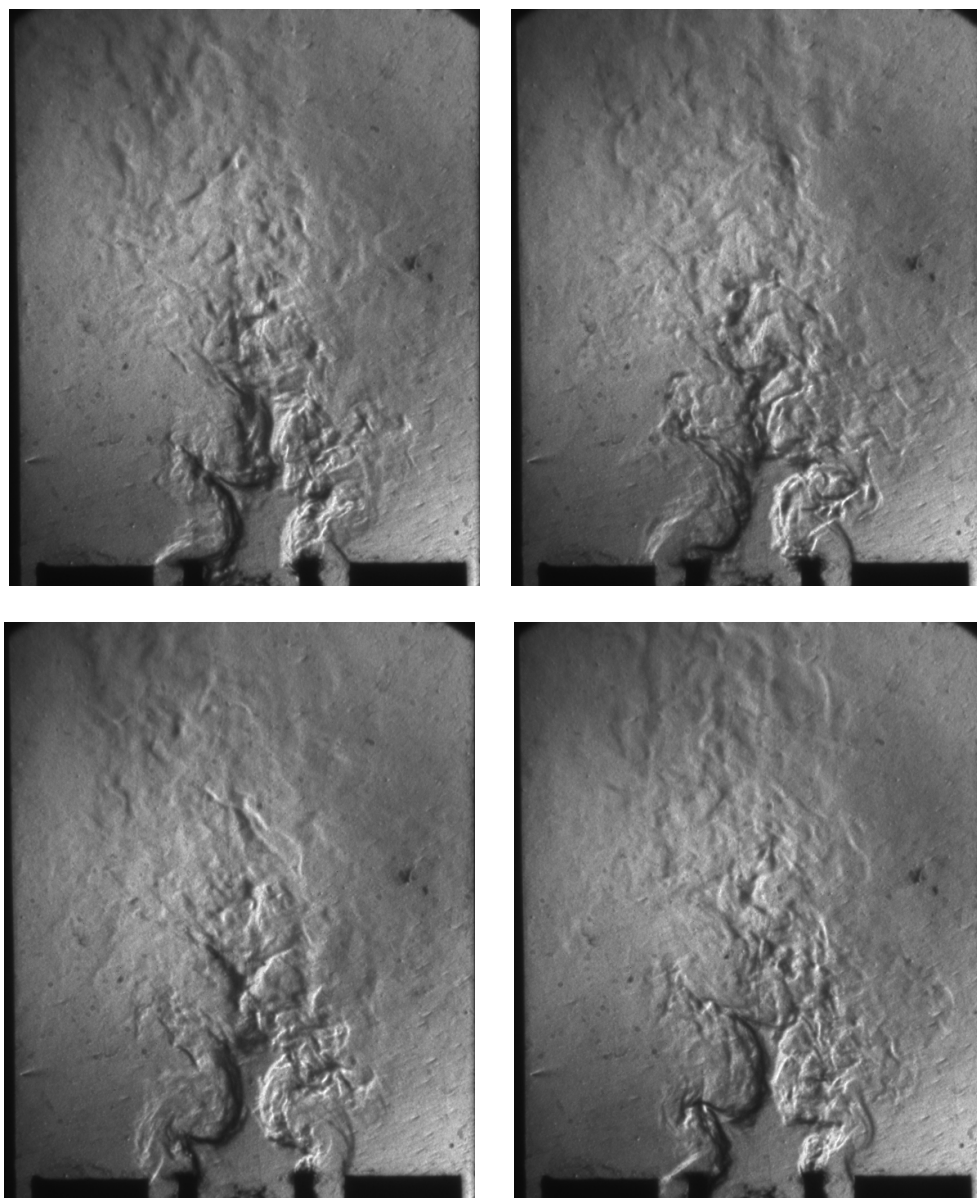


Figure 6.11(h). Flow response to forcing from left at 429.7 Hz, 50 Vpp.
Exposure – 30 μ s, He-18m/s-Air-6m/s-He-18m/s.

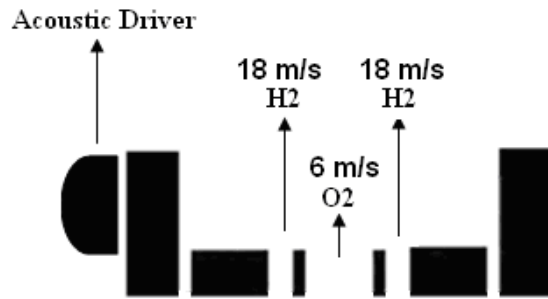


Figure 7.1. Flow arrangement for the GH₂ / GO₂ / GH₂ turbulent diffusion flame system. $V_{O_2} = 6$ m/s, $V_{H_2} = 18$ m/s, $Re_{O_2} = 4900$. Acoustic forcing is from the left.

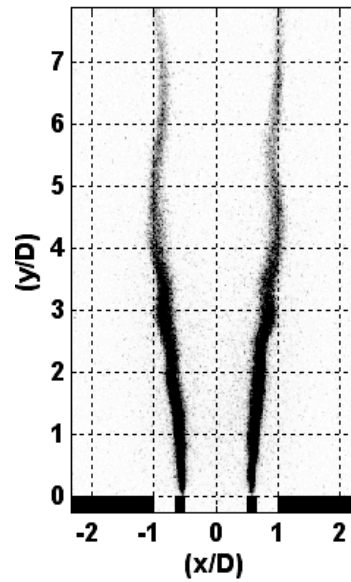


Figure 7.2. OH* chemiluminescence showing natural instabilities in an unforced GH₂ / GO₂ / GH₂ turbulent flame. $V_{O_2} = 6$ m/s, $V_{H_2} = 18$ m/s, $Re_{O_2} = 4900$.

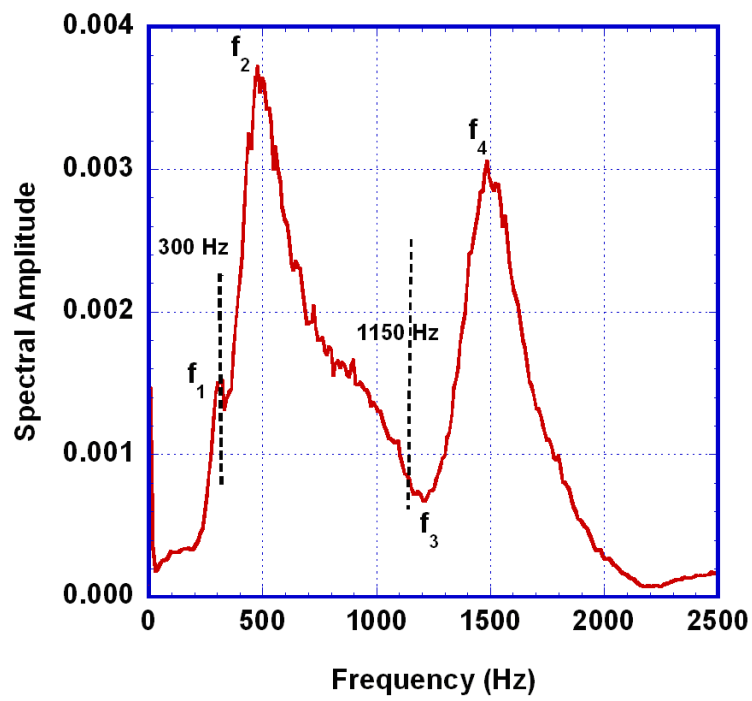


Figure 7.3. Pressure spectrum from Tap #4 under band limited (100Hz-10kHz) white noise excitation (9 watts).

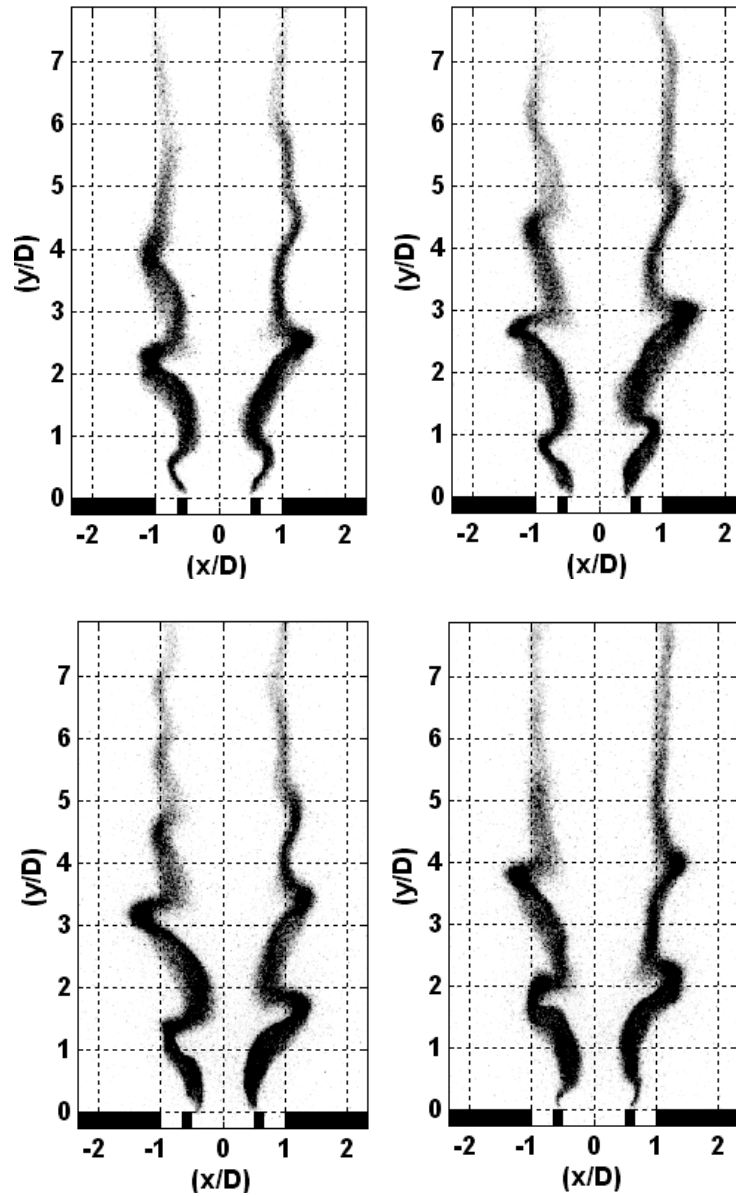


Figure 7.4. OH* chemiluminescence at various phases of oscillation (0° , 90° , 180° and 270°) of a GH₂ / GO₂ / GH₂ turbulent flame forced at 300 Hz from the left. $V_{O_2} = 6$ m/s, $V_{H_2} = 18$ m/s, $Re_{O_2} = 4900$. D is the width of the center jet = 0.75 inch.

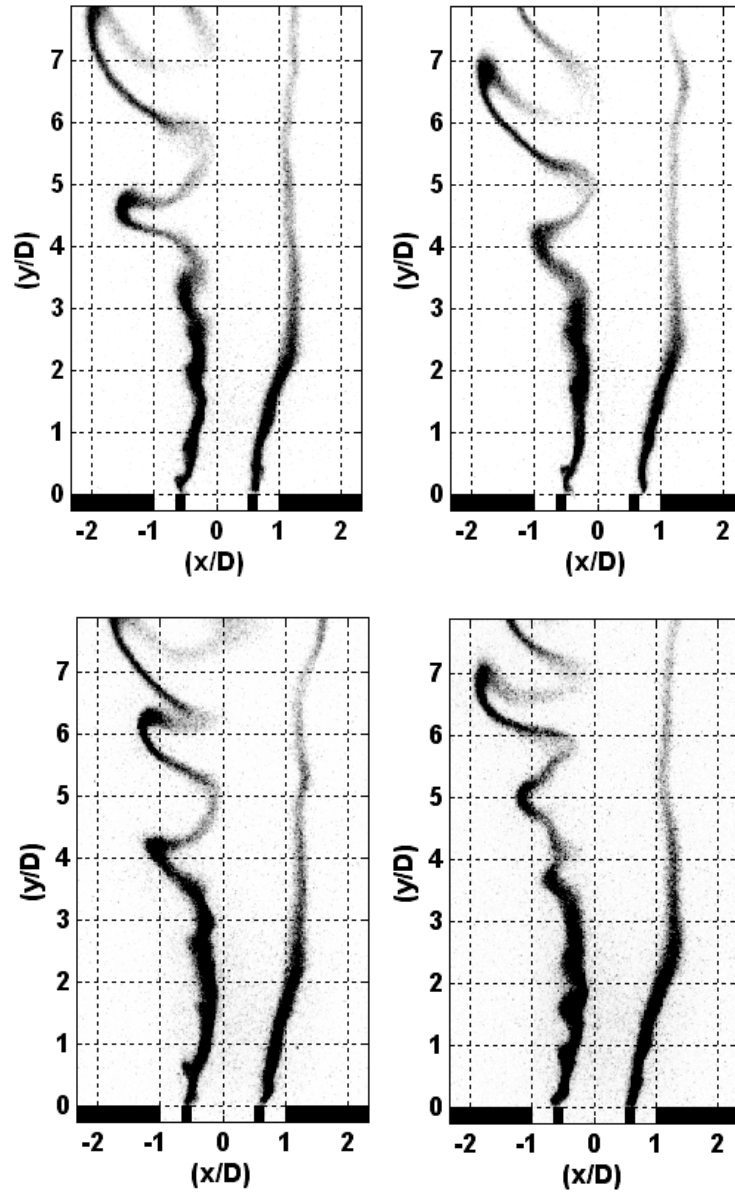


Figure 7.5. OH* chemiluminescence at various phases of oscillation (0° , 90° , 180° and 270°) of a GH₂ / GO₂ / GH₂ turbulent flame forced at 1150 Hz from the left. $V_{O_2} = 6$ m/s, $V_{H_2} = 18$ m/s, $Re_{O_2} = 4900$. D is the width of the center jet = 0.75 inch

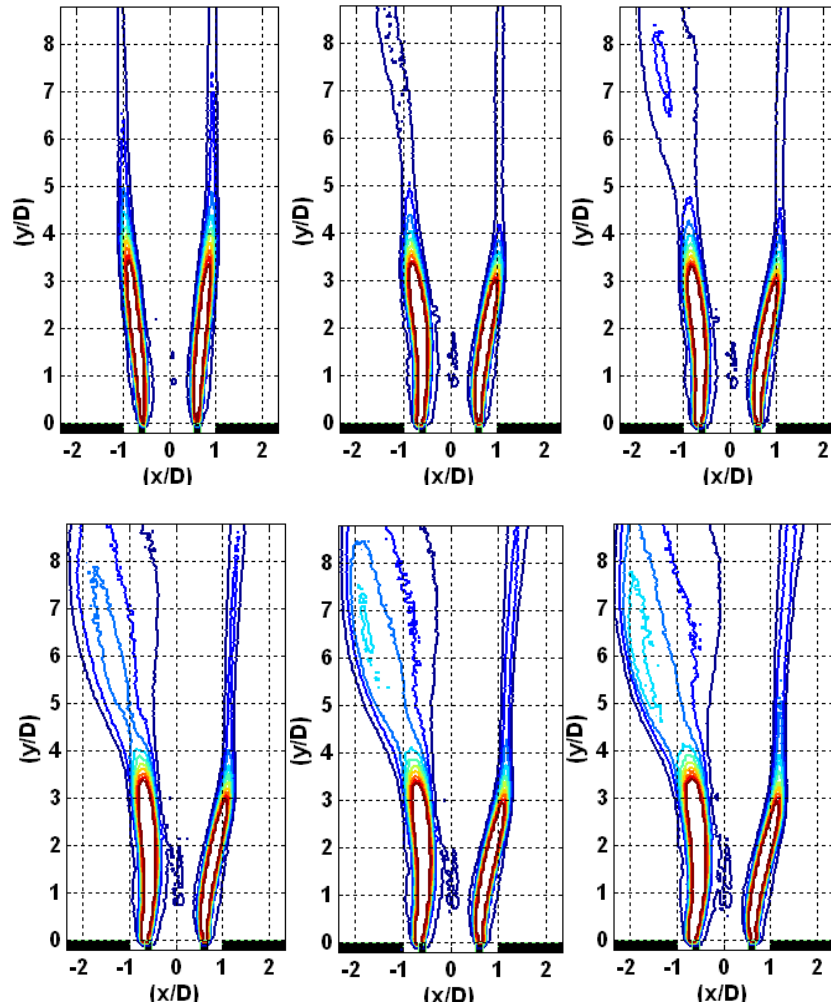


Figure 7.6. Contour plots showing flame response to an increasing set of acoustic forcing amplitude. $V_{O_2} = 4.5$ m/s, $V_{H_2} = 13.5$ m/s, $Re_{O_2} = 3700$. Forcing is increasing from left to right and top to bottom, 0 watts, 4.5 watts, 5.3 watts, 7 watts, 9.6 watts and 12.5 watts.

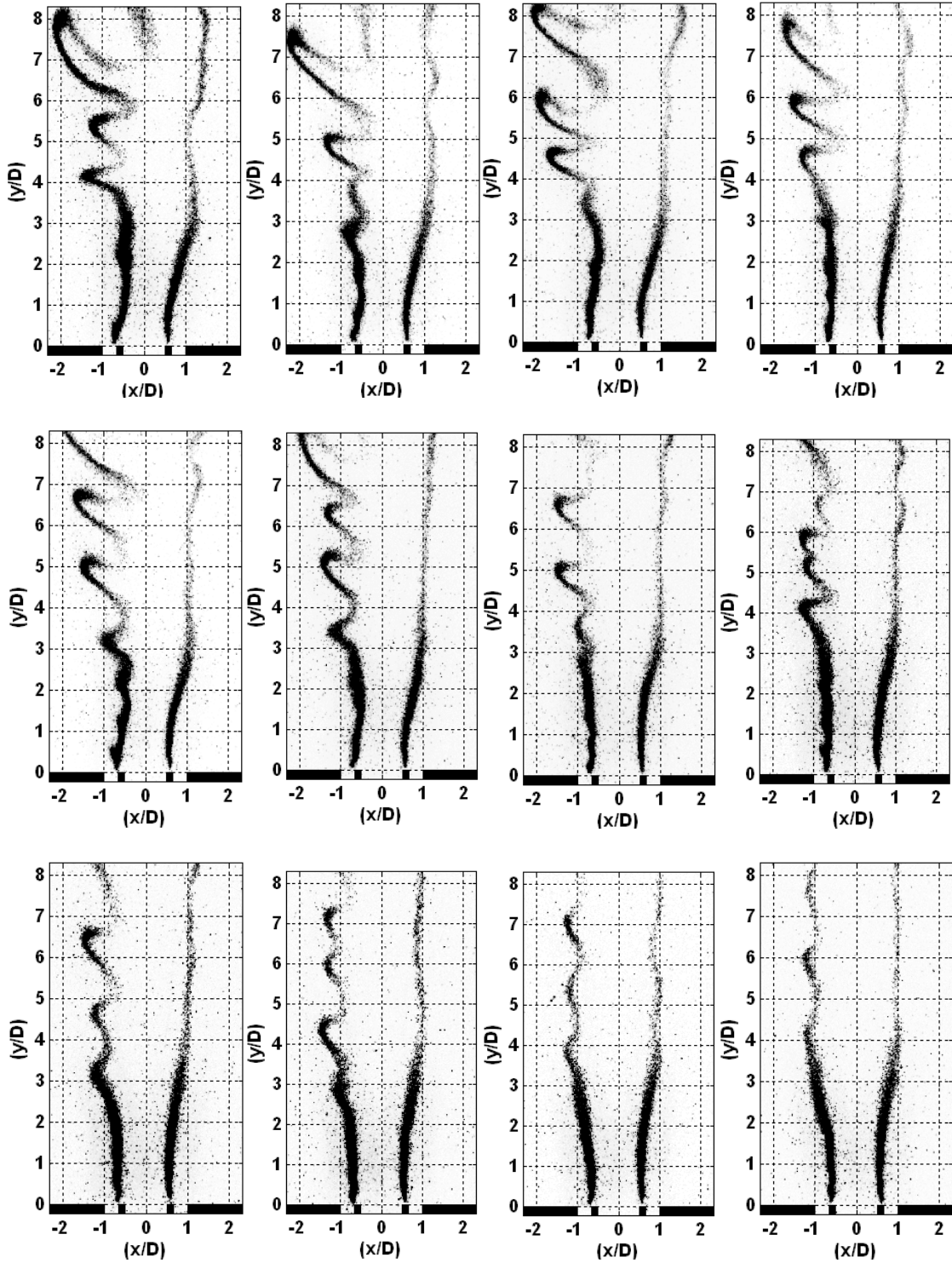


Figure 7.7(a). Instantaneous OH^* chemiluminescence images showing a monotonic decay of oscillations as density ratio between fuel and oxidizer is decreased from 15.9 to 5. $V_{\text{O}_2} = 4.5 \text{ m/s}$, $V_{\text{H}_2} = 13.5 \text{ m/s}$, $\text{Re}_{\text{O}_2} = 3700$.

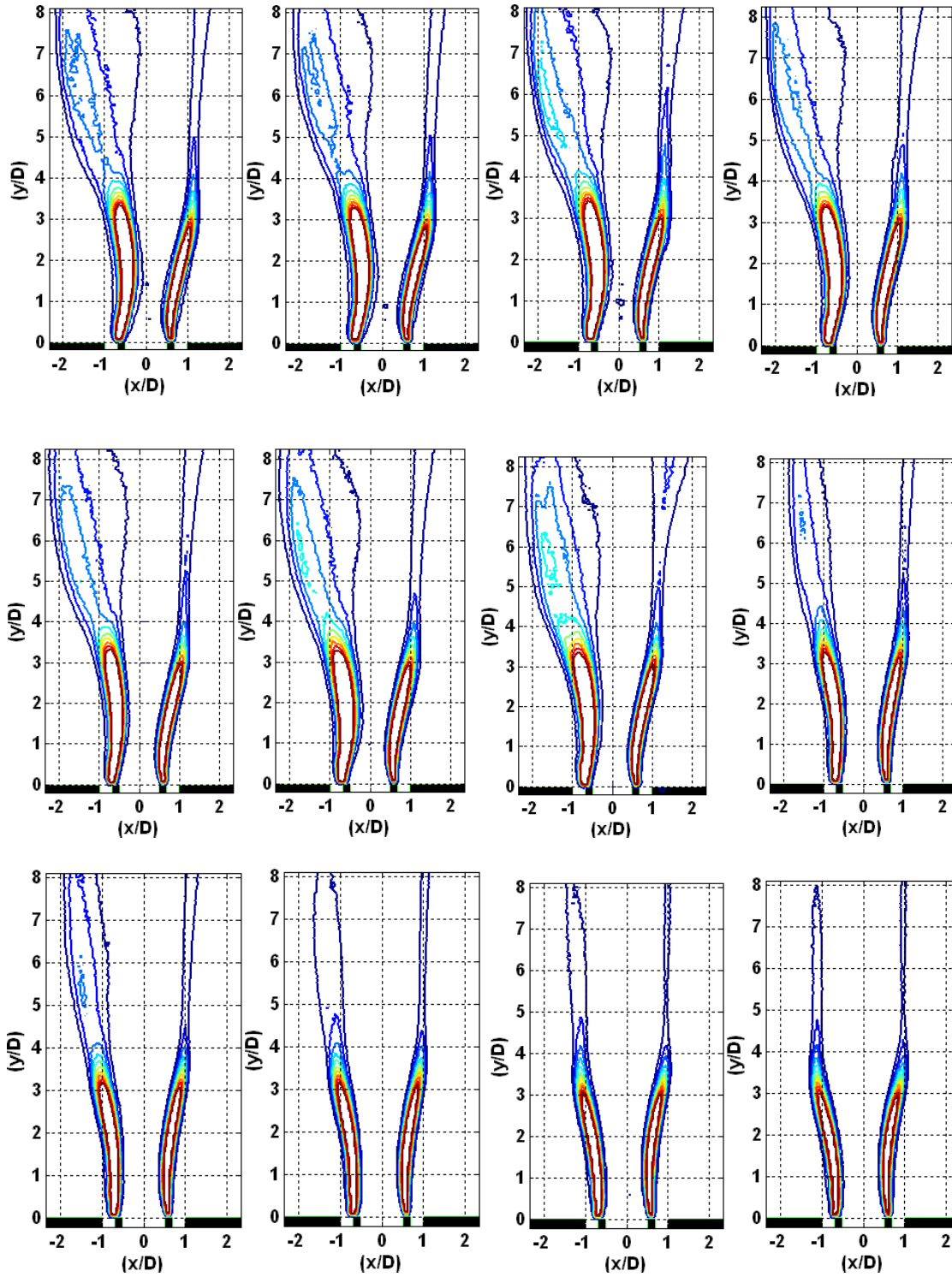


Figure 7.7(b). Contour plots of ensemble averaged OH* chemiluminescence images showing a monotonic decay of oscillations as density ratio between fuel and oxidizer is decreased from 15.9 to 5. $V_{O_2} = 4.5$ m/s, $V_{H_2} = 13.5$ m/s, $Re_{O_2} = 3700$.

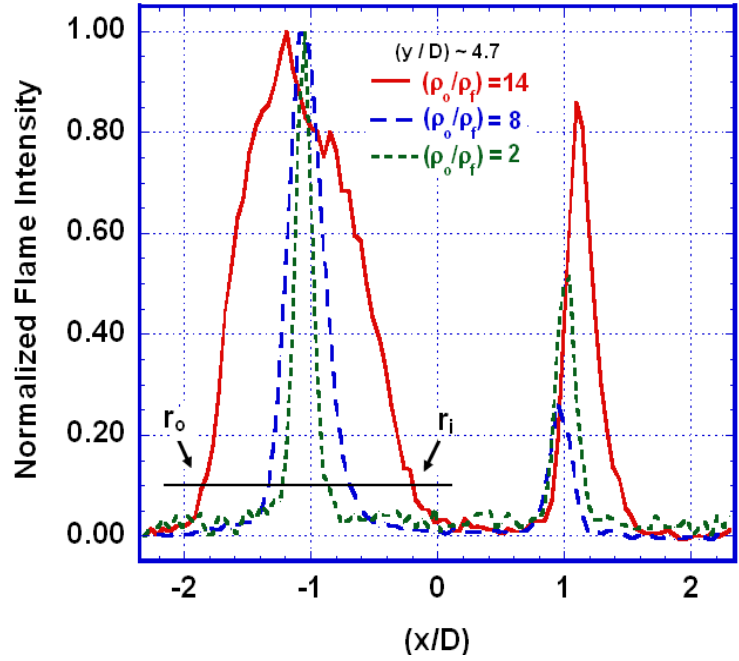


Figure 7.8. Normalized intensity for flame across the width of the combustion chamber for different oxidizer-fuel density ratios at an axial location $y/D=4.7$. At a given axial location, width of flame, $\delta(y) = |r_o - r_i|$, where the horizontal line corresponds to an intensity of 10% of the maximum.

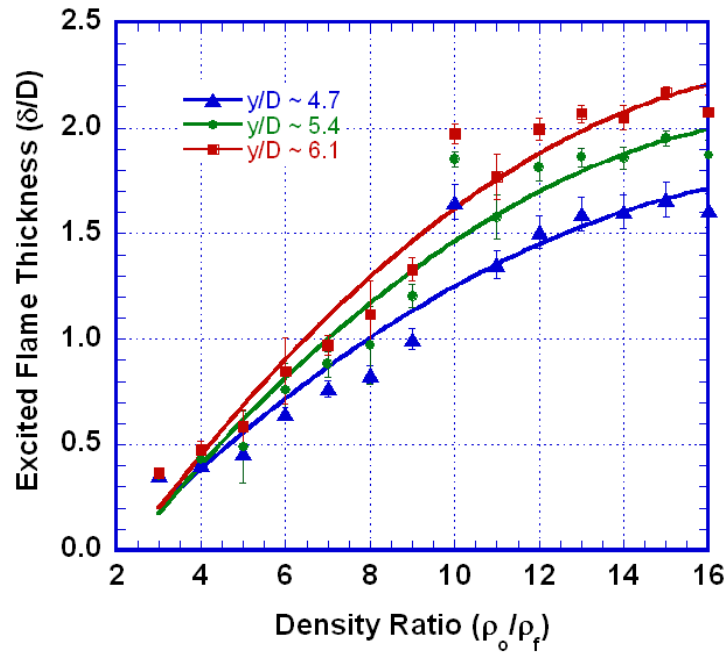


Figure 7.9. Measured flame brush thickness at various density ratios and axial locations

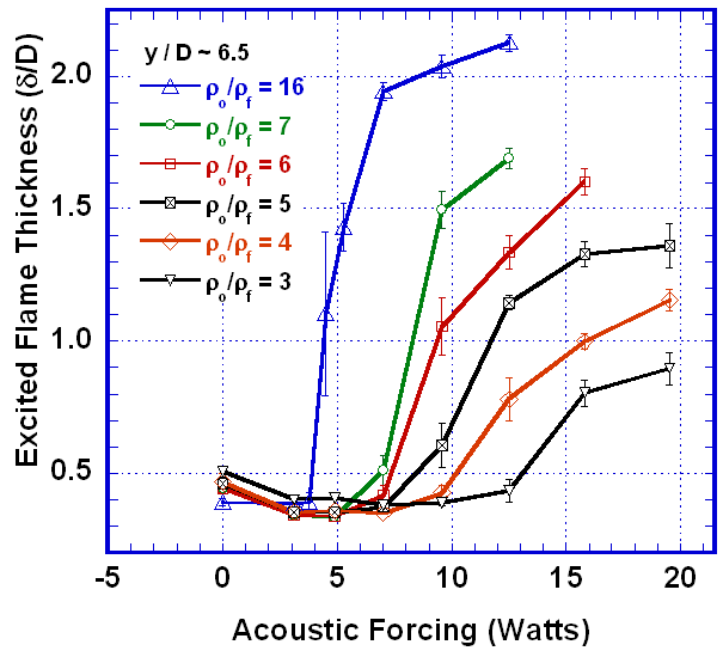


Figure 7.10. Flame brush thickness as a function of density ratio and acoustic forcing amplitude.

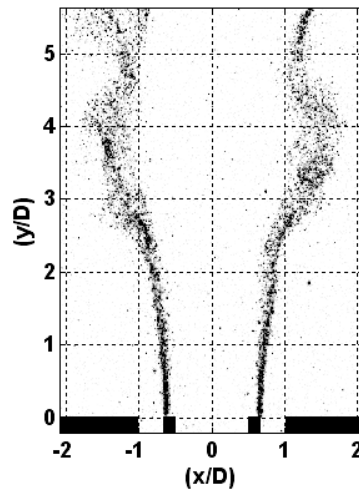


Figure 7.11. UV filtered flame image showing natural instabilities in an unforced Hydrogen-in-the-center turbulent diffusion flame. $V_{O_2/N_2} = 17.8$ m/s, $V_{H_2} = 5$ m/s, $Re_{H_2} \sim 600$, $Re_{O_2/N_2} \sim 8800$.

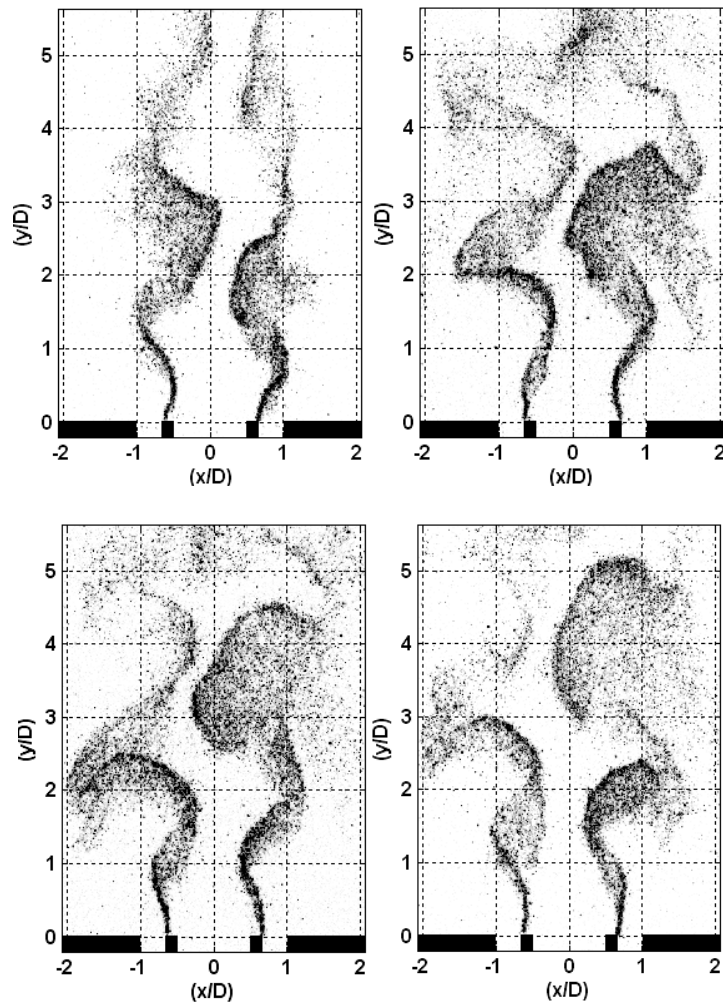


Figure 7.12(a). UV filtered images at various phases of oscillation (0° , 90° , 180° and 270°) of a Hydrogen-in-the-center turbulent diffusion flame forced at 300 Hz (at 30 Vpp) from the left. $V_{O_2/N_2} = 17.8$ m/s, $V_{H_2} = 5$ m/s, $Re_{H_2} \sim 600$, $Re_{O_2/N_2} \sim 8800$.

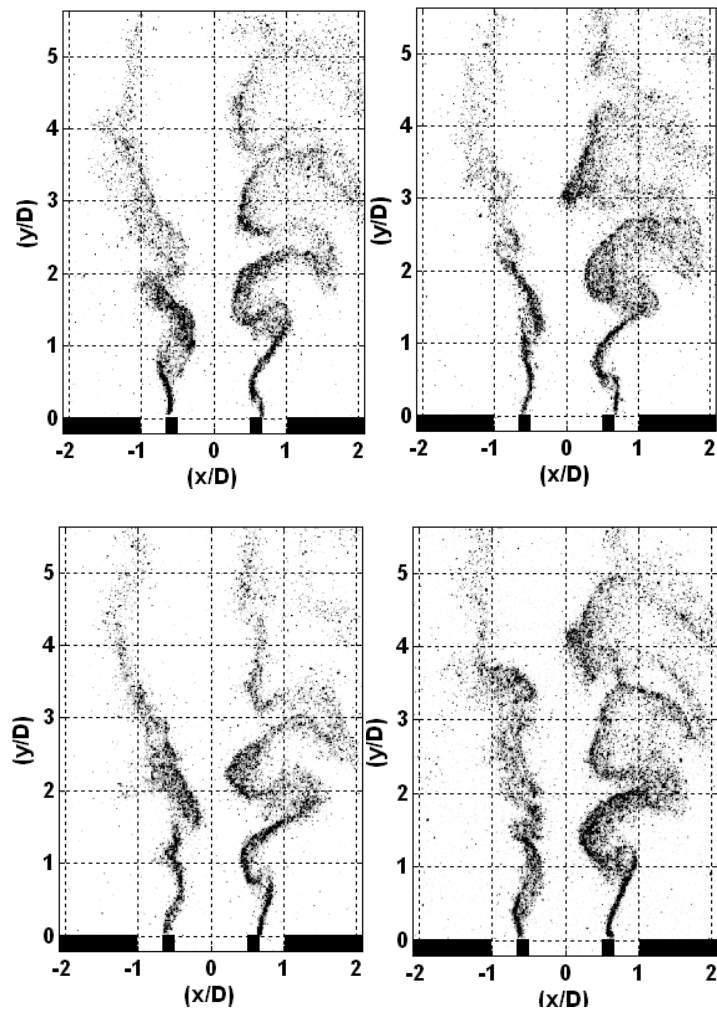


Figure 7.12(b). UV filtered images at various phases of oscillation (0° , 90° , 180° and 270°) of a Hydrogen-in-the-center turbulent diffusion flame forced at 580 Hz (55 Vpp) from the left. $V_{O_2/N_2} = 17.8$ m/s, $V_{H_2} = 5$ m/s, $Re_{H_2} \sim 600$, $Re_{O_2/N_2} \sim 8800$.

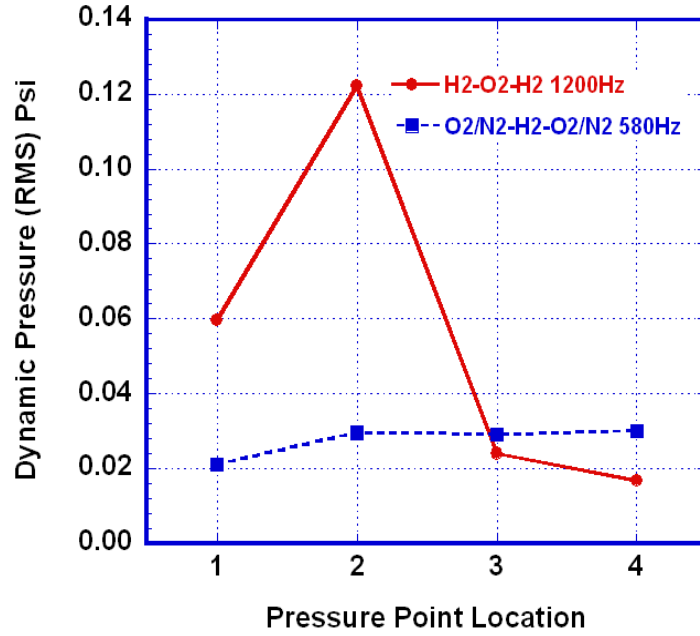


Figure 7.13. Dynamic pressure distribution across the flames. Pressure Tap # 1 is closest to the speaker.

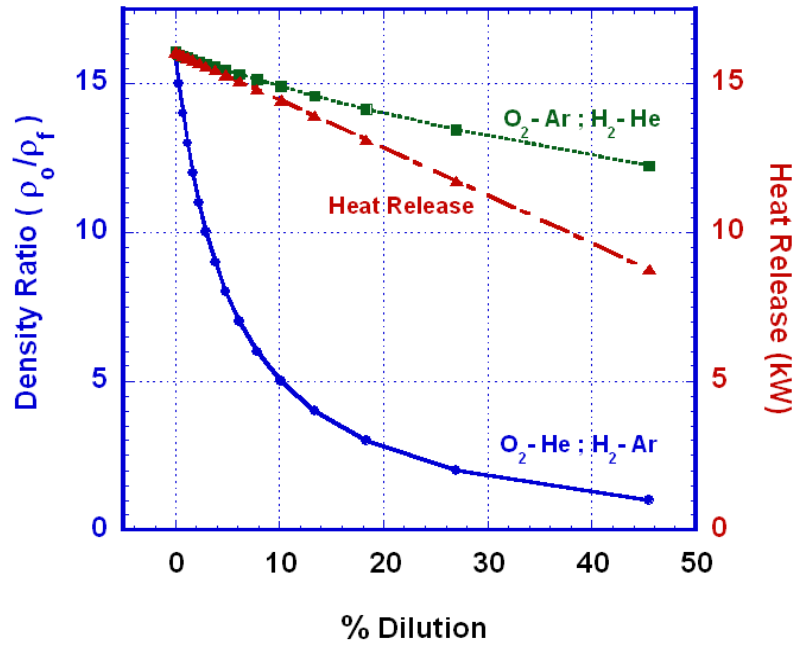


Figure 7.14. Variation of density ratio and heat release rate with molar dilution.

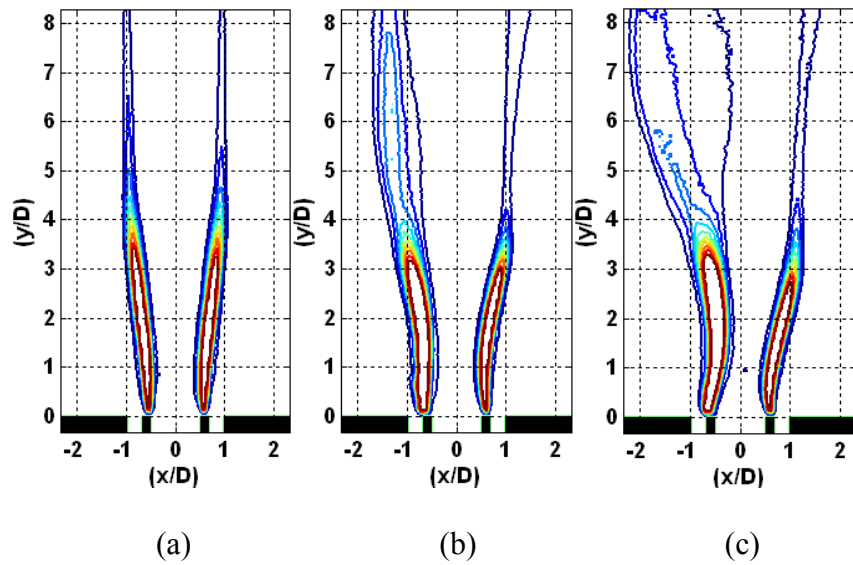


Figure 7.15. Comparison of flame-acoustic interaction under similar forcing and heat release conditions (15 kW) but different density ratios. OH* chemiluminescence images. Density ratios from left to right are as 7.0 or 15.2, 7.0 and 15.2 respectively.

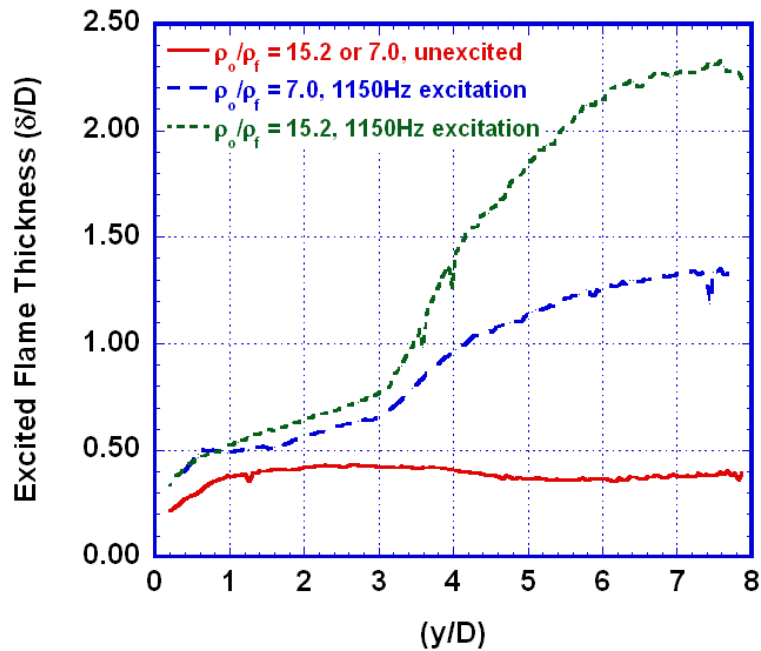


Figure 7.16. Growth rate of flame perturbation thickness as a function of streamwise location.

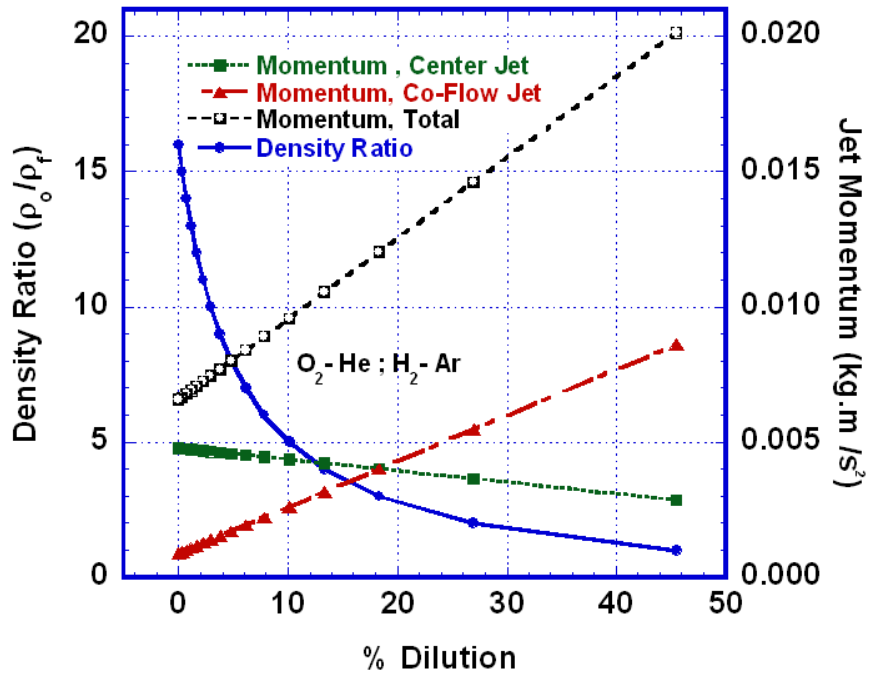


Figure 7.17. Variation of density ratio and jet momentums with molar dilution. Momentum, Total = Momentum, center Jet + 2x Momentum, Co-Flow Jet.

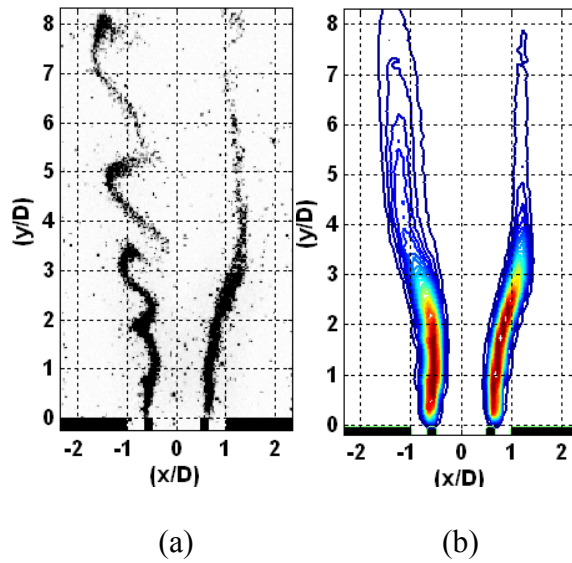


Figure 7.18. Outer jet momentum = 0.0055 kg.m/s^2 , center jet momentum = 0.0047 kg.m/s^2 Density ratio between oxidizer and fuel is ~ 8 . Acoustic forcing is from the left and is held fixed at 15.8 Watts.

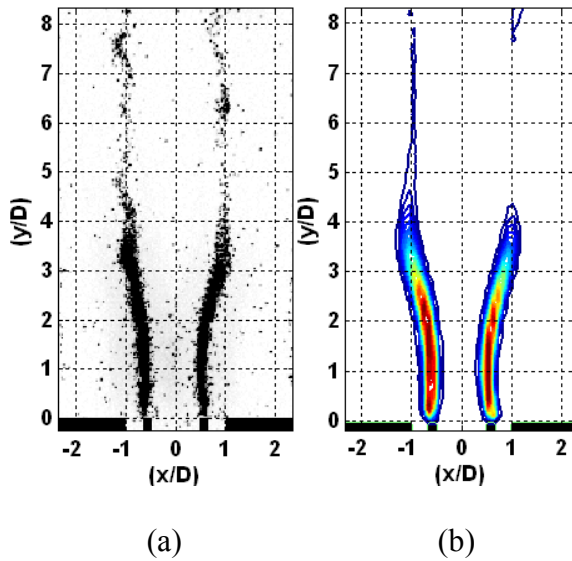
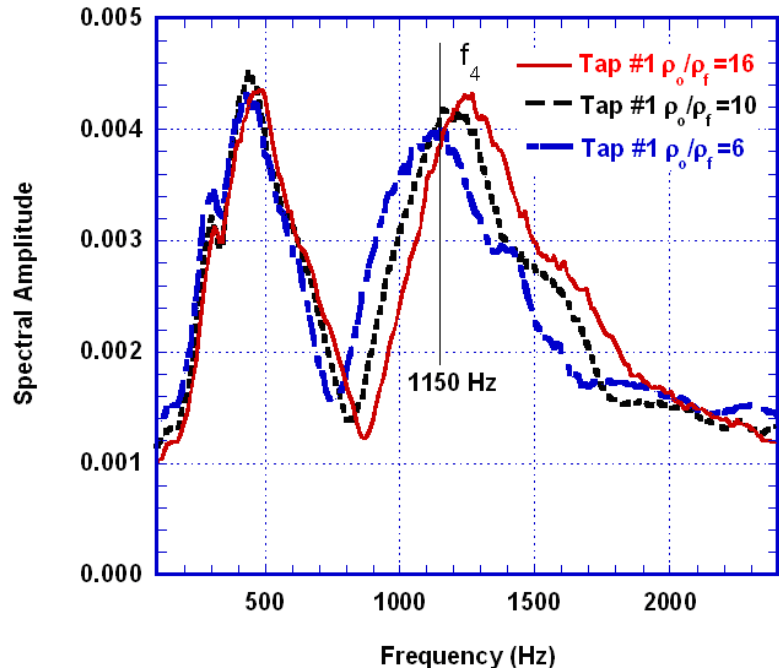
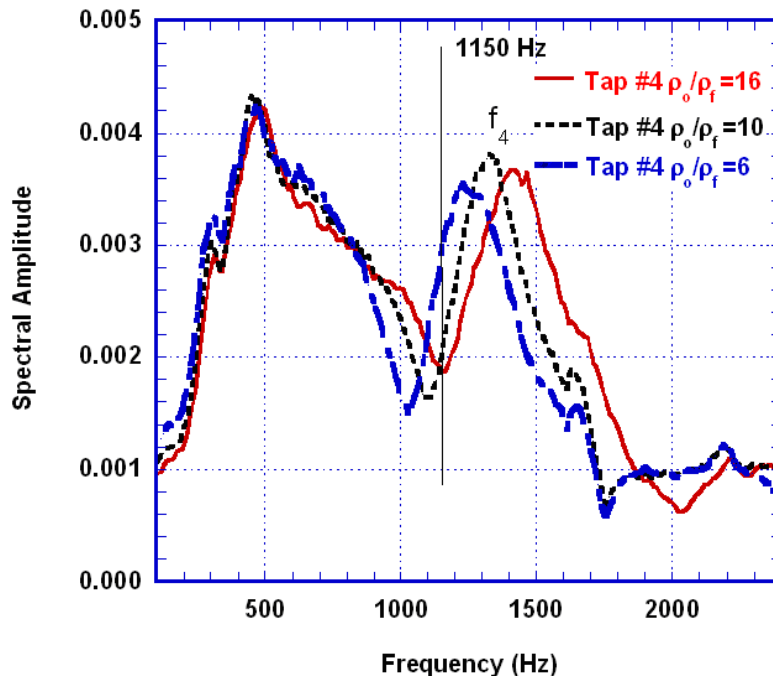


Figure 7.19. Outer jet momentum = 0.0055 kg.m/s^2 , center jet momentum = 0.0036 kg.m/s^2 Density ratio between oxidizer and fuel is ~ 2 . Acoustic forcing is from the left and is held fixed at 15.8 Watts.

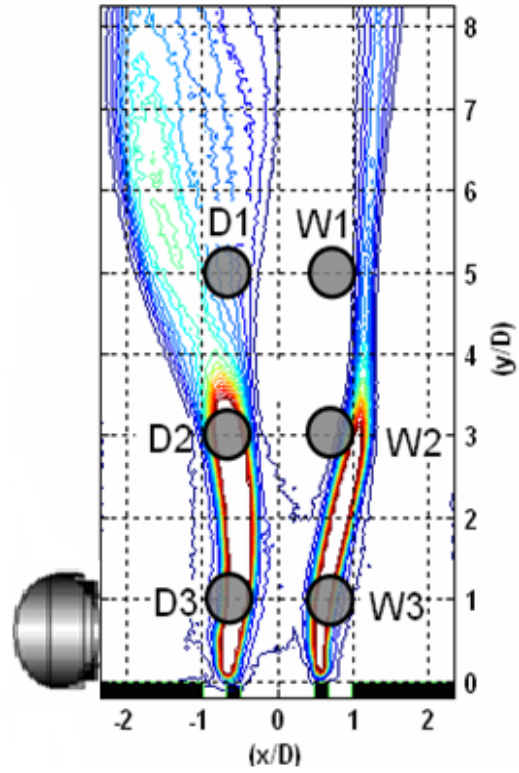


(a)



(b)

Figure 7.20. Pressure spectrum at Tap #1 (a) and at Tap #4 (b) for reacting flow-fields under white noise excitation for density ratios 16, 10 and 6.



Tap#	D3	W3	D2	W2	D1	W1
x (in)	-0.500	0.500	-0.500	0.500	-0.500	0.500
y (in)	0.750	0.750	2.250	2.250	3.750	3.750

Figure 7.21. Location of pressure measurement and OH* chemiluminescence oscillation measurement ports.

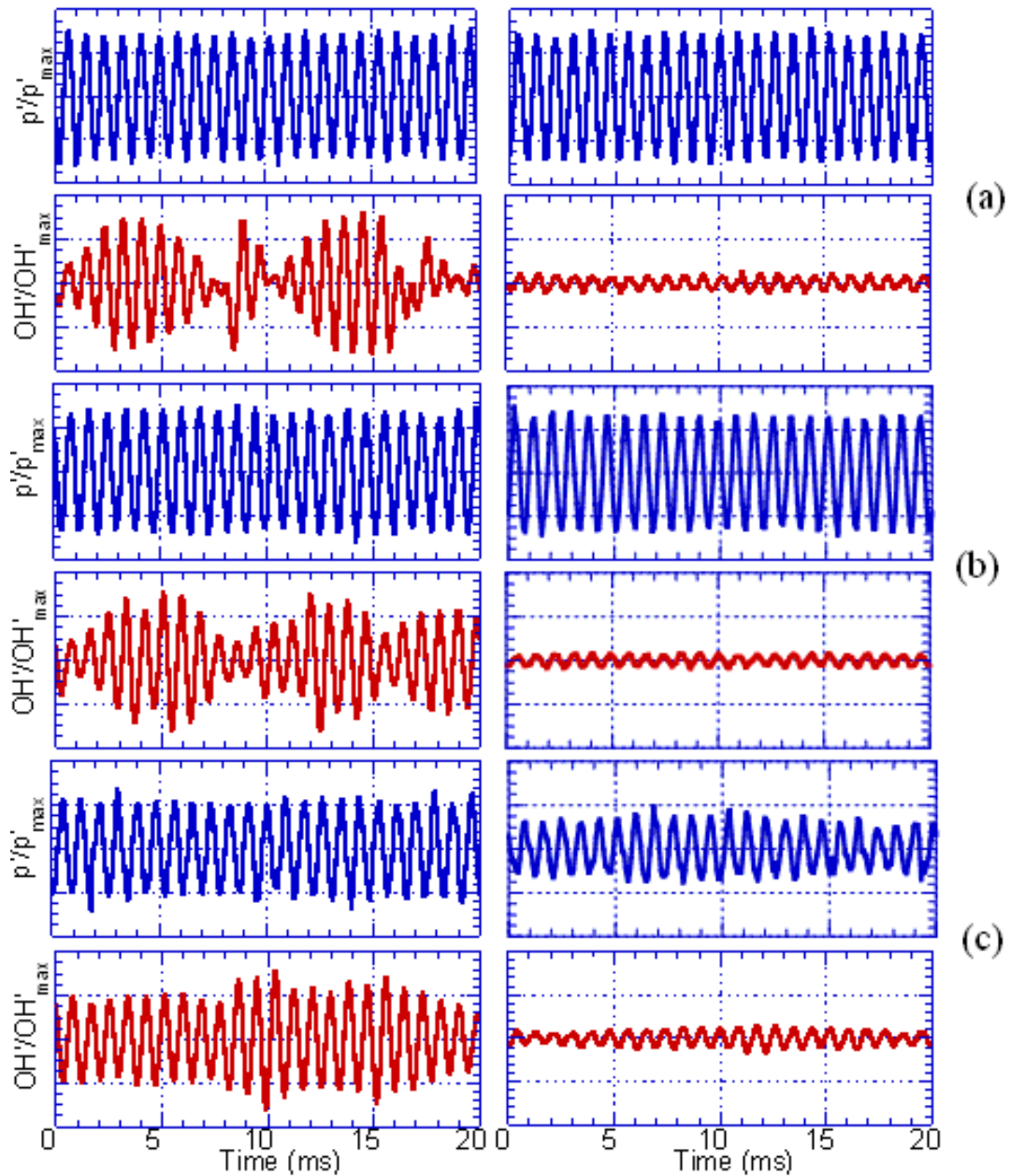


Fig. 7.22. Comparison of local OH* chemiluminescence fluctuations responding to pressure oscillation at density ratio=14.5. The sensors are located horizontally at $x=-0.67D$ (left column) and $x=0.67D$ (right column), and vertically at (a) $y=5D$, (b) $y=3D$, (c) $y=1D$

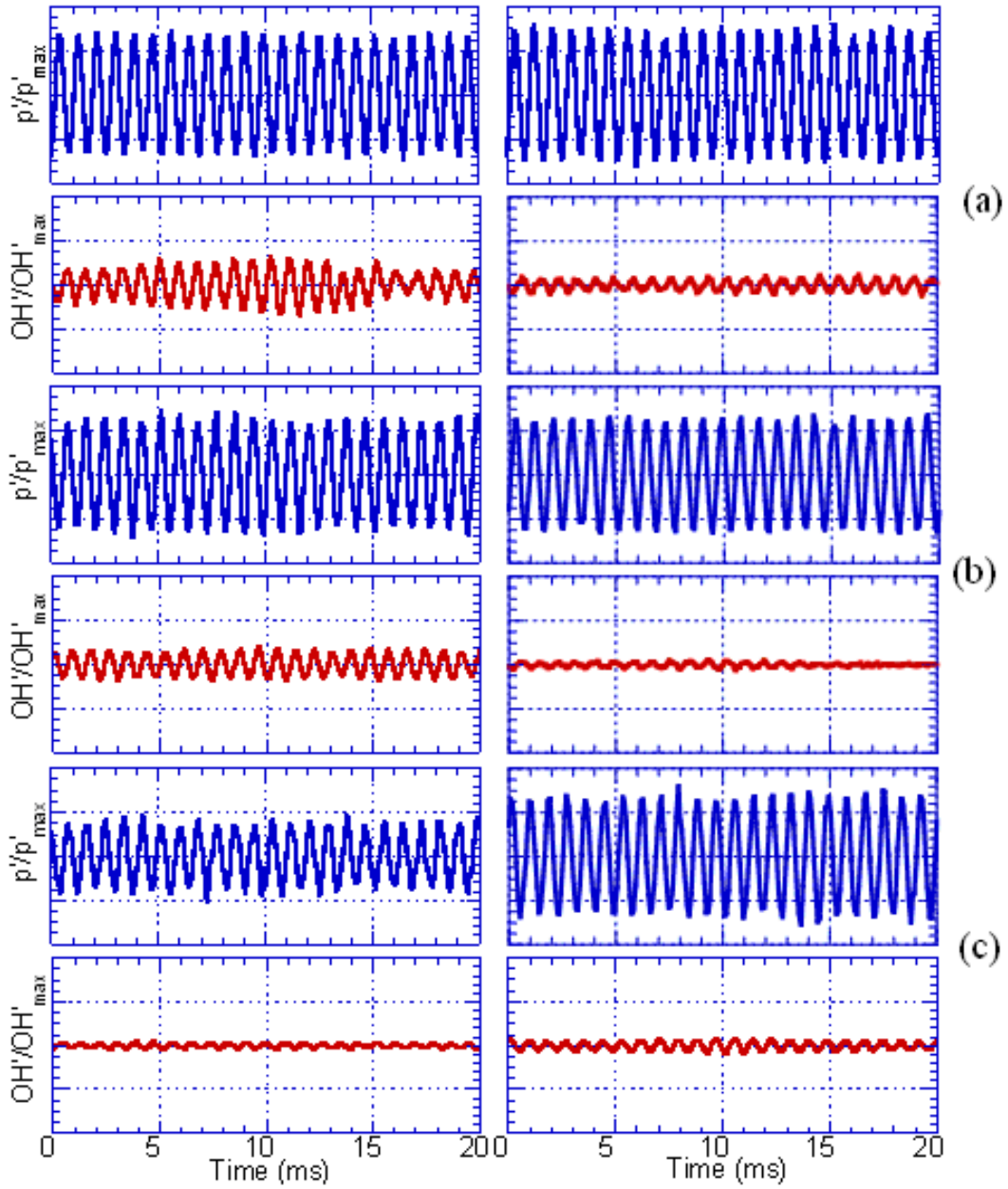


Figure 7.23. Comparison of local OH^* chemiluminescence fluctuations responding to pressure oscillation at density ratio=3. The sensors are located horizontally at $x=-0.67D$ (left column) and $x=0.67D$ (right column), and vertically at (a) $y=5D$, (b) $y=3D$, (c) $y=1D$.

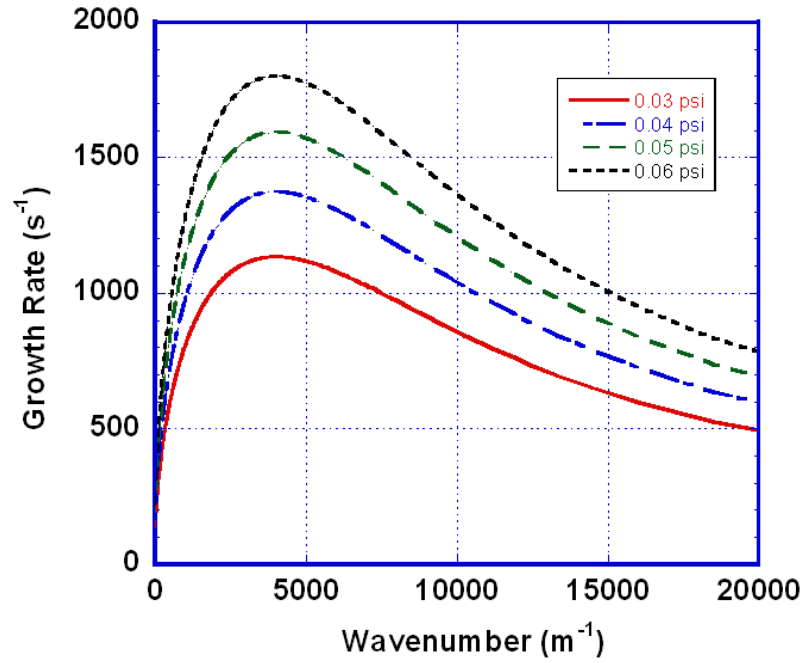


Figure 7.24. Classical RT mode instability analysis yields wavelength-dependent growth rate.

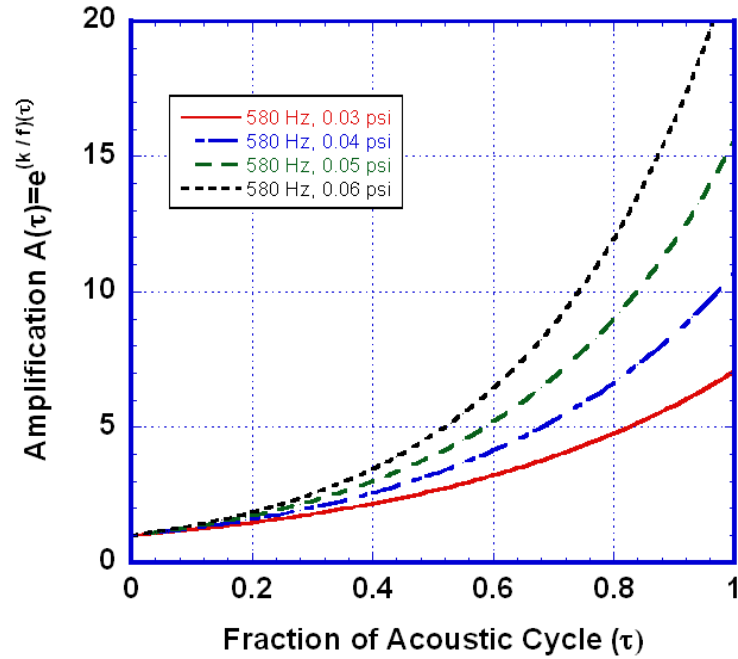


Figure 7.25. Amplification in growth rates as function of acoustic cycle.

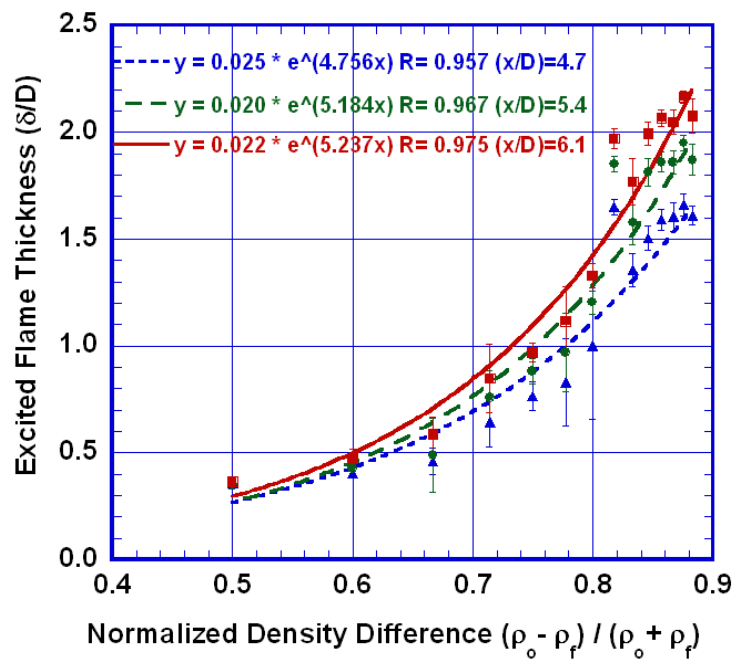


Figure 7.26. Measured flame brush thickness at various density ratios and streamwise locations.

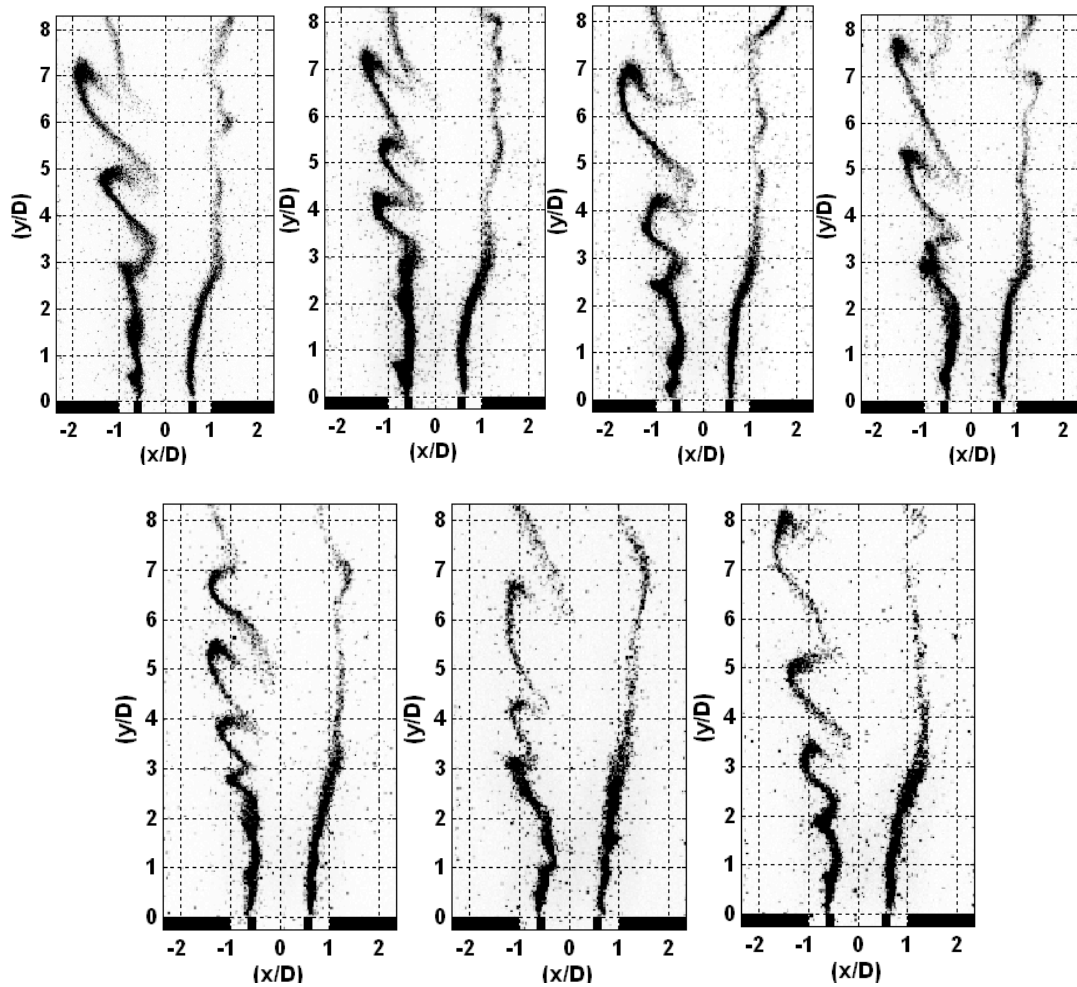


Figure 7.27. Instantaneous OH* chemiluminescence images showing flame perturbations affected by fuel-oxidizer velocity ratio. Fuel oxidizer velocity ratios are in increasing order from left to right and from top to bottom. Velocity ratios are as $u_f/u_o=3.02$, $u_f/u_o=3.36$, $u_f/u_o=3.64$, $u_f/u_o=4.01$, $u_f/u_o=4.51$, $u_f/u_o=5.03$ and $u_f/u_o=5.27$.

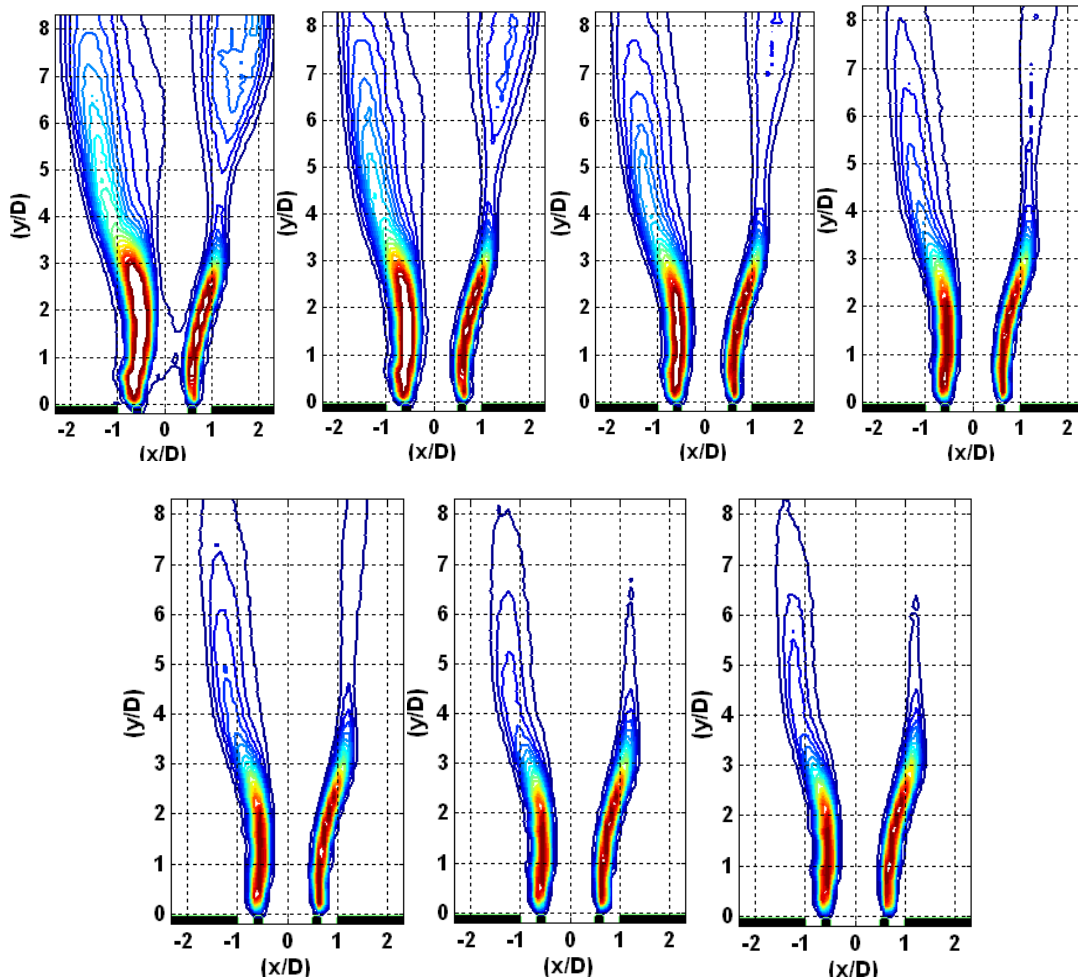


Figure 7.28. Time averaged OH* chemiluminescence images showing flame perturbations affected by fuel-oxidizer velocity ratio. Fuel oxidizer velocity ratios are in increasing order from left to right and from top to bottom. Velocity ratios are as $u_f / u_o = 3.02$, $u_f / u_o = 3.36$, $u_f / u_o = 3.64$, $u_f / u_o = 4.01$, $u_f / u_o = 4.51$, $u_f / u_o = 5.03$ and $u_f / u_o = 5.27$.

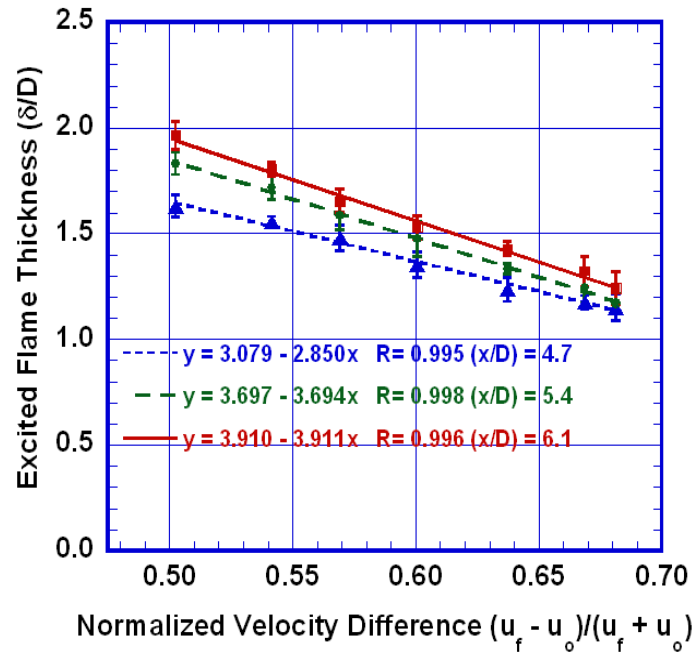


Figure 7.29. Measured flame brush thickness at various velocity ratios and streamwise locations.

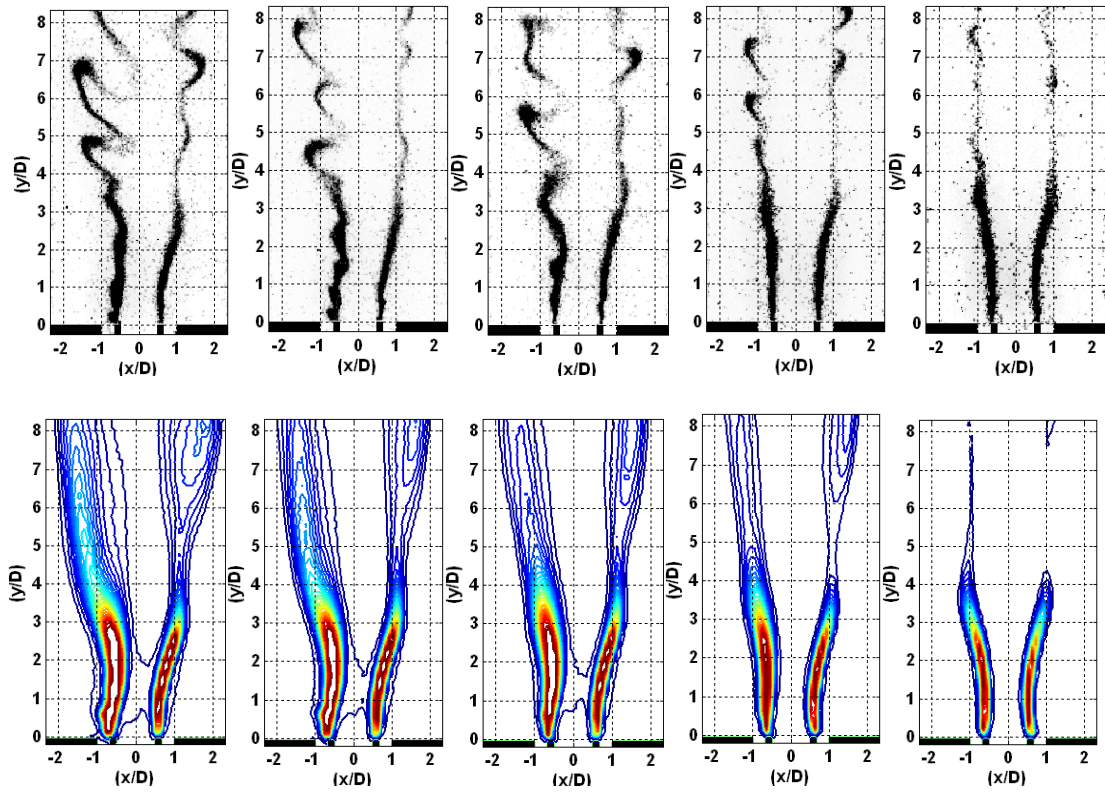


Figure 7.30. Flame perturbations affected by fuel-oxidizer momentum ratio involving no change in velocity ratio. $u_f / u_o = 3$, $\rho_o / \rho_f = 6$, $\rho_o / \rho_f = 5$, $\rho_o / \rho_f = 4$, $\rho_o / \rho_f = 3$, $\rho_o / \rho_f = 2$, $J_o / J_f = 1.99$, $J_o / J_f = 1.67$, $J_o / J_f = 1.33$, $J_o / J_f = 1.00$, $J_o / J_f = 0.67$.

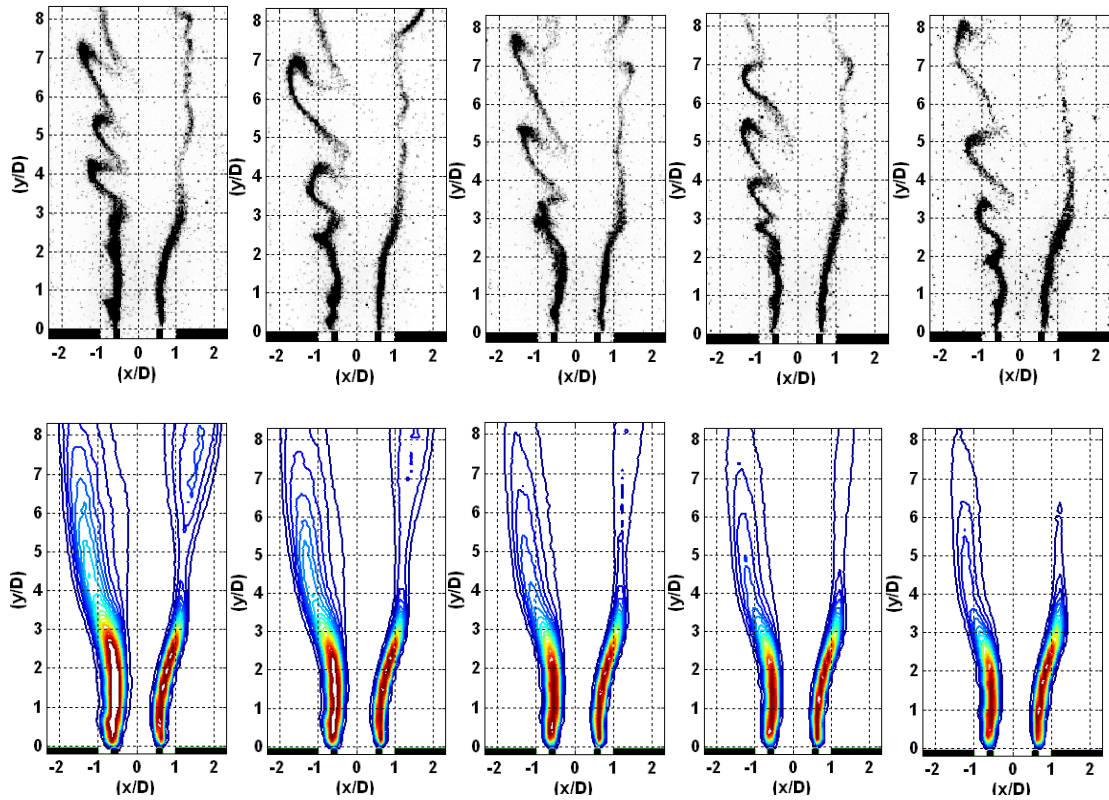
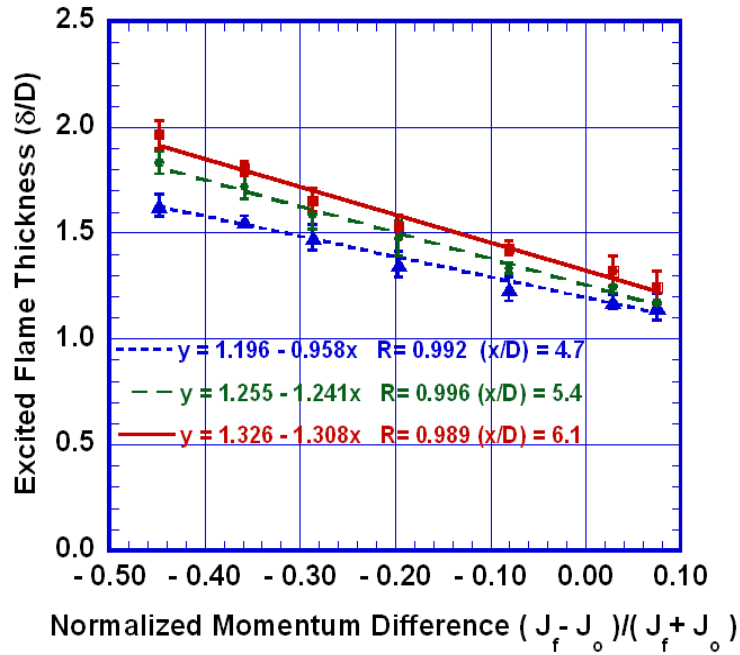
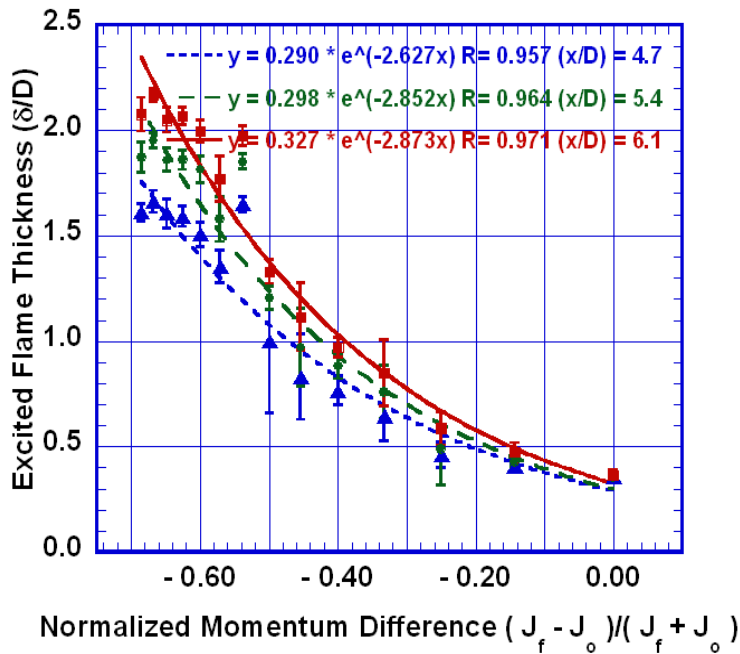


Figure 7.31. Flame perturbations affected by fuel-oxidizer momentum ratio involving no change in density ratio. $\rho_o / \rho_f = 7.99$, $u_f / u_o = 3.36$, $u_f / u_o = 3.64$, $u_f / u_o = 4.01$, $u_f / u_o = 4.51$, $u_f / u_o = 5.27$, $J_o / J_f = 2.12$, $J_o / J_f = 1.80$, $J_o / J_f = 1.49$, $J_o / J_f = 1.18$, $J_o / J_f = 0.86$.



(a)



(b)

Figure 7.32. Flame perturbations affected by non-dimensionalized fuel-oxidizer momentum difference. (a) Momentum change through velocity change. (b) Momentum change through density change.

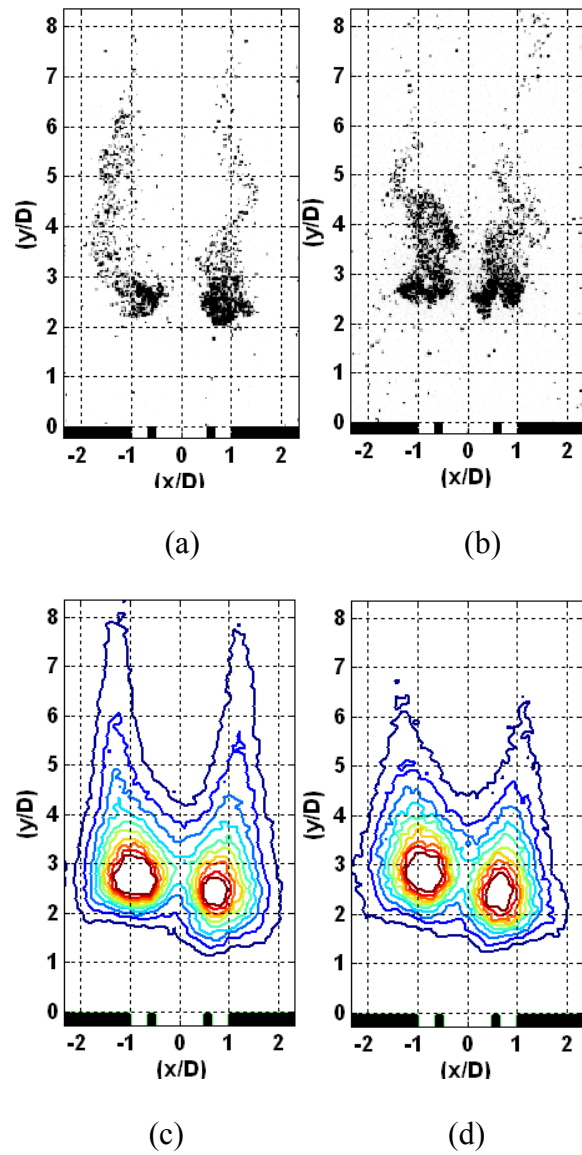


Figure 7.33. Lifted flame using 100% CH_4 . No acoustic excitation. (a) Instantaneous CH^* chemiluminescence image (b) Instantaneous OH^* chemiluminescence image (c) Average CH^* chemiluminescence image (d) Average OH^* chemiluminescence image.

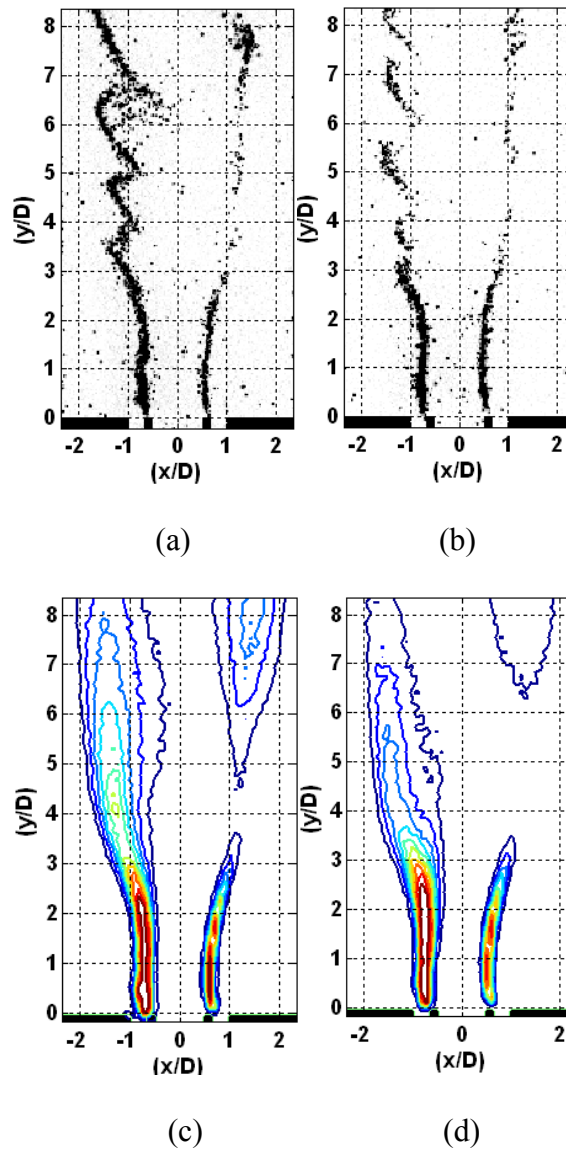


Figure 7.34. 50% CH_4 , 50% H_2 fueled flame acoustically excited from left at 1150 Hz. (a) Instantaneous CH^* chemiluminescence image. (b) Instantaneous OH^* chemiluminescence image. (c) Average CH^* chemiluminescence image. (d) Average OH^* chemiluminescence image.

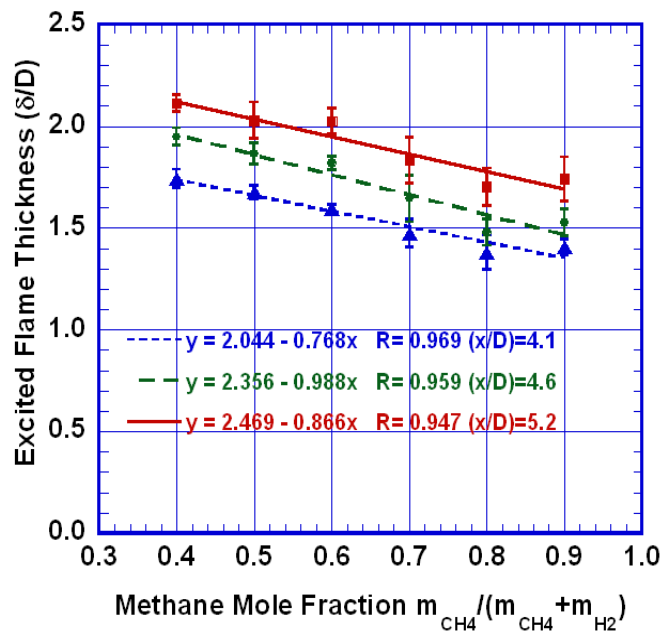


Figure 7.35. Measured flame brush thickness at various fuel compositions and axial locations.

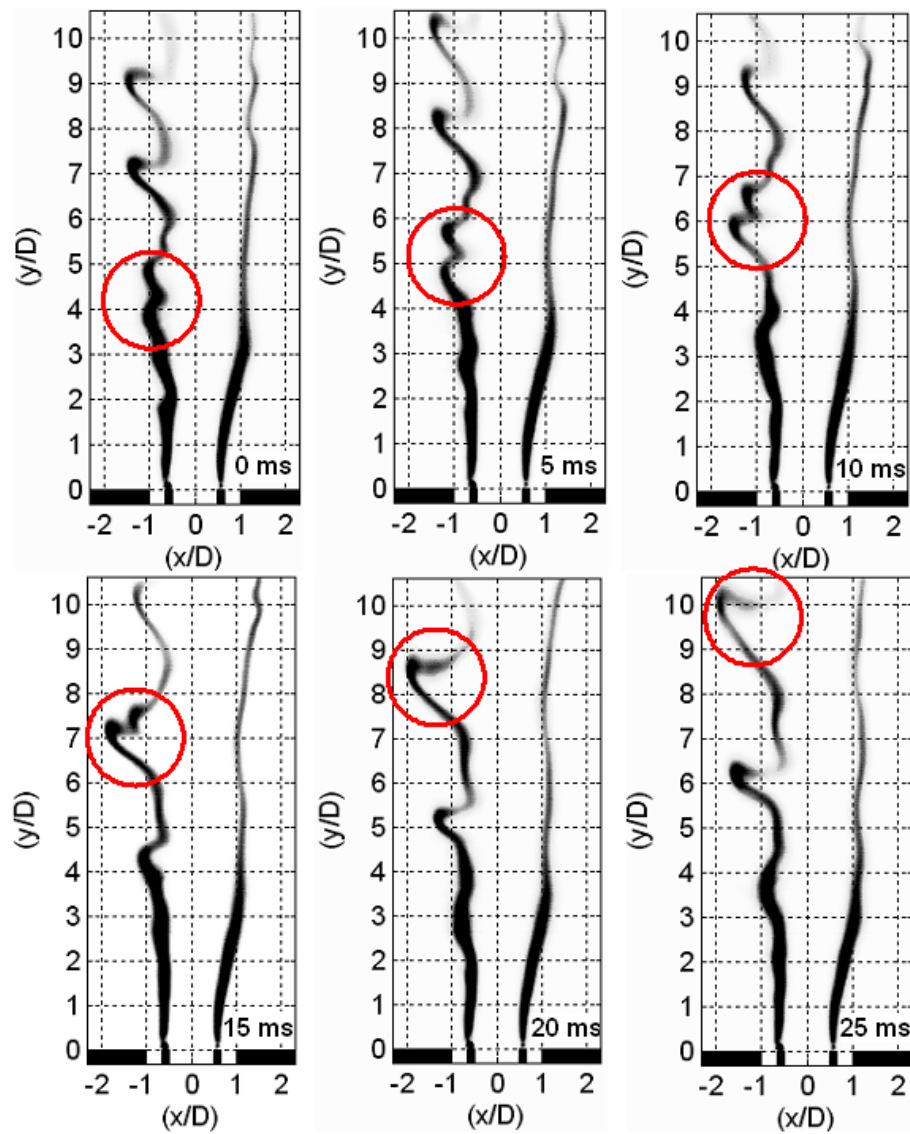
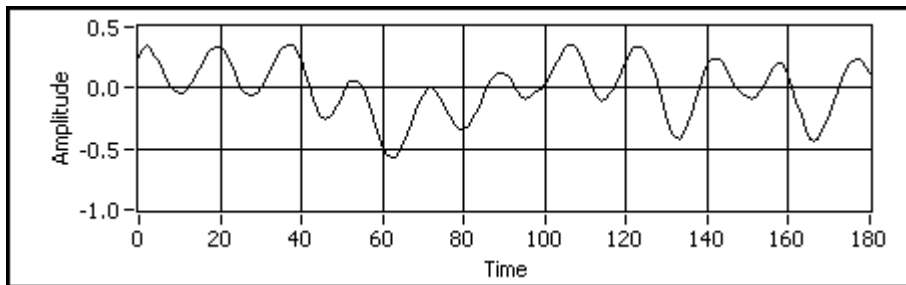


Figure 7.36. High-speed imaging showing a typical vortex pairing event when the GO₂ / GH₂ turbulent flame is forced at 1150 Hz. $V_{O_2} = 4.5$ m/s, $V_{H_2} = 13.5$ m/s., Center jet width, $D = 0.75$ inch.



(1 time unit=0.05 msec)

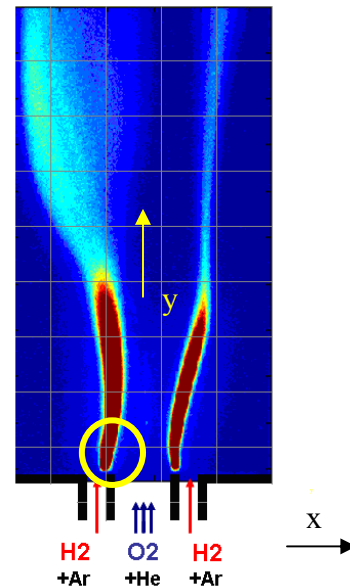
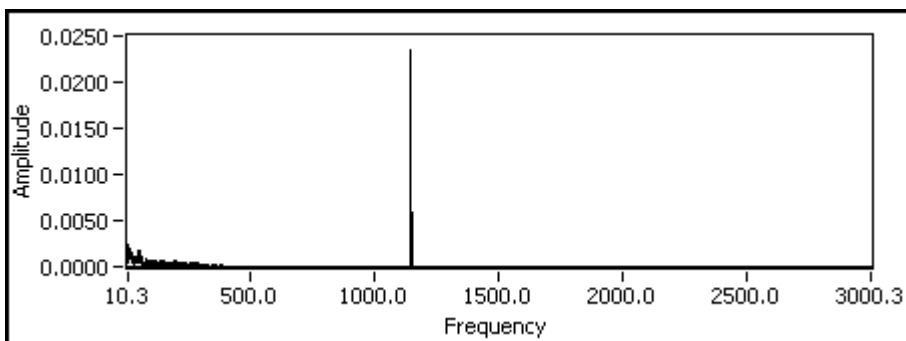
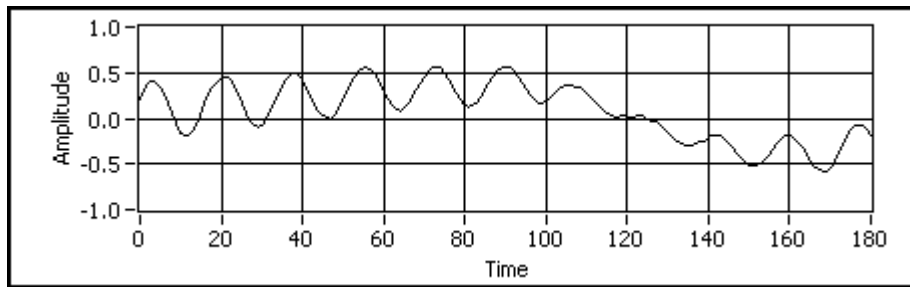


Figure 7.37. Time domain and frequency domain measurement of OH* chemiluminescence oscillations using PMT. Probe location $(x, y) = (-0.375'', 0.375'')$ is shown by the circle on the flame image. $V_{O_2} = 4.5$ m/s, $V_{H_2} = 13.5$ m/s., Center jet width, $D = 0.75$ inch. Forcing is from left at 1150 Hz.



(1 time unit=0.05 msec)

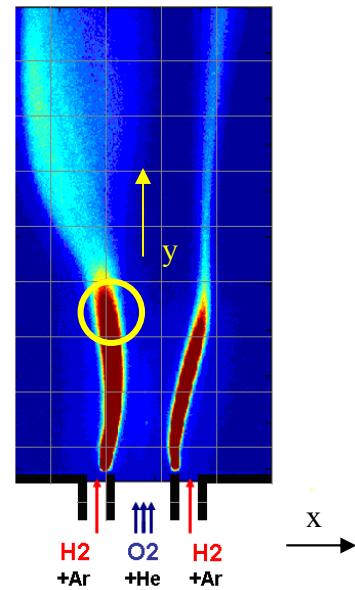
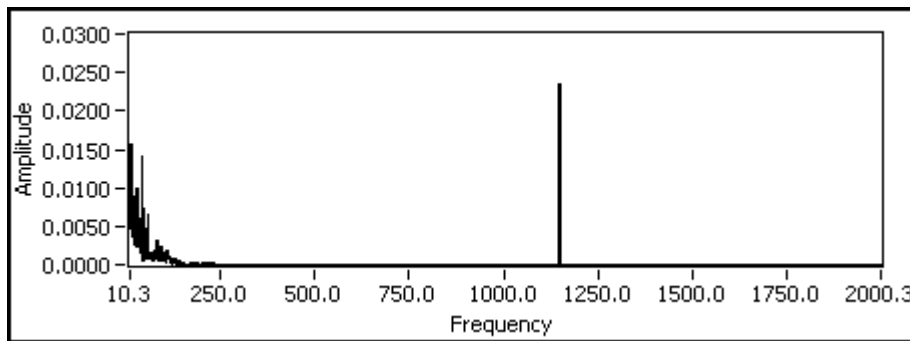
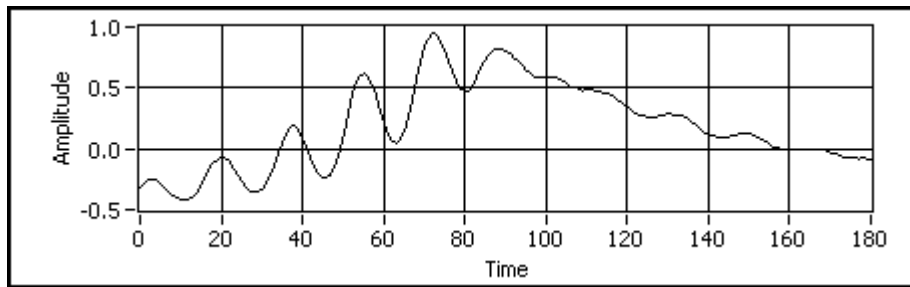


Figure 7.38. Time domain and frequency domain measurement of OH* chemiluminescence oscillations using PMT. Probe location $(x, y) = (-0.375'', 2.25'')$ is shown by the circle on the flame image. $V_{O_2} = 4.5$ m/s, $V_{H_2} = 13.5$ m/s., Center jet width, $D = 0.75$ inch. Forcing is from left at 1150 Hz.



(1 time unit=0.05 msec)

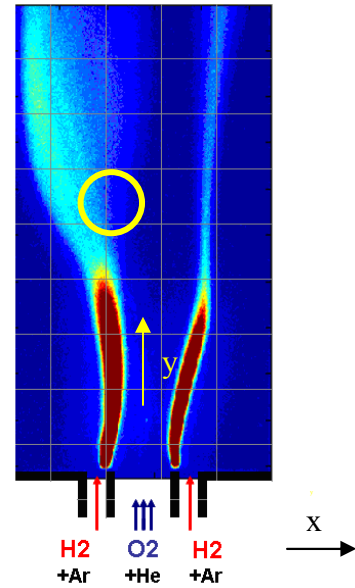
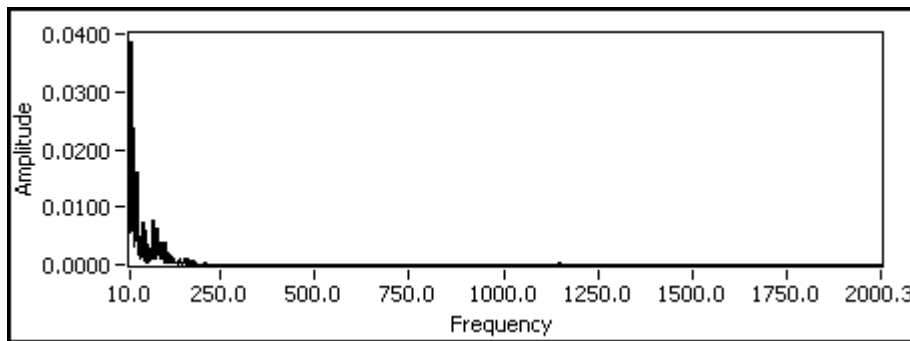
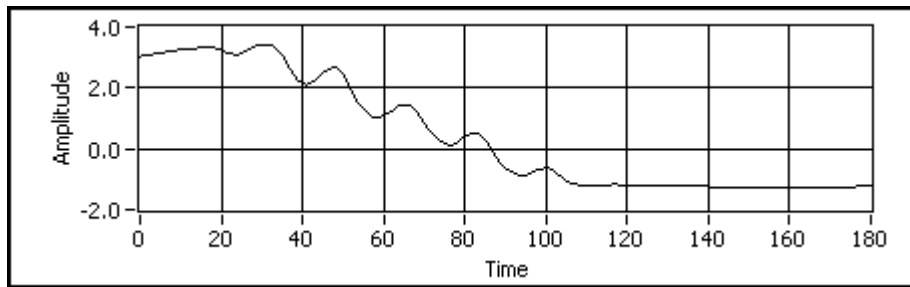


Figure 7.39. Time domain and frequency domain measurement of OH* chemiluminescence oscillations using PMT. Probe location $(x, y) = (-0.375'', 3.75'')$ is shown by the circle on the flame image. $V_{O_2} = 4.5$ m/s, $V_{H_2} = 13.5$ m/s., Center jet width, $D = 0.75$ inch. Forcing is from left at 1150 Hz.



(1 time unit=0.05 msec)

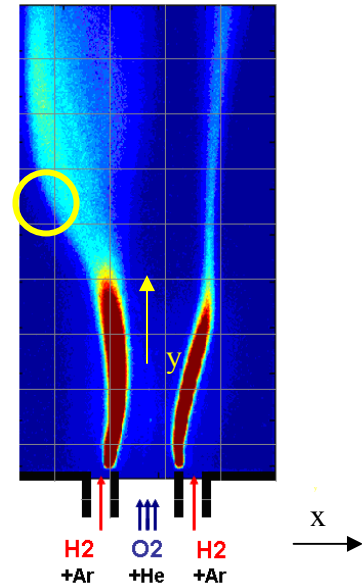
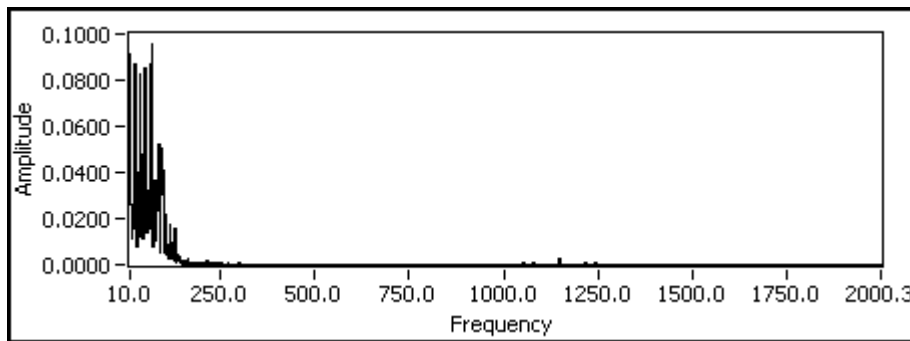


Figure 7.40. Time domain and frequency domain measurement of OH* chemiluminescence oscillations using PMT. Probe location $(x, y) = (-1.375'', 3.75'')$ is shown by the circle on the flame image. $V_{O_2} = 4.5$ m/s, $V_{H_2} = 13.5$ m/s., Center jet width, $D = 0.75$ inch. Forcing is from left at 1150 Hz.

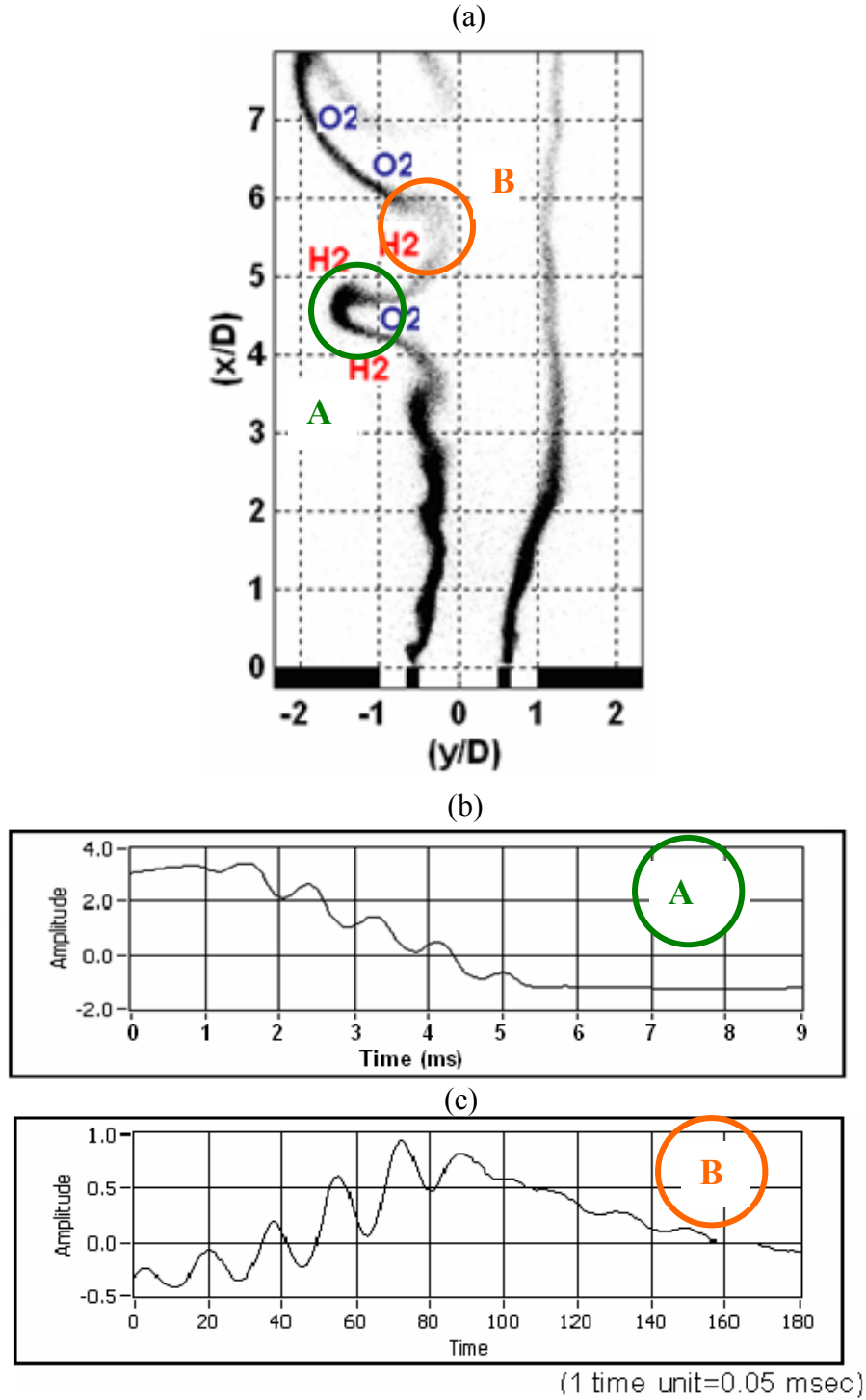


Figure 7.41. Instantaneous OH^* chemiluminescence image for a $\text{GH}_2/\text{GO}_2/\text{GH}_2$ flame forced at 1150 Hz from left (a) and OH^* oscillation as picked up by PMT sensor at location marked 'A' (b) and 'B' (c). OH^* oscillations are large when acoustic waves from driver are passing from lighter H_2 to denser O_2 .

Appendix B: Tables

Tap #	1	2	3	4
x(in)	-1.625	-0.500	0.500	1.625
y(in)	0.500	0.500	0.500	0.500

Table 3.1. Location of pressure taps. y-axis is streamwise, x-axis is transverse.

Tap #	Mode	No Flow (Quiescent Air)	
		Measured (Hz)	Calculated (Hz)
4	f1	136±10	141 ^a
	f2	392	399 ^b
	f3	600	639 ^c
	f4	1024	976 ^d
	f5	1920	1952 ^e

^a – Quarter-wave mode longitudinal in the combustor with oxidizer post.

^b – Quarter-wave mode longitudinal in oxidizer post.

^c – Three-quarter-wave mode longitudinal in the combustion chamber.

^d – Quarter-wave mode (Transverse) across the chamber width.

^e – Half-wave mode (Transverse) across the chamber width.

Table 5.1. Comparison of measured spectral peak frequencies and calculated resonance frequencies for no-flow with quiescent air.

Flow Conditions		A	B	C	D
Density Ratio (ρ_0/ρ_f)		14.5	11	7	3
Oxygen	O₂ flow rate (g/s)	1.06	1.06	1.06	1.06
	Velocity (m/s)	4.5	4.5	4.5	4.5
	Reynolds number	5500	5500	5500	5500
Fuel	H₂ flowrate (g/s)	0.125	0.104	0.070	0.018
	CH₄ flowrate (g/s)	0.015	0.058	0.126	0.231
	H₂ mole fraction	99%	94%	82%	37%
	CH₄ mole fraction	1%	6%	18%	63%
	Velocity (m/s)	13.0	11.3	8.7	4.6
Velocity Ratio (u_f/u_0)		2.9	2.5	1.9	1.0
Rate of Heat Release (kW)		15.9	15.5	14.9	13.8

Table 5.2. Flow conditions for the different test runs for model development.

Location	Mode	Density Ratio = 14.5		Density Ratio = 11.0		Density Ratio = 7.0	
		Measured (Hz)	Calculated (Hz)	Measured (Hz)	Calculated (Hz)	Measured (Hz)	Calculated (Hz)
Tap #1	f1	434±10	430	423±10	430	423±10	430
			980 ^a		928 ^a		843 ^a
	f2	900	912 ^b 900 ^c	868	877 ^b 859 ^c	752	817 ^b 791 ^c
	f3	1508	1430	1453	1370	1270	1269
Tap #2	f1	434	430	434	430	423	430
	f2	933	980	868	928	770	843
	f3	1508	1430	1453	1370	1269	1269
Tap #3	f1	433	430	434	430	423	430
	f2	1017	980	889	928	791 / 900	843
	f3	1580	1430	1518	1370	1400	1269
Tap #4	f1	438	430	434	430	423	430
			980 ^a		928 ^a		843 ^a
	f2	1011	912 ^b 1011 ^c	911	877 ^b 955 ^c	781 / 900	817 ^b 864 ^c
	f3	1528	1430	1453	1370	1399	1269

a – Frequency calculated using full mixing model.

b – Frequency calculated using jet mixing length model.

c – Frequency calculated using acoustically driven entrainment model.

When method is not indicated for a calculated frequency, a full mixing model is used by default.

Table 5.3. Comparison of measured spectral peak frequencies and calculated resonance frequencies for isothermal flow conditions

Location	Mode	Density Ratio = 14.5	Density Ratio = 11.0	Density Ratio = 7.0
Tap #1	f1	477 Hz \pm 10Hz	466 Hz \pm 10Hz	434 Hz \pm 10Hz
	f2	1323	1270	1171
Tap #2	f1	477	455	445
	f2	1345	1312	1117
Tap #3	f1	520	474	445
	f2	1410	1331	1204
Tap #4	f1	520	465	434
	f2	1410	1331	1204

Table 5.4. Comparison of measured spectral peak frequencies under reacting flow conditions.

ρ_o / ρ_f	u_f / u_o	u_f (m/s)	u_o (m/s)	Heat Release (kW)	Forcing frequency (Hz)	Flame-Acoustic Interaction	Re_{O_2}
16	3	18	6	22.1	None	Low	3700, 4900, 7300
16	3	18	6	22.1	300 Hz	High-Symmetric	3700, 4900, 7300
16	3	18	6	22.1	1150 Hz	High-Asymmetric	3700, 4900, 7300

Table 7.1. Test conditions for flame response to acoustic forcing at characteristic frequencies.

ρ_o / ρ_f	u_f / u_o	Oxidizer		Fuel	
		Y_{O_2}	Y_{He}	Y_{H_2}	Y_{Ar}
16	3	1	0	1	0
15	3	0.997	0.003	0.997	0.003
14	3	0.993	0.007	0.993	0.007
13	3	0.988	0.012	0.988	0.012
12	3	0.983	0.017	0.983	0.017
11	3	0.978	0.022	0.978	0.022
10	3	0.971	0.029	0.971	0.029
9	3	0.962	0.038	0.962	0.038
8	3	0.952	0.048	0.952	0.048
7	3	0.939	0.061	0.939	0.061
6	3	0.922	0.078	0.922	0.078
5	3	0.899	0.101	0.899	0.101
4	3	0.867	0.134	0.867	0.134
3	3	0.817	0.183	0.817	0.183
2	3	0.731	0.27	0.731	0.27
1	3	0.545	0.455	0.545	0.455

Table 7.2. Test conditions for the density ratio variation experiments.

Configuration	Velocity		Mass Flow		Re	
	(m/s)		(kg/s)			
	O2	H2	O2	H2	O2	H2
H2-O2-H2	6	18	1.425E-3	1.825E-4	3700,4900,7300	1100,1300,1600
	O2/N2	H2	O2/N2	H2	O2/N2	H2
O2/N2-H2-O2/N2	17.8	5	2.603E-3	7.603 E-5	7320,8783,10980	450,600,900

Table 7.3. Test conditions for the reversal of density gradient experiments.

Configuration	Velocity		Density Ratio	Heat Release (kW)	Forcing
	(m/s)				
	Center	Co-Flow			
Baseline ^ψ	4.5	13.5	7.0 or 15.2	15	Unforced
H2+Ar – O2+He – H2+Ar	4.5	13.5	7.0	15	Forced, 1150Hz
H2+He – O2+Ar – H2+He	4.5	13.5	15.2	15	Forced, 1150Hz

Table 7.4. Test conditions for change in flame heat release experiments.

Case	ρ_o / ρ_f	u_f / u_o	J_o / J_f	ρ_o	ρ_f	u_o	u_f	J_o	J_f
				(kg/m ³)	(kg/m ³)	(m/s)	(m/s)	(kg.m/s ²)	(kg.m/s ²)
1	7.99	5.27	0.86	1.3	0.163	4.47	23.57	0.0047	0.0055
2	2.0	3.0	0.67	0.99	0.50	4.5	13.5	0.0036	0.0055

Table 7.5. Test conditions for variation in jet momentum experiments.

^ψ Baseline Case could be either H2+Ar – O2+He – H2+Ar or H2+He – O2+Ar – H2+He.

Flow Conditions		A	D
Density Ratio (ρ_o/ρ_f)		14.5	3
Oxygen	O ₂ flow rate (g/s)	1.06	1.06
	Velocity (m/s)	4.5	4.5
	Reynolds number	5500	5500
Fuel	H ₂ flow rate (g/s)	0.125	0.018
	CH ₄ flow rate (g/s)	0.015	0.231
	H ₂ mole fraction	98.53%	37.41%
	CH ₄ mole fraction	1.47%	62.59%
	Velocity (m/s)	13.0	4.6
Velocity Ratio (u_f/u_o)		2.9	1.0
Rate of Heat Release (kW)		15.9	13.8

Table 7.6. Flow conditions for the simultaneous measurement of pressure and chemiluminescence oscillations.

Case	ρ_o/ρ_f	u_f/u_o	J_o/J_f	ρ_o (kg/ m ³)	ρ_f (kg/ m ³)	u_o (m/s)	u_f (m/s)	J_o (kg.m/ s ²)	J_f (kg.m/ s ²)
1	7.99	3.02	2.62	1.3	0.163	4.47	13.50	0.0047	0.0018
2	7.99	3.36	2.12	1.3	0.163	4.47	15.03	0.0047	0.0022
3	7.99	3.64	1.80	1.3	0.163	4.47	16.28	0.0047	0.0026
4	7.99	4.01	1.49	1.3	0.163	4.47	17.91	0.0047	0.0032
5	7.99	4.51	1.18	1.3	0.163	4.47	20.17	0.0047	0.0040
6	7.99	5.03	0.94	1.3	0.163	4.47	22.50	0.0047	0.0050
7	7.99	5.27	0.86	1.3	0.163	4.47	23.57	0.0047	0.0055

Table 7.7. Test conditions for velocity ratio experiments.

Case	ρ_o / ρ_f	u_f / u_o	J_o / J_f	ρ_o (kg/m ³)	ρ_f (kg/m ³)	u_o (m/s)	u_f (m/s)	J_o (kg.m/s ²)	J_f (kg.m/s ²)
1	6.0	3.0	1.99	1.21	0.20	4.5	13.5	0.0045	0.0022
2	5.0	3.0	1.67	1.18	0.24	4.5	13.5	0.0044	0.0026
3	4.0	3.0	1.33	1.15	0.29	4.5	13.5	0.0042	0.0032
4	3.0	3.0	1.00	1.09	0.36	4.5	13.5	0.0040	0.0040
5	2.0	3.0	0.67	0.99	0.50	4.5	13.5	0.0036	0.0055

Table 7.8. Test conditions for variation in jet momentum through variation in jet densities.

Case	ρ_o / ρ_f	u_f / u_o	J_o / J_f	ρ_o (kg/m ³)	ρ_f (kg/m ³)	u_o (m/s)	u_f (m/s)	J_o (kg.m/s ²)	J_f (kg.m/s ²)
1	7.99	3.36	2.12	1.3	0.163	4.47	15.03	0.0047	0.0022
2	7.99	3.64	1.80	1.3	0.163	4.47	16.28	0.0047	0.0026
3	7.99	4.01	1.49	1.3	0.163	4.47	17.91	0.0047	0.0032
4	7.99	4.51	1.18	1.3	0.163	4.47	20.17	0.0047	0.0040
5	7.99	5.27	0.86	1.3	0.163	4.47	23.57	0.0047	0.0055

Table 7.9. Test conditions for variation in jet momentum through variation in jet velocities.

Case	Y_{CH_4}	Y_{H_2}	ρ_o / ρ_f	u_f / u_o	u_o (m/s)	u_f (m/s)	Heat Release (kW)	ρ_f (kg/m ³)	ρ_o (kg/m ³)
1	0.4	0.6	6	3	4.5	13.5	12.8	0.222	1.33
2	0.5	0.5	6	3	4.5	13.5	11.2	0.227	1.36
3	0.6	0.4	6	3	4.5	13.5	10.2	0.231	1.38
4	0.7	0.3	6	3	4.5	13.5	9.53	0.233	1.40
5	0.8	0.2	6	3	4.5	13.5	9.02	0.235	1.41
6	0.9	0.1	6	3	4.5	13.5	8.62	0.236	1.42

Table 7.10. Test conditions for flame-acoustic experiments using GH₂-GCH₄ blended fuel and Oxygen.

Appendix C: Gas Properties

Gas	γ	MW (gm/mole)	μ (kg/m.s)	Q (Joules/Mole)
Air	1.40	28.94	1.860860611x10E-5	-
Helium	1.667	4.0026	-	-
Argon	1.667	39.95	-	-
Methane	1.31	16.00	-	814000
Oxygen	1.40	32.00	2.0497443625x10E-5	-
Hydrogen	1.41	2.00	8.8459046629x10E-6	242000

Ambient Temperature (T_a): 300K

Ambient Pressure (P_a) : 1 atm

Universal Gas Constant (R_u) 8.314 (J/K/mole)

Gas Specific Gas Constant : (R_u / MW)

Bibliography

- Abramzon, B. and Sirignano, W.A. (1988) "Droplet Vaporization Model for Spray Combustion Calculations," *AIAA 88-0636*.
- Anderson, T.J., and Winter, M. (1992) "Measurement of the Effect of Acoustic Disturbances on Droplet Vaporization Rate," *AIAA 92-0108*.
- Anderson, W.E., Miller, K.L., Ryan, H.M., Pal, S., and Santoro, R.J. (1998) "Effects of Periodic Atomization on Combustion Instability in Liquid-Fueled Propulsion Systems," *Journal of Propulsion and Power*, vol. 14, no. 5.
- Annaswamy, A.M., Fleifil, M., Rumsey, J.W., Prasanth, R., Hathout, J.P., and Ghoniem, A.F. (2000) "Thermoacoustic instability: model-based optimal control designs and experimental validation," *IEEE Trans. Control Systems Technol.* 8 (6), pp. 905–918.
- Ashurst, W.T., and McMurtry, P.A. (1989) "Flame Generation of Turbulence: Vortex Dipoles from Monopoles", *Combustion Science and Technology*, vol.66, nos.1,2, pp.17-37.
- Baker, L., Jr. and Steffen, F.W. (1958) "Screaming tendency of the gaseous-Hydrogen - liquid-Oxygen propellant combination," NACA-RM-E58E09.
- Barr, P.K., and Keller, J.O. (1994) "Premixed combustion in a periodic flow field. Part II: The importance of flame extinction by fluid dynamic strain", *Combustion and Flame*, vol. 99, issue 1, pp. 43-46.
- Barrère, M., and Williams, F.A. (1969) "Combustion Oscillations in Industrial Combustion Chambers", *Twelfth Symposium (International) on Combustion*, The Combustion Institute, pp. 169-181.
- Barsotti, R.J., Datsko, S.C., Louison, R., Kovach, R.J., Miller, D.J., and Pulliam, W.P., (1968) "Development of liquid Oxygen/liquid Hydrogen thrust chamber for the M-1 engine," NASA-CR-54813
- Batley, G.A., McIntosh, A.C., Brindley, J., Falle, S.A.E.G. (1994) "A numerical study of the vorticity field generated by the baroclinic effect due to the propagation of a planar pressure wave through a cylindrical premixed laminar flame", *J. Fluid Mech.* vol. 279, pp. 217-237
- Batley, G.A., McIntosh, A.C., Brindley, J. (1996) "Baroclinic distortion of laminar flames", *Proceedings: Mathematical, Physical and Engineering Sciences*, vol. 452, no. 1945. pp. 199-221.

Bellman, D.R., Humphrey, J.C., and Male, T. (1953) "Photographic Investigation of Combustion in a Two-Dimensional Transparent Rocket Engine", *NACA Report no. 1134*

Berman, K., and Cheney, S.H (1953) "Combustion Studies in Rocket Motors," *Journ. Amer. Rocket Soc.*, vol. 23, no. 2, p. 89.

Bisio, G. and Rubatto, G. (1999) "Sondhauss and Rijke oscillations – thermodynamic analysis, possible applications and analogies", *Energy* 24:117-131.

Bloxside, G., Dowling, A., Langhorne, P. (1988) "Reheat Buzz: An Acoustically Coupled Combustion Instability. Part 2. Theory", *J. Fluid Mech.* vol. (193), pp. 445-473.

Boys, S.F. and Schofield, A. (1943) "Investigations of Secondary Peaks," Propulsion Development Establishment, Report 1943/5, Abesorth, England, UK.

Broda, J.C., Seo, S., Santoro, R.J., Shirhattikar, G., Yang, V. (1991) "An experimental study of combustion dynamics of a premixed swirl injector," *Proc. Combust. Inst.* 27 pp.1849–1856.

Büchner, H., and Leuckel, W. (1996) "The influence of fuel / air mixture oscillations on the formation of self-sustained combustion instabilities in premixed combustion systems," *Unsteady Combustion*, F. Culick *et al.* (eds.), Kluwer Academic Publishers, pp. 71-82.

Buckmaster, J., and Clavin, P. (1992) *Proc. Combust. Inst.* vol. 24, pp.29–36.

Buffum, F.G., and Williams, F.A. (1967) "The Response of a Turbulent Jet to Transverse Acoustic Fields," *Proceedings of the 1967 Heat Transfer and Fluid Mechanics Institute*, P.A., Libby, D.B. Olfe and C.W. Van Atta, Eds., Stanford University Press, pp. 247-276

Candel, S.M. (1992) "Combustion Instabilities Coupled by Pressure Waves and Their Active Control," *Twenty-fourth Symposium (International) on Combustion*, The Combustion Institute, pp. 1277-1296.

Candel, S.M., Durox, D. and Schuller, T. (2004) "Flame interactions as a source of noise and combustion instabilities," *Collection of Technical Papers - 10th AIAA/CEAS Aeroacoustics Conference*, p 1444-1454

Chandrasekhar, S. (1961) *Hydrodynamic and Hydromagnetic Stability*. Dover, New York; Chap X, p.444, Sec.94

- Chehroudi, B., and Talley, D. G. (2002) "Interaction of Acoustic Waves with a Cryogenic Nitrogen Jet at Sub- and Supercritical Pressures," *AIAA-2002-34*.
- Chiang, C.H., Raju, M.S. and Sirignano, W.A. (1989) "Numerical Analysis of Convecting Vaporizing Fuel Droplet with Variable Properties," *AIAA 89-0834*.
- Chu, B.T. (1953) "Mechanism of Generation of pressure waves at a plane flame front," 4th Symposium (International) on Combustion, pp 603-612.
- Chu, B.T. (1956) "Stability of systems containing a heat source - the Rayleigh criterion," NACA-RM-56D27. Washington D.C.: NACA
- Chu, B.T. (1965) "On the energy transfer to small disturbances in fluid flow," *Acta Mechanica* vol. 1, pp. 215-234.
- Clark, B.J. (1964), "Breakup of a Liquid Jet in a Transverse Flow of Gas," NASA TN D-2424.
- Clavin, P., and Sun, J., (1991), "Theory of Acoustic Instabilities of Planar Flames Propagating in Sprays or Particle-Laden Gases," *Combust. Sci. Technol.* vol. 78, pp.265–288.
- Clavin, P., Pelcé, P., He, L. (1990) "One-dimensional vibratory instability of planar flames propagating in tubes," *J. Fluid Mech.* vol. 216, pp. 299–322.
- Clayton, R. M.; Rogero, R. S. (1965) "Experimental measurements on a rotating detonation-like wave observed during liquid rocket resonant combustion", Report Number: JPL-TR-32-788, NASA-CR-67259
- Cohen, J.M., Wake, B.E., and Choi, D. (2003) "Investigation of Instabilities in a Lean, Premixed Step Combustor," *J. Propuls. Power* 19 (1) pp. 81–88.
- Conley, A., Vaidyanathan, A., and Segal, C. (2007) "Heat Flux Measurements for a GO₂/GH₂ Single-Element, Shear Injector," *Journal of Spacecraft and Rockets*, vol. 44, no. 3.
- Crocco, L. (1951) "Aspects of Combustion Instability in Liquid Propellant Rockets," *Journ. Amer. Rocket Soc.*, Part I: vol. 21
- Crocco, L. (1952) "Aspects of Combustion Instability in Liquid Propellant Rockets," *Journ. Amer. Rocket Soc.*, Part II: vol. 22.
- Crocco, L., Cheng, S.I. (1953) "High Frequency Combustion Instability in Rocket Motor with Concentrated Combustion," *Jour. Am. Rocket Soc.*, vol. 23, no. 5, pp. 301-313.

Crocco, L., Cheng, S.I. (1956) *Theory of Combustion Instability in Liquid Propellant Rocket Motors*, AGARD monograph, No. 8, Butterworths Scientific Publications, London..

Crocco, L., Grey, J., and Harrje, D.T. (1960) "Theory of Liquid Propellant Rocket Combustion Instability and its Experimental Verification," *ARS Journal*, vol. 30, no. 2.

Crocco, L. (1965) *Tenth Symposium (International) on Combustion*, The Combustion Institute, pp. 1011.

Crocco, L., Harrje, D.T., Sirignano, W.A., Bracco, F.V., Mitchell, C.E., Tang, P.K., Williams, R.M., Black, G.R., Stinger, W.A. (1967) "Nonlinear Aspect of Combustion Instability in Liquid Rocket Motors," NASA CR 72270.

Crocco, L., and Sirignano, W.A. (1967) "Behavior of Supercritical Nozzles Under Three-Dimensional Oscillatory Conditions," AGARDograph No. 117

Crocco, L. (1969) "Research on Combustion Instability in Liquid Propellant Rockets," *Twelfth Symposium (International) on Combustion*, The Combustion Institute, pp. 85- 99.

Crump, J.E., Schadow, K.C., Yang, V., Culick, E.C. (1986) "Longitudinal Combustion Instabilities in Ramjet Engines : Identification of Acoustic Modes," *J. Propuls. Power* 2 (2) pp. 105 -109.

Culick, F.E.C. (1971) "Nonlinear Growth and Limiting Amplitude of Acoustic Waves in Combustion Chambers," *Comb. Sci. and Tech.*, vol..3, no.1, p. 16.

Culick, F.E.C. (1973) "The Stability of One-Dimensional Motions in a Rocket Motor," *Comb. Sci. and Tech.*, vol.7, no.4, pp.165-175.

Culick, F.E.C. (1975 a) "Nonlinear behavior of acoustic waves in combustion chambers," Report Number: NASA-CR-149367.

Culick, F.E.C. (1975 b) "Stability of Three-Dimensional Motions in a Combustion Chamber," *Comb. Sci. and Tech.*, vol. 10, issue 3 -4, pp 109-124 .

Culick, F. E. C. (1976) "Nonlinear behavior of acoustic waves in combustion chambers," Parts I and II, *Acta Astronautica* vol. 3, pp.714-757.

Culick, F. E. C. (1987) "A Note on Rayleigh Criterion," *Combustion Science and Technology* vol. 56, issue 4-6, pp.159-166

- Culick, F., and Yang, V. (1995) “Overview of Combustion Instabilities in Liquid-Propellant Rocket Engines,” *Liquid Rocket Engine Combustion Instability*, volume 169 of *Progress in Astronautics and Aeronautics*, pp. 3–37. AIAA.
- Culick, F.E.C. (1996) “Combustion Instabilities in Propulsion Systems,” *Unsteady Combustion*, edited by F. Culick *et al.* , NATO ASI Series, Series E: Applied Sciences – vol. 306, pp. 173-241.
- Dattarajan, S., Lutomirski, A., Lobbia, R., Smith, O.I., Karagozian, A.R. (2006) “Acoustic excitation of droplet combustion in microgravity and normal gravity”, *Combustion and Flame*, vol. 144, issues 1-2, pp. 299-317
- Davis, D.W., Chehroudi, B. (2007) “Measurements in an Acoustically Driven Coaxial Jet under Sub-, Near-, and Supercritical Conditions,” *Journal of Propulsion and Power*, (0748-4658) vol. 23 no. 2, pp. 364-374
- Deckker, B.E.L., and Sampath, P. (1971) “The Mechanism of Vibration in Enclosed Laminar Diffusion Flames,” *Thirteenth Symposium (International) on Combustion*, The Combustion Institute, pp. 505 - 516.
- Dowling, A.P. (1992) “Thermoacoustic Sources and Instabilities,” in *Modern Methods in Analytical Acoustics – Lecture Notes*, Springer-Verlag, pp. 378-404.
- Dowling, A.P.(1997) “Nonlinear self-excited oscillations of a ducted flame”, *J. Fluid Mech.* vol. 346, pp.271-290
- Dowling, A.P., and Morgans, A.S. (2005) “Feedback Control of Combustion Oscillations,” *Annu. Rev. Fluid Mech.* vol. 37, pp.151–182
- Ducruix, S., Durox, D., and Candel, S. (2001) *Proc. Combust. Institute* 28:765-773
- Ducruix, S., Schuller, T., Durox, D., and Candel, S. (2003) “Combustion Dynamics and Instabilities: Elementary Coupling and Driving Mechanisms,” *J. Propul. Power* 19, pp. 722-734
- Duff, R.E., Harlow, F.H., and Hirt, C.W. (1962) “Effects of diffusion on interface instability between gases,” *Phys. Fluids*, vol. 5, pp.417-425.
- Durox, D., Schuller, T., and Candel, S. (2002), *Proc. Combust. Inst.*, 29, 69–75.
- Ebrahimi, R., Mazaheri, K., and Ghafourian, A. (2000) “Mode Identification of High Amplitude Pressure Waves in Liquid Rocket Engines,” *Journal of Sound and Vibration*, vol. 229, issue 4, pp. 973-991.

- Ellis, H., Odgers, I., Stosick, A.J., Van de Verg, N., and Wick, R.S. (1953) "Experimental Investigation of Combustion Instability in Rocket Motors," Fourth Symposium on Combustion.
- Ellis, H. (1960) "*Liquid Propellant Rocket Combustion Research*," Edwin G. Baetger, II Colloquium, Princeton University, February 9.
- Farhat, S., Kleiner, D., and Zhang, Y. (2005) "Jet diffusion flame characteristics in a loudspeaker-induced standing wave", *Combustion and Flame*, volume 142, issue 3, pp. 317-323
- Feldman, K.T.Jr, Hirsch, H., and Carrier, R.L. (1966) "Experiments on the Sondhauss Thermoacoustical Phenomenon," *J. Acoust. Soc. Am.* vol.39, p.1236
- Feldman, K.T. (1968) "Review of the literature on Rijke thermoacoustic phenomena," *Journal of Sound and Vibration*, vol. 7, issue 1, pp. 83-89.
- Fichot, F., Harstad, K., and Bellan, J. (1993) "Unsteady Evaporation and Combustion of a Drop Cluster Inside a Vortex," *AIAA 93-0695*
- Fischbach, S.R., Flandro, G.A., and Majdalani, J. (2007) "Acoustic Streaming Effects in Liquid Rocket Engines with Transverse Mode Oscillations," *AIAA 2007-5561*.
- Flandro, G.A., Majdalani, J., and Sims, J.D. (2004) "On Nonlinear Combustion Instability in Liquid Propellant Rocket Engines," *AIAA-2004-3516*
- Foust, M.J., Deshpande, M., Pal, S., Ni, T., Merkle, C.L., and Santoro, R.J. (1996) "Experimental and analytical characterization of a shear coaxial combustor GO₂/GH₂ flowfield," *AIAA-1996-646*
- Gaydon, A.G. and Wolfhard, H.G. (1960) *Flames, Their Structure, Radiation and Temperature*, Chap. VII, Chapman & Hall.
- Gerk, T. J. and Karagozian, A. R. (1996) *Twenty-sixth Symposium (International) on Combustion* pp. 1095-1102. The Combustion Institute, , Pittsburgh, PA
- Glogowski, M., Bar-Gill, M., Puissant, C., Kaltz, T., Milicic, M., and Miccit, M. (1994) "Shear Coaxial Injector Instability Mechanisms," *AIAA-1994-2774*
- Grad, H. (1949) "Resonance Burning in Rocket Motors," *Communications on Pure and Applied Mathematics*, vol. 2, pp. 79-102.
- Gulati, A., Mani, R. (1992) "Active Control of Unsteady Combustion-Induced Oscillations," *J. Propulsion Power*, vol. 8, issue 5, pp.1109–1115.

- Gunder, D.F., and Friant, D.R. (1950) "Stability of Flow in a Rocket Motor," *Journal of Applied Mechanics*, vol. 17, pp 327-333.
- Gutmark, E., Parr, T.P., Hanson-Parr, D.M., Schadow, K.C. (1989) Seventh Symposium on Turbulent Shear Flows 23, 1–6.
- Harrje, D.T., Stinger, W.A., and Sirignano, W.A. (1967) "Flow Behavior with Acoustic Liners," ICRPG 4th Combustion Conference, Menlo Park, California.
- Harrje, D.T., and Reardon, F.H. (eds.) (1972) *Liquid Propellant Rocket Combustion Instability*, NASA SP-194
- Hegde, U.G., Reuter, D., Daniel, B.R., Zinn, B.T. (1987) "Flame Driving of Longitudinal Instabilities in Dump Type Ramjet Combustors," *Comb. Sci. and Tech.*, vol. 55, pp. 125-138.
- Heidmann, M.F. (1965) "Oxygen-Jet Behavior During Combustion Instability in a Two-Dimensional Combustor," NASA TN D-2725
- Heidmann, M.F., and Feiler, C. E. (1967) "Control of transverse instability in rocket combustors Patent," NASA-CASE-XLE-04603
- Heidmann, M.F., and Wieber, P.R. (1966) "Analysis of frequency response characteristics of propellant vaporization," NASA TN D-3749
- Heidmann, M.F., and Groeneweg, J.F. (1969) "Analysis of the dynamic response of liquid jet atomization to acoustic oscillations," NASA TN D-5339
- Herding, G., Snyder, R., Scouflaire, P., Rolon, C. and Candel, S. (1996) "Flame Stabilization in Cryogenic Propellant Combustion," *Twenty-Sixth Symposium (International) on Combustion*, The Combustion Institute, pp. 2041 – 2047.
- Howe, M.S. (1998) *Acoustics of Fluid-Structure Interactions*. Cambridge University Press, Cambridge.
- Hsieh, D.Y. (1978) "Interfacial stability with mass and heat-transfer," *Phys. Fluids*, vol. 21, pp.745 -748.
- Hulka, J. and Hutt, J. (1994) "Instability Phenomena in Liquid Oxygen/Hydrogen Propellant Rocket Engines," *Liquid Rocket Engine Combustion Instability*, volume 169 of *Progress in Astronautics and Aeronautics*, AIAA, pp 39-71.
- Ingebo, R. D. (1966) "Atomization of ethanol jets in a combustor with oscillatory combustion-gas flow," NASA-TN-D-3513

Jahnke, C.C and Culick, F.E.C., (1994) "Application of dynamical systems theory to nonlinear combustion instabilities," *Journal of Propulsion and Power* (0748-4658) vol. 10 no. 4, pp 508-517

Keller, J.J. (1995) "Thermoacoustic Oscillations in Combustion Chambers of Gas Turbines," *AIAA Journal*, vol. 33 (12), pp. 2280-2287

Kendrick, D.W., Zsak, T.W., and Zukoski, E.E. (1996) "An experimental and numerical investigation of premixed combustion in a vortex in a laboratory dump combustor," *Unsteady Combustion*, F. Culick et al. (eds.), *Kluwer Academic Publishers*, pp. 33-69.

Kim, J.S., Williams, F.A., Ronney, P.D. (1996) "Diffusional-thermal instability of diffusion flames," *J. Fluid Mech* , vol. 327, pp. 273-301

Kim, J. S. and Williams, F. A. (1998) "Effects of non-homogeneities on the eigenmodes of acoustic pressure in combustion chambers," *Journal of Sound and Vibration*, vol. 209, no 5, pp 821-843.

Kinsler, L.E., Frey, A.R., Coppens, A.B., Sanders, J.V. (1982) *Fundamentals of Acoustics*. John Wiley and Sons; Chap 5, p.107, Sec.5.7

Kumar, S. (2003) "An Experimental Investigation of Richtmyer-Meshkov Instability," PhD Thesis, California Institute of Technology.

Kydd, P.H. (1969) "Analysis and Experiments on Unsteady Flow in Gas Turbine Main Combustors," *Twelfth Symposium (International) on Combustion*, The Combustion Institute, pp. 183 – 192.

Lang, W., Poinso, T., Candel, S.M. (1987) "Active control of combustion instability," *Combust. Flame*, vol. 70, pp.281–289.

Langhorne, P.J. (1988) "Reheat Buzz: An Acoustically Coupled Combustion Instability. Part 1. Experiment," *J. Fluid Mech.*, vol. 193, pp. 417-443.

Langhorne, P.J., Dowling, A.P., and Hooper, N. (1990) "Practical Active Control System for Combustion Oscillations," *J. Propulsion and Power*, vol. 6, No. 3, pp. 324-333.

Laverdant, A., Poinso, T. and Candel, S. (1986), "Mean temperature field effect on acoustic mode structure in dump combustor," *J. Propulsion and Power*, vol. 2, pp 311-316.

Lecourt, R, and Foucaud, R. (1987) "Experiments on stability of liquid propellant rocket motors," *AIAA-1987-1772*

- Ledder, G., and Kapha, A.K. (1991) "The Response of Premixed Flames to Pressure Perturbations," *Combust. Sci. Technol.* vol.76, pp. 21–44.
- Lelevier, R., Lasher, G.J. and Bjorklund, F. (1955) "Effect of a density gradient on Taylor instability," Technical Report UCRL-4459, University of California Radiation Laboratory.
- Lieuwen, T.C. (1999) "Investigation of Combustion Instability Mechanisms in Premixed Gas Turbines," PhD Thesis, Georgia Institute of Technology.
- Lieuwen, T., Neumeier, Y., Zinn, B. (1998) "The Role of Unmixedness and Chemical Kinetics in Driving Combustion Instabilities in Lean Premixed Combustors," *Combust. Sci. Technol.* vol.135, pp.193–211.
- Lieuwen, T., (2001) "Theoretical Investigation of Unsteady Flow Interactions With a Premixed Planar Flame," *J.Fluid Mech.* vol. 435, pp.289-303
- Lieuwen, T. (2002) "Experimental Investigation of Limit-Cycle Oscillations in an Unstable Gas Turbine Combustor," *J. Propuls. Power* 18 (1) pp. 61–67.
- Lieuwen, T. (2003) "Statistical Characteristics of Pressure Oscillations in a Premixed Combustor," *Journal of Sound and Vibration*, Volume 260, pp.3-17
- Liu, F., McIntosh, A. C. and Brindley, J. (1993) "A numerical investigation of Rayleigh-Taylor effects in pressure wave-premixed flame interactions," *Combust. Sci. Technol.* 91. 373-386.
- Male, T., Kerslake, W.R., and Tischler, A.O. (1954) "Photographic study of rotary screaming and other oscillations in a rocket engine," NACA-RM-E54A29
- Male, T. and Kerslake, W.R (1954) "A method for prevention of screaming in rocket engines," NACA-RM-E54F28A
- Mallard, E.E., and Le Chatelier, H. (1883) *Ann. Mines, Partie Scientifique* Ser. 8, no. 4, 274.
- Marble, F.E., and Candel, S.M., (1978) "An Analytical Study of the Non-Steady Behavior of Large Combustors," *Proc. Combust. Inst.* 17 pp. 761–769.
- Marble, F.E., and Cox, D.W., Jr. (1953) "Servo-Stabilization of Low-Frequency Oscillations in a Liquid Bipropellant Rocket Motor," *Am. Rocket Soc. Journal* vol. 23 pp. 63-81
- Margolis, S.B. (1993) "Nonlinear Stability of Combustion-Drive Acoustic-Oscillations in Resonance Tubes," *Journal of Fluid Mechanics*, vol. 253, pp. 67-103.

Markstein, G.H., and Squire, W. (1955) "On the stability of a plane flame front in oscillating flow," *The Journal of the Acoustical Society of America*, vol. 27 issue 3 pp:416 -424.

Markstein, G. (1970) in: Proc. Sixth Natl. Congr. Appl. Mech., Cambridge, MA, pp. 11-33.

Marxman, G.A. and Wooldridge, C.E. (1969) "Finite-Amplitude Axial Instability in Solid-Rocket Combustion," *Twelfth Symposium (International) on Combustion*, The Combustion Institute, pp. 115-127.

Maslen, S.H., and Moore, F.K. (1956) "On Strong Transverse Waves Without Shocks in a Circular Cylinder," *Journ. Aero Sci.*, vol. 23, no. 6, pp. 583-593.

Matalon, M. (2007) "Intrinsic Flame Instabilities in Premixed and Nonpremixed Combustion," *Annu. Rev. Fluid Mech.* 39:163-91

McIntosh, A.C. (1991) "Pressure Disturbances of Different Length Scales Interacting with Conventional Flames," *Combustion Science and Technology*, vol. 75, pp. 287-309.

McIntosh, A.C. (1993) "The Linearised Response of the Mass Burning Rate of a Premixed Flame to Rapid Pressure Changes," *Combust. Sci. Technol.* vol. 91, issue 4-6, pp. 329-346.

McIntosh, A.C, (1999) *Philos. Trans. R. Soc. London A* 357, 3523-3538.

McQuay, M.Q., Dubey, R.K., Carvalho Jr., A. (2000) "The effect of acoustic mode on time-resolved temperature measurements in a Rijke-tube pulse combustor," *Fuel* 79 pp.1645-1655.

Meshkov, E.E. (1969) "Instability of the interface of two gases accelerated by a shock wave," *Sov. Fluid Dyn.*, 4:101.

Miesse, C.C. (1955) "Correlation of Experimental Data on the Disintegration of Liquid Jets," *Ind. Eng. Chem.*, vol. 47, no. 9, pp. 1690-1701.

Mitchell, C.E. (1994) "Analytical Models for Combustion Instability," *Liquid Rocket Engine Combustion Instability*, volume 169 of *Progress in Astronautics and Aeronautics*, AIAA, pp 403-430.

Moore, F.K., and Maslen, S.H. (1954) "Transverse Oscillations in a Cylindrical Combustion Chamber," NACA TN 3152, 1954.

Mongia, H.C., Held, T.J., Hsiao, G.C. and Pandalai, R.P. (2003) "Challenges and progress in controlling dynamics in gas turbine combustors," *J. Prop. Power* 19(5) : 822-29

Morrell, G. (1963) "Rate of Liquid Jet Breakup by a Transverse Shock Wave," NASA-TN-D-1728.

Morrell, G., Povinelli, F. P. (1963) "Breakup of various liquid jets by shock waves," NASA-TP-3-63

Morrell, G., Povinelli, F. P. (1964) "Breakup of various liquid jets by shock waves and applications to resonant combustion," NASA-TN-D-2423

Oefelein, J.C. and Yang, V. (1997) "Analysis of Hydrogen-Oxygen mixing and combustion processes at high pressures," *AIAA-1997-0798*

Oran, E.S., and Gardner J.H. (1985) "Chemical-Acoustic Interactions in Combustion Systems", *Prog. Energy Combust. Sci.* 11, 253-276.

Osborn, J.R., and Bonnell, J.M (1960 a) "On the Importance of Combustion Chamber Geometry in High Frequency Oscillations in Rocket Motors," paper presented at the ARS Semi-Annual Meeting, Los Angeles, California, May 9-12, 1960.

Osborn, J.R., and Bonnell, J.M (1960 b) "On the Effect of Fuel Composition on High Frequency Oscillations in Rocket Motors Burning Premixed Hydrocarbon Gases and Air," paper presented at the ARS 15th Annual Meeting, Washington D.C., December 5-8, 1960.

Pariel, J.M., and Martin, L. S. (1969) "Contribution to the Study of Nonsteady-State Combustion in Industrial Hearths," *Twelfth Symposium (International) on Combustion*, The Combustion Institute, pp. 193- 201.

Pelcé, P., and Rochwerger, D.(1992), "Vibratory instability of cellular flames propagating in tubes," *J. Fluid Mech.* 239, 293–307.

Petchenko, A., Bychkov, V., Akkerman, V., Eriksson, L. (2006) "Violent Folding of a Flame Front in a Flame-Acoustic Resonance," *Physical Review Letters*, PRL 97, 164501

Pickford, R., and Peoples, R.G. (1960) "The inherent Stability of the Combustion Processes," paper presented at the ARS 15th Annual Meeting, Washington , D.C., December 5-8, 1960.

Poinsot, T., Trouvé, A., Veynante, D., Candel, S. (1987) "Vortex driven acoustically coupled combustion instabilities," *J. Fluid Mech.* 177: 265–92

Poinsot, T., Veynante, D., Bourienne, F., Candel, S., Esposito, E., and Surget, J. (1988) "Initiation and Suppression of Combustion Instabilities by Active Control", *Twenty-Second Symposium (International) on Combustion*, The Combustion Institute, pp. 1363-1370.

Prasad, A., and Williamson, C.H.K. (1997) "The instability of the shear layer separating from a bluff body", *Journal of Fluid Mechanics*, 133, pp. 375-402.

Preetham, and Lieuwen, T. (2004) "Nonlinear Flame-Flow Transfer Function Calculations: Flow Disturbance Celerity Effects Part 2," AIAA-2005-0543.

Preetham, and Lieuwen, T. (2005) "Nonlinear Flame-Flow Transfer Function Calculations: Flow Disturbance Celerity Effects ," AIAA-2004-4035.

Price, E.W. (1959) "Combustion Instabilities in Solid Propellant Rocket Motors," *Astronautica Acta*, vol. 5.

Price, E.W. (1969) "Recent Advances in Solid Propellant Combustion Instability," *Twelfth Symposium (International) on Combustion*, The Combustion Institute, pp. 101 – 113.

Priem, R.J., and Rice, E.J. (1969) "Combustion Instability with Finite Mach Number Flow and Acoustic Liners," *Twelfth Symposium (International) on Combustion*, The Combustion Institute, pp. 149 - 159.

Putnam, A. and Williams, R. (1952) *Proc. Combust. Inst.* 4, 556–575.

Putnam, A. A., and Dennis, W. R. (1953) "A Study of Burner Oscillations of the Organ-Pipe Type," *Trans. A.S.M.E.*, vol. 75, no. 1, pp. 15-28

Putman, A. A. and Dennis, W. R. (1954) "Burner oscillations of the gauze-tone type," *Journal of the Acoustical Society of America* 26(5): 716-725.

Putnam, A.A. (1971) *Combustion-Driven Oscillations in Industry*, Elsevier, New York.

Raghu, S. (1987) "Control of combustion and acoustically coupled fluid dynamic instabilities," PhD Thesis, Yale University.

Raun, R.L., Beckstead, M.W., Finlinson, J.C. and Brooks, K.P. (1993) "A Review of Rijke tubes, Rijke burners and related devices," *Progress in Energy and Combustion Science*, vol. 19, pp.313-364.

Rayleigh, L.J.W.S. (1945) *The Theory of Sound*, vol. 2. Dover Publications.

- Reardon, F.,H. (1961) "An Investigation of Transverse Mode Combustion Instability in Liquid Propellant Rocket Motors," PhD Thesis, Princeton University.
- Reardon, F.,H., Crocco, L., and Harrje, D.T. (1967) "Velocity effects in transverse mode liquid propellant rocket combustion instability," NASA-CR-80234
- Reba, I., and Brosilow, C. (1960) Wright Air Dev. Center Tech. Report 59-720, Part III.
- Rehab, H., Villermaux, E., and Hopfinger, J. (1997) "Flow regimes of large-velocity-ratio coaxial jets," *J. Fluid Mech.* vol. 345, pp. 357-381.
- Renard, P.H., Thevenin, D, Rolon, J.C., Candel, S. (2000) "Dynamics of flame/vortex interactions," *Prog. Energy Combust. Sci.* 26(3):pp.225–82
- Richards, G.A., Janus, M.C. (1998) "Characterization of oscillations during premix gas turbine combustion" ASME J. Eng. Gas Turbines Power 120:294–302
- Richecoeur, F., Scouflaire, P., Ducruix, S., and Candel, S. (2006) "High Frequency Transverse Acoustic Coupling in a Multiple-Injector Cryogenic Combustor," *Journal of Propulsion and Power*, vol. 22 (4) 790-799.
- Richtmyer, R.D. (1960) "Taylor instability in shock acceleration of compressible Fluids," *Commun. on Pure and Appl. Math.*, 8:297.
- Rijke, P.L. (1859) "Notiz über eine neue Art, die Luft in einer an beiden Enden offenen Röhre in Schwingungen zu versetzen," *Annalen der Physik* 107, pp. 339–343
- Rudinger, G. (1958) "Shock wave and flame interactions," Presented at *Combust. Prop. Third AGARD Colloq.*, p. 153. Neuilly-Sur-Seine, France: AGARD, NATO
- Rupe, J. H., Jaivin, G. I. (1964) "The effects of injection mass flux distributions and resonant combustion on local heat transfer in a liquid-propellant rocket engine," Report Number: JPL-TR-32-648, NASA-CR-59902
- Santoro, R.J. (1997) "An Experimental Study of Characteristic Combustion-Driven Flow For CFD Validation," NASA Contract NAS8-38862
- Scala, S.,M. (1957) "Transverse Wave and Entropy Wave Combustion Instability in Liquid Propellant Rockets," Princeton University (PhD) Thesis, Aero. Engng. Rep. no. 380.
- Schadow, K.C., Wilson, K.J., Gutmark, E. (1987) "Characterization of Large Scale Structures in a Forced Ducted Flow with Dump," *AIAA Journal*, vol. 25 (9), pp. 1164-1170.

Schadow, K. C., Gutmark, E. (1992) "Combustion Instabilities Related to Vortex Shedding in Dump Combustors and Their Passive Control," *Prog. Energy Combust. Sci.*, vol. 18, pp. 117-132.

Schuller, T., Durox, D. and Candel, S. (2003) "A Unified Model for the Prediction of Laminar Flame Transfer Functions Comparisons between Conical and V-Flame Dynamics," *Combust. Flame* 134, 21-34

Searby, G., and Rochwerger, D. (1991) "A parametric acoustic instability in premixed flames" *J. Fluid Mech.* vol. 231, pp.529-543.

Selerland, T. and Karagozian, A.R. (1998) "Ignition, Burning and Extinction of a Strained Fuel Strip with Complex Kinetics," *Combustion Science and Technology*, vol. 131, issue 1 - 6, pp. 251-276.

Shanbhogue, S.J. (2008) "Dynamics of Perturbed Exothermic Bluff-Body Flow-Fields," PhD Thesis, Georgia Institute of Technology.

Sharp, D.H. (1984) "An Overview of Rayleigh-Taylor Instability," *Physica D* 12:3

Sheridian, J., Soria, J., Jie, W., and Welsch, M.C. (1992) "The Kelvin-Helmholtz instability of the separated shear layer from a circular cylinder," IUTAM Symposium, Gottingen, Germany.

Sinibaldi, J.O., Mueller, C.J., Tulkki, A.E., and Driscoll, J.F. (1998) "Suppression of Flame Wrinkling by Buoyancy: The Baroclinic Stabilization Mechanism," *AIAA Journal*, vol. 36, no. 8.

Sirignano, W.A., Crocco, L., and Harrje, D.T. (1967) Acoustic Liner Studies, ICRPG 3rd Combustion Conference, CPIA Publication No. 138, p.581.

Sirignano, W.A. (1969) "A Theory of Axial-Mode Shock-Wave oscillations in a solid rocket combustor," *Proceedings of the Twelfth Symposium (International) on Combustion*, pp. 129-137.

Smith, R.P. and Sprenger, D.F. (1953) "Combustion Instability in Solid Propellant Rockets," *Proceedings of the Fourth Symposium (International) on Combustion*, Williams and Wilkins, Baltimore MD, p. 893.

Sreenivasan K.R., Raghun S. (2000) "The control of combustion instability: A perspective," *Current Science* 79 (6): 867-883.

Strahle, W.C. (1965) "Unsteady Laminar Jet Flame at Large Frequencies of Oscillation," *AIAA Journal*, vol. 3, no. 6, pp. 957-960.

Strahle, W.C. (1967) "High-Frequency Behavior of the Laminar Jet Flame Subjected to Transverse Sound Waves," *Eleventh Symposium (International) on Combustion*, Combustion Inst., Pittsburgh, PA, pp. 747-754.

Subbaiah, M.V. (1983) "Nonsteady flame spreading in two-dimensional ducts," *AIAA J.* 21 (11) pp. 1557-1564.

Summerfield, M. (1951) "A Theory of Unstable Combustion in Liquid Propellant Rocket Systems," *ARS Journal*, vol. 21, no. 5, pp. 108-114

Sunhara, A., Takeuchi, H., Takabe, H. and Mima, K. (1996) "Shock wave driven instability at material interface in laser driven implosion," *Jpn. J. Appl. Phys.*, 35(10):5501.

Suzuki, M., Atarashi, T., and Masuda, W. (2007) "Behavior and Structure of Internal Fuel-Jet in Diffusion Flame under transverse acoustic excitation" *Combustion Science and Technology*, vol. 179, issue 12, pp. 2581-2597

Swanson, C.D. (1951) "Resonance Burning in Rocket Grains," U.S. Naval Ordnance Test Station, NOTS TM 439.

Taylor, G.I. (1950) "The instability of liquid surfaces when accelerated in a direction perpendicular to their planes, II." *Proc. Royal Soc. Lond.*, A(201):192.

Thring, M.W. (1969) "Combustion Oscillations in Industrial Combustion Chambers," *Twelfth Symposium (International) on Combustion*, The Combustion Institute, pp. 163-168.

Toong, T.Y., Salant, R.F., Stopford, J.M., and Anderson, G.Y. (1965) "Mechanisms of Combustion Instability," *Tenth Symposium (International) on Combustion*, The Combustion Institute, pp. 1301-1313.

Tsien, H.S. (1952) "Servo-Stabilization of Combustion in Rocket Motors," *ARS Journal*, vol. 22, pp. 256-263

Tsuji, H., Takeno, T. (1965) "An Experimental Investigation on High Frequency Combustion Oscillations," *Tenth Symposium (International) on Combustion*, The Combustion Institute, pp. 1327-1335.

Tucker, P.K., Klem, M.D., Smith, T.D., Farhangi, S., Fisher, S.C., and Santoro, R.J. (1997) "Design of efficient GO₂/GH₂ injectors - A NASA, industry and university cooperative effort," *AIAA-1997-3350*.

Tyndall, J. (1867) *Sound.*, Appleton & Company, New York.

- Wangher, A., Searby, G., and Quinard, J. (2008) "Experimental investigation of the unsteady response of premixed flame fronts to acoustic pressure waves", *Combustion and Flame*, vol. 154, issues 1-2, pp. 310-318
- Wanhainen, J.P., Parish, H.C., and Conrad, E.W. (1966) "Effect of Propellant Injection Velocity on Screech in 20 000-Pound Hydrogen-Oxygen Rocket Engine," NASA TN D-3373.
- Wanhainen, J. P. , Bloomer, H. E., Vincent, D. V and Curley, J. K. (1967) "Experimental investigation of acoustic liners to suppress screech in Hydrogen-Oxygen rockets," NASA-TN-D-3822
- Wieber, P.R., Mickelsen, W.R.(1960) "Effect of transverse acoustic oscillations on the vaporization of a liquid-fuel droplet," NASA-TN-D-287
- Williams, F.A. (1984) *Combustion Theory*, Benjamin Cummings, Menlo park, CA, 1984, second edition, chapter 9, pp. 294–372.
- Yachter, M. (1951) Discussion of the Paper by Gunder, D.F., and Friant, D.R., (1950), *Journal of Applied Mechanics*, vol. 18, pp 114-116.
- Yang, V., Culick, F.E.C (1986) "Analysis of Low Frequency Combustion Instabilities in a Laboratory Ramjet Combustor", *Comb. Sci. and Tech.*, vol. 45, pp. 1-25.
- Yang, W. (2001) *Handbook of Flow Visualization*, Taylor & Francis, Second Edition.
- Youngs, D.L. (1984) "Numerical simulation of turbulent mixing by Rayleigh-Taylor instability," *Physica D: Nonlinear Phenomena*, vol. 12, issues 1-3, July 1984, pp. 32-44
- Yu, K., Lee, S., Trouvé, A., Stewart, H., Daily, J.W., (1987) "Vortex Nozzle Interactions in Ramjet Combustors," *AIAA paper # 87-1871*.
- Yu, K., Trouvé, A., and Daily, J. (1991) "Low-frequency pressure oscillation in a model ramjet combustor," *Journal of Fluid Mechanics*, vol. 232, pp. 47-72.
- Zambon, A.C., and Chelliah, H.K. (2006) "Self-sustained acoustic-wave interactions with counterflow flames," *J. Fluid Mech.*, vol. 560, pp. 249–278.
- Zinn, B.T., and Savell, C.T., (1969), "A Theoretical Study of Three-Dimensional Combustion Instability in Liquid-Propellant Rocket Engines," *Twelfth Symposium (International) on Combustion*, The Combustion Institute, pp. 139-148.
- Zinn, B.T. (1986) "Pulsating Combustion" In Weinberg, F. (ed.), *Advanced Combustion Methods*, Academic Press, 1986, chapter 2.

Zinn, B.T., Powell, E.A. (1971) "Nonlinear Combustion Instability in Liquid Propellant Rocket Engines," *Thirteenth Symposium (International) on Combustion*, The Combustion Institute, pp. 491-503.